35. Particle Detectors at Accelerators

Revised March 2026. See the various sections for authors.

35.1 Introduction . . . 2
35.2 Photon detectors . . . 3
35.2.1 Vacuum photodetectors . . . 4
35.2.2 Gaseous photon detectors . . . 6
35.2.3 Solid-state photon detectors . . . 7
35.2.4 Superconducting photon detectors . . . 8
35.3 Organic scintillators . . . 9
35.3.1 Scintillation mechanism . . . 9
35.3.2 Plastic scintillator practicalities . . . 11
35.3.3 Organic glass scintillators . . . 12
35.3.4 Liquid scintillator practicalities . . . 12
35.3.5 Summary . . . 12
35.4 Inorganic scintillators . . . 13
35.5 Cherenkov detectors . . . 18
35.6 Gaseous detectors . . . 24
35.6.1 Energy loss and charge transport in gases . . . 24
35.6.2 Multi-Wire Proportional and Drift Chambers . . . 30
35.6.3 Micro-Pattern Gas Detectors . . . 33
35.6.4 Time-projection chambers . . . 40
35.6.5 Transition radiation detectors (TRD's) . . . 44
35.6.6 Resistive-plate chambers . . . 48
35.7 LAr Time Projection Chamber . . . 55
35.7.1 Introduction . . . 55
35.7.2 Ultra-pure Liquid Argon . . . 55
35.7.3 Charge and Light Signals . . . 57
35.7.4 LAr TPC topologies . . . 58
35.7.5 Data Acquisition . . . 60
35.7.6 Event reconstruction . . . 60
35.7.7 Developments . . . 61
35.8 Semiconductor detectors . . . 62
35.8.1 Signal generation in semiconductors . . . 63
35.8.2 Junction detectors . . . 65
35.8.3 Detectors with structured electrodes . . . 68
35.8.4 Precise timing with silicon detectors . . . 72
35.8.5 Radiation damage in silicon detectors . . . 73
35.9 Low-noise detector readout . . . 78
35.9.1 Principal noise origins . . . 80
35.9.2 Noise in MOS devices . . . 81
35.9.3 Equivalent noise analysis . . . 82
35.9.4 Timing measurements . . . 87
35.9.5 Digital signal processing . . . 88
35.9.6 What to use when? . . . 89

35.10 Calorimeters . . . 89
35.10.1 Introduction . . . 89
35.10.2 Electromagnetic calorimeters . . . 95
35.10.3 Hadronic calorimeters . . . 97
35.10.4 Free electron drift velocities in liquid ionization chambers . . . 106
35.11 Superconducting magnets for collider detectors . . . 107
35.11.1 Solenoid Magnets . . . 107
35.11.2 Properties of collider detector magnets . . . 109
35.11.3 Toroidal magnets . . . 110
35.12 Measurement of particle momenta in a uniform magnetic field . . . 111

35.1 Introduction

This review summarizes the detector technologies employed at accelerator particle physics experiments. Several of these detectors are also used in a non-accelerator context and examples of such applications will be provided. The detector techniques which are specific to non-accelerator particle physics experiments are the subject of Chap. 36. More detailed discussions of detectors and their underlying physics can be found in books by Kolanoski & Wermes [1], Ferbel [2], Kleinknecht [3], Knoll [4], Green [5], Leroy & Rancoita [6], and Grupen [7].

Table 35.1: Typical resolutions and deadtimes of common charged particle detectors in tracking applications. See respective sections for details on R&D efforts and their achieved performances. Revised September 2025.

Detector Type	Intrinsinc Spatial Resolution (rms)	Time Resolution	Dead Time
Resistive plate chamber	50 μm	50–1000 ps[*]	10 ns[†]
Liquid argon TPC	0.5–1 mm[‡]	0.01-1 μs[§]	—[¶]
Scintillation tracker	$\sim$100 μm	100 ps/n[‖]	10 ns
Bubble chamber	10–150 μm	1 ms	50 ms[**]
Wire chambers (proportional and drift chambers)	50–100 μm	5–10 ns[††]	20–200 ns[‡‡]
Micro-pattern gas detector	30–40 μm	5–10 ns[††]	20–200 ns[‡‡]
Silicon strips/pixels	$\lesssim$ 10 μm[§§]	few ns[¶¶ ‡‡]	$\lesssim$ 50 ns[‡‡]

[*] LHC: $\sim$2 mm gap, $\sim$1 ns. HL-LHC: $\sim$1 mm gap, $\sim$350 ps. Timing RPC: $\sim$50 ps
[†] Limited by amplifier and discriminator bandwidth, usually around 100 MHz
[‡] Detector geometry dependent
[§] Using the scintillation signal
[¶] No deadtime for medium
[‖] n = index of refraction.
[**] Multiple pulsing time.
[††] For MIPs
[‡‡] Depending/limited by the analog and digital front-end electronics (see [8] and 35.9)
[§§] Depending on electrode pitch, best values around a few μm have been achieved
[¶¶] Resolutions $<$ 30 ps are reached in dedicated developments

In Table 35.1 are given typical resolutions and deadtimes of common charged particle detectors. The quoted numbers are usually based on typical devices, and should be regarded only as rough

approximations for new designs. The spatial resolution refers to the intrinsic detector resolution, i.e. without multiple scattering. We note that analog detector readout can provide better spatial resolution than digital readout by measuring and averaging the deposited charge in neighboring channels. Quoted ranges attempt to be representative of both possibilities. The time resolution is defined by how accurately the time at which a particle crossed the detector can be determined. The deadtime is the minimum separation in time between two resolved hits on the same channel. Typical performance of calorimetry and particle identification are provided in the relevant sections below.

35.2 Photon detectors

Revised August 2023 by P. Križan (Ljubljana U; Jozef Stefan Inst.).

Most detectors in high-energy, nuclear, and astrophysics rely on the detection of photons in or near the visible range, $100\,\text{nm} \lesssim \lambda \lesssim 1000\,\text{nm}$, or $1\,\text{eV} \lesssim E \lesssim 10\,\text{eV}$. This range covers scintillation and Cherenkov radiation as well as the light detected in many astronomical observations.

Generally, photodetection involves generating a detectable electrical signal proportional to the (usually very small) number of incident photons. The process involves three distinct steps:

1. generation of a primary photoelectron or electron-hole (e-h) pair by an incident photon by the photoelectric or photoconductive effect,
2. multiplication of the photoelectron or electron-hole pair signal to detectable levels, usually by one or more multiplicative bombardment steps and/or an avalanche process, and,
3. detection of charges induced by secondary electrons.

The important characteristics of a photodetector include the following:

1. quantum efficiency (QE or ϵ_Q): the average number of primary photoelectrons generated per incident photon ($0 \leq \epsilon_Q \leq 1$; in silicon more than one e-h pair per incident photon can be generated for $\lambda \lesssim 165$ nm),
2. collection efficiency (CE or ϵ_C): the overall acceptance factor other than the generation of photoelectrons ($0 \leq \epsilon_C \leq 1$),
3. gain (G): the number of electrons collected for each photoelectron generated,
4. dark current or dark noise: the electrical signal when there is no incident photon,
5. precision of measuring the intensity I of the incoming light: electronic noise (ENC or N_e) and statistical fluctuations in the amplification process compound the Poisson distribution of n_γ photons from a given source:

$$\frac{\sigma(I)}{\langle I \rangle} = \sqrt{\frac{f_N}{n_\gamma \epsilon_Q \epsilon_C} + \left(\frac{N_e}{G n_\gamma \epsilon_Q \epsilon_C}\right)^2}, \tag{35.1}$$

   where f_N, or the excess noise factor (ENF), is the contribution to the intensity distribution variance due to multiplication statistics [9],
6. dynamic range, linearity and saturation: relation between the number of incident photons and the sensor output in the pulsed mode,
7. time dependence of the response: this includes the transit time, which is the time between the arrival of the photon and the electrical pulse, and the transit time spread, and
8. rate capability: maximal rate of light pulses at which detection is still possible.

Table 35.2: Representative characteristics of some photodetectors commonly used in particle physics.

Type	λ (nm)	$\epsilon_Q\,\epsilon_C$	Gain	Risetime (ns)	Single photon time resol. (ps)	Area (mm^2)	1-p.e noise * (Hz/mm^2)	HV (V)
PMT †	115–1700	0.15–0.25	10^5–10^7	0.7–10	∼200	10–10^5	10^{-2}–10^2	500–3000
MCP-PMT†	115–650	0.01–0.10	10^3–10^7	0.15–0.3	∼20	1–10^4	1–10	500–3500
HPD†	115–850	0.1–0.3	10^3–10^4	$O(1)$	∼1000	10–10^5	10–100	$\sim 2\times10^4$
HAPD†	115–850	0.1–0.3	10^4–10^5	$O(1)$	∼30	10–10^5	∼1	$\sim 1\times10^4$
GPD†	115–500	0.15–0.3	10^3–10^6	$O(0.1)$	∼100	$O(10)$	∼1	300–2000
APD	300–1700	∼0.7	10–10^8	$O(1)$	- ‡	1–10^3	$O(10^7)$ §	400–1400
SiPM	125–1000	0.15–0.4	10^5–10^6	∼ 1	∼50	1–36	10^4–10^5	30–60

*Normalized to photocathode/sensor area; room temperature operation assumed.
†These devices often come in multi-anode configurations. In such cases, the area is to be considered on a “per readout-channel" basis.

‡No single photon detection possible.
§Since in an APD no single photon detection is possible, dark current is usually quoted instead of the dark count rate; here we assumed a gain of 50 to convert from the dark current to the dark count rate.

The QE is a strong function of the photon wavelength (λ), and is usually quoted at maximum, together with a range of λ where the QE is comparable to its maximum. Spatial uniformity and linearity with respect to the number of photons are highly desirable in a photodetector response.

Optimization of these factors involves many trade-offs and varies widely between applications. For example, while a large gain is desirable, attempts to increase the gain for a given device also increases the ENF and after-pulsing ("echos" of the main pulse). In solid-state devices, a higher QE often requires a compromise in the timing properties. In other types, coverage of large areas by focusing photoelectrons increases the transit time spread.

Other important considerations also are highly application-specific. These include the photon flux and wavelength range, the total area to be covered, and the efficiency required, the volume available to accommodate the detectors, characteristics of the environment such as chemical composition, temperature, magnetic field, ambient background, as well as ambient radiation of different types, mode of operation (continuous or triggered), bias (high-voltage) requirements, power consumption, calibration needs, aging, cost, and so on. Several technologies employing different phenomena for the three steps described above, and many variants within each, offer a wide range of solutions to choose from. The salient features of the main technologies and the common variants are described below. Some key characteristics are summarized in Table 35.2.

35.2.1 *Vacuum photodetectors*

Vacuum photodetectors can be broadly subdivided into three types: photomultiplier tubes, microchannel plate photomultiplier tubes, and hybrid photodetectors.

35.2.1.1 *Photomultiplier tubes*

A versatile class of photon detectors, vacuum photomultiplier tube (PMT) has been employed by a vast majority of all particle physics experiments to date [9]. Both “transmission-" and “reflection-type" PMTs are widely used. In the former, the photocathode material is deposited on the inside of a transparent window through which the photons enter, while in the latter, the photocathode material rests on a separate surface that the incident photons strike. The cathode material has a low work function, chosen for the wavelength band of interest. When a photon hits the cathode and liberates an electron (the photoelectric effect), the latter is accelerated and guided by electric fields

to impinge on a secondary-emission electrode, or dynode, which then emits several(~ 5) secondary electrons. The multiplication process is repeated typically about 10 times in series to generate a sufficient number of electrons, which are collected at the anode for delivery to the external circuit. The total gain of a PMT depends on the applied high voltage V as $G = AV^{kn}$, where $k \approx 0.7$–0.8 (depending on the dynode material), n is the number of dynodes in the chain, and A a constant (which also depends on n). Typically, G is in the range of 10^5–10^7; time resolution is $O(1ns)$ but can be as good as ≈ 100 ps for certain PMT types.

A large variety of PMTs covers a wide span of wavelength ranges from infrared (IR) to extreme ultraviolet (XUV) [10]. They are categorized by the window materials, photocathode materials, dynode structures, and anode configurations. Common window materials are borosilicate glass for IR to near-UV, fused quartz and sapphire (Al_2O_3) for UV, and MgF_2 or LiF for XUV. The choice of photocathode materials include a variety of mostly Cs- and/or Sb-based compounds such as CsI, CsTe, bi-alkali (SbRbCs, SbKCs), multi-alkali (SbNaKCs), GaAs(Cs), GaAsP(Cs), *etc.* Sensitive wavelengths and peak quantum efficiencies for these materials are summarized in Table-35.3. Typical dynode structures used in PMTs are circular cage, line focusing, box-and-grid, venetian blind, and fine mesh.

Multianode PMTs (MaPMTs) of up to 5×5 cm^2 in size are based on the parallel (side-by-side) arrangement of several dynode channels and anodes in the same tube, requiring advanced micro-machining and processing techniques. Fast PMTs with very large windows—measuring up to 508 mm across—have been developed for detection of Cherenkov radiation in neutrino experiments such as Super-Kamiokande and KamLAND among many others. Specially prepared low-radioactivity glass is used to make these PMTs, and they are also able to withstand the high pressure of the surrounding liquid.

PMTs are vulnerable to magnetic fields—sometimes even the geomagnetic field causes large orientation-dependent gain changes. A high-permeability metal shield is often necessary. However, proximity-focused PMTs, *e.g.* the fine-mesh types, can be used even in a high magnetic field ($\geq$ 1 T) if the direction of electric field of the tube is close to the direction of the external magnetic field. CMS uses custom-made vacuum phototriodes (VPT) mounted on the back face of projective lead tungstate crystals to detect scintillation light in the endcap sections of its electromagnetic calorimeters, which are inside a 3.8 T superconducting solenoid. A VPT employs a single dynode (thus, $G \approx 10$) placed close to the photocathode, and a mesh anode plane between the two, to help it cope with the strong magnetic field, which is not too unfavorably oriented with respect to the photodetector axis in the endcaps (within 25°), but where the radiation level is too high for Avalanche Photodiodes (APDs) like those used in the barrel section.

35.2.1.2 *Microchannel plate photomultiplier tubes*

A typical microchannel plate photomultiplier tube (MCP-PMT) consists of two or more $\sim$1 mm thick glass plates with densely packed $O(10\ \mu$m)-diameter cylindrical holes, or "microchannels", sitting between the transmission-type photocathode and anode planes, separated by $O(1$ mm) gaps. Instead of discrete dynodes, the inner surface of each cylindrical hole with a length-to-diameter ratio of 40-100 serves as a continuous dynode for the entire cascade of multiplicative bombardments initiated by a photoelectron. Gain fluctuations are reduced by operating each of the MCPs in the saturation mode. MCPs are stacked in a "chevron" configuration that alternates their bias angle; this reduces ion and photon feed-back effects and optimizes the overall amplification gain.

MCP-PMTs are thin, offer good spatial resolution, have excellent time resolution ($\sim$20 ps), and can tolerate magnetic fields up to 0.1 T and axial fields up to $1 - 2$ T. The technology has significantly evolved over the past 10 years [11]. A main breakthrough was the introduction of the atomic layer deposition (ALD) coatings on the MCP surfaces to increase the lifetime (>20 C/cm^2 of

charge accumulated on the anode) and gain. The Large Area Picosecond Photo-Detector (LAPPD) project [12] is an important attempt to produce at a reasonable cost large (20 by 20 cm^2) sensors with a transit time spread of 50-70 ps.

35.2.1.3 *Hybrid photon detectors*

Hybrid photon detectors (HPD) combine the sensitivity of a vacuum PMT with the excellent spatial and energy resolutions of a silicon sensor [13]. A single photoelectron ejected from the photocathode is accelerated through a large potential difference of ∼20 kV before it impinges on the silicon sensor/anode. The gain nearly equals the maximum number of *e*-*h* pairs that could be created from the entire kinetic energy of the accelerated electron: $G \approx \mathrm{eV}/w$, where e is the electronic charge, V is the applied potential difference, and $w \approx 3.7$ eV is the mean energy required to create an *e*-*h* pair in Si at room temperature. Since the gain is achieved in a single step, one can expect to have the excellent resolution of a simple Poisson statistic with large mean, but in fact it is even better, thanks to the Fano effect discussed in Sec. 35.8.

Low-noise electronics must be used to read out HPDs if one intends to take advantage of the low fluctuations in gain, *e.g.* when counting small numbers of photons. HPDs can have the same $\epsilon_Q\,\epsilon_C$ and window geometries as PMTs and can be segmented down to ∼50 μm. However, they require rather high biases and will not function in a magnetic field. The exception is proximity-focused devices (⇒ no (de)magnification) in an axial field. With time resolutions of ∼10 ps and superior rate capability, proximity-focused HPDs can be an alternative to MCP-PMTs. Applications of HPDs include the CMS hadronic calorimeter and the RICH detector in LHCb. Large-size HPDs with sophisticated focusing may be suitable for future water Cherenkov experiments.

Hybrid APDs (HAPDs) add an avalanche multiplication step following the electron bombardment to boost the gain by a factor of ∼50. This affords a higher gain and/or a lower bias voltage, but also increases the detector capacitance and fluctuations in multiplication. The forward RICH detector of Belle II uses a 144-channel device of this type [14].

Table 35.3: Properties of photocathode and window materials commonly used in vacuum photodetectors. [10]

Photocathode material	λ (nm)	Window material	Peak ϵ_Q (λ/nm)
CsI	115–200	MgF_2	0.13 (130)
CsTe	115–320	MgF_2	0.17 (200)
Bi-alkali	300–650	Borosilicate	0.27 (390)
	160-650	Synthetic Silica	0.27 (390)
"Ultra Bi-alkali"	300–650	Borosilicate	0.43 (350)
	160-650	Synthetic Silica	0.43 (350)
Multi-alkali	300–850	Borosilicate	0.20 (375)
	160-850	Synthetic Silica	0.25 (380)
GaAsP(Cs)	280-720	Borosilicate	0.40 (480-530)

35.2.2 *Gaseous photon detectors*

In a gaseous photon detector (GPD) a photoelectron in a suitable gas mixture initiates an avalanche in a high-field region, producing a large number of secondary impact-ionization electrons. In principle the charge multiplication and collection processes are identical to those employed in gaseous tracking detectors such as multiwire proportional chambers (MWPC), micromesh gaseous detectors (Micromegas), or gas electron multipliers (GEM). These are discussed in Sec. 35.6.3.

The devices can be divided into two types depending on the photosensitive material. One type uses solid photocathode materials much in the same way as PMTs. Since it is resistant to gas mixtures typically used in tracking chambers, CsI is a common choice. In the other type, photoionization occurs on suitable molecules vaporized and mixed in the drift volume. Most gases have photoionization work functions in excess of 10 eV, which would limit their sensitivity to wavelengths far too short. However, vapors of tetrakis dimethyl-amine ethylene (TMAE) or tri-ethyl-amine (TEA), which have smaller work functions (5.3 eV for TMAE and 7.5 eV for TEA), are suited for XUV photon detection [15]. Since devices like GEMs offer sub-mm spatial resolution, GPDs are often used as position-sensitive photon detectors. They can be made into flat panels to cover large areas ($O(1\ \mathrm{m}^2)$), can operate in high magnetic fields, and are relatively inexpensive. Many of the ring imaging Cherenkov (RICH) detectors have used GPDs for the detection of Cherenkov light [16–19]. Special care must be taken to suppress the ion-feedback and photon-feedback processes in GPDs. It is also important to maintain high purity of the gas as minute traces of O_2 or H_2O can significantly degrade the detection efficiency.

35.2.3 *Solid-state photon detectors*

In a phase of rapid development, solid-state photodetectors are competing with vacuum- or gas-based devices for many existing applications and making way for a multitude of new ones. Compared to traditional vacuum- and gaseous photodetectors, solid-state devices are more compact, lightweight, rugged, tolerant to magnetic fields, and often cheaper. They also allow fine pixelization, are easy to integrate into large systems, and can operate at low electric potentials, while matching or exceeding most performance criteria.

Silicon photodiodes (PD) are widely used in high-energy physics as particle detectors and in a large number of applications as photon detectors. The structure is discussed in some detail in Sec. 35.8. In its simplest form, the PD is a reverse-biased p-n junction. Photons with energies above the indirect bandgap energy (wavelengths shorter than about 1050 nm, depending on the temperature) can create e-h pairs (the photoconductive effect), which are collected on the p and n sides, respectively. Often, as in the PDs used for crystal scintillator readout in CLEO, L3, Belle, BaBar, and GLAST, intrinsic silicon is doped to create a p-i-n structure. The reverse bias increases the thickness of the depleted region; in the case of these particular detectors, to full depletion at a depth of about 100 μm. Increasing the depletion depth decreases the capacitance (and hence electronic noise) and extends the red response. Quantum efficiency can exceed 90%, but falls toward the red because of the decrease of the light absorption probability in silicon; the absorption length reaches 100 μm at 985 nm. However, since $G = 1$, electronic signal amplification is necessary. Optimal low-noise amplifiers are slow, but, even so, noise limits the minimum detectable signal in room-temperature devices to several hundred photons.

In APDs, an exponential cascade of impact ionizations initiated by the original photogenerated e-h pair under a large reverse-bias voltage leads to an avalanche multiplication [20–23], and eventually to breakdown in Geiger-mode APDs. As a result, detectable electrical response can be obtained from low-intensity optical signals down to single photons. Excellent junction uniformity is critical, and a guard ring is generally used as a protection against edge breakdown. Well-designed APDs, such as those used in CMS crystal-based electromagnetic calorimeter, have achieved $\epsilon_Q\,\epsilon_C \approx 0.7$ with sub-ns response time. The sensitive wavelength window and gain depend on the semiconductor used. The gain is typically 10–200 in linear and up to 10^8 in Geiger mode of operation. Stability and close monitoring of the operating temperature are important for linear-mode operation, and substantial cooling is often necessary.

One of the most promising recent developments in the field is SiPMs ("Silicon Photomultiplier"), a device consisting of large arrays ($O(10^3)$) of tiny APDs packed over a small area ($O(1\ \mathrm{mm}^2)$) and

operated in a limited Geiger mode [24–26]. Although each cell only offers a binary output, linearity with respect to the number of photons is achieved by summing the cell outputs. The sum of all cells is proportional to the number of photons received so long as the probability of an individual cell receiving multiple photons during a single time gate is negligible. SiPMs are being adopted as the preferred solution for various purposes including medical imaging, *e.g.* positron emission tomography (PET). These compact, rugged, and economical devices allow auto-calibration through decent separation of photoelectron peaks and offer gains of $O(10^6)$ at a moderate bias voltage (∼30 V). However, the single-photoelectron noise of a SiPM, being the logical "or" of $O(10^3)$ Geiger APDs, is rather large: O(10-100 kHz/mm^2) at room temperature. Intensive R&D in recent years [27] led to a substantial reduction in dark count rates and in correlated noise levels, resulting in coverage of larger areas and in a wider range of applications. One way to further improve the signal-to-noise ratio in SiPMs is by using dedicated light collectors, either as quartz Winston cone like arrays [28] or suitably designed meta-materials [29]. In this way, photons propagate from a larger entry window to a considerably smaller semiconductor sensor, resulting in an improved signal photon to dark-count ratio. Intense R&D is expected to improve radiation hardness of these sensors. The fabrication of the sensors and the front-end electronics combined in the same process with the goal of making SiPMs extremely easy to use has already been successful (digital SiPMs) [30], and remains a topic of intense R&D.

More solid-state light sensors have either been developed or are potentially interesting for use in HEP experiments. The Run 2 DØ detector used 86000 Visible-light photon counters (VLPC) to read the optical signal from its scintillating-fiber tracker and scintillator-strip preshower detectors. These light sensors utilize the formation of an impurity band only 50 meV below the conduction band in As-doped Si to generate strong ($G \approx 5 \times 10^4$) yet sharp response to single photons with $\epsilon_Q \approx 0.9$ [31–33]. Only a very small bias (∼7 V) is needed, but high sensitivity to infrared photons requires cooling below 10 K. Another interesting light sensor that has not yet found its use in HEP instrumentation are quantum dots, realized by nanometer-sized semiconductor 'particles' embedded in a semiconductor bulk.

35.2.4 *Superconducting photon detectors*

In this rapidly developing technology field, three most established technologies are the superconducting nano-wire single photon detector (SNSPD), the transition edge sensor (TES), and the microwave kinetic inductance detector (MKID). An SNSPD consists of a thin (4 nm) and narrow (100-250 nm) superconducting nanostrip that is current-biased just below its critical current. Absorption of a photon generates a resistive domain in the superconducting nanostrip, which leads to a transient voltage signal that can be detected. SNSPDs offer a unique combination of speed, both in terms of count rate (∼GHz) and low timing jitter (< 3 ps [34]), large range of wavelength sensitivity from VUV (120 nm) to mid-IR (10 μm), high detection efficiencies (approaching 100% for UV to near-IR), and low dark count rates (∼5-10 Hz), making them appealing for a wide variety of demanding applications.

Examples of present use in particle physics are small nanowire detectors for dark matter and dark photons. Work is in progress that could make these sensors relevant to HEP applications by increasing the area (using 300 mm wafers and larger) and pixel size, coupling via windows to cryogenic stages, and readout of arrays (superconducting electronics for data processing). While the performance of these sensors is impressive, an application in large accelerator-based detectors would require an extensive R&D program because of the severe cryogenic requirements.

35.3 Organic scintillators

Revised August 2025 by S.C. Eno (U. Maryland) and M. Hamel (Paris-Saclay U. CEA, LIST).

Organic scintillators produce light when transversed by a charged particle. They can be broadly categorized into four types: single crystal, liquid, plastic, and a recently emerged organic glass [35]. The most useful scintillators produce photons with wavelengths between 370-750 nm (ultraviolet to red), typically peaking at 425 nm [36] via a series of processes that are initialized when charged particles interact with the material via both excitation and ionization/recombination (see Sec. 34.2 of this *Review*). Typical light yields are about 1 photon per 100 eV of energy deposit [37], although the collected and transduced signal can be much lower. Methods to guide the light towards the photon-electron converter, such as diffusive paint, reflectors, photonic crystals, or light guides, may be required to optimize light yield.

Organic scintillators have found use in a wide variety of detectors [38]. Plastics are mostly used in collider detectors, and liquids in neutrino experiments. Ease of fabrication into desired shapes and low cost has made plastic scintillator ideal for large detectors. In the form of scintillating fiber, it has found widespread use in tracking and calorimetry. Demand for large volume detectors (e.g. neutrino detectors: MiniBooNE, NOvA) has led to increased use of liquid scintillator, which can be very low cost.

35.3.1 *Scintillation mechanism*

Plastic and liquid scintillators are based on an aromatic "matrix" such as benzene. The p electrons form both "pi" and "sigma" bonds between the atoms; the pi bonds are responsible for scintillation. Scintillation is produced via standard photophysical interactions, shown schematically in Fig. 35.1. Via radiation-matter interactions, the matrix is excited to various singlet states. By internal conversion (which is non radiative), the system relaxes to the S_1 state. Vibrational relaxation can also lead to non-radiative decays from excited singlet states. Intersystem crossing occurs primarily for particles with large energy deposition per unit path length dE/dx, and can be be used for their identification. While there have been claims of delayed light production on long time scales (labeled "phosphorescence" in the figure), this is still a subject of active debate in the community. As aromatic molecules scintillate in the ultraviolet (UV), useful scintillators have one or several fluorophores dissolved into the matrix as dopants. Common fluorophores include 2,5-diphenyloxazole, *p*-terphenyl, 9,10-diphenylanthracene (9,10-DPA), 1,4-bis(2-methylstyryl)benzene (bis-MSB) and 1,4-bis(5-phenyl-2-oxazolyl)benzene (POPOP). The key aspects of their molecular structure include pi-conjugated systems and steric effects; in particular functional groups located on the aromatic rings strongly influence their scintillation performance. Each molecule has its own role: the matrix (whether liquid or plastic) is where most of the radiation/matter interaction occurs. Numerous publications have demonstrated the strong dependence of the scintillator's response to the fluorophores concentration. At high concentrations, the probability of quenching increases, and the light output generally plateaus. After radiation interaction, ions may recombine giving birth to excited molecules (excitons). Excitons in the matrix are transferred to a "primary fluorophore", whose concentration is typically 1-3 weight % in commercial plastic and liquid scintillators. This concentration is large enough to ensure exciton transfer – primarily via the Förster mechanism, a resonant dipole-dipole interaction which decreases at sixth the power of the distance between molecules. The concentration, however, can be up to the solubility limit. Transfer via the Förster mechanism increases both speed and light output of the organic scintillator. To reduce reabsorption of the emitted light by the matrix or the primary fluorophore, and the resulting shortened attenuation length, a "secondary fluorophore" is also used to shift the light to longer wavelengths. Transfer from the primary to the secondary is generally radiative. Typical secondary concentrations in plastic and liquids are 0.01-0.2 weight %. The chain of emission and absorption from the matrix

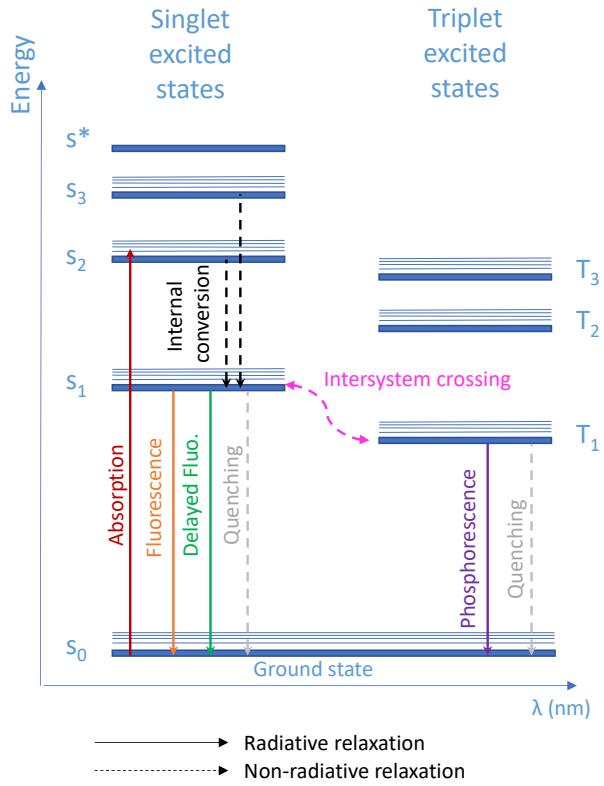

Figure 35.1: Schematic of scintillation mechanism. Schematic of typical excitation and de-excitation of matrix modules.

to the subsequent fluorophores is shown in Fig. 35.2.

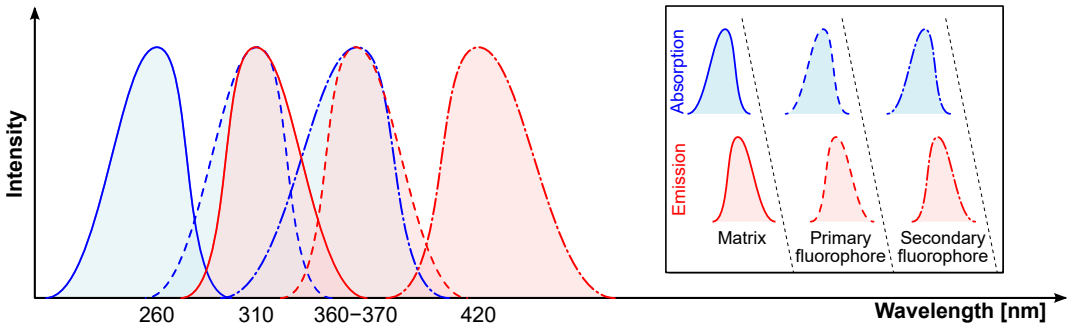

Figure 35.2: Schematic of scintillation mechanism. Typical emission and absorption spectra for the matrix, the primary, and the secondary fluorophore.

Scintillators with two fluorophores typically have absorption lengths of several meters. The longest attenuation lengths require a third fluorophore: when the matrix is transparent up to 1 cm, adding a primary fluorophore increases the light transmission up to ≈ 10 cm, whereas the ternary cocktail is transparent up to 2 m and longer [39].

For most scintillators, decay times are in the ns range; rise times are much faster. Sub-ns timing resolutions have been achieved [40].

Organic scintillators do not respond linearly to the ionization density. Very dense ionization tracks, with large dE/dx, emit less light than expected compared to minimum-ionizing particles.

A widely used semi-empirical model by Birks posits that recombination and quenching effects between the excited molecules reduce the light yield [41]. These effects are more pronounced when the density of excited molecules is larger. Birks' formula is

$$\frac{d\mathcal{L}}{dx} = \mathcal{L}_0 \frac{dE/dx}{1 + kB\, dE/dx}, \tag{35.2}$$

where $\mathcal{L}$ is the luminescence, $\mathcal{L}_0$ is the luminescence at low specific ionization density, and the product kB is known as Birks' constant, which must be determined for each scintillator by measurement. The value of kB for polystyrene is 0.126 mm/MeV, which is large enough to play an important role in compensation in scintillator-based calorimetry. The high hydrogen content of plastic, which enhances the neutron interaction cross section, as well as its large mass stopping power, also contributes to calorimetry compensation. In the case of large or small [42] dE/dx values (e.g. with alpha particles or tritium, respectively), ion recombination may lead to the creation of triplet excited states instead of singlet excited states. If two triplet states are close enough (typically in the order of 10Å), then triplet-triplet annihilation may occur following the Dexter process [43], leading to delayed fluorescence. This phenomenon is useful for α/β or neutron/γ discrimination and is more efficient in liquid scintillators than in plastics due to the molecular motion.

Extensive research for new efficient molecules that can act as matrix, primary, or secondary fluorophores, is ongoing [44]. Other chemical modifications can affect the scintillator emission wavelength and decay time, or be used *e.g.* as stabilizers or to enhance thermal neutron sensitivity. Other parameters that can be modified are the density and the effective atomic number. Recently a new chemical formulation was developed for the search for double beta plus decays at the NuDoubt^{++} experiment. The new scintillator is a combination of hybrid ("slow" plastic scintillator for Cherenkov rejection) and opaque scintillator (to confine scintillation light through Mie scattering of optical photons) [45]. Also of note is a development related to the Mobile Antineutrino Demonstrator Project: embedding ^{6}Li-doped pulse shape discriminating plastic scintillators into 1 m long segments at 6 cm ×6,cm cross section assembled as a 2D array [46].

A major issue is efficiently choosing the most promising molecules, and so usually new organic scintillators are found via a lengthy trial-and-error procedure. A neural architecture built for organic molecule selection for sub-GeV dark matter detection [47] obtained promising results, notably by confirming the backbone of well-known fluorophores.

35.3.2 *Plastic scintillator practicalities*

Plastic scintillators are cheap, can be prepared at large volumes and purity, are reliable, robust, and convenient. Their high chemical versatility allows innovations in material science to open new research fields in high-energy physics. Most commercial plastic scintillators use either polystyrene (PS) or poly(vinyltoluene) (PVT) as matrix. A variety of manufacturing techniques [44] are used in the production of plastic scintillator. Cast plastic has the highest light yield, while extruded scintillator is less expensive and allows creation of the scintillator and coating with a diffusive reflector in a single process. 3D printing of plastic scintillator has also emerged as a reliable production method. The technique has been applied to plastics for pulse-shape discrimination [48] and 3D tracking [49]. However, large-scale production (10+ liters) has not yet been achieved. Plastic scintillator is also used to produce scintillating, wavelength-shifting, and clear fibers. These fibers can be useful to guide light to photodetectors, and as the active element in the type of calorimeter pioneered by the RD52/DREAM collaboration [50]. They have even been used in the construction of trackers [51, 52]. A 3D-segmented detector for particle tracking and calorimetry has been achieved. SuperCube is a $5 \times 5 \times 5$ configuration of 1 cm^3 PS-based plastic scintillators prepared by additive manufacturing (fused deposition modeling) with embedded Kuraray Y11 wavelength-shifting fibers connected to Multi-Pixel Photon Counters [53].

Plastic scintillators are reliable, robust, and convenient. However, exposure to solvent vapors, high temperatures, mechanical flexing, irradiation, or rough handling will cause degradation. The surface is a particularly fragile region and can "craze" – develop microcracks which degrade transmission of light by total internal reflection. Crazing is particularly likely where oils, solvents, or fingerprints have contacted the surface or when mechanical stresses are present. The light yield is influenced by several environmental factors: it decreases with the partial pressure of oxygen [54] and increases with increasing magnetic field [55]. In particular, the combination of elevated temperature with relative humidity accelerates aging. This apparent fogging is typically observed in radiation portal monitors, which are exposed to harsh environmental conditions. The aging can become irreversible after multiple cycles. Recently the T2K collaboration reported a 10-year light-yield measurement showing damage due to aging [56].

Plastics are susceptible to radiation damage [57, 58]. At high enough dose, the visible color of the plastic can change to yellow or even brown. The amount of damage for a fixed dose is higher at lower dose rates [59–61]. During irradiation, the transparency of the plastic decreases. When the irradiation ends, this can reverse and the transparency can increase ("anneal"). This process is faster in the presence of oxygen, which can diffuse into the plastic. Oxygen can also suppress temporary damage during irradiation, although this mechanism can be strongly suppressed at low enough temperatures [62]. The ratio of the light output to the unirradiated light output can roughly be parameterized as an exponential. For dose rates typical of current collider detectors at the Large Hadron Collider (from a few 10^{-3} to 10 Gy/hr), an exponential dose constant of tens of kGy is observed.

35.3.3 *Organic glass scintillators*

Starting in 2016, extensive research by Sandia National Laboratories lead to a new organic scintillator family: organic glasses (OGSs) [63]. Whereas polymers are long-chain molecules built from a standard unit called a monomer, OGSs consist of small organic molecules. In addition, polymers such as PS or PVT require dopants, when OGSs are intrinsically good scintillators. This new material has the useful properties present in inorganic single crystals (light yield, pulse-shape discrimination properties, along with fast-timing properties), without the poor mechanical characteristics seen in single crystals. The maintenance of the amorphous state of these bulk optical materials was achieved mainly either by using molecules with high configurational disorder or by introducing compositional disorder. OGSs can be prepared in medium to large scales when they are blended with polymers, or pixelated for neutron detection systems, and they can eventually be loaded with heavy elements. In 2021 Blueshift Optics secured a license from Sandia National Laboratories for the industrial production of OGSs.

35.3.4 *Liquid scintillator practicalities*

Liquid scintillators have been used in large scale neutrino experiments 36.3.1.1 due to their low cost. They can hermetically fill any vessel shape. Liquid scintillators are also, due to the mobility of the molecules, much less susceptible to radiation damage.

Care must be taken to avoid dissolved water, solvents such as isopropyl alcohol, and oxygen, which reduce light yield. As they can dissolve many materials (e.g. plastics, adhesives, paints..) care must be taken in their handling. Flammability concerns limit their use in practical experiments in intense radiation fields.

35.3.5 *Summary*

Table 35.4 summarizes some of the characteristics of and differences between plastic, liquid and organic glass scintillators.

Table 35.4: Typical properties of plastic, liquid, and organic glass scintillators.

Property	Plastic	Liquid	Organic glass
Light output (ph/MeV)	up to 10,000	up to 12,000	17,000 - 20,000
Stability	Generally stable; partial fogging with moisture	Stable if properly encapsulate; otherwize oxygen sensitive	Improved when blended with polymers
Density	1.04-1.56	$\approx$ 1.0 - $\approx$ 1.3	not available
Emission wavelength	Highly tunable	Highly tunable	Usually around 430 nm; should be tunable
Decay Time	0.3-280 ns, low after glow	fast, down to sub-ns	1.3-1.6 ns prompt
Loading with elements	Easy	Easy	B or Sn loading performed so far
Radiopurity	Highly pure	Highly pure	Highly pure
Achievable volumes	Bulk up to ca. 100 L	Virtually no limit	Ca. 0.3 L for pure OGS, larger volumes for OGS blended with polymers
Fast neutron/gamma discrimination	Moderate to good	Good to excellent	Excellent

35.4 Inorganic scintillators

Revised August 2025 by C.L. Woody (BNL) and R.-Y. Zhu (HEP California Inst. of Technology).

Inorganic crystals form a class of scintillating materials with much higher densities than organic plastic scintillators (typically $\sim$ 4–8 g/cm^3) with a variety of different properties for use as scintillation detectors. Due to their high density and high effective atomic number, they can be used in applications where high stopping power or a high conversion efficiency for electrons or photons is required. These include total absorption electromagnetic calorimeters (see Sec. 35.10.2), which consist of a totally active absorber (as opposed to a sampling calorimeter), and time of flight detectors as well as serving as gamma-ray detectors over a wide range of energies. Many of these crystals also have very high light output, and can therefore provide excellent energy resolution down to very low energies ($\sim$ few hundred keV).

Some crystals are intrinsic scintillators in which the luminescence is produced by a part of the crystal lattice itself. However, other crystals require the addition of a dopant, typically fluorescent ions such as thallium (Tl) or cerium (Ce), which is responsible for producing the scintillation light. However, in both cases, the scintillation mechanism is the same. For charged particles, energy is deposited in the crystal by ionization. For photons, energy is deposited by Compton electrons, photoelectrons, and electron-positron pairs, and the corresponding cross sections depend on the photon energy and the scintillator material. This energy is transferred to the luminescent centers which then radiate scintillation photons. The light yield LY in terms of the number of scintillation photons produced per MeV of energy deposited in the crystal can be expressed as [64]

$$LY = 10^6 \; S \cdot Q/(\beta \cdot E_g), \tag{35.3}$$

Table 35.5: Properties of several inorganic crystals used in high-energy or nuclear physics experiments. Most of the notation is defined in Sec. 6 of this *Review*.

Parameter:	ρ	MP	X_0*	R_M*	dE/dx*	λ_I*	$\tau_{\rm decay}$	$\lambda_{\rm max}$	n†	Relative light yield	Hygro-scopic?	d(LY)/dT
Units:	g/cm^3	°C	cm	cm	MeV/cm	cm	ns	nm		%‡		%/°C§
NaI(Tl)	3.67	651	2.59	4.13	4.8	42.9	245	410	1.85	100	yes	−0.2
BGO	7.13	1050	1.12	2.23	9.0	22.8	300	480	2.15	21	no	−0.9
BaF_2	4.89	1280	2.03	3.10	6.5	30.7	650^s	300^s	1.50	36^s	no	−1.9^s
							<0.6^f	220^f		4.1^f		0.1^f
CsI(Tl)	4.51	621	1.86	3.57	5.6	39.3	1220	550	1.79	165	slight	0.4
CsI(Na)	4.51	621	1.86	3.57	5.6	39.3	690	420	1.84	88	yes	0.4
CsI(pure)	4.51	621	1.86	3.57	5.6	39.3	30^s	310	1.95	3.6^s	slight	−1.4
							6^f			1.1^f		
$PbWO_4$	8.30	1123	0.89	2.00	10.1	20.7	30^s	425^s	2.20	0.3^s	no	−2.5
							10^f	420^f		0.077^f		
LSO(Ce)	7.40	2050	1.14	2.07	9.6	20.9	40	402	1.82	85	no	−0.2
PbF_2	7.77	824	0.93	2.21	9.4	21.0	-	-	-	Cherenkov	no	-
CeF_3	6.16	1460	1.70	2.41	8.42	23.2	30	340	1.62	7.3	no	0
$LaBr_3$(Ce)	5.29	783	1.88	2.85	6.90	30.4	20	356	1.9	180	yes	0.2
$CeBr_3$	5.23	722	1.96	2.97	6.65	31.5	17	371	1.9	165	yes	−0.1

*Numerical values calculated using formulae in this review.
†Refractive index at the wavelength of the emission maximum.
‡Relative light yield measured for samples of 1.5 X_0 cube with a Tyvek paper wrapping and a full end face coupled to a photodetector. The quantum efficiencies of the photodetector are taken out.
§Variation of light yield with temperature evaluated at room temperature.
f = fast component, s = slow component

where $\beta \cdot E_g$ is the energy required to create an e-h pair expressed as a multiple of the band gap energy Eg (eV), S is the efficiency of energy transfer to the luminescent center and Q is the quantum efficiency of the luminescent center. The values of β, S and Q are crystal dependent and are the main factors in determining the intrinsic light yield of the scintillator. The decay time of the scintillator is mainly dominated by the decay time of the luminescent center.

Table-35.5 lists the basic properties of inorganic crystals commonly used in high energy or nuclear physics experiments. A more extensive list of organic and inorganic scintillators and their properties can be found in [65], which describes the open access library https://scintillator.lbl.gov/.

NaI(Tl) is one of the most common and widely used scintillators, with an emission that is well matched to a bialkali photomultiplier tube, but it is highly hygroscopic and difficult to work with, and has a rather low density. CsI(Tl) and CsI(Na) have high light yield, low cost, and are mechanically robust (high plasticity and resistance to cracking). However, they need careful surface treatment and are slightly and highly hygroscopic respectively. Pure CsI has identical mechanical properties as CsI(Tl), but has a faster emission at shorter wavelength and a much lower light yield.

Undoped BaF_2 has a fast component with a less than 0.6 ns decay time, and is the fastest known scintillator. However, it also has a slow component with a much longer decay time ($\sim$ 630 ns). Bismuth gemanate ($Bi_4Ge_3O_{12}$ or BGO) has a high density, and consequently a short radiation length X_0 and Molière radius R_M. Similar to CsI(Tl), BGO's emission is well-matched to

the spectral sensitivity of silicon photodiodes, and it is easy to handle and not hygroscopic. Lead tungstate ($PbWO_4$ or PWO) has a very high density, with a very short X_0 and R_M, but its intrinsic light yield is rather low.

Cerium doped lutetium oxyorthosilicate (Lu_2SiO_5:Ce, or LSO:Ce) [66] and cerium doped lutetium-yttrium oxyorthosilicate ($Lu_{2(1-x)}Y_{2x}SiO_5$, LYSO:Ce) [67] are dense crystal scintillators which have a high light yield and a fast decay time. Only the properties of LSO:Ce are listed in Table-35.5 since the properties of LYSO:Ce are similar to that of LSO:Ce except a slightly lower density than LSO:Ce depending on the yttrium fraction (typically 5 to 10%) in LYSO:Ce. This material also exhibits excellent radiation hardness [68,69], and can be used where extraordinary radiation hardness is required, such as the HL-LHC and FCC-hh.

Also listed in Table-35.5 are other fluoride crystals such as PbF_2 , which is a Cherenkov material, and CeF_3, which has been shown to provide excellent energy resolution in calorimeter applications [70,71]. Table-35.5 also includes lanthanum tri-halides, such as $LaBr_3$(Ce) [72] and $CeBr_3$ [73], which are brighter and faster than LSO:Ce, but are highly hygroscopic and have a lower density. The FWHM energy resolution measured for these materials coupled to a PMT with bi-alkali photocathode for 0.662 MeV γ-rays from a ^{137}Cs source is about 3%, and has been improved to 2% by co-doping with calcium and strontium [74], which is the best among all inorganic crystal scintillators. For this reason, $LaBr_3$(Ce) and $CeBr_3$ are used in applications where good energy resolution for low energy photons are required, such as homeland security.

Beside the crystals listed in Table-35.5, a number of newer crystals are being investigated that may have potential applications in high energy or nuclear physics. Of particular interest is the family of yttrium and lutetium perovskites and garnets, which include YAP ($YAlO_3$:Ce), LuAP ($LuAlO_3$:Ce), YAG ($Y_3Al_5O_{12}$:Ce), LuAG ($Lu_3Al_5O_{12}$:Ce), GAGG ($Gd_3Al_2Ga_3O_{12}$:Ce) and their mixed compositions. These have been shown to be linear over a large energy range [75], and have the potential for providing good intrinsic energy resolution. Cerium doped garnets (YAG, LuAG and GAGG) are also radiation hard [76–80], and have been proposed for future applications in a severe radiation environment.

Aiming at the best jet-mass resolution, inorganic scintillators are being investigated for HEP calorimeters with dual readout for both Cherenkov and scintillation light to be used at future lepton colliders. These materials may be used for an electromagnetic calorimeter [81] or a homogeneous hadronic calorimetry (HHCAL) detector concept, including both electromagnetic and hadronic parts [82, 83]. Because of the unprecedented volume (70 to 100 m^3) foreseen for the HHCAL detector concept, the materials must be dense to minimize the leakage and also cost-effective. It should also be UV transparent (for effective collection of the Cherenkov light) and allow for a clear discrimination between the Cherenkov and scintillation light. The preferred scintillation light is thus at a longer wavelength, and not necessarily bright or fast.

Scintillating glasses [84] offer a very attractive option where large volumes of scintillating material are required, such as for the HHCAL detector concept, and are currently under development for future collider applications. Recent investigations of cerium doped ABS (Aluminoborosilicate) [85, 86] and DSB ($BaO \bullet 2SiO2$) [87, 88] show high density (6 and 4.3 g/cc respectively) for large samples heavily loaded with Gd. Their main limitation is a poorer optical quality, with light attenuation lengths at a level $\sim$ ten cm, as compared to longer than a meter for scintillating crystals used in total absorption calorimeters.

Fast scintillation light also provides timing information about electromagnetic interactions and showers, which may be used to mitigate pile-up effects and/or for particle identification, since the time development of electromagnetic and hadronic showers, as well as minimum ionizing particles, are different. The timing information is primarily determined by the scintillator rise time and decay time, and the number of photons produced. For fast timing, it is important to have a large number

of photons emitted in the initial part of the scintillation pulse, e.g. in the first ns, since one is often measuring the arrival time of the particle in the crystal using the leading edge of the light pulse. A good example of this is BaF_2, which has $\sim 10\%$ of its light in its fast component with a decay time of less than 0.6 ns. Investigations also show that doping BaF_2 with yttrium reduces its slow component significantly, while keeping its ultrafast scintillation component unchanged [89,90]. Ultrafast crystals of this type provide the best timing resolution [91,92]. However, light propagation can spread out the arrival time of the scintillation photons at the photodetector due to time dispersion [93]. The time response of the photodetector also plays a major role in achieving good time resolution with fast scintillating crystals.

In summary, the timing precision of a scintillation detector generally depends on five parameters: the rise and decay times of the scintillator, the time dispersion of optical photons in the scintillator, the time response and jitter of the photodetector signal for single photons, and the number of photons that produce the photodetector signal. The numerical formulas that estimate the timing precision as a function of these parameters can be found in [64].

Table-35.5 gives the light yield of other crystals relative to NaI(Tl) and their dependence to temperature variations. The light output was measured for 1.5 X_0 cube crystal samples with a Tyvek paper wrapping and a full end face coupled to a photodetector [94]. The quantum efficiency of the photodetector is taken out to facilitate a direct comparison of crystal's light yield. However, the measured light output produced by a scintillator is usually quoted in terms of the number of photoelectrons per MeV produced by a given photodetector. The relationship between the light yield (LY) in number of photons/MeV produced (N_{photons}/MeV) and the light output (LO) in number of photoelectrons/MeV detected involves the factors for the light collection efficiency (LCE) and the quantum efficiency (QE) of the photodetector:

$$LO = LY \cdot LCE \cdot QE. \tag{35.4}$$

LCE depends on the size and shape of the crystal sample, and includes effects such as the transmission of scintillation light within the crystal (i.e., the bulk attenuation length of the material), scattering from within the crystal, reflections and scattering from the crystal surfaces, and reflections back into the crystal by wrapping materials. These factors can vary considerably depending on the sample, but can be in the range of ∼10–60%. The internal light transmission depends on the intrinsic properties of the material, e.g. the density and type of scattering centers and defects that can produce internal absorption within the crystal, and can be highly affected by factors such as radiation damage, as discussed below.

The quantum efficiency depends on the type of photodetector used to detect the scintillation light, which is typically ∼15–30% for photomultiplier tubes and higher for silicon photodetectors for visible wavelengths. The response of the detector is usually highly wavelength dependent and should be matched to the particular crystal of interest to give the highest quantum yield at the wavelength corresponding to the peak of the scintillation emission. Fig. 35.3 shows the quantum efficiency for a Hamamatsu R2059 PMT with bi-alkali cathode and quartz window, and the photon detection efficiency (PDE) for a Hamamatsu S14160-3015ps multi-pixel photon counter (MPPC), which is also called a silicon photomultiplier (SiPM), as a function of wavelength. Also shown in the figure are emission spectra of three crystal scintillators, BGO, LSO:Ce/LYSO:Ce and CsI(Tl), and the numerical values of the emission weighted quantum efficiency. The area under each emission spectrum is proportional to crystal's light yield, as shown in Table-35.5, where the quantum efficiencies of the photodetector has been taken out. Results with different photodetectors can be significantly different. For example, the response of CsI(Tl) relative to NaI(Tl) with a standard photomultiplier tube with a bi-alkali photo-cathode (e.g. Hamamatsu R2059) would be 45% rather

than 165% because of the photomultiplier's low quantum efficiency at longer wavelengths. For scintillators which emit in the UV, a detector with a quartz window should be used.

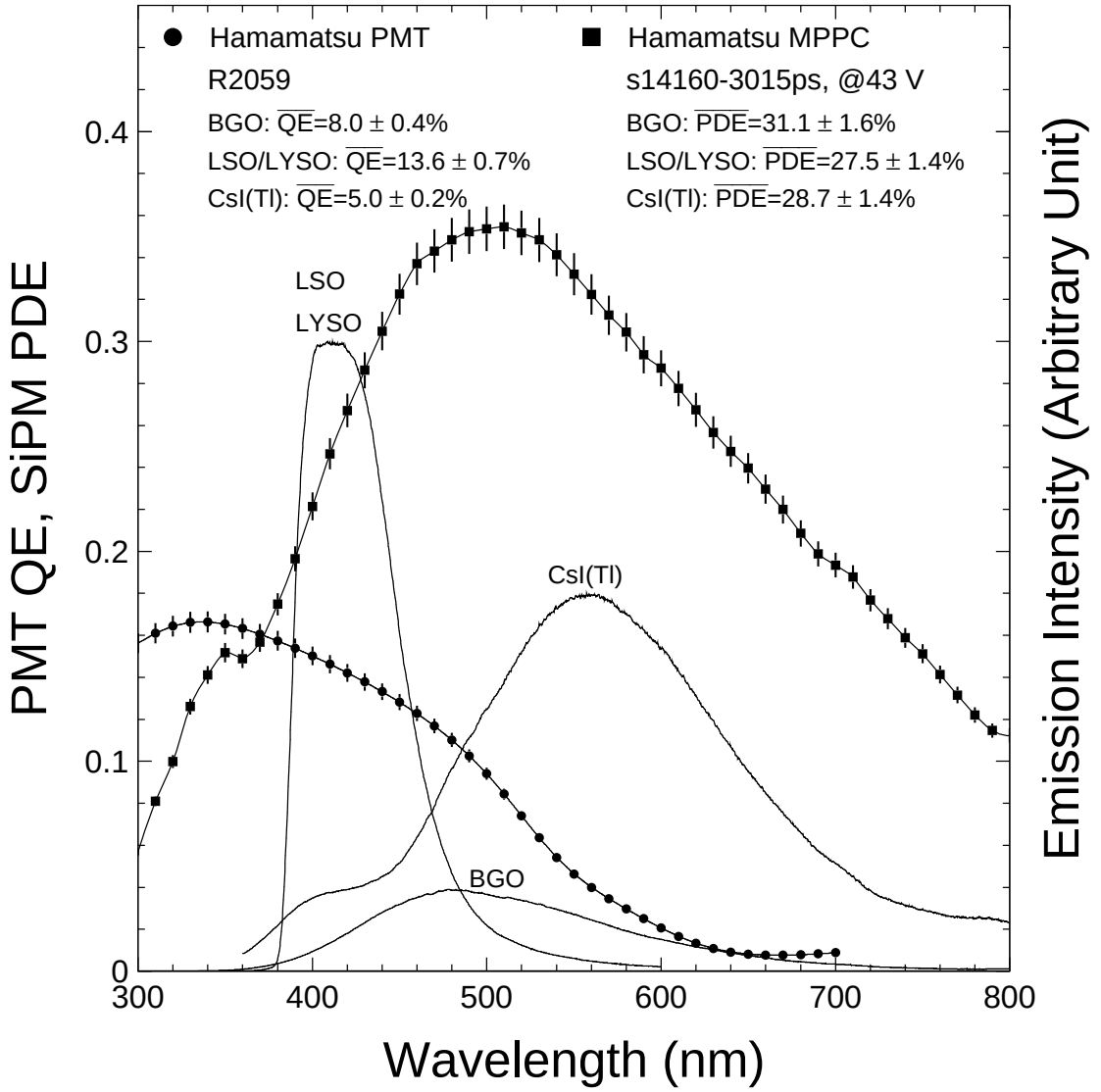

Figure 35.3: The quantum efficiency for a Hamamatsu R2059 PMT with bi-alkali cathode and quartz window and the particle detection efficiency (PDE) for a Hamamatsu S14160-3015ps multi-pixel photon counter (MPPC), which is also called a silicon photomultiplier (SiPM), are shown as a function of wavelength. Also shown in the figure are emission spectra of three crystal scintillators, BGO, LSO and CsI(Tl), and the numerical values of the emission weighted quantum efficiencies. The area under each emission spectrum is proportional to crystal's light yield.

For very low energy applications (typically below 1 MeV), the non-proportionality of the scintillation light yield may be important. It has been known for a long time that the number of photons produced is not proportional to the absorbed energy. It is also known that the energy resolution measured by all crystal scintillators for low energy γ-rays is significantly worse than the contribution from photo-electron statistics alone, indicating an intrinsic contribution from the scintillator itself. Precision measurements using a low energy electron beam show that this non-proportionality

is crystal dependent [95, 96]. Followup investigations have greatly improved our understanding on this issue [97–102].

One important issue related to the application of a crystal scintillator is its radiation hardness. Stability of its light output, or the ability to track and monitor the variation of its light output in a radiation environment, is required for high resolution and precision calibration [103]. All known crystal scintillators suffer from ionization dose induced radiation damage [104], where a common damage phenomenon is the appearance of radiation induced absorption caused by the formation of color centers originating from the impurities or point defects in the crystal. This radiation induced absorption reduces the light attenuation length in the crystal, and hence its light output. For crystals with high defect density, a severe reduction of light attenuation length may cause a distortion of the light response uniformity, leading to a degradation of the energy resolution. Additional radiation damage effects may include a reduced intrinsic scintillation light yield (damage to the luminescent centers) and an increased phosphorescence (afterglow). For crystals to be used in a high precision calorimeter in a radiation environment, its scintillation mechanism must not be damaged and its light attenuation length in the expected radiation environment must be long enough so that its light response uniformity, and thus its energy resolution, does not change.

While radiation damage induced by ionization dose is well understood [105], further investigations have been carried out to understand radiation damage caused by hadrons, including both charged hadrons [106] and neutrons [107]. Hadrons may cause damage by two additional fundamental processes: displacement damage and nuclear breakup. Charged hadrons can produce all three types of damage (and it's often difficult to separate them), but neutrons can only produce damage from the last two, and electrons and photons only produce ionization damage. Studies on hadron induced radiation damage in lead tungstate [108] show a proton-specific damage component caused by fragments from fission induced in lead and tungsten by particles in the hadronic shower. The fragments cause severe, local damage to the crystalline lattice due to their extremely high energy loss over a short distance [108]. An investigation also shows evidence of neutron-specfic damage in various crystals [107]. A more extensive list of investigations on this topic can be found in https://www.its.caltech.edu/~rzhu/.

Most of the crystals listed in Table-35.5 have been used in high energy or nuclear physics experiments when the ultimate energy resolution for electrons and photons is desired, as discussed in Sec. 35.10.2. Examples are the Crystal Ball NaI(Tl) calorimeter at SPEAR, the L3 BGO calorimeter at LEP, the CLEO CsI(Tl) calorimeter at CESR, the KTeV CsI calorimeter at the Tevatron, and the BaBar, BELLE and BES III CsI(Tl) calorimeters at PEP-II, KEK and BEPC II, respectively. Because of their high density and relatively low cost, PWO calorimeters have been used by CMS and ALICE at LHC, by CLAS and PrimEx at CEBAF, and by PANDA at GSI, and is planned to be used for the Backward Endcap Calorimeter for the ePIC experiment at the EIC. Similarly, PbF_2 calorimeters are used by the A4 experiment at MAINZ and by the g-2 experiment at Fermilab. CsI calorimeters are used by KTeV at Fermilab and by the Mu2e experiment at Fermilab. LYSO:Ce crystals are used by the COMET experiment at J-PARC, and by the CMS experiment to build a precision timing layer for the HL-LHC. GAGG:Ce crystals are considered as a candidate scintillator for the LHCb ECAL upgrade for the HL-LHC. Heavy scintillating glass, BaF_2:Y crystal and LuAG:Ce ceramics are considered for CEPC/FCC-ee, Mu2e-II and FCC-hh, respectively.

35.5 Cherenkov detectors

Revised March 2026 by J. Schwiening (GSI Darmstadt).

Although devices using Cherenkov radiation are often thought of as only particle identification (PID) detectors, in practice they are used over a much broader range of applications including;

(1) fast particle counters; (2) hadronic PID; (3) electromagnetic calorimeters (EMC); and (4) tracking detectors performing complete event reconstruction. Examples of applications from each category include; (1) the BaBar luminosity detector [109] and the Quartic fast timing counter for the ATLAS Forward Proton Detector, designed to measure small angle scatters at the LHC [110]; (2) the hadronic PID detectors at the B factory detectors—DIRC in BaBar [111], and the modern Imaging Aerogel and TOP counters at Belle II [112]; (3) the CMS Hadron Forward calorimeter based on Cherenkov light emitted in quartz fibers embedded in a steel absorber [113]; and (4) large water Cherenkov counters such as Super-Kamiokande [114].

Cherenkov counters contain two main elements; (1) a radiator through which the charged particle passes, and (2) a photodetector. As Cherenkov radiation is a weak source of photons, light collection and detection must be as efficient as possible. The refractive index n and the particle's path length through the radiator L appear in the Cherenkov relations allowing the tuning of these quantities for particular applications. One or more of the properties of Cherenkov radiation discussed in the Passages of Particles through Matter section (Sec. 34 of this *Review*) are utilized in Cherenkov detectors: the prompt emission of a light pulse; the existence of a velocity threshold for radiation; and the dependence of the Cherenkov cone half-angle θ_c and the number of emitted photons on the velocity of the particle v_p and the refractive index n of the medium. The Cherenkov angle can be calculated as

$$\cos\theta_c = \frac{1}{n(E)\beta}, \tag{35.5}$$

where $\beta = v_p/c$ with c being the speed of light, and E the photon energy. The number of photoelectrons ($N_{\text{p.e.}}$) detected in a given device with radiator of length L is

$$N_{\text{p.e.}} = L\frac{\alpha^2 z^2}{r_e\, m_e c^2}\int \epsilon(E)\, \sin^2\theta_c(E) dE, \tag{35.6}$$

where $\epsilon(E)$ is the efficiency for collecting the Cherenkov light and transducing it into photoelectrons, and $\alpha^2/(r_e\, m_e c^2) = 370\ \text{cm}^{-1}\text{eV}^{-1}$. The quantities ϵ and θ_c are functions of the photon energy. As the typical energy dependent variation of the index of refraction is modest, a quantity called the *Cherenkov detector quality factor* N_0 can be defined as

$$N_0 = \frac{\alpha^2 z^2}{r_e\, m_e c^2}\ \int \epsilon\, dE, \tag{35.7}$$

so that, taking the charge number $z = 1$ (the usual case in high-energy physics),

$$N_{\text{p.e.}} \approx L N_0 \langle \sin^2\theta_c \rangle. \tag{35.8}$$

This definition of the quality factor N_0 is not universal, nor, indeed, very useful for those common situations where ϵ factorizes as $\epsilon = \epsilon_{\text{coll}}\epsilon_{\text{det}}$ with the geometrical photon collection efficiency (ϵ_{coll}) varying substantially for different tracks while the photon detector efficiency (ϵ_{det}) remains nearly track independent. In this case, it can be useful to explicitly remove (ϵ_{coll}) from the definition of N_0. A typical value of N_0 for a photomultiplier (PMT) detection system working in the visible and near UV, and collecting most of the Cherenkov light, is about 100 cm^{-1}. Practical counters, utilizing a variety of different photodetectors, have values ranging between about 30 and 180 cm^{-1}. Radiators can be chosen from a variety of transparent materials (Sec. 34 of this *Review* and Table 6). In addition to refractive index, the choice requires consideration of factors such as material density, radiation length and radiation hardness, transmission bandwidth, absorption length, chromatic dispersion, optical workability (for solids), availability, environmental impact, and cost. When the

momenta of particles to be identified is high, the refractive index must be set close to one, so that the photon yield per unit length is low and a long particle path in the radiator is required. In recent years, the gap in refractive index that has traditionally existed between gases and liquid or solid materials has been partially closed with transparent *silica aerogels* with indices that range between about 1.003 and 1.26. Due to the potential ability to tune the refractive index to the exact requirements of an experiment, metamaterials, including photonic crystals, are being investigated as radiators for future Cherenkov counters [115–117].

Cherenkov counters may be classified as either *imaging* or *threshold* types, depending on whether they do or do not make use of Cherenkov angle (θ_c) information. Imaging counters may be used to track particles as well as identify them. The recent development of very fast photodetectors such as micro-channel plate PMTs (MCP-PMT) (see 35.2 of this *Review*) also potentially allows very fast Cherenkov based time of flight (TOF) detectors of either class [115–117]. The track timing resolution of imaging detectors can be extremely good as it scales approximately as $\frac{1}{\sqrt{N_{\rm p.e.}}}$.

Threshold Cherenkov detectors [118], in their simplest form, make a yes/no decision based on whether the particle is above or below the Cherenkov threshold velocity $\beta_t = 1/n$. A straightforward enhancement of such detectors uses the number of observed photoelectrons (or a calibrated pulse height) to discriminate between species or to set probabilities for each particle species [119]. This strategy can increase the momentum range of particle separation by a modest amount (to a momentum some 20% above the threshold momentum of the heavier particle in a typical case).

Careful designs give $\langle \epsilon_{\rm coll} \rangle \gtrsim 90\%$. For a photomultiplier with a typical bialkali cathode, $\int \epsilon_{\rm det} dE \approx 0.27$ eV, so that

$$N_{\rm p.e.}/L \approx 90 \text{ cm}^{-1} \langle \sin^2 \theta_c \rangle \quad (i.e., N_0 = 90 \text{ cm}^{-1}). \tag{35.9}$$

Suppose, for example, that n is chosen so that the threshold for species a is p_t; that is, at this momentum species a has velocity $\beta_a = 1/n$. A second, lighter, species b with the same momentum has velocity β_b, so $\cos\theta_c = \beta_a/\beta_b$, and

$$N_{\rm p.e.}/L \approx 90 \text{ cm}^{-1} \frac{m_a^2 - m_b^2}{p_t^2 + m_a^2}. \tag{35.10}$$

For K/π separation at $p = p_t = 1(5)$ GeV/c, $N_{\rm p.e.}/L \approx 16(0.8)$ cm^{-1} for π's and (by design) 0 for K's.

For limited path lengths $N_{\rm p.e.}$ will usually be small. The overall efficiency of the device is controlled by Poisson fluctuations, which can be especially critical for separation of species where one particle type is dominant. Moreover, the effective number of photoelectrons is often less than the average number calculated above due to additional equivalent noise from the photodetector (see the discussion of the excess noise factor in 35.2 of this *Review*). It is common to design for at least 10 photoelectrons for the high velocity particle in order to obtain a robust counter. As rejection of the particle that is below threshold depends on *not* seeing a signal, electronic and other background noise, especially overlapping tracks, can be important. Physics sources of light production for the below threshold particle, such as decay to an above threshold particle, scintillation light, or the production of delta rays in the radiator, often limit the separation attainable, and need to be carefully considered. Well designed, modern multi-channel counters, such as the ACC at Belle [120], can attain adequate particle separation performance over a substantial momentum range.

Imaging counters make the most powerful use of the information available by measuring the ring-correlated angles of emission of the individual Cherenkov photons. They typically provide positive ID information both for the "wanted" and the "unwanted" particles, thus reducing misidentification substantially. Since low-energy photon detectors can measure only the position (and,

perhaps, a precise detection time) of the individual Cherenkov photons (not the angles directly), the photons must be "imaged" onto a detector so that their angles can be derived [121]. Typically the optics map the Cherenkov cone onto (a portion of) a distorted "circle" at the photodetector. Though the imaging process is directly analogous to familiar imaging techniques used in telescopes and other optical instruments, there is a somewhat bewildering variety of methods used in a wide variety of counter types with different names. Some of the imaging methods used include (1) focusing by a lens or mirror; (2) proximity focusing (i.e., focusing by limiting the emission region of the radiation); and (3) focusing through an aperture (a pinhole). In addition, the prompt Cherenkov emission coupled with the speed of some modern photon detectors allows the use of (4) time imaging, a method which is little used in conventional imaging technology, and may allow some separation with particle TOF. Finally, (5) correlated tracking (and event reconstruction) can be performed in large water counters by combining the individual space position and time of each photon together with the constraint that Cherenkov photons are emitted from each track at the same polar angle (Sec. 36.3.1of this *Review*).

In a simple model of an imaging PID counter, the fractional error on the particle velocity (δ_β) is given by

$$\delta_\beta = \frac{\sigma_\beta}{\beta} = \tan\theta_c \sigma(\theta_c) \ , \tag{35.11}$$

where

$$\sigma(\theta_c) = \frac{\langle\sigma(\theta_i)\rangle}{\sqrt{N_{\rm p.e.}}} \oplus C, \tag{35.12}$$

and $\langle\sigma(\theta_i)\rangle$ is the average single photoelectron resolution, as defined by the optics, detector resolution and the intrinsic chromaticity spread of the radiator index of refraction averaged over the photon detection bandwidth. C combines a number of other contributions to resolution including, (1) correlated terms such as tracking, alignment, and multiple scattering, (2) hit ambiguities, (3) background hits from random sources, and (4) hits coming from other tracks. The actual separation performance is also limited by physics effects such as decays in flight and particle interactions in the material of the detector. In many practical cases, the performance is limited by these effects.

For a $\beta \approx 1$ particle of momentum (p) well above threshold entering a radiator with index of refraction (n), the number of σ separation (N_σ) between particles of mass m_1 and m_2 is approximately

$$N_\sigma \approx \frac{|m_1^2 - m_2^2|}{2p^2\sigma(\theta_c)\sqrt{n^2-1}}. \tag{35.13}$$

In practical counters, the angular resolution term $\sigma(\theta_c)$ varies between about 0.1 and 5 mrad depending on the size, radiator, and photodetector type of the particular counter. The range of momenta over which a particular counter can separate particle species extends from the point at which the number of photons emitted becomes sufficient for the counter to operate efficiently as a threshold device (∼20% above the threshold for the lighter species) to the value in the imaging region given by the equation above. For example, for $\sigma(\theta_c)$ =2 mrad, a fused silica radiator ($n = 1.474$), or a fluorocarbon gas radiator (C_5F_{12}, $n = 1.0017$), would separate π/K's from the threshold region starting around 0.15(3) GeV/c through the imaging region up to about 4.2(18) GeV/c at better than 3σ.

Many different imaging counters have been built during the last several decades [115–117]. Among the earliest examples of this class of counters are the very limited acceptance *Differential Cherenkov detectors*, designed for particle selection in high momentum beam lines. These devices use optical focusing and/or geometrical masking to select particles having velocities in a specified region. With careful design, a velocity resolution of $\sigma_\beta/\beta \approx 10^{-4}$–$10^{-5}$ can be obtained [118].

Practical multi-track *Ring-Imaging Cherenkov detectors* (generically called RICH counters) are a more recent development. RICH counters are sometimes further classified by 'generations' that differ based on historical timing, performance, design, and photodetection techniques. Prototypical examples of first generation RICH counters are those used in the DELPHI and SLD detectors at the LEP and SLC Z factory e^+e^- colliders [115–117]. They have both liquid (C_6F_{14}, $n = 1.276$) and gas (C_5F_{12}, $n = 1.0017$) radiators, the former being proximity imaged with the latter using mirrors. The phototransducers are a TPC/wire-chamber combination. They are made sensitive to photons by doping the TPC gas (usually, ethane/methane) with $\sim 0.05\%$ TMAE (tetrakis(dimethylamino)ethylene). Great attention to detail is required, (1) to avoid absorbing the UV photons to which TMAE is sensitive, (2) to avoid absorbing the single photoelectrons as they drift in the long TPC, and (3) to keep the chemically active TMAE vapor from interacting with materials in the system. In spite of their unforgiving operational characteristics, these counters attained good $e/\pi/K/p$ separation over wide momentum ranges (from about 0.25 to 20 GeV/c) during several years of operation at LEP and SLC. Related but smaller acceptance devices include the OMEGA RICH at the CERN SPS, and the RICH in the balloon-borne CAPRICE detector [115–117]. Despite their excellent match to the radiator requirement for gaseous RICHes, saturated fluorocarbons may soon need to be replaced due to their high global warming impact. Possible alternatives for a similar refractive index include hydrofluoroolefins or Argon, pressurized at a few bar [115–117].

Later generation counters [115–117] generally operate at much higher rates, with more detection channels, than the first generation detectors just described. They also utilize faster, more forgiving photon detectors, covering different photon detection bandwidths. Radiator choices have broadened to include materials such as lithium fluoride, fused silica, and aerogel.

Vacuum-based photodetection systems (*e.g.*, single or multi anode PMTs, MCP-PMTs, or hybrid photodiodes (HPD)) have become increasingly common (see 35.2 of this *Review*). They handle high rates, and can be used with a wide choice of radiators. Examples include (1) the SELEX RICH at Fermilab, which mirror focuses the Cherenkov photons from a neon radiator onto a camera array made of ~ 2000 PMTs to separate hadrons over a wide momentum range (to well above 200 GeV/c for heavy hadrons);(2) the NA62 RICH at CERN, which uses a 17 m long tank filled with neon gas as radiator and spherical mirrors to focus the photons on two arrays of 2 000 PMTs to separate pions from muons for momenta between 15 and 35 GeV/c; (3) the CBM RICH under construction at FAIR where the Cherenkov photons, produced in about 30 m^3 of CO_2 radiator gas, are mirror-focused on arrays of multi-anode PMTs (MaPMTs) with a total of about 55,000 pixels, to identify electrons with momenta up to 8 GeV/c; and (4) the LHCb detector now running at the LHC. It uses two separate counters. One volume contains C_4F_{10} (originally in combination with aerogel, which was removed in 2015) while the second volume contains CF_4. Photons are mirror-focused onto arrays of photon detectors to cover a π/K separation momentum range between 1 and 150 GeV/c. Additional upgrades, including the replacement of the HPDs by MaPMTs and improved readout electronics, were performed to deal with increases in luminosity.

Other fast detection systems that use solid cesium iodide (CsI) photocathodes or triethylamine (TEA) doping in proportional chambers are useful with certain radiator types and geometries. Examples include (1) the CLEO-III RICH at CESR that uses a LiF radiator with TEA doped proportional chambers; (2) the ALICE detector at the LHC that uses proximity focused liquid (C_6F_{14} radiators and solid CsI photocathodes (similar photodectors have been used for several years by the HADES and COMPASS detectors), and the hadron blind detector (HBD) in the PHENIX detector at RHIC that couples a low index CF_4 radiator to a photodetector based on electron multiplier (GEM) chambers with reflective CsI photocathodes [115–117].

Recent technological advances in the production of aerogel with improved transparency in the

UV range and finely tuned refractive indices enable several new RICH designs. The innovative hybrid geometry of the CLAS12 RICH, with complex photon paths that feature multiple passes through the aerogel tiles, is only possible due to the improved scattering length of the aerogel. It minimizes the material inside of the detector acceptance as well as the size and cost of the photon sensor array. Beam tests have demonstrated that the counter will be able to provide clean π/K separation up to 8 GeV/c. The forward endcap Aerogel RICH (ARICH) for the Belle II upgrade at KEKB, designed to provide clean π/K separation for momenta up to 3.5 GeV/c, is an example of the so-called focusing aerogel approach [122]. The radiator is a dual-layer aerogel, with a thickness of 20 mm for each layer and increasing refractive indices of $n = 1.045$ and $n = 1.055$ along the particle path. The Cherenkov ring images from the two layers overlap on the array of Hybrid Avalanche Photo Detectors (HAPDs), which provide efficient single photon detection in the 1.5 T magnetic field.

A DIRC (Detection [of] Internally Reflected Cherenkov [light]) is a distinctive, compact RICH subtype first used in the BaBar detector [111]. A DIRC "inverts" the usual RICH principle for use of light from the radiator by collecting and imaging the total internally reflected light rather than the transmitted light. It utilizes the optical material of the radiator in two ways, simultaneously: as a Cherenkov radiator and as a light pipe. The magnitudes of the photon angles are preserved during transport by the flat, rectangular cross section radiators, allowing the photons to be efficiently transported to a detector outside the path of the particle where they may be imaged in up to three independent dimensions (the usual two in space and, due to the long photon paths lengths, one in time). Because the index of refraction in the radiator is large ($n \sim 1.47$ for fused silica), the momentum range with good π/K separation goes up to 4–5 GeV/c. It is plausible, but difficult, to extend it up to about 10 GeV/c with an improved design.

The BaBar experiment at the asymmetric PEP-II e^+e^- collider studied CP violation in $\Upsilon(4S)$ decays. Excellent pion/kaon separation for particle momenta up to 4 GeV/c was required. The BaBar DIRC used 4.9 m long, rectangular bars made from synthetic fused silica as radiator and light guide. The photons were imaged via a "pin-hole" through an expansion region filled with 6 000 liters of purified water onto an array of 10 752 densely packed photomultiplier tubes placed at a distance of about 1.2 m from the bar end. During more than 8 years of operation, the BaBar DIRC achieved π/K separation of 2.5 standard deviations or more up to 4 GeV/c momentum. For a pion identification rate around 85% the DIRC provided a kaon misidentification rate well below 1% up to 3 GeV/c.

The next generation of DIRC detectors [123] takes advantage of the new, very fast, pixelated photodetectors becoming available, such as MaPMTs and MCP-PMTs. They typically utilize either time imaging or lens/mirror-focused optics, or both, leading not only to a precision measurement of the Cherenkov angle, but in some cases, to a precise measurement of the particle time of flight, and/or to correction of the chromatic dispersion in the radiator. Examples [115–117] include (1) the Belle II Time of Propagation (TOP) counter that emphasizes precision timing for both Cherenkov imaging and TOF to perform π/K separation of at least 3 standard deviations up to 4 GeV/c; (2) the DIRC upgrade of the GlueX experiment at Jefferson Lab that places four decommissioned BaBar DIRC modules, coupled to upgraded optics and readout, perpendicular to the beamline, the first application of a DIRC in a detector endcap; (3) the high-performance DIRC for the ePIC detector at the EIC, to be installed in 2032, that will combine lens focusing with fast photon time imaging and is expected to provide more than 3 standard deviations π/K separation up to 6 GeV/c; and (4) the TORCH counter being developed for an LHCb upgrade in 2034 which uses DIRC imaging for individual photons with fast photon detectors to provide π/K separation up to 10 GeV/c via particle TOF with a precision of 10-15 ps per particle over a flight path length of 9.5 m.

35.6 Gaseous detectors

35.6.1 *Energy loss and charge transport in gases*

Revised August 2025 by P. Gasik (GSI Darmstadt; FAIR Darmstadt; Technische U., Darmstadt).

Gas-filled detectors rely on localized ionization produced by ionizing particles—charged particles or photons (via photoelectrons)—typically followed by charge multiplication. The statistics of ionization processes, which exhibit asymmetries in the ionization trails, impact the coordinate determination derived from measurements of drift time or the center of gravity of the collected charge. For thin gas layers, the width of the energy loss distribution can be larger than its average, requiring multi-sampling devices or truncated mean analysis for reliable particle identification. In the truncated mean method for calculating $\langle \mathrm{d}E/\mathrm{d}x \rangle$, the ionization measurements along the particle track are divided into many samples, and a fixed fraction of high-side (and sometimes low-side) values are discarded [124].

Table 35.6: Properties of noble and molecular gases at normal temperature and pressure (NTP: 20° C, 1 atm). E_X, E_I: first excitation, ionization energy; W_I: average energy for creation of electron-ion pair; $\mathrm{d}E/\mathrm{d}x|_{\min}$, N_P, N_T: differential energy loss, primary and total number of electron-ion pairs per cm, for unit-charge minimum ionizing particles. Values often vary, depending on the source, and those in the table should be considered approximate.

Gas	Density, $\mathrm{mg\,cm^{-3}}$	E_X eV	E_I eV	W_I eV	$\mathrm{d}E/\mathrm{d}x\|_{\min}$ $\mathrm{keV\,cm^{-1}}$	N_P $\mathrm{cm^{-1}}$	N_T $\mathrm{cm^{-1}}$
H_2	0.084	10.8	15.4	37	0.34	5.2	9.2
He	0.179	19.8	24.6	41.3	0.32	3.5	8
Ne	0.839	16.7	21.6	37	1.45	13	40
Ar	1.66	11.6	15.7	26	2.53	25	97
Xe	5.495	8.4	12.1	22	6.87	41	312
CH_4	0.667	8.8	12.6	30	1.61	28	54
C_2H_6	1.26	8.2	11.5	26	2.91	48	112
iC_4H_{10}	2.49	6.5	10.6	26	5.67	90	220
CO_2	1.84	7.0	13.8	34	3.35	35	100
CF_4	3.78	10.0	16.0	35-52	6.38	52-63	120

The energy loss of charged particles and photons in matter is discussed in Sec. 34. Every ionization process is a quantum mechanical transition initiated by the Coulomb field of the particle and the field created by neighbouring polarizable atoms. The average energy losses are described by the Bethe-Bloch formula with Sternheimer's density effect corrections. The fluctuations caused by Rutherford scattering on quasi-free electrons follow a Landau distribution and the influence of atomic shells is described by the photoabsorption ionization (PAI) model, which allows simulation of each energy transfer [125], with relaxation cascades and simulation of delta-electrons [126]. Table 35.6 provides values of relevant parameters in some commonly used gases at NTP for unit-charge minimum ionizing particles (MIPs) [127] [128]. When an ionizing particle passes through a gas, it produces electron-ion pairs. In many cases, the ejected (primary) electrons possess enough energy to further ionize the medium, giving rise to secondary ionizations. These secondary electrons are generated in the immediate vicinity of the primary ionization site, and together with the primary electrons, they form clusters consisting of one, several, or sometimes many electron-ion pairs. The

probability distribution describing the number of electron-ion pairs – both primary and secondary – produced in a single ionization encounter is referred to as the cluster-size distribution. As shown in Table 35.6, the total number of pairs (N_T) is a few times larger than the number of primaries (N_P). For different conditions and for mixtures, and neglecting energy transfer processes (*e.g.* Penning effect), one can scale the density, N_P, and N_T with temperature and pressure assuming a perfect gas law.

The probability for a released electron to have an energy E or larger follows an approximate $1/E^2$ dependence (Rutherford law), shown in Fig. 35.4 for Ar at NTP (dotted line, left scale). More detailed estimates taking into account the electronic structure of the medium are shown in the figure, for three values of the particle velocity factor $\beta\gamma$ [129]. The dot-dashed line provides, on the right scale, the practical range of electrons (including scattering) of energy E. As an example, about 0.6% of released electrons have 1 keV or more energy, substantially increasing the total ionization loss. The practical range of 1 keV electrons in argon is approximately 70 μm, which can contribute to the uncertainty in the coordinate determination.

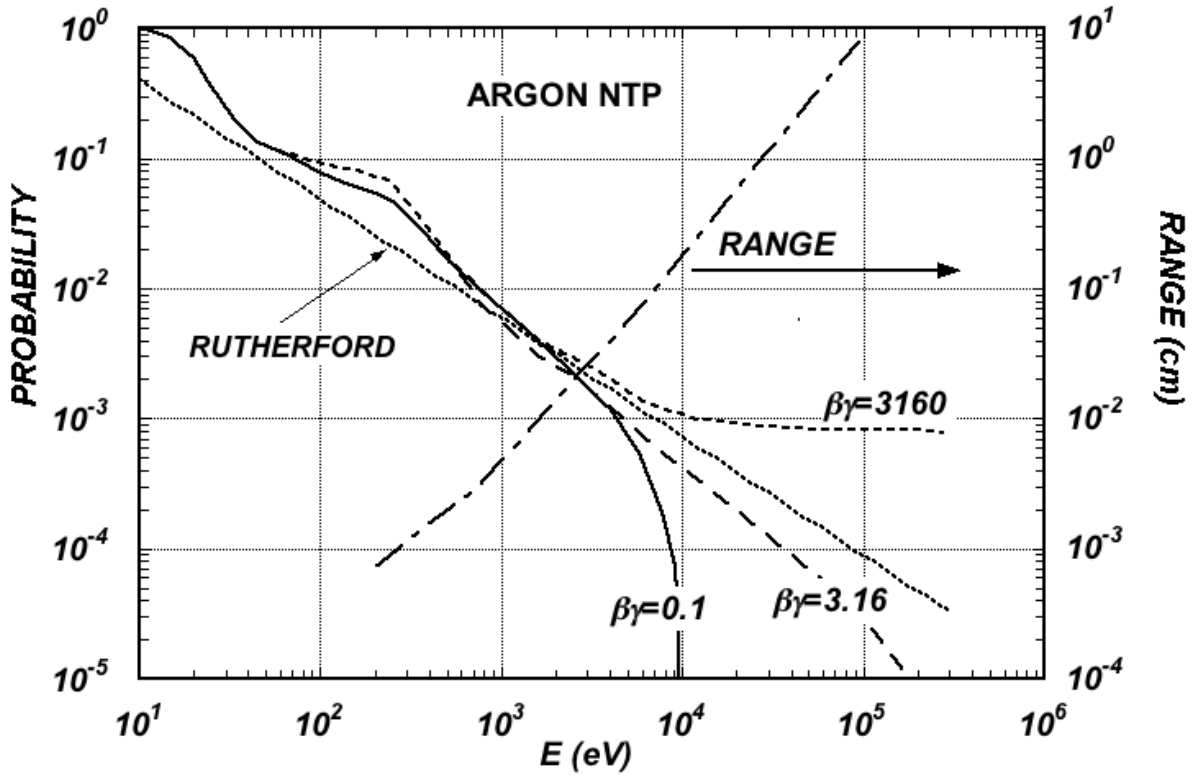

Figure 35.4: Probability of single collisions in which released electrons have an energy E or larger (left scale) and practical range of electrons in Ar at NTP (dot-dashed curve, right scale) [129].

Garfield^{++} [130], together with HEED [126], Degrad [131], Magboltz [132,133], SRIM, ANSYS, COMSOL, and neBEM [134] software packages represent the core simulation tools for microscopic modeling of gaseous detector response. The number of electron-ion pairs per primary ionization, or cluster size, depends little on the medium; it can be computed with the programs mentioned above or experimentally measured. For example, there is about 3% probability for primary clusters to contain ten or more electron-ion pairs in argon [135].

Once released into the gas, electrons and ions drift in opposite directions under the influence of an applied electric field, while simultaneously undergoing diffusion. The electron-molecule collision

cross sections are determined by the details of atomic and molecular structure and depend strongly on the electron energy and therefore on the electric field $\boldsymbol{E}$ for most gases. High values of the total electron scattering cross section reduce the electron diffusion and increase the drift velocity; a large inelasticity implies that high fields are required to raise the electron energy. For noble gases, the inelastic cross section is zero until the electrons reach the first excitation and ionization energies, which are on the order of 10 eV; on the contrary, for molecular gases, like CH_4, inelastic channels, involving rotational and vibrational levels, open up at energies above ∼0.1 eV. Large drift velocities are achieved by adding polyatomic gases (usually hydrocarbons C_x H_y, CO_2, CF_4) which have significant inelastic scattering components at moderate electron energies of a few electronvolts; this results in the electron "cooling" into the energy range of the Ramsauer-Townsend minimum (∼0.3 eV in argon) of the elastic ("momentum-transfer") cross-section [128]. Similar to argon, krypton, and xenon also show the Ramsauer-Townsend minimum, while helium and neon do not. Under these circumstances, it is clear that the addition of very small quantities of one gas to another can dramatically modify the average electron energy and alter the dependence of the drift velocity (v_d) on $\boldsymbol{E}/p$, where p is the gas pressure, and temperature T; this has a particularly strong effect for noble gases, as illustrated in Fig. 35.5 for argon. Carbon tetrafluoride (CF_4) has the largest drift velocity and the lowest electron diffusion among known gases due to the sizeable Ramsauer-Townsend dip in the elastic cross-section, which coincides with very large vibrational modes. Another principal role of the polyatomic gas is to absorb the ultraviolet photons emitted by the excited noble gas atoms. Addition of molecular gases (hydrocarbons or CO_2 is widely used in the proportional counters as a quencher) to noble gas allows to dissipate a good fraction of energy through rotational and vibrational radiationless transitions without the creation of photons or ions. On the contrary, CF_4 has a small quenching cross-section of excited Ar states and light emission in CF_4 (from the far UV to the visible light) is a complex process, involving the creation of CF_3^+ excited states [136].

Extensive collections of experimental data [137] and theoretical calculations based on transport theory permit evaluation of drift and diffusion properties in pure gases and their mixtures. Modern compilations of the electron-molecule cross sections are available at the open-access website LXCAT [138]. Fig. 35.5 and Fig. 35.6 show the drift velocity as well as transverse and longitudinal diffusion for some commonly used gases at NTP, computed with the Magboltz program [132, 133]. For different conditions, the horizontal axis must be scaled inversely with the gas density. The standard deviations for longitudinal (σ_L) and transverse diffusion (σ_T) are specified per centimeter of drift and scale with the square root of the drift distance.

In a simple approximation, gas kinetic theory provides the drift velocity v_d as a function of the mean collision time τ and the electric field E: $v_\mathrm{d} = eE\tau/m_e$ (Townsend's expression). In the presence of an external magnetic field, the Lorentz force acting on electrons between collisions deflects the drifting electrons and modifies the drift properties. The electron trajectories, velocities and diffusion parameters can be computed with Magboltz. The friction force model provides an approximate expression for the vector drift velocity $\boldsymbol{v_\mathrm{d}}$ as a function of electric and magnetic field vectors $\boldsymbol{E}$ and $\boldsymbol{B}$, of the Larmor frequency $\omega = eB/m_e$, and of the mean collision time τ (a more precise calculation is available in Magboltz, which computes the drift velocity by tracing electrons at the microscopic level through numerous collisions with gas molecules):

$$\boldsymbol{v_\mathrm{d}} = \frac{e}{m_e}\frac{\tau}{1+\omega^2\tau^2}\left(\boldsymbol{E} + \frac{\omega\tau}{B}(\boldsymbol{E}\times\boldsymbol{B}) + \frac{\omega^2\tau^2}{B^2}(\boldsymbol{E}\cdot\boldsymbol{B})\boldsymbol{B}\right) \tag{35.14}$$

To a good approximation, and for moderate fields, one can assume that the energy of the electrons is not affected by the magnetic field, and use for τ the values deduced from the drift velocity at $B = 0$ (Townsend's expression). For $\boldsymbol{E}$ perpendicular to $\boldsymbol{B}$, the drift angle relative to

the electric field vector is $\tan\theta_B = \omega\tau$ and $v_d = (E/B)(\omega\tau/\sqrt{1+\omega^2\tau^2})$. For parallel electric and magnetic fields, the drift velocity and longitudinal diffusion are not affected, whereas the transverse diffusion can be strongly reduced: $\sigma_T(B) = \sigma_T(B=0)/\sqrt{1+\omega^2\tau^2}$. As an example, the dotted line in Fig. 35.6 represents σ_T for the classic Ar-CH_4 (90-10) mixture at 4 T. Large values of $\omega\tau \approx 20$ at 5 T are consistent with the measurement of the diffusion coefficient in Ar-CF_4-iC_4H_{10} (95-3-2). This reduction is exploited to substantially improve spatial resolution in the Drift (Sec. 35.6.2) and Time Projection Chambers (Sec. 35.6.4).

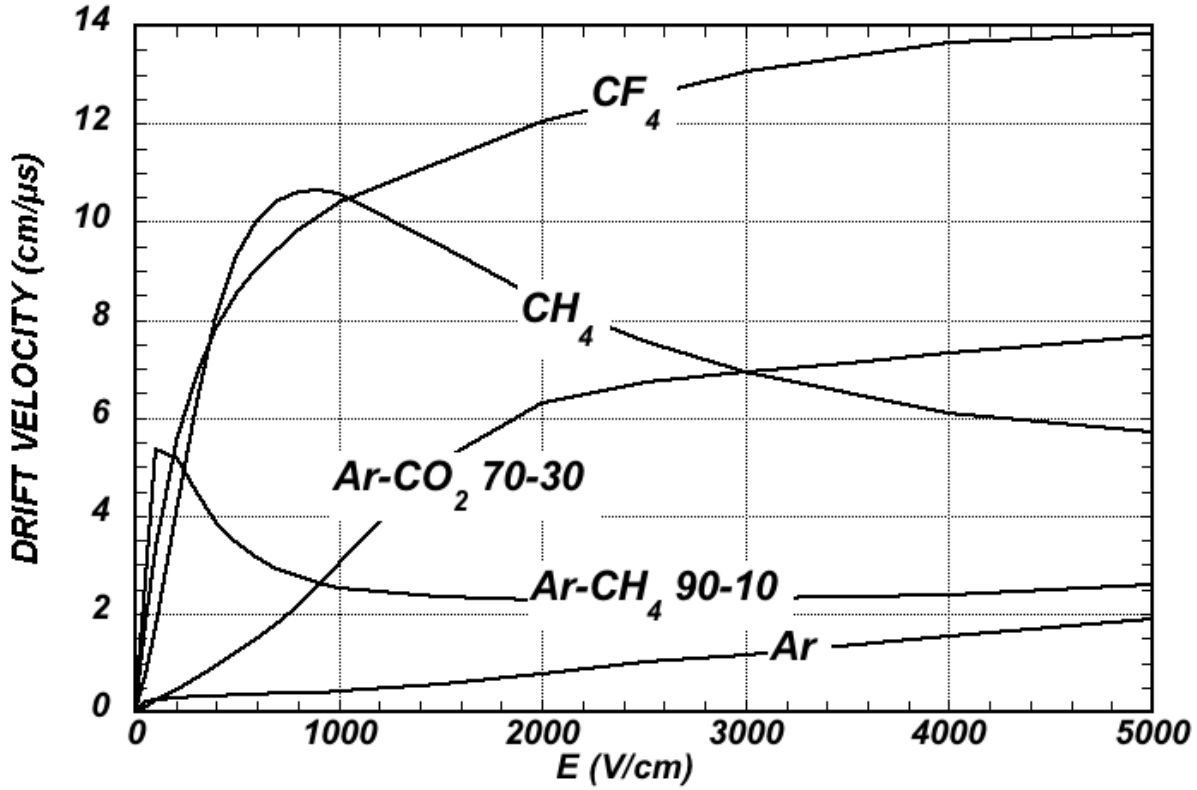

Figure 35.5: Computed electron drift velocity as a function of electric field in several gases at NTP and $B = 0$ [132, 133].

In some mixtures containing molecules with electronic affinity, electrons can be captured to form negative ions. Capture cross sections vary considerably with energy and, hence, the electric field. As a consequence, the three-body electron attachment coefficients may differ significantly for the same additive in different mixtures. As an example, at moderate fields (up to 1 kV/cm), the addition of 0.1% of oxygen to an Ar-CO_2 mixture results in an electron capture probability about twenty times larger than in Ar-CH_4. Among common molecules, the largest electron affinities are found for the halogenides, O_2 and H_2O. The attachment probability in O_2 or H_2O is large at low fields and electron energies close to thermal, but decreases at increasing fields. On the contrary, CF_4 is not electronegative at low and moderate fields, but has a large electron capture cross section at fields above ∼8 kV/cm, before reaching the avalanche field strengths. Depending on the exact mixture and detector geometry, some signal reduction and energy resolution loss is expected in this gas.

If the electric field is increased sufficiently, electrons gain enough energy between collisions to excite and ionize molecules. Above a gas-dependent threshold, the mean free path for ionization,

λ_i, decreases exponentially with the field; its inverse, $\alpha = 1/\lambda_i$, is named the first Townsend coefficient. Free charges originally deposited in the chamber volume are multiplied in the electron avalanche process. Gains of the order of 10^5–10^6 can be achieved, and the detected charge is proportional, via the multiplication factor, to the primary charge liberated by the incoming particle. The detector is operated in the proportional counter mode. In uniform fields, N_0 initial electrons multiply over a length x forming an electron avalanche of size $N = N_0\, e^{\alpha x}$; N/N_0 is the gain of the detector. Fig. 35.7 shows examples of Townsend coefficients for several gas mixtures, computed with Magboltz [132, 133].

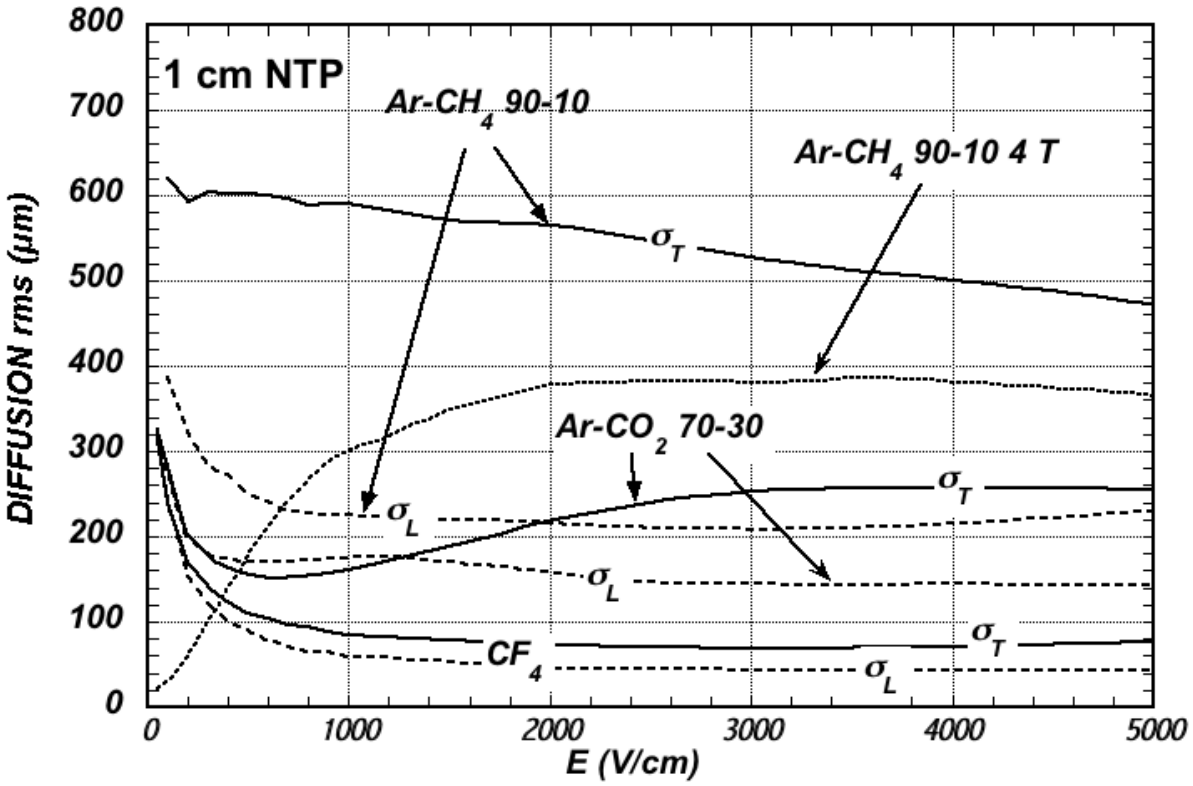

Figure 35.6: Electron longitudinal diffusion ($\sigma_{\rm L}$) (dashed lines) and transverse diffusion ($\sigma_{\rm T}$) (full lines) for 1 cm of drift at NTP and $B = 0$. The dotted line shows $\sigma_{\rm T}$ for the P10 mixture at 4 T [132, 133].

Additional ionizing energy transfer mechanisms due to the excited noble gas atoms, called collisional Penning energy transfers, occur when the excitation energy of a noble gas is higher than the ionization potential of an admixture gas. The energy transfer rate, the probability that an excited atom ionizes a quenching agent, is a priori not known for a mixture, but can be extracted from the fits of the experimental gas gain data [139] using the Magboltz simulations [132, 133]. In the gain calculations, the Penning adjusted Townsend coefficient is defined in terms of the total production frequencies of the noble gas excitations and direct ionizations of the mixture. Systematic gas gain measurements for varying mixing ratios and pressures are critical for determining the efficiency of the different mechanisms involved in the transfers. Collisional energy transfer mostly scales linearly with the gas pressure and the fraction of quenching gas in the mixture, while ionization by photons emitted from excitations is independent of the medium [140]. In addition, collisional Penning transfers of some higher excited states can occur before they decay at atmospheric pressure and are not restricted to metastable states of the excited noble gas. For example, the impact of the

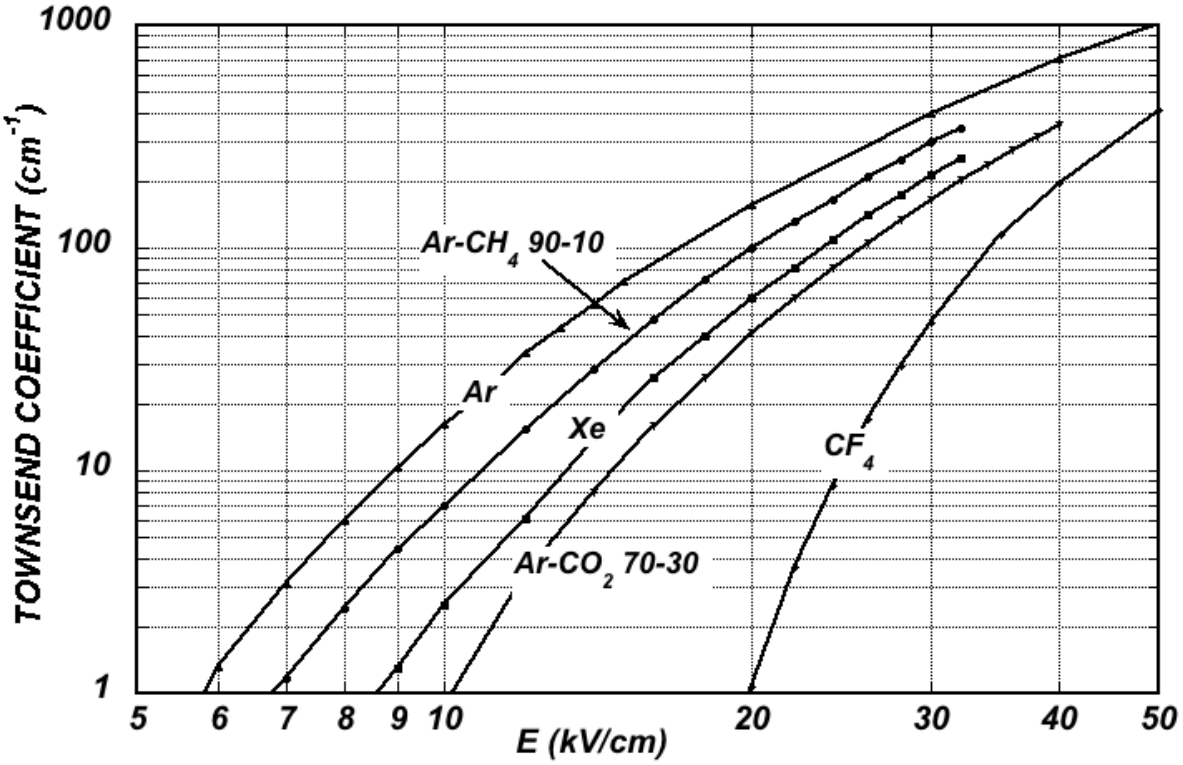

Figure 35.7: Computed first Townsend coefficient α as a function of the electric field in several gases at NTP [132, 133].

Penning effect on gas gain is roughly a factor of 10 in Ar-CO_2 mixtures and exceeding a factor of 100 in Ar-C_2H_2 mixtures [140].

The proportionality of the amplification process is gradually lost at continuously increasing voltages, due to the electric field distortions (screening) resulting from the large charge densities around the wire. At the end of the region of limited proportionality, the gain is saturated and does not depend on the initial value of the deposited charge anymore. This is a region of the Geiger-Müller counter where the photon-mediated avalanche over the full length of the anode wire takes place. Finally, after reaching the so-called breakdown voltage V_b, a discharge region is reached, corresponding to the self-sustaining discharges in which a steady discharge current flows between the electrodes. The voltage beyond V_b is so high that, once ionization takes place in the gas, a continuous discharge develops, and the detector can not be used for radiation detection anymore.

Positive ions originating from primary ionization or generated in avalanches undergo drift and diffusion under the influence of the electric field. Negatively charged ions may also be produced by electron attachment to gas molecules. The drift velocity of ions in the fields encountered in gaseous detectors (up to a few kV/cm) is typically about three orders of magnitude smaller than for electrons. The ion mobility μ, the ratio of drift velocity to electric field, is constant for a given ion type up to very high fields. Values of ion mobility at NTP are given in Table 35.7 [141]. For different temperatures and pressures, the mobility can be scaled inversely with the density, assuming an ideal gas law. Both the longitudinal and transverse diffusion of ions are proportional to the square root of the drift time, with a coefficient that depends on temperature but not on the ion mass. Historically, it was assumed that, due to efficient charge-transfer processes, only the ions with the lowest ionization potential would survive after a short drift path in a gas mixture.

Recent experimental data, however, indicate that in CO_2-quenched Ar or Ne mixtures the actual signal carriers are $CO_2^+!\cdot(CO_2)_n$ cluster ions rather than bare CO_2^+ or noble-gas ions [142]. Since such cluster ions drift more slowly than the primary ions, the time structure of the induced signals is correspondingly modified. The effect can be present in constant-field detectors and TPCs (see Sec. 35.6.4), and might affect devices such as Micromegas (see Sec. 35.6.3) and drift tubes.

Negative ions, formed through the capture of primary ionization electrons by highly electronegative gas components (e.g., CS_2), can be utilized in negative-ion time projection chambers (TPCs). In such detectors, the negative ions drift toward the anode under the influence of an electric field, with their diffusion reduced to the thermal limit. This technique enables high spatial resolution and can extend the sensitivity of directional dark matter searches [143].

Table 35.7: Mobility of ions in gases and mixtures at NTP [141].

Gas	Mobility μ ($cm^2\ V^{-1}\ s^{-1}$)
He	10.4
Ne	4.7
Ar	1.54
Ar-CH_4	1.87
Ar-CO_2	1.72
CH_4	2.26
CO_2	1.09

35.6.2 *Multi-Wire Proportional and Drift Chambers*

Revised August 2025 by P. Gasik (GSI Darmstadt; FAIR Darmstadt; Technische U., Darmstadt).

Single-wire counters that detect the ionization produced in a gas by a charged particle, followed by charge multiplication and collection around a thin (typically 20 – 50 µm diameter) wire, have been used for decades. Good energy resolution is obtained in the proportional amplification mode, while very large saturated pulses can be detected in the streamer and Geiger modes [144].

35.6.2.1 *Multi-wire proportional chamber, MWPC*

Modern fully electronic devices, multiwire proportional chambers (MWPCs) [145, 146] introduced in the late 1960s, detect, localize, and measure energy deposit by charged particles over large areas. A plane of parallel anode wires at a suitable potential, inserted between two cathodes, can be regarded as a set of independent proportional counters (see Fig. 35.8a). Electrons released in the gas volume drift towards the anodes and produce avalanches in the increasing field. Analytic expressions for the electric field can be found in many textbooks. The fields close to the wires $E(r)$, in the drift region E_D, and the capacitance C per unit length of anode wire is approximately given by

$$E(r) = \frac{CV_0}{2\pi\epsilon_0}\frac{1}{r} \qquad E_D = \frac{CV_0}{2\epsilon_0 s} \qquad C = \frac{2\pi\epsilon_0}{\pi(\ell/s) - \ln(2\pi a/s)}\ , \tag{35.15}$$

where r is the distance from the center of the anode, s is the wire spacing, ℓ and V_0 are the distance and potential difference between anode and cathode, and a is the anode wire radius.

In wire chambers, most of the increase of avalanche particle density occurs very close to the anode wires, and a simple electrostatic consideration shows that the largest fraction of the detected signal is due to the motion of positive ions receding from the wires. The electron component, although very fast, contributes very little to the signal. This determines the characteristic shape

of the detected signals in the proportional mode: an extremely sharp onset followed by a long "ion tail". The latter limits the time resolution of the detector, and is usually removed by differentiation of the signal.

Because of electrostatic forces, anode wires are in equilibrium only for a perfect geometry. Small deviations result in forces displacing the wires alternatively below and above the symmetry plane, sometimes with catastrophic results [147]. These displacement forces are countered by the mechanical tension of the wire, up to a maximum unsupported stable length, L_M [148], above which the wire displaces:

$$L_M = \frac{s}{CV_0}\sqrt{4\pi\epsilon_0 T_M} \tag{35.16}$$

The maximum tension T_M depends on the wire diameter and modulus of elasticity. Internal supports and spacers can be used in the construction of longer detectors to overcome limits on the wire length imposed by Eq. (35.16).

Detection of charge on the wires over a predefined threshold provides the transverse coordinate to the wire with an accuracy comparable to that of the wire spacing. The coordinate along each wire can be obtained by measuring the ratio of the collected charge at the two ends of the resistive wires. The cathode planes can be fabricated in the form of a group of wires or isolated strips, which are often patterned in orthogonal directions. By exploiting the charge profile induced by avalanches on segmented cathodes, the so-called electronic center-of-gravity (COG) method enables track localization with sub-millimeter accuracy. Due to the statistics of energy loss and asymmetric ionization clusters, the position accuracy is ∼50 µm rms for fast particles perpendicular to the wire plane, but degrades to ∼250 µm at 30° to the normal [149].

35.6.2.2 *Drift chambers*

Drift chambers, developed in the early '70s, can be used to estimate the space coordinate perpendicular to the wires by exploiting the arrival time of electrons at the anodes if the time of interaction is known [150]. The distance between anode wires is typically several centimeters, enabling the coverage of large areas at reduced cost. In the original design, a thicker wire (the field wire, often from Cu-Be or Al) at the proper voltage, placed between the anode wires (e.g., gold-plated tungsten), removes the low-field region at the mid-point between anodes and improves charge collection (Fig. 35.8b). In some drift chamber designs, and with the help of suitable voltages applied to field-shaping electrodes, the electric field structure is adjusted to improve the linearity of the space-to-drift-time relation, resulting in better spatial resolution [151].

Drift chambers can achieve a longitudinal spatial resolution from timing measurements on the order of 100 µm (rms) or better for minimum ionizing particles, depending on the geometry and operating conditions. However, a degradation of resolution is observed due to primary ionization statistics for tracks close to the anode wires, caused by the spread in arrival time of the nearest ionization clusters [152]. The effect can be reduced by operating the detector at higher pressures. Sampling the drift time on rows of anodes led to the concept of multiple arrays, such as the multi-drift module [153] and the JET chamber [154]. A measurement of drift time, together with the recording of charge sharing from the two ends of the anode wires, provides the coordinates of segments of tracks. An ultimate drift chamber design is the Time Projection Chamber (TPC) concept [155], which provides 3D precision tracking with low material budget and enables particle identification through differential energy loss $\mathrm{d}E/\mathrm{d}x$ measurement or cluster counting $\mathrm{d}N_{\mathrm{cl}}/\mathrm{d}x$ techniques (see Sec. 35.6.4). In all cases, a good knowledge of electron drift velocity and diffusion properties is required. This has to be combined with the knowledge of the electric fields in the structures [133]. For an overview of detectors exploiting the drift time for coordinate measurement, see Refs. [148, 156].

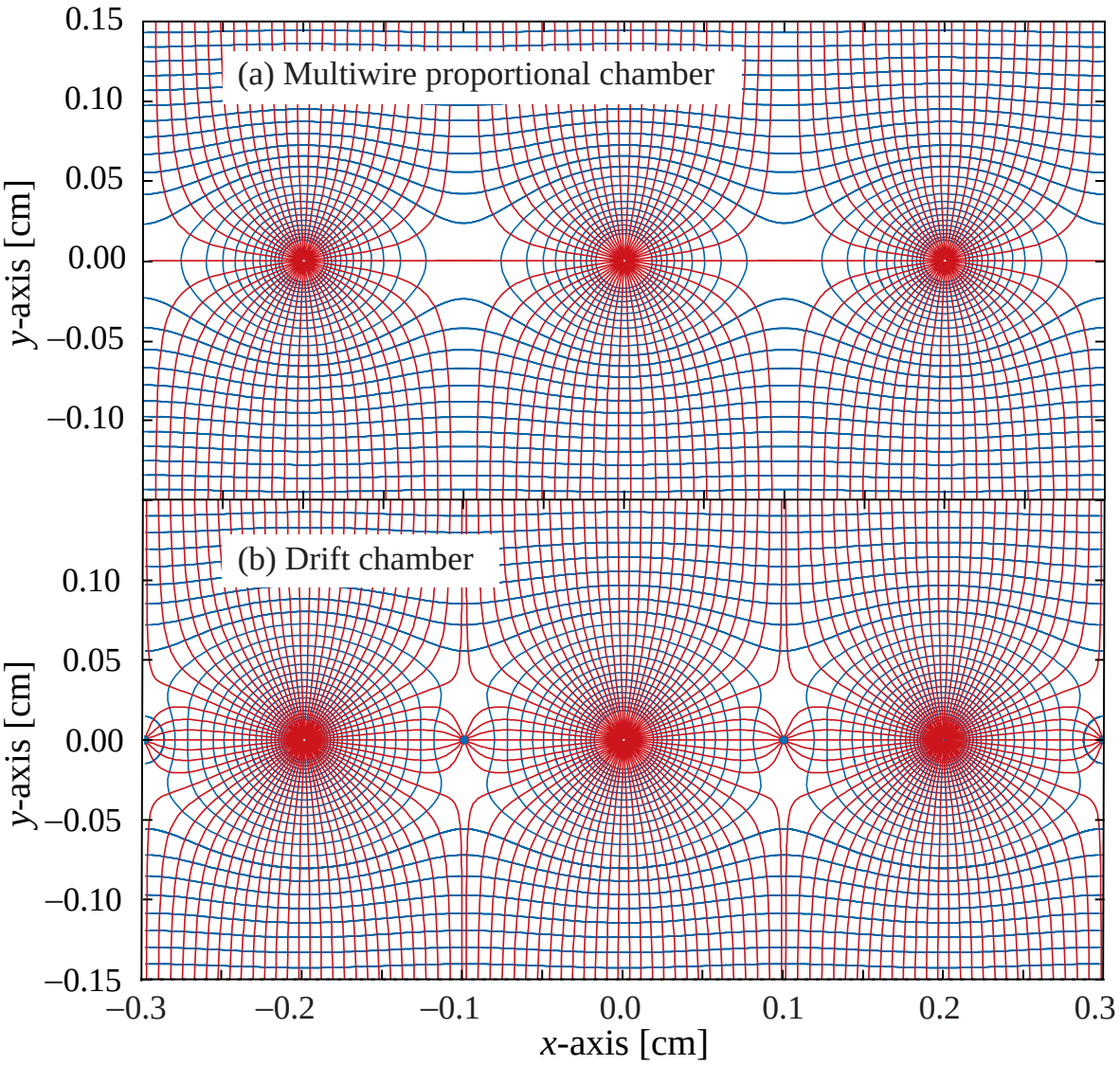

Figure 35.8: Electric field lines and equipotentials in (a) a multiwire proportional chamber and (b) a drift chamber.

Multiwire and drift chambers have been operated with a variety of gas fillings and operating modes, depending on experimental requirements. For example, a mixture of argon, isobutane and freon in the volume proportions 70-29.6-0.4 [146], permits very high and saturated gains ($\sim 10^6$), i.e., a pulse-height distribution independent of the number of primary ionization charges. While this mixture was successfully used in early wire chambers, it was later found to suffer from severe aging effects. Similarly, light mixtures based on helium and hydrocarbons, although commonly employed, do not provide the reliability needed for long-term, high-rate operation [157]. To meet the demands of future colliders, dedicated R&D is required to identify suitable hydrocarbon-free gas mixtures that can ensure both stable operation and the desired detector performance.

The next generation of ultralight central trackers for future colliders aims at minimizing material budget, where the dominant contribution to the radiation length originates from tungsten wires. Significant progress has been achieved through the development of alternative wire materi-

als (e.g., carbon monofilaments) and novel wiring and assembly procedures, building on experience from detectors such as the DAFNE KLOE Drift Chamber and its recent evolution for the MEG2 experiment [158].

35.6.2.3 *Straw and drift tubes*

Although very powerful in terms of performance, multi-wire structures can have reliability issues, as a single broken wire can disable a larger part or even the entire detector. Introduced in the 1980s, straw and drift tube systems make use of large arrays of proportional counters where each wire is encased and protected in a tube and acts as an independent wire counter [159]. Techniques for low-cost mass production of these detectors have been developed for large experiments, such as the Transition Radiation Tracker and the Drift Tubes arrays for CERN's LHC experiments [160]. The state-of-the-art straw trackers utilize new construction techniques of ultrasonic welding of the straw film tube, keeping it straight and withstanding the surrounding vacuum pressure without breaking (see [161], for example). Future efforts for straw detectors, e.g., COMET Phase-II at JPARC, Mu2e-II at Fermilab, or SHiP at CERN, will focus on ultra-thin wall developments, smaller tube diameters, long and thin wire handling, precise mechanics, and innovative designs.

35.6.2.4 *High-rate effects*

The production of positive ions in the avalanches and their slow drift before neutralization result in a rate-dependent accumulation of positive charge in the detector. This may result in significant field distortion, gain reduction, and degradation of spatial resolution. As shown in Fig. 35.9 [162], the proportional gain drops above a charge production rate around 10^9 electrons per second per millimeter of wire, independently of the avalanche size. For a proportional gain of 10^4 and 100 electrons per track, this corresponds to a particle flux of $10^3\,\mathrm{s}^{-1}\mathrm{mm}^{-1}$ (1 kHz/mm^2 for 1 mm wire spacing). Improvement of rate capability can be achieved by reducing the anode-to-cathode distance.

During the operation of gaseous detectors in particle accelerator experiments, performance degradation due to the formation of polymer deposits (so-called ageing) on electrode surfaces is often observed. Ageing phenomena can lead to operational instabilities and even total malfunctioning of the detectors operated under increasing charge density doses [163]. This process has been extensively investigated both in operating experiments and in dedicated laboratory studies. In general, gas polymerisation originates from the use of hydrocarbons as quenchers as well as from the outgassing of organic pollutants from certain insulators, glues, and silicon oils. Since the deposited layers are usually insulating, the addition of water vapour can sometimes mitigate performance degradation, although it does not necessarily stop the polymerisation process. Modern detectors, therefore, rely on a strict selection of construction materials and carefully controlled gas mixtures and purities, allowing the collection of several C/cm^2 on the relevant electrodes without observable ageing effects.

35.6.3 *Micro-Pattern Gas Detectors*

Revised August 2025 by P. Gasik (GSI Darmstadt; FAIR Darmstadt; Technische U., Darmstadt).

Despite continuous improvements, position-sensitive detectors based on wire structures remain fundamentally limited by diffusion processes and space-charge effects, which restrict localization accuracies to about 50–100 µm [164]. Advances in microelectronics and photolithographic technology on flexible and standard PCB substrates enabled, toward the end of the 20th century, the development of novel Micro-Pattern Gaseous Detectors (MPGD) [165–167]. From the outset, the objective was to design devices combining high-rate capability (up to 10^6 Hz/mm^2), excellent spatial resolution (down to 30 µm), single-photoelectron timing in the nanosecond range, large sensitive area and dynamic range, superior radiation hardness, and cost-effectiveness for large-area coverage. Today,

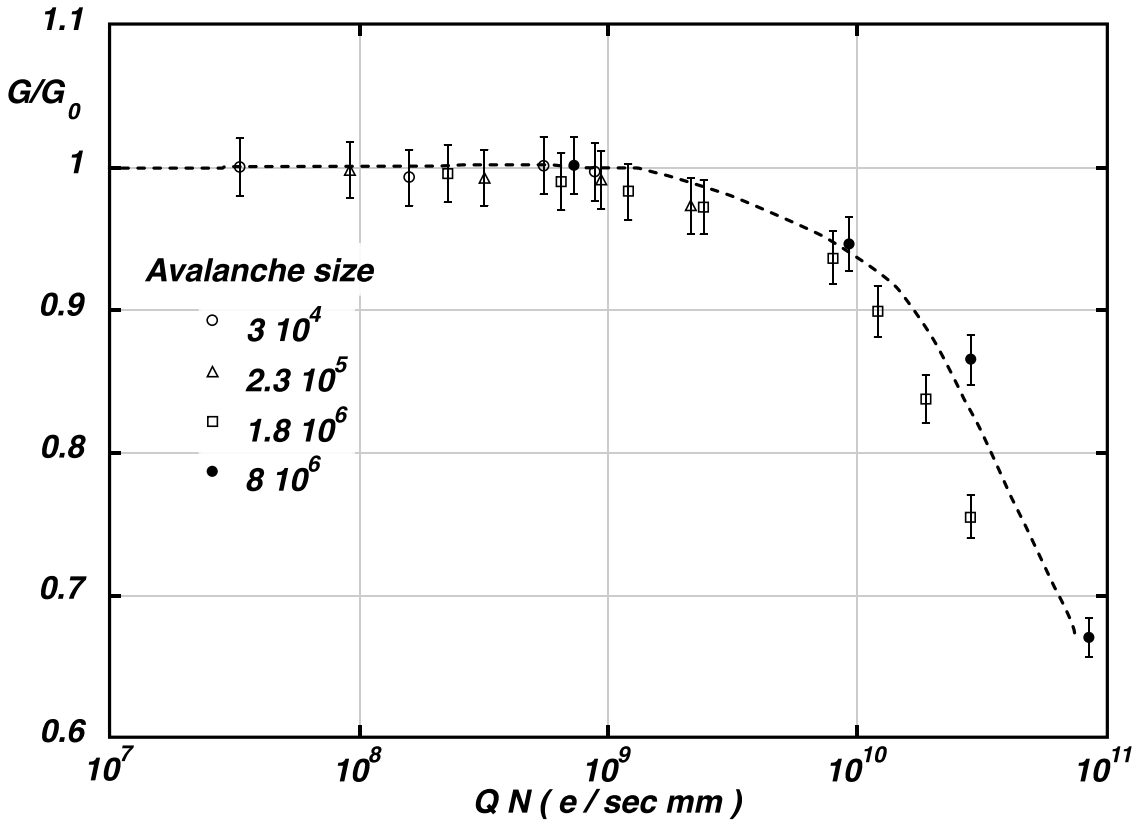

Figure 35.9: Charge rate dependence of normalized gas gain G/G_0 (relative to zero counting rate) in proportional thin-wire detectors [162]. Q is the total charge in a single avalanche; N is the particle rate per wire length.

a broad family of MPGD technologies is being developed and optimized for a wide spectrum of applications, including [168,169]: the Micro-Strip Gas Chamber (MSGC), Gas Electron Multiplier (GEM), Micro-Mesh Gaseous Structure (Micromegas), THick GEMs (THGEM, also referred to as Large Electron Multipliers, LEM), Resistive Plate WELL (RPWELL), GEM-derived architectures such as the µ-RWELL, the Micro-Pixel Gas Chamber (µ-PIC), and integrated gaseous detector readout concepts (GridPix, InGrid) that couple amplification stages with solid-state pixel detector ASICs (e.g., Medipix or Timepix).

The **MSGC** concept, invented in 1988, was the first of the micro-structure gas chambers [165]. It consists of a set of tiny parallel metal strips laid on a thin resistive support, alternatively connected as anodes and cathodes, and resembles a multi-anode proportional counter. Through an accurate and simple photolithography process, the anode strips can be made very narrow (∼10 µm) with a typical pitch (distance between strips) of ∼100 µm. When appropriate potentials are applied to the electrodes, electrons released in the drift volume move toward the strips and multiply in the high-field region. Owing to the small anode-to-cathode distance, the fast removal of positive ions by nearby cathode strips reduces space charge build-up and significantly improves the rate capability, compared to the wire counter. Despite their promising performance, experience with MSGCs has raised serious concerns about their long-term behavior. There are several major processes, particularly at high rates, leading to the MSGC operational instabilities: substrate charging-up and time-dependent distortions of the electric field, surface deposition of polymers ("ageing") during

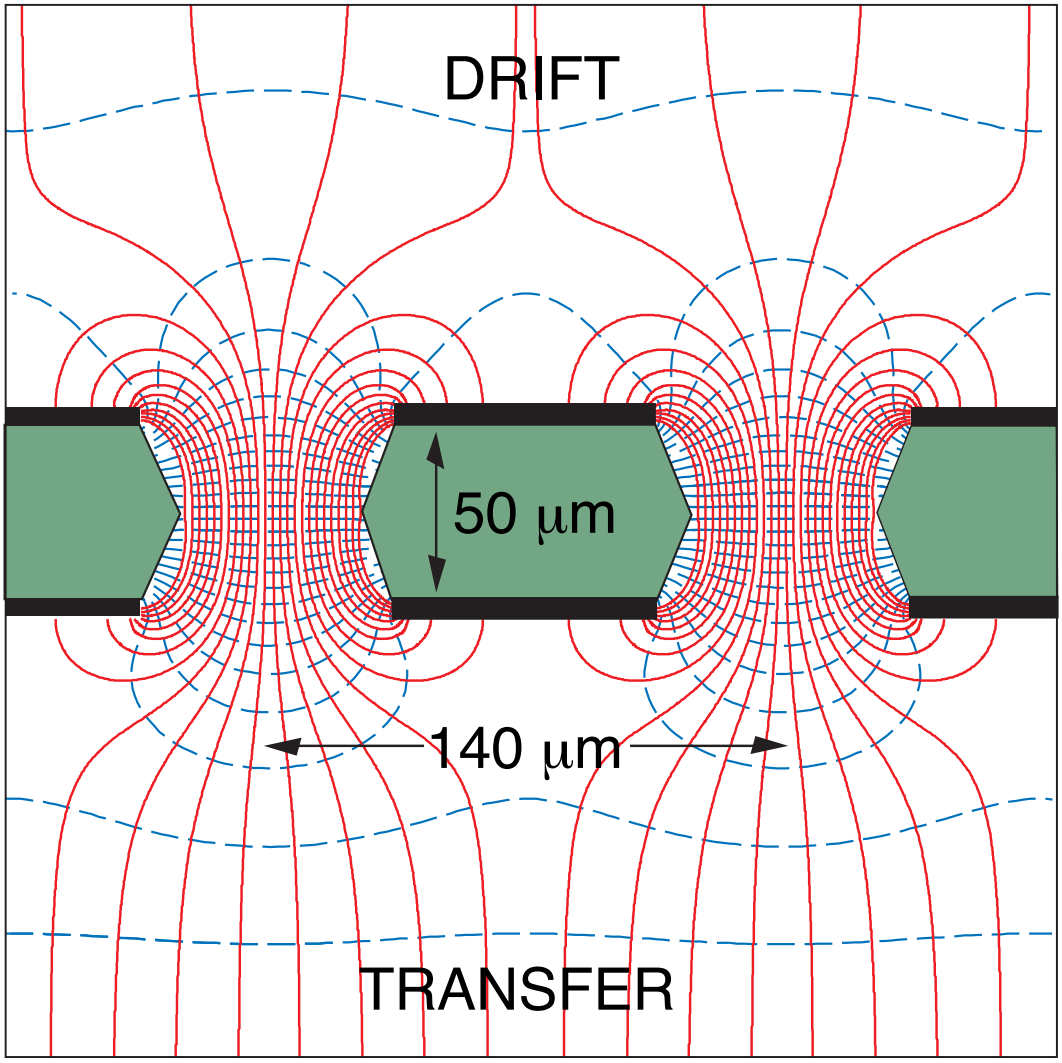

Figure 35.10: Schematic view and typical dimensions of the hole structure in the GEM amplification cell. Electric field lines (solid) and equipotentials (dashed) are shown. Electron trajectories do not strictly follow the electric field lines, since drifting electrons undergo isotropic scattering with gas molecules and, consequently, diffuse transversely.

sustained irradiation, and destructive discharges under exposure to heavily ionizing particles [170]. The physical parameters used to manufacture and operate these detectors (substrate material, metal of strips, type and purity of the gas mixture) appeared to play dominant roles in determining the medium- and long-term stability. The problems encountered inspired the development of novel structures, using modern photolithographic processes: GEM, Micromegas, and others, having increased reliability and radiation hardness.

A **GEM** detector consists of a thin-foil copper-insulator-copper sandwich chemically perforated to obtain a high density of holes in which avalanches occur [166, 171]. The hole diameter is typically of $\mathcal{O}(50\ \mu\text{m})$, with a hole pitch of 140 µm, which can be further optimized depending on the application. The central insulator is usually (in the original design) a polyimid foil, with a thickness of 50 µm. Application of a potential difference between the two metal sides of the GEM generates the electric fields indicated in Fig. 35.10. Each hole acts as an independent proportional

counter. Electrons created by primary ionization in the drift gap above the GEM foil drift into its holes, where they undergo avalanche multiplication in the strong electric field (50–70 kV/cm). A significant fraction of the avalanche electrons exits the multiplication region and is extracted into the transfer gap below the foil, from where it can either be collected by an electrode or injected into a subsequent amplification stage. Systematic measurements with cascaded multi-GEM structures confirm that the gains and charge transfer processes are predictable from electrostatic considerations and avalanche development models; an overall gas gain well above 10^4 can be reached in the presence of highly ionizing particles, while strongly reducing the risk of discharges [172]. Other important parameters, such as attachment or diffusion, depend on the gas mixture composition and the reduced electric field E/p, where E is the electric field and p is the gas pressure. The majority of charges created in the avalanche process follow the electric field lines and are collected by the metallic electrodes. Owing to diffusion, however, a fraction may instead deposit on dielectric surfaces, thereby modifying the field configuration and affecting both the gain and the transparency of the structures [173]. This phenomenon is known as the "charging-up" effect; its time constant and amplitude depend strongly on the hole geometry.

The negative signal on the readout anode (below the last GEM in a multi-GEM structure) is primarily induced by the motion of electrons, with only a minor contribution from the ions produced in the amplification process. As a result, the signal is very fast, with a width determined by the drift of the high-mobility electrons over a distance of a few millimetres. Depending on the gas mixture, this enables time resolutions better than 10 ns. The achievable energy resolution is comparable to that of conventional proportional counters, around 17% FWHM for 5.9 keV X-rays [169].

For position measurements, the readout anode can be segmented into strips or pads. Because of the diffusion of the electron cloud in the transfer gaps between GEM foils and in the induction gap above the anode, the charge is shared among several neighbouring readout elements. A centre-of-gravity reconstruction of this charge distribution yields a spatial resolution that surpasses the segmentation pitch. In practice, resolutions well below 100 µm can be obtained, reaching 30 µm with finely segmented electrodes.

A **Micromegas** is a thin parallel-plate avalanche counter, as illustrated in Fig. 35.11 [167]. It employs a stretched metallic mesh, suspended on insulating pillars at a distance of $\mathcal{O}(100\,\mu\text{m})$ above a readout electrode, consisting of strips or pads of conductor printed on an insulating board. The pillars are attached to the mesh and patterned regularly using photolithography techniques. Electrons from the primary ionization drift through the mesh into the narrow multiplication gap, where they are amplified. The electric field is largely homogeneous in both the drift region (∼1 kV/cm) and the amplification region (50–70 kV/cm), but assumes a funnel-like shape near the micromesh openings: the field lines are compressed into a diameter of only a few micrometers, depending on the field ratio between the two gaps. The electron transparency, i.e. the fraction of ionization electrons transmitted into the amplification gap, is determined by the mesh geometry and the ratio of drift to amplification fields. High collection efficiency is obtained when the drift field exceeds the amplification field by a factor of 30–40 [169]. In the narrow multiplication region, small variations of the amplification gap are approximately compensated by the inverse dependence of the Townsend coefficient on the electric field, resulting in a more uniform gain. The transverse size of the electron avalanche due to diffusion is on the order of 10–15 µm, depending on the gas mixture, the electric field, and the gap width. This results in excellent spatial resolution, reaching about 12 µm for MIPs [174]. Most positive ions created in the avalanche process are quickly removed by the micromesh. This prevents space-charge accumulation and leads to very fast signals (∼100 ns), dominated by the electrons, with a small tail contribution from the ions.

Employment of photolithography and etching techniques allows for an improved spatial resolution and improved rate capabilities (up to a few MHz/cm^2). For the same reason, the $E \times B$

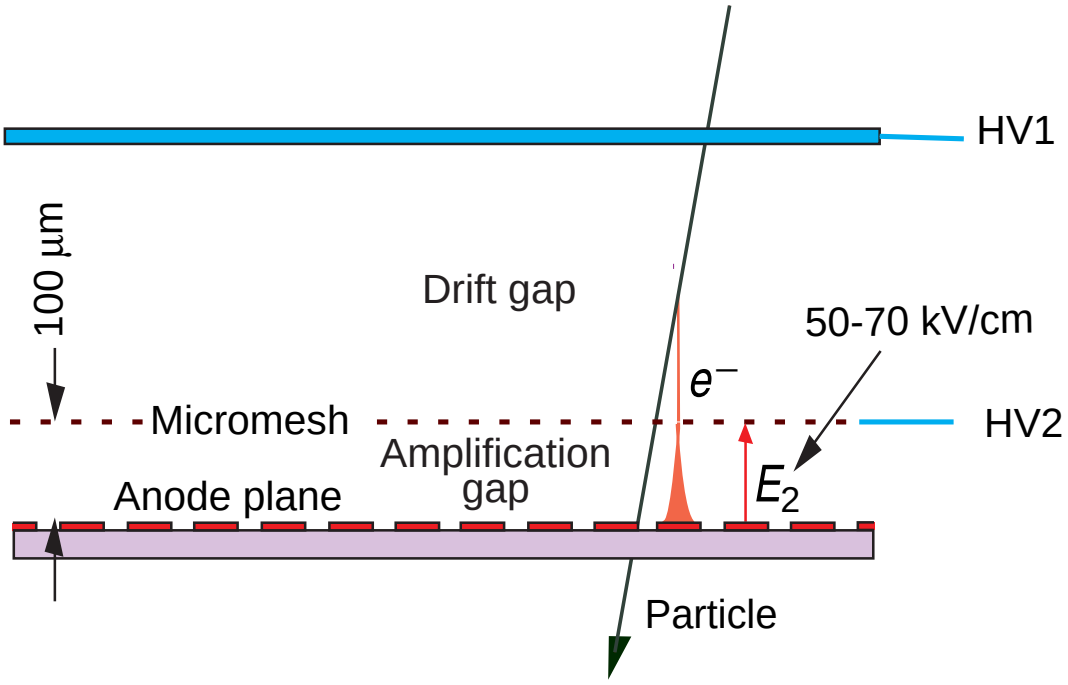

Figure 35.11: Schematic drawing of the Micromegas detector.

effects can be neglected. The absence of space-charge effects in GEMs at the highest rates reached so far, thanks to its fine-pitch structure of a few hundred microns, improves the maximum rate capability by more than two orders of magnitude compared to MWPC (see Fig.35.12) [175] [176]. Even larger rate capability has been reported for Micromegas [177]. In addition, the peculiar shape of the electric field lines obtained in MPGD structures provides intrinsic ion feedback reduction capabilities (see also Sec. 35.6.4).

The fine granularity and high-rate capability of GEM and Micromegas can be fully exploited by using high-density pixel readout with a size corresponding to the intrinsic width of the detected avalanche charge. An elegant solution is the use of a CMOS pixel ASIC, assembled directly below the GEM or Micromegas amplification structure. Modern wafer post-processing technology allows an integration of a small-scale micromesh grid directly on top of a Timepix chip, thus forming an integrated MPGD readout, called GridPix concept (see Fig.35.13) [178]. With this arrangement, avalanche electrons are collected on the metalized input pads, exposed to the gas, and signals are induced at the input gate of a charge-sensitive preamplifier. Every pixel is then directly connected to the amplification and digitization circuits, integrated in the underlying CMOS layers. A thin insulating layer, e.g., a few µm of silicon nitride, is usually deposited on top of CMOS ASIC to protect against destructive discharges across the $\mathcal{O}(50\ \mu\text{m})$ amplification gap. The GridPix concept provides the high granularity needed to resolve individual electron clusters (separated by an average distance of a few hundred µm) and to determine energy loss by the cluster counting technique ($\mathrm{d}N/\mathrm{d}x$), rather than by the charge measurement, with a precision better than 3 %. New structures, where a GEM foil is facing the Medipix chip, forming the GEMpix detector, are in use for medical applications [179] as well as for monitoring the radioactive waste [180].

Gaseous detectors represent the most cost-effective solution to cover very large areas with photosensitive elements. MPGD-based gaseous photomultipliers, conceived to overcome the limitations of MWPCs, with semi-transparent or reflective photocathodes (PC), allow for minimizing PC aging

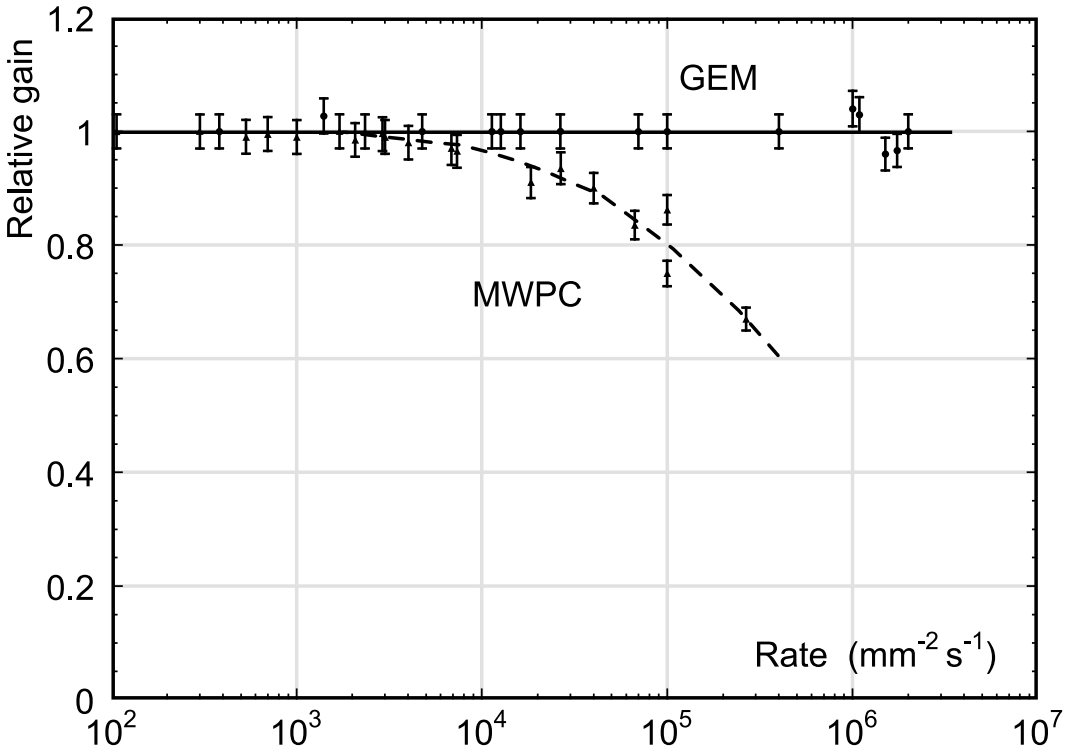

Figure 35.12: Normalized gas gain as a function of particle rate for MWPC [175] and GEM [176].

due to the ion and photon feedback and to avoid secondary effects causing electrical instability. For RICH applications requiring large-area coverage and moderate spatial resolution, coarser macro-patterned structures such as THGEM offer an interesting, cheaper solution [181].

Following the same principles, a **THGEM** shares a structural similarity with a GEM foil but features dimensions larger by roughly an order of magnitude in all directions. Instead of a thin polyimide sheet, it employs a thick PCB substrate as the dielectric, with holes produced through mechanical drilling and subsequent chemical rim etching of the metal cladding. While the spatial resolution of a THGEM is reduced compared to that of GEMs, it offers a robust alternative for large-area cryogenic detectors or photodetectors. Notably, MPGDs are already applied in single-photon detection—for instance, in the COMPASS RICH detector, which uses a hybrid architecture composed of two THGEM layers (one coated with a CsI photocathode) followed by a Micromegas as the final amplification stage.

Resistive electrodes are increasingly employed in MPGD-based detectors to enhance spatial resolution and reduce the number of readout channels via charge sharing. Moreover, they provide effective spark protection for front-end electronics and reduce the discharge probability. When used as a high-voltage electrode or as a resistive layer capacitively coupled to the readout elements (e.g., strips or pads), they introduce a self-quenching mechanism that suppresses discharge development.

As an example, closed-geometry THGEM-based structures, known as **RPWELL** [182], have been developed, incorporating resistive anodes and combining features of THGEMs with those of Resistive Plate Chambers (RPCs, see Sec. 35.6.6). The concept consists of a single-faced THGEM, copper-clad only on its top side, placed directly on a resistive film deposited on a thin insulating sheet. Compared to a standard THGEM with an induction gap, the RPWELL configuration allows higher gains to be reached at lower applied voltages across the THGEM electrode, owing to the

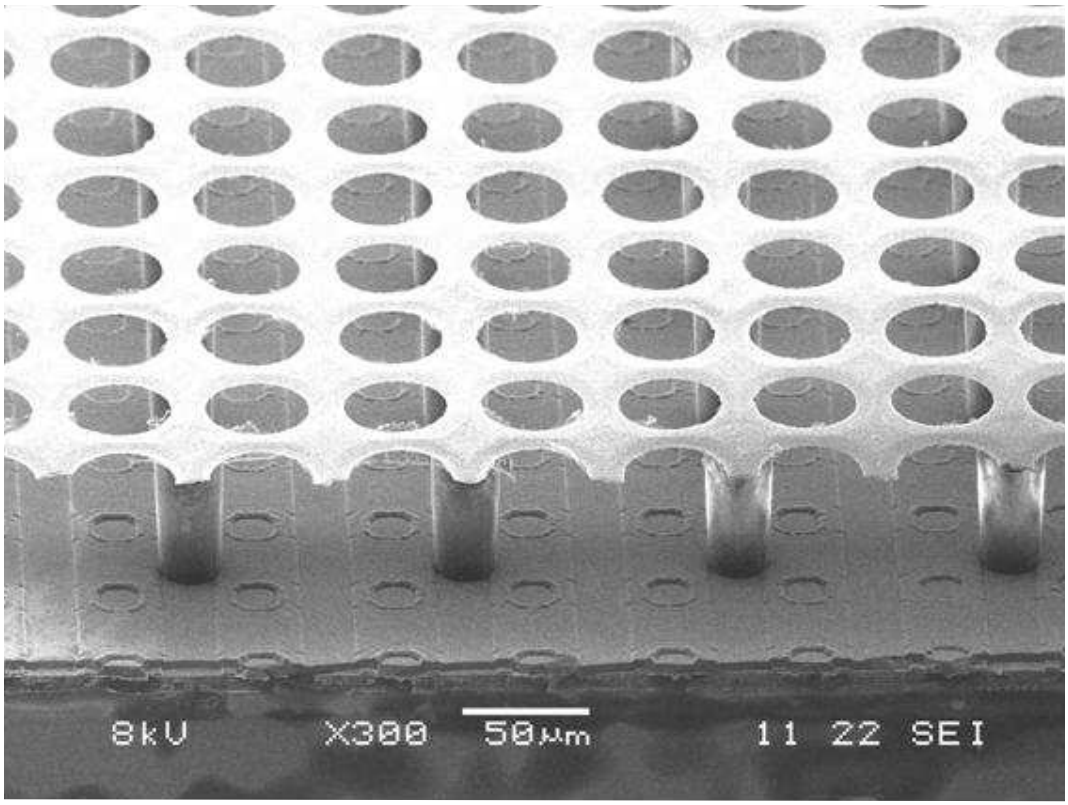

Figure 35.13: Photo of the Micromegas ('GridPix") detector. The grid holes can be accurately aligned with the readout pixels of the Timepix CMOS chip. The insulating pillars are centered between the grid holes, thus avoiding dead regions.

stronger electric field inside the closed holes.

With the gas discharge quenching capabilities, on the other hand, gain reduction comes into play at higher rates. In one of the pioneering studies with resistive Micromegas it was shown that the signal amplitude slowly decreases with increasing rate, reaching a drop of ∼20% at the rate of $10\,\mathrm{kHz/cm^2}$ [183, 184].

Further improvements in resistive-electrode technology continue. A diamond-like carbon (DLC), a class of meta-stable amorphous carbon material that contains both diamond-structure and graphite-structure, has recently attracted much attention in the MPGD community and is exploited to make resistive electrodes to suppress discharges occurring in MPGDs [185, 186]). The DLC coating can also reduce gain variations over time and minimize charging-up effects.

One such implementation is the **µ-PIC** structure, an industrially manufactured PCB featuring anode strips on one side and orthogonal cathode strips on the opposite side. Along the cathode strips, a regular pattern of uncoated regions is formed; at the center of each, a conductive "dot" connected via a buried electrode in the thin substrate transmits the anode potential. Electron avalanches develop in the high-electric-field region surrounding these point-like anodes. Compared to MSGCs, the electric field near the cathode edges is significantly reduced, leading to a lower discharge probability. Furthermore, a DLC coating on the cathode strips ensures tolerance to occasional discharges [187].

A very promising GEM-derived architecture is the **µ-RWELL** [188], featuring a pitch approximately seven times smaller than that of the RPWELL. Various configurations of the resistive stage

(DLC) have been explored during the detector's development, culminating in a high-rate-optimized design that incorporates 3D charge evacuation through conductive vias [189]. This layout enables the detector to achieve gains up to 10^4 in a single amplification stage, and a rate capability exceeding $10\,\mathrm{MHz/cm^2}$.

A major step toward large-scale applications has been achieved through both conceptual consolidation and the development of industrial, cost-effective MPGD manufacturing techniques, such as resistive Micromegas [183] and single-mask or self-stretching GEM methods [190]. The successful scaling of MPGDs to very large single-unit detectors of $\mathcal{O}(\mathrm{m}^2)$ has enabled their deployment in the High-Luminosity LHC upgrades: Micromegas now cover an area of about $1000\,\mathrm{m}^2$ in the New Small Wheel of the ATLAS muon endcaps, GEMs are employed in the CMS muon system and the ALICE TPC readout, and a GEM+μRWELL hybrid is foreseen for the upgrade of the innermost regions of the LHCb muon system.

Exploiting the Micromegas, GEM, and μ-RWELL ability to measure both position and arrival time of the charge released in the drift gap, a novel μ-TPC concept has been developed. It permits achieving nearly constant spatial resolution over a wide range of particle incident angles and allows 3D track reconstruction with a single MPGD layer [191]

The consolidation of well-established technologies has been accompanied by the emergence of novel ones, often tailored to specific applications. Building on the Micromegas and GEM concepts, modern developments increasingly adopt hybrid approaches that integrate different elements within a single device – for instance, combining gaseous with non-gaseous detectors, as in optically read out detectors. Hybrid structures, combining various MPGD technologies, aimed at enhancing detector performance, remains a valuable strategy to address future experimental challenges such as high granularity and picosecond-level timing (e.g., the PICOSEC-Micromegas concept [192]). Moreover, GEMs, Micromegas, and μ-RWELLs can be bent to form cylindrically curved, ultra-light inner tracking systems that operate without support or cooling structures [193].

A clear direction for future MPGD developments is the use of resistive materials and related detector architectures. Their introduction enhances detector stability and allows higher gain to be reached within a single multiplication stage. Beyond resistive electrodes, further progress requires novel materials and advanced fabrication techniques. Contributions to detector concepts are needed in several areas, including resistive layers, solid-state photon and neutron converters, and innovative nanotechnology components. Material studies are particularly relevant for meeting stringent requirements such as low outgassing, radiation hardness, radio-purity, converter robustness, and compatibility with eco-friendly gases. The next generation of MPGDs can also profit from emerging technologies, such as Micro-Electro-Mechanical Systems (MEMS), advanced sputtering methods, novel photoconverters, and 3D-printed amplification structures or cooling circuits. These developments are being actively pursued in the framework of the world-wide CERN-DRD1 collaboration and its broad program of R&D on gaseous detector technologies [194].

35.6.4 *Time-projection chambers*

Revised August 2023 by C. Lippmann (GSI Darmstadt).

The Time Projection Chamber (TPC) concept was invented by David Nygren in the 1970's [195]. It consists of a cylindrical or square field cage that is filled with a gaseous (or liquid) detection medium. Charged particles produce tracks of ionization electrons that drift in a uniform electric field towards a position-sensitive amplification stage which provides a 2D projection of the particle trajectories. The third coordinate can be calculated from the arrival times of the drifted electrons. The start for this drift time measurement is usually derived from an external detector, e.g. a fast

interaction trigger detector.

This section focuses on the gas-filled TPCs that are often used in particle or nuclear physics experiments at accelerators on account of their low material budget. For neutrino physics (Sec. 36) or for detecting rare events (Sec. 36.4), on the contrary, usually high density and large active mass are required, and a liquid detection medium is favored.

The TPC enables full 3D measurements of charged particle tracks, which gives it a distinct advantage over other tracking detector designs which record information only in two-dimensional detector planes and have less overall segmentation. The track points recorded in a TPC are basically adjacent, which facilitates the track finding enormously. This advantage is often exploited for pattern recognition in events with large numbers of particles, e.g. heavy-ion collisions. Two examples of modern large-volume gaseous TPCs are shown in (Figure 35.14) and (Figure 35.15).

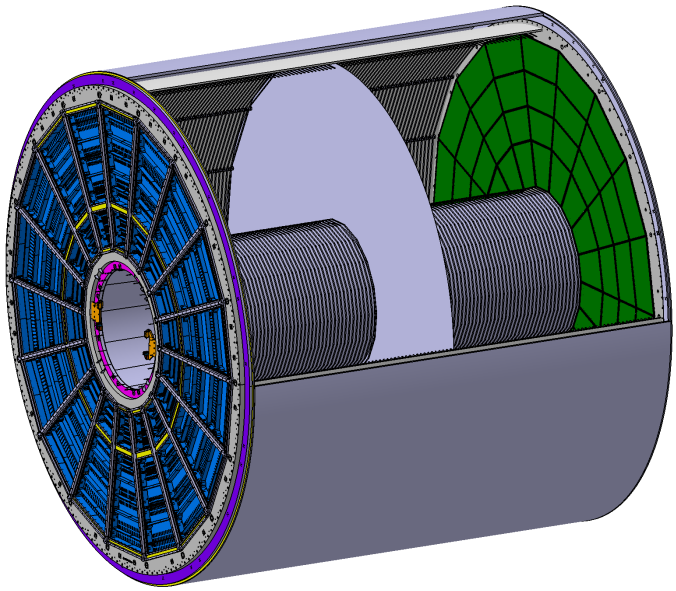

Figure 35.14: Schematic view of the ALICE TPC [196,197]. The drift volume with 5 m diameter is divided into two halves, each providing 2.5 m drift length. The amplification stage has recently been upgraded from wire planes to GEMs.

Identification of the charged particles crossing the TPC is possible by simultaneously measuring their momentum and specific energy deposit through ionisation ($\mathrm{d}E/\mathrm{d}x$). The momentum, as well as the charge sign, are calculated from a helix fit to the particle trajectory in the presence of a magnetic field (typically parallel to the drift field). For this application, precise spatial measurements in the plane transverse to the magnetic field are most important. The specific energy deposit is estimated from many charge measurements along the particle trajectory (e.g. one measurement per anode wire or per row of readout pads). As the charge collected per readout segment depends on the track angle and on the ambient conditions, the measured values are corrected for the effective length of the track segments and for variations of the gas temperature and pressure. The most probable value of the corrected signal amplitudes for a given track provides the best estimator for the specific energy deposit (see Sec. 34.2.3); it is usually approximated by the truncated mean, i.e. the average of the 50%–70% smallest values. The resulting particle identification performance is illustrated in (Figure 35.16), for the ALICE TPC.

The dependence of the achievable energy resolution on the number of measurements N, on the

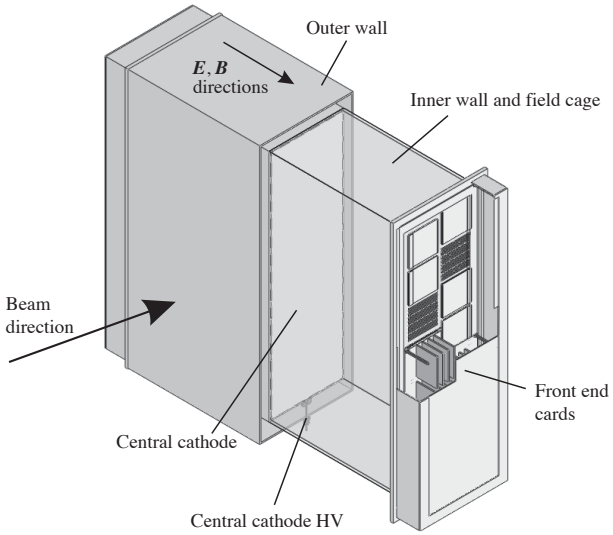

Figure 35.15: One of the 3 TPC modules for the near detector of the T2K experiment [198]. The size is $2 \times 2 \times 0.8\,\mathrm{m}^3$. Micromegas devices are used for gas amplification and readout.

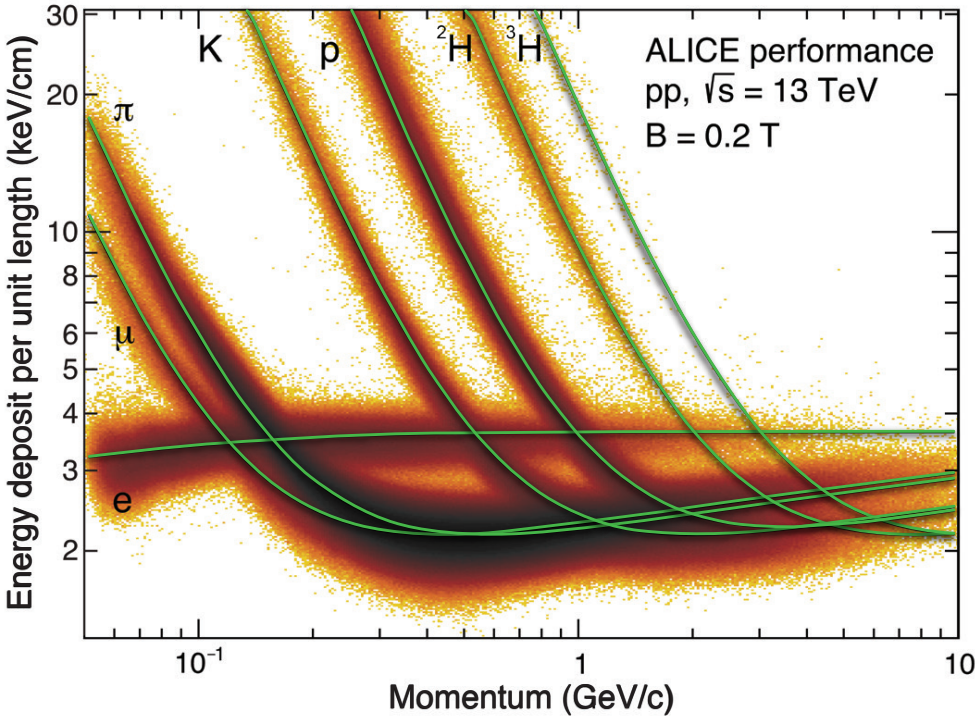

Figure 35.16: Energy deposit versus momentum measured in the ALICE TPC.

thickness of the sampling layers t, and on the gas pressure P can be estimated using an empirical formula [199]:

$$\sigma_{dE/dx} = 0.41\ N^{-0.43}(t\,P)^{-0.32}. \tag{35.17}$$

Typical values at nominal pressure are $\sigma_{dE/dx} = 4.5$ to 7.5%, with $t = 0.4$ to 1.5 cm and $N = 40$ up to more than 300. The record, with an unprecedented energy resolution of 3%, is held by the PEP-4/9 TPC [200], due to the high gas pressure of 8.5 bar.

The greatest challenges for a large TPC are due to the length of the drift of up to a few meters. In particular, it can make the device sensitive to small distortions in the electric field. Such distortions can arise from a number of sources, e.g. imperfections in the field cage construction or the presence of ions in the drift volume. The electron drift in a TPC in the presence of a magnetic field is defined by Eq. (35.14). The $E \times B$ term of Eq. (35.14) vanishes for perfectly aligned electric and magnetic fields, which can however be difficult to achieve in practice. Furthermore, the electron drift depends on the $\omega\tau$ factor, which is defined by the gas mixture and the magnetic field strength. The electrons will tend to follow the magnetic field lines for $\omega\tau > 1$, or the electric field lines for $\omega\tau < 1$. The former mode of operation makes the TPC less sensitive to non-uniformities of the electric field, which is usually desirable.

The drift of the ionization electrons is superposed with a random diffusion motion which degrades their position information. The ultimate resolution of a single position measurement is limited to around

$$\sigma_x = \frac{\sigma_D\sqrt{L}}{\sqrt{n}}\,, \tag{35.18}$$

where σ_D is the transverse diffusion coefficient for 1 cm drift, L is the drift length in cm and n is the effective number of electrons collected. Without a magnetic field, $\sigma_{D,B=0}\sqrt{L}$ is typically a few mm after a drift of $L = 100$ cm. However, in a strong magnetic field parallel to the drift field, a large value of $\omega\tau$ can significantly reduce diffusion:

$$\frac{\sigma_{D,B>0}}{\sigma_{D,B=0}} = \frac{1}{\sqrt{1+\omega^2\tau^2}}\,. \tag{35.19}$$

This factor can reach values of up to 10. In practice, the final resolution limit due to diffusion typically lies around $\sigma_x = 100\,\mu$m.

The drift and diffusion of electrons depend strongly on the gas mixture. The optimal gas mixture varies according to the environment in which the TPC operates. In all cases, the oxygen concentration must be kept very low (few ten parts per million in a large TPC) in order to avoid electron loss through attachment.

Ideally, the drift velocity should depend only weakly on the electric field at the nominal operating condition. The classic Ar/CH_4 (90:10) mixture, known as P10, has a drift velocity maximum of 5 cm/μs at an electric field of only 125 V/cm (Figure 35.5). In this regime, the electron arrival time is not affected by small variations in the ambient conditions. Moreover, low electric fields simplify the design and operation of the field cage. The mixture has a large transverse diffusion at $B = 0$, but this can be reduced significantly in a strong magnetic field due to the relatively large value of $\omega\tau$.

For some applications organic gases like CH_4 are not desirable since they may cause aging. An alternative is to replace CH_4 with CO_2. An Ar/CO_2 (90:10) mixture has a low transverse diffusion at all magnetic field strengths, but does not provide a saturated drift velocity for the typical electric fields used in TPCs (up to a few 100 V/cm). As a consequence, it is quite sensitive to the ambient

conditions. Freon admixtures like CF_4 can be an attractive option for a TPC as well, since the resulting gas mixtures provide high drift velocities at low electric fields. However, the use of CF_4 always needs to be thoroughly validated for compatibility with all materials of the detector and the gas system.

Historically, the amplification stages used in gaseous TPCs have been planes of anode wires operated in proportional mode. The performance is limited by effects related to the feature size (wire spacing) of a few mm. Since near the wires the electric and magnetic fields are not parallel, the incoming ionisation electrons are displaced in the direction of the wires ("wire $E \times B$ effect"), which degrades the resolution. The smaller feature sizes of Micro-Pattern Gas Detectors (MPGDs) like GEMs and Micromegas lead to many advantages as compared to wire planes (see Sec. 35.6.3). In particular, $E \times B$ effects in the amplification stage are much smaller. Moreover, the signal induction process in MPGDs leads to a very narrow pad response, allowing for a much finer segmentation, which improves the separation for two very close tracks. Combinations of MPGDs with silicon sensors have resulted in the highest granularity readout systems so far (see Sec. 35.6.3). These devices make it possible to count the number of ionization clusters along the length of a track, which can, in principle, improve the particle identification capability. However, the big challenge for such a system is the huge number of readout channels for a TPC of a typical size.

The accumulation of the positive ions created by the ionization from the particle tracks can lead to time-dependent distortions of the drift field. Due to their low drift velocity, ions from many events may coexist in the drift volume. To reduce the effect of such a build-up of space charge, Argon can be replaced by Neon as the main component of the gas mixture. Neon features a lower number of ionisation electrons per unit of track length (see 35.6) and a higher ion mobility (see 35.7).

Of greater concern are the ions produced in the gas amplification stage. In order to prevent them from entering the drift volume, large TPCs built until now have a gating grid. The gating grid can be switched to transparent mode (usually in the presence of an interaction trigger) to allow the ionization electrons to pass into the amplification region. After all electrons have reached the amplification region, it is usually closed such that it is rendered opaque to electrons and ions. For triggered operation, a combination of a MPGD and a gating structure may be an attractive solution. However, a gating grid implies a principal rate limitation to a few kHz.

A next generation of TPCs (e.g. ALICE [197], sPHENIX [201]) has been developed for applications where a triggered operation would lead to inacceptable data loss. The employed readout schemes are based on MPGDs, as these can be optimised in order to drastically reduce the ion back-flow. Extensive work has been carried out during the 2010's to design such readout structures. In ALICE and sPHENIX ion back-flow values below 1 % are achieved with a thorough adjustment of the various fields in a quadruple GEM system. Similar levels of ion back-flow can be reached with Micromegas detectors [202].

35.6.5 *Transition radiation detectors (TRD's)*

Revised August 2025 by P. Nevski (BNL) and A. Romaniouk (Innsbruck U.; Istinye U.).

Transition radiation (TR) x-rays are produced when a highly relativistic particle with Lorentz factor $\gamma \gtrsim 10^3$ crosses a refractive index interface, as discussed in Sec. 34.7. Since the TR yield is about a few % per boundary crossing, radiation from multiple surface crossings (e.g., a stack of foils) is used in practical detectors. The x-rays, ranging from a few keV to a few dozen keV or more, are emitted in a forward direction at small angles (within few mrad) to the particle trajectory. The TR intensity for a single boundary crossing always increases with γ, but, for multiple boundary crossings, interference leads to saturation above $\gamma_{\,\mathrm{sat}} = 0.6\ \omega_1\sqrt{\ell_1\ell_2}/c$ [203], where ω_1 is the radiator material plasma frequency, ℓ_1 is its thickness, and ℓ_2 the spacing between

material elements. The probability density function of TR is a fairly complex function of γ, radiator parameters, photon energy (ω) and its emission angle (θ). For well defined radiator parameters a measured two-dimensional distribution of photon energy vs its reconstructed emission angle is in very good agreement with the theory predictions [204].

Integration over the angle yields the TR spectrum, which typically features many maxima (see Sec. 34.7). Most of the TR energy is emitted near the last maximum of the spectra determined by radiator material parameters at $\omega_{max} = \ell_1\omega_1^2/2\pi c$. The effective TR photon emission starts at about $\gamma_{thr} = \ell_1\omega_1/c$. By varying radiator parameters one may optimize the particle separation for a given range of the γ-factor. The angular distribution of TR photons has a few maxima and extends up to $\theta_{max} = (1/\gamma^2 + \omega_1^2/\omega^2)^{1/2}$ [205]. For a single foil the largest part of the TR energy is emitted around the most probable angle $\theta = (1/\gamma^2 + \omega_2^2/\omega^2)^{1/2}$, where ω_2 is the plasma frequency of the gas surrounding the radiator material elements. However, in case of multiple interfaces, interference effects may significantly change this angle and more realistic expression for the angle which corresponds to the last interference maximum of the energy spectra is $\theta \approx \sqrt{1.4\pi^2/\gamma_{\rm sat}^2 - 1/\gamma^2}$ [204]. The higher is the gamma-factor, the larger is the angle of the first interference maximum. It reaches almost its asymptotic limit at $\gamma = \gamma_{sat}$. This effect is illustrated in Fig. 35.17 [204] which shows two-dimensional distribution of the TR photon energy versus the reconstructed production angle obtained in 20 GeV electron beam with the radiator containing a stack of foils of 15.5 μm thickness spaced by 210 μm (the left plot) using a Si-pixel detector. TR produced by 20 GeV electrons is emitted mostly around $\theta \sim 0.9$ mrad. All features of this distribution are well reproduced with MC simulations (the right plot).

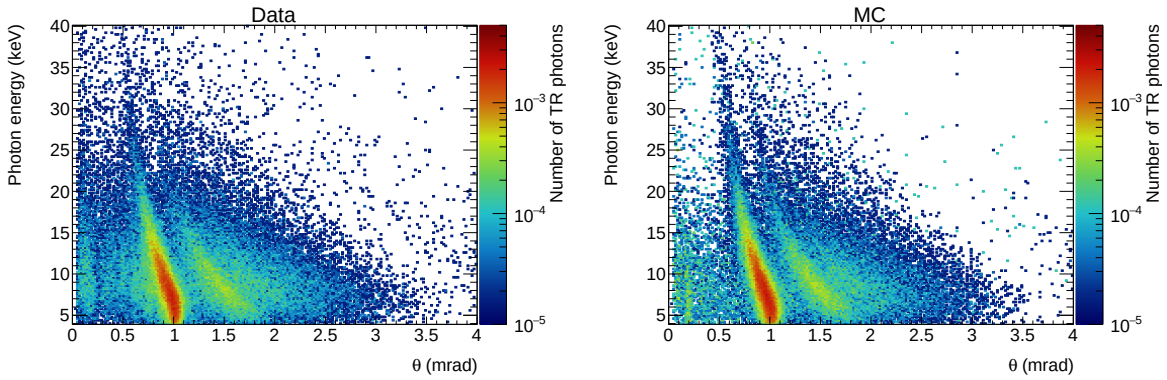

Figure 35.17: Two dimensional distributions of photon energy versus reconstructed production angle obtained with the polypropylene radiator with 20 GeV/c electron beam. Data - the left plot, MC - the right plot. Z-axis is a number of photons per particle [204]

The simplified numerical expressions can be used for practical estimation of the main TR production parameters [204]: $\theta \sim 1.2/\omega_1\sqrt{l_1 l_2}$, $\gamma_{thr} \sim 3 \times 10^3\ \omega_1\ell_1$, $\gamma_{\rm sat} \sim 3 \times 10^3\ \omega_1\sqrt{\ell_1\ell_2}$ and $\omega_{max} = 0.65\ \ell_1\omega_1^2$, where θ in mrad, ω_1 in eV, ω_{max} in keV and l_1 and l_2 in mm.

In the simplest concept, a detector module might consist of a low-Z TR radiator followed by a high-Z active layer made of proportional counters filled with a Xe-rich gas mixture. The atomic number considerations follow from the dominant photoelectric absorption cross section per atom going roughly as Z^n/ω^3, where n varies between 4 and 5 over the region of interest.[1] To minimize self-absorption, materials such as polypropylene, Mylar, carbon, and (rarely) lithium in the form

[1]Photon absorption coefficients for the elements (via a NIST link), and $dE/dx|_{\rm min}$ and plasma energies for many materials are given in https://pdg.lbl.gov/current/AtomicNuclearProperties.

of foils, fibers or foams are used as radiators. The TR signal in the active regions is in most cases superimposed upon the particle ionization losses, which are proportional to Z. In most of the detectors used in particle physics the radiator parameters are chosen to provide $\gamma_{\,\mathrm{sat}} \approx 3000$. Those detectors normally work as threshold devices, ensuring the best electron/pion separation in the momentum range 1 GeV/$c \lesssim p \lesssim$ 150 GeV/c.

One can distinguish two design concepts—"thick" and "thin" detectors. In "thick" detectors the radiator, optimized for a fixed total radiation length at maximum TR yield and maximum TR absorption in the detector, consists of few hundred foils (for instance 300 20 μm thick polypropylene foils). Most of the TR photons are absorbed in the radiator itself. To maximise the number of TR photons reaching the detector, part of the radiator far from the active layers is often made of thicker foils, which shifts the x-ray spectrum to higher energies. The detector thickness, about 2-4 cm for Xe-filled gas chambers, is optimized to absorb most of the incoming x-ray spectrum. A classical detector is composed of several similar modules which respond nearly independently. Such detectors were used in the UA2, NA34 and other experiments [206], are being used in the ALICE experiment [207, 208] and are built for the CBM experiment [209]. In another TRD concept a fine granular radiator/detector structure exploits the soft part of the TR spectrum more efficiently. This can be achieved, for instance, by distributing small-diameter straw-tube detectors uniformly or in thin layers throughout the radiator material. This approach allows to realise a TRD as an integral part of a tracking detector providing many points of measurements on the particle track. Even with a relatively thin radiator stack, radiation below 4 keV is mostly lost in the radiators themselves. However, for photon energies above this value, the absorption is reduced and the radiation can be registered by several consecutive detector layers, thus creating a strong TR build-up effect. Descriptions of detectors using this approach in both accelerator and space experiments can be found in [207, 210–213]. For example, in the ATLAS TR tracker (TRT), charged particles on average cross about 35 straw tube layers embedded in the radiator material [210]. The effective thickness of the Xe gas per straw is about 2.5 mm and the average number of foils per straw is about 40 with an effective foil thickness of about 18 μm. In this approach straw walls also act as radiator and make some contribution to the TR spectrum.

Although the radiator parameters mentioned above are typical, they can vary significantly depending on the specific requirements of the detector. Careful simulations are usually needed to build a detector optimized for a particular application. For TRD simulations the codes are based on well understood TR emission formulas (see for instance [205] for regular radiators and [214] for irregular radiators). They are realised as the stand-alone simulation programs [204, 215, 216] or GEANT4 based ones [217] and give both a good agreement of the TR energy spectra and of the angular distributions with data [204, 218, 219].

Discrimination between electrons and pions can be based on the total energy deposition measured in each detection module, the number of clusters – defined as energy depositions exceeding an optimal threshold (typically 5—7 keV) – or on more sophisticated methods, such as pulse-shape analysis as a function of time. The total energy measurement technique is more suitable for thick gas volumes, which absorb most of the TR radiation and where the ionization loss fluctuations are relatively small. The cluster-counting method works better for detectors with thin gas layers, where the fluctuations of the ionization losses are bigger. Cluster-counting replaces the Landau-Vavilov distribution of background ionization energy losses with the Poisson statistics of δ-electrons, responsible for the distribution tails. The latter distribution is narrower than the Landau-Vavilov distribution. In practice, most of the experiments use a likelihood method, which exploits detailed knowledge of the detector response for different particles and gives the best separation. The neural network method is the most powerful tool. When used by the ALICE TRD (ALICE point in Fig. 35.18), it led to an increase in rejection power by a factor of 2–3 compared to the likelihood

method [207]. However, the more parameters are included in the likelihood method, the better the achievable separation power, approaching the performance level of the neural network method [208].

Once the detector structure is optimized, the particle separation power critically depends on the overall detector length. This is illustrated in Fig. 35.18, which shows, for a variety of detectors, the pion efficiency at a fixed electron efficiency of 90% as a function of the overall detector length. As TRD performance depends on particle energy, the experimental data in this figure covering a range of particle energies from 1 GeV to 40 GeV, are rescaled to an energy of 10 GeV when possible. Phenomenologically, the rejection power against pions increases as $5 \cdot 10^{L/38}$, where the range of validity is $L \approx 20$–100 cm. Apart from the beam energy variations, the observed scattering of the points in the plot reflects how effectively the detector space is used and how well the exact response to different particles is taken into account in the analysis. For instance, the ATLAS TRT was built as a compromise between TR and tracking requirements; that is why the test-beam prototype result (lower point) is better than the real End-Cap TRT performance at the LHC shown in Fig. 35.18 for different regions in the detector (in agreement with MC).

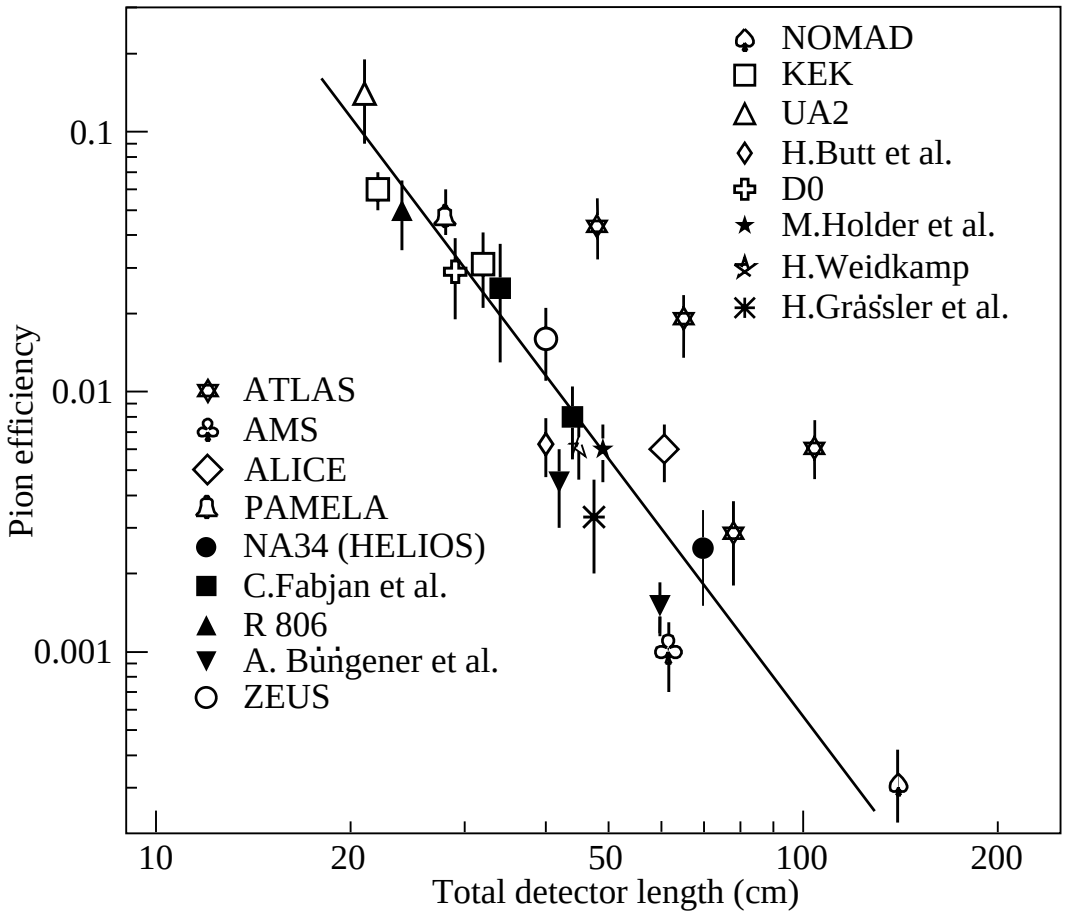

Figure 35.18: Pion efficiency measured (or predicted) for different TRDs as a function of the detector length for a fixed electron efficiency of 90%. The plot is based on the table given in [206]. Results from more recent detectors are added from [207, 211–213, 220].

In most cases, recent TRDs combine particle identification with charged-track measurement in the same detector [207, 209, 212]. This is particularly important for collider experiments, where the available space for the inner detector is very limited and the primary function of all detectors

is particle tracking. For a modest increase of the radiation length due to the radiator (∼4% X0), a significant enhancement of the electron identification was obtained in the case of the ATLAS TRT. Here, the combination of the two detector functions provides a powerful tool for electron identification even at very high particle densities.

In addition to the enhancement of the electron identification during offline data analysis, TRD signatures are often used in the trigger algorithms at collider experiments. The ALICE experiment [208] is a good example for the use of the TRD in a First Level Trigger. In the ATLAS experiment, the TRT information is used in the High Level Trigger (HLT) algorithms. At increasing luminosities, the electron trigger output rate becomes so high that special measures must be taken to keep it at an acceptable level. Even a very soft TR cut at the HLT level, which preserves high electron efficiency (98%), allows to suppress a significant part of fake triggers and enhance the purity for physics events with electrons in a final state. The TRT also plays a crucial role in the studies where an electron suppression is required (e.g. hadronic mode of τ–decays). TR information is a completely independent tool for electron identification and allows to study systematic uncertainties of other electron reconstruction methods.

Electron identification is not the only application of TRDs. They are also sometimes used for hadron separation, which is a more challenging task, as the mass ratio of the particles involved is smaller. In the past, the TRD technique was successfully used to separate pions from protons and kaons at momenta up to 200 GeV/c (see, for example, [221]). In the TeV energy range, TRD remains the only viable technique for hadron separation [222]. For particle astrophysics some TRDs are designed to directly measure the Lorentz factor of high-energy nuclei by using the quadratic dependence of the TR yield on nuclear charge; see, for instance, in [223]. The radiator configuration (ℓ_1, ℓ_2) is tuned to extend the TR yield rise up to $\gamma \approx 10^5$ using the more energetic part of the TR spectrum (up to 100 keV). High density radiator materials (such as Al) are the best for this purpose. Direct absorption of the TR-photons of these energies with thin detectors becomes problematic and TR detection methods based on Compton scattering have been proposed, see in [224].

New detector techniques for TRDs are also under consideration. GasPixel detectors allow to reconstruct a track segment with a space point accuracy of $< 30\ \mu m$ and exploit all details of the particle tracks to highlight individual TR clusters in the gas, see in [225]. However, their ability to separate TR clusters from the energy losses of particles in space is limited by electron cloud diffusion in the gas. Semiconductor pixel or microstrip detectors with high granularity are promising candidates for the spatial separation of TR photons and dE/dx signals at relatively short distances between the radiator and the detector. This capability allows for the reconstruction of the TR production angle, which – together with the TR energy measurements – can help improve the particle identification (PID) performance of the TRD. Such detectors may be the basis for novel devices which combine precise tracking and PID properties [204, 216, 226]. The presence of a magnetic field could enhance the separation between TR photons and dE/dx losses [227]. Thin films of heavy scintillators might be a very attractive option for non-gas based TRD [228].

35.6.6 *Resistive-plate chambers*

Revised August 2025 by G. Aielli (Rome U. Tor Vergata).

The resistive-plate chamber (RPC) is a gaseous detector working at atmospheric pressure developed by R. Santonico and R. Cardarelli in the early 1980's [229]. A precursor of the RPC was the Pestov spark chamber [230] [231], which had a metallic plate cathode and a thick glass plate anode, designed to work at 12 bar to obtain an outstanding 0.1 ns time resolution. Although the original purpose of RPCs was to provide a competitive alternative to large scintillator counters, the RPC's potential for timing tracker systems was quickly recognized given its high detection efficiency (>95%), excellent temporal and spatial resolutions and ease of constructing large-format

single frame detectors. The RPC, as sketched in Fig. 35.19, is a large planar capacitor with two parallel high bulk resistivity electrode plates (10^9–10^{13} Ω·cm) separated by a set of insulating spacers. The spacers define a gap in the range from a few millimeters down to 0.1 mm with a precision of a few μm. The gap is filled with a suitable atmospheric-pressure gas mixture which serves as a target for ionizing radiation. A thinner gas gap corresponds practically to an higher time resolution, on the other hand, the minimum gaseous target for reaching full detection efficiency at atmospheric pressure is typically 1 mm (also influenced by the gas molecular weight). Since the primary ionization released in sub-millimeter gas gaps is limited, multiple gaps can be combined to effectively obtain a high detection efficiency [232]. The electrodes are most commonly made of high pressure phenolic-melaminic laminate (HPL), commonly referred to as "bakelite", or glass. In

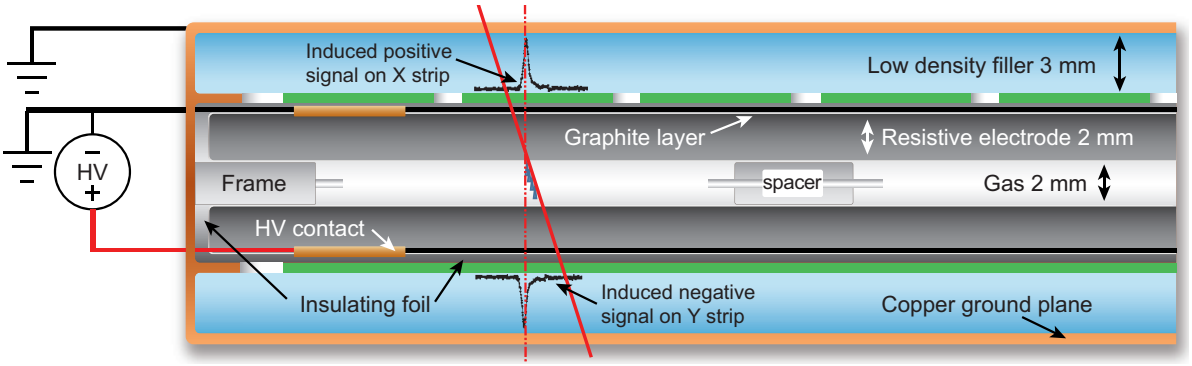

Figure 35.19: Schematic cross section of a generic single gap RPC. The thickness values shown are given just as an example.

the last case, typically soda-lime or alumino-silicate glass types are used, having a lower resistivity than borosilicate glass. An uniform electric field of several kV/mm is established on the gas gap, sufficient to promptly start an avalanche multiplication of the primary electrons. The electric field is typically applied through a moderately conductive ($\sim 10^5 to 10^8$ $\Omega/\square$) graphite varnish, forming an ohmic contact with the external faces of the electrodes. Its conductivity is sufficiently low to be transparent to the fast avalanche signal transients, and high enough to suppress surface voltage gradients arising from the working current flowing in it. Due to the high electrode resistivity in RPCs, the time constant of the equivalent RC circuit ($\tau = \rho\epsilon_r$ being ρ the electrode resistivity and ϵ_r its dielectric constant) is much longer than the discharge processes duration. Therefore only the locally-stored electrostatic energy contributes to the discharge, preventing the formation of sparks and leaving the rest of the detector field unaffected. The gas-facing surface of HPL electrodes are commonly coated with $\sim$ μm-thick layer of polymerized linseed oil [233] with the function of smoothing the electrode surface, improving the electric field uniformity. It also has the function of protecting the electrode from the being eventually etched by free radicals generated in the discharge e.g. in presence of fluorocarbons. Glass-based RPCs don't require such treatment. In RPCs the gaseous target and the multiplication region coincide. In the early stage of the avalanche multiplication the uniform electric field exponentially amplifies each primary ionization cluster, as the avalanche progresses away from the location of the primary ionization. Since the ionization clusters generated by the incident MIP are randomly distributed along the ionizing particle track, for low gains the observed RPC charge spectrum is broad and approximately exponentially distributed[2] with the mode close to zero. Because of this, it is difficult to separate noise from signals using a discrimination threshold. This is not the case in gaseous detectors where ionization and

[2] An analytic treatment of the low gain avalanche process shows that the charge distribution is well described by the Γ function [234]

amplification occur in separate regions.

For increasingly larger avalanches, the space-charge progressively saturates the avalanche growth from exponential to almost linear, producing a peaked charge spectrum, essential to efficiently separate the signal from the noise [235]. For large gains[3] the avalanche, with increasing probability, onsets a transition to "streamer" [236], a plasma filament connecting the electrodes, depleting all the locally-available energy [237], and generating an almost fixed amplitude signal. This prevents any further evolution of the discharge. This streamer mode was the first ever used by RPCs, until the introduction of very electronegative gases and more sensitive front end electronics made it possible to detect the precursor avalanche independently on the streamer [238, 239] Any of this operating regimes can be used in RPC detectors, depending on the application.

As with other gaseous detectors, the gas mixture is optimized for each specific application. In general it needs to contain a UV photons quencher suppressing the photon-mediated feedback that can lead to self generated after-pulse discharges, and one or more electronegative components, to extend the avalanche growth limit before increasing significantly the probability of generating a streamer. Even though there is not yet an accepted and robust avalanche-to-streamer-transition model, this effect is commonly explained as a delay in the growth of the electron density of the avalanche front, which perturbates the electric field driving the transition to streamer. The addition of small fractions of electronegative molecules with a very high capture cross section for slow electrons, such as SF_6, was proven [240] to inhibit the transition to streamer over a wide electric field range above the working point. Having such a wide interval is crucial in real applications, to cope with all the unavoidable gas gaps size fluctuations and surface quality, stabilizing and making uniform the detector response. In the last decades ATLAS and CMS adopted as a standard the mixture $C_2H_2F_4$/i-C_4H_10/SF_6=94.5%/5%/0.3% for stable avalanche operation (ATLAS changed it since 2023 as explained in Section 35.6.6.4).

The avalanche induces a fast electron signal on a set of metallic readout electrodes (e.g. pads or strips) commonly placed externally and electrically insulated from the resistive electrodes. The induced charge is isotropically distributed on the electrode plans with equal but opposite amplitude on both sides of the RPC. This symmetry makes both sides of the RPC functionally equivalent for the signal readout. The induced charge density distribution can be calculated for a simplified RPC model [241] [242] as: $\sigma(x) = A/\cosh[(r)/\delta]$ where A is a normalization constant, r is the distance from the center of the avalanche axis and $\delta = (g + 2d)/\pi$ depends on the gap and electrode width (g and d, respectively). Depending on the specific RPC layout and geometry, the interplay between conductive coating and pick-up electrodes typically broadens, by means of a diffusion-like process (see [242] [243]). This effect mostly preserves the information on the avalanche position, which can be obtained using the charge centroid method, with the drawback of increasing the signal space occupancy. A fast detector response, requires to preserve sensitivity to the high-end of electron avalanche signal frequency spectrum, and guaranteeing this across large RPC areas, requires a correspondingly adequate Faraday cage and readout design. At the same time, to preserve the excellent timing features of the RPC signal, the front end electronics should have a short rise time (ideally $\ll$ than the signal rise time) and low noise, although these are competing requirements [244].

35.6.6.1 *RPC types and applications*

RPCs are generally classified in two categories depending on the gas gap structure: single gap RPCs (described above) and multiple gap RPCs [232] (typically referred as MRPCs). While they are both based on the same principle they have different construction techniques, performance and limitations, making them suitable for different applications. Due to its simplicity and robustness, the single gap RPC is ideal for covering very large surfaces. Typical detector systems can have

[3] A multiplicity of the order of 10^8 electrons is classically referred as Raether/Meek limit for on-setting a streamer

sensitive surface areas up to $\sim 10^4$ m^2, with single module areas of a few m^2, a space resolution up to 100 μm [245] and a time resolution up to $\sim$0.4 ns [246]. Representative examples are the muon systems of ATLAS [247] and CMS [248] or ground and underground based cosmic rays [249] and neutrino arrays [250]. It is interesting to note that CMS implemented a bi-gap structure, i.e. the pickup signal is sandwiched by 2 single gas gaps, both contributing to the signal induction, improving efficiency and time resolution with respect to the single gas gap. Relevant new trends for single gap RPC applications are represented by new Dark Matter search experiments such as CODEX-B [251] and ANUBIS [252], in both cases exploiting RPCs to enclose and instrument large detection volumes with a good space-time tracker. Single gap RPCs have also recently demonstrated good candidates for application in tracking calorimetry [253].

The MRPC [254], as sketched in Fig. 35.20, segments the gaseous target by means of a stack of floating glass electrodes separated by a monofilament (i.e. fishing line) sandwiched between two external electrodes providing the high-voltage bias. Since the current flowing in between the gas gaps must be in average equal, the difference of potential between each couple of adjacent floating electrodes will tend to be the same. An extensive description can be found in [255]. It has been observed that higher time resolution is inversely correlated to the gas gap size, so this configuration allows for smaller gas thicknesses while maintaining a sufficient total gas thickness. This tends to separate primary clusters avalanches in different gas gaps, treating them independently, and determines a shorter avalanche growth time, increasing time resolution by one order of magnitude with respect to the classic RPCs [256]. The mechanical fragility of sub-mm-gap structures makes this technique less suitable for very large detector areas. Moreover the only material nowadays practically suitable for building such structures is glass with resistivity above 10^{12} Ω·cm, limiting the rate capability to about 500 Hz/cm^2 [257].

MRPCs have been largely used in Time of Flight systems such as ALICE [258], HADES [259], FOPI [260] and BESSIII [261], and in applications such as timing PET [262]. In perspective MRPC will be used for upgraded and new nuclear physics experiments such as CBM@FAIR [263] and SoLID [264].

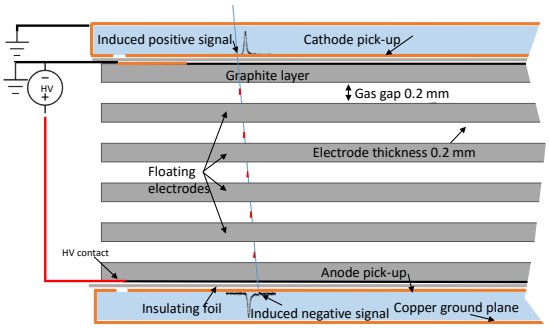

Figure 35.20: Schematic cross section of a generic multi gap RPC.

35.6.6.2 *Time and space resolution*

Space-time uncertainties in RPCs are intrinsically determined by the statistical fluctuations of the primary and secondary ionization, the avalanche multiplication rate and drift velocity, which are both a function of the electric field and gas composition. The Signal/Noise ratio of the front end electronics is crucial to preserve this information. The intrinsic signal latency (time lapsed between the ionizing event and the growth of the signal above detection threshold) is commonly in a few ns range, making the RPC suitable for applications where a low latency is essential.

The gas gap size is a crucial feature for the RPC timing performance: producing the same

total charge (for a detectable signal) in a smaller gas gap implies the necessity of increasing the first Townsend coefficient by increasing the electric field, reducing at the same time the total signal duration and the related time fluctuations. Moreover, a thinner gas gap reduces the number on effective clusters participating to the signal formation, for an unknown amount of time, corresponding to their distance from the anode, thus decreasing the charge collection fluctuations [265]. Another important factor is the gas mixture, affecting both the drift velocity and multiplication rate. Depending on the gas mixture and on applied voltage, typical intrinsic resolution, ranges between $\sim$ 1 ns and $\sim$1.5 ns, for a 2 mm gas, and between $\sim$0.3 ns and $\sim$0.4 ns for a 1 mm gas gap [266].

The intrinsic position sensitivity of an RPC is in the range of tens of μm depending on the lateral spread of the avalanche induced charge distribution, influenced also by the gap size. In typical RPC applications the pick up electrodes pitch L ($\sim$1 cm) is much broader than the intrinsic resolution, and being readout via a discriminator, the spatial resolution is geometrically limited in the range of $\mathrm{L}/\sqrt{12}$. A much better result is obtained by using a finer electrodes granularity and measuring the charge in each strip collecting the avalanche charge, so to reconstruct the charge centroid. It has been demonstrated, through charge centroid techniques, that the RPC avalanche space-time localization can be as good as $\sim$50 ps $\times$ 40 μm [267] [268]. Nevertheless, the high space resolution for large size RPCs, as well for any other planar detector structure, is often practically limited by the extensive mechanical precision of the readout electrode (which bulk is typically made of plastic), challenging to be kept negligible with respect to the intrinsic local resolution of the detector.

35.6.6.3 *Rate capability and ageing*

RPC rate capability is limited by the voltage drop on resistive electrodes, $\Delta V = V_{\mathrm{a}} - V_{\mathrm{gas}} = I \cdot R$ [269]. Here V_{a} is the applied voltage, V_{gas} is the effective voltage on the gas, $R = \rho \cdot d/S$ is the total electrode resistance, ρ being the resistivity and d,S the sample thickness and surface respectively, and I is the working current. Assuming uniform irradiation we can express $I = \phi \cdot S \cdot \langle Q \rangle$ where ϕ is the particle fluence and $\langle Q \rangle$ is average charge per avalanche. So we obtain a state equation for the RPC rate capability:

$$\Delta V/\phi = \rho \cdot d \cdot \langle Q \rangle$$

A large I not only limits the rate capability but also affects the long term performance of the detector, for three leading effects. Firstly, the working current, depletes the ionic electrode's carriers [270]. Secondly, the current builds up an electric field RI/d in the electrode bulk, accelerating the drif of internal ionic components to opposite surfaces. Thirdly, in presence of fluorocarbons and water, discharges generate hydrofluoric acid (HF) and other fluorinated compounds, which may damage internal detector surfaces. In case of electrodes made of glass, known to be not resistant to HF [271], it is necessary to suppress HF formation preventing water vapor contamination. Conversely, HPL electrodes, coated with linseed oil, notwithstanding the necessary presence of water which drives the conduction mechanism, demonstrated to be tolerant to HF in moderate concentrations, obtained by removing it with a forced flow of clean gas through the gas gap. Several ageing test have been carried out [272–275], confirming that measurable ageing effects were limited to a controlled increase of the ohmic current, of the electrode resistance and of the spontaneous counts. However, in extreme conditions, etching and surface damage have also been observed.

Operating in streamer regime places low requirements on the front end electronics sensitivity, but generally limits the counting rate capability to $\sim$100 Hz/cm^2. Higher-rate operation can be achieved by reducing gas gain in favor of electronic amplification, operating the detector in avalanche mode. Increasing concentrations of electronegative gases, such as $C_2H_2F_4$ and SF_6 [240], extends the avalanche signal distribution, requiring the front-end electronics a high sensitivity to the low

end signal distribution and stability in presence of large signals. By further lowering the avalanche mode gas gain, efficient and stable performance at high rates (e.g. 10 kHz/cm^2) has been achieved for large area single gap RPCs [244].

Further increasing the rate capability, can be achieved with complementary strategies: increasing the front end sensitivity to smaller signals and operating with a smaller amplification, relying on redundancy and higher signal yield of multiple micro gap structures [276] or lowering the electrodes resistivity [277]. The last strategy is increasingly difficult to be pursued, in presence of high electric field, since high resistivity limits the appearance of larger discharge events and increase of spurious counts, induced by the effect of local electrode defects on the field gradient. It seems in this case, that lowering the electrodes resistivity would require at the same time to reduce the operating electric field, achieving at the same time a lower average charge per count.

35.6.6.4 *Alternative gas mixtures*

The standard gas mixture mentioned above is based on Hydrofluorocarbon (HFC), specifically the R134a, and SF6, both extensively used in the industry. R134a features matches very well the RPCs performance requirements: high primary ionization yield; electronegative, limiting secondary discharge phenomena; not flammable; the absence of saturated bonds makes it robust to UV degradation, which is responsible for the production of fluoride radicals. SF6, as mentioned above is crucial to extend the streamer-free avalanche regime. The drawback is the high Global Warming Potential (GWP) of these gases (1430 and 24300 respectively), for which reason, their industrial application will be progressively limited in future according to the European Regulation [278]. In the last years the search for a possible replacement of R134a, relied on the Hydro-Fluoro-Olefins [279,280], a category of gases recently proposed for industrial applications. However, HFOs exhibit important limitations with respect to HFCs, if used as main component of the mixture: for its electronegativity (higher than for R134a [281]) increasing the HV working point, and the charge per count, due to a large fraction of negative ions produced by electron capture [282, 283]. Moreover it is expected to produce a larger amount of fluoride radicals by UV decomposition of the gas, increasing the operative current and worsening the detector longevity [284, 285]. To contrast the ageing acceleration, driven by the effects stated above, the proposed strategy was to largely dilute HFO with a neutral gas, such as CO_2, compatibly with keeping an enough dense gaseous target, and, for future systems, operate at a lower gain by using very performing front end electronics. It has to be said that increasing of CO_2 finds its limits in the correspondingly increasing probability of inducing streamers [282, 283], which is further worsened by operating the RPC with an high discrimination threshold. A representative example of the several variants tested [286] is $CO_2/C_3H_2F_4$/i-C_4H_{10}/SF_6=59%/35%/5%/1%. This mixture with a large fraction of CO_2 is suitable for thicker (2mm) gas gap. The presence of CO_2 in 1 mm gas gaps reduces the amount of primary electrons, practically limiting its fraction to no more than 30% to keep the efficiency above 95%. Thus for a safe operation a reduction of the charge per count by an order of magnitude is necessary to compensate the expected stronger ageing phenomena. Detector performance and physics summaries can be found in [287, 288], not yet conclusive results about the detector longevity [284] confirm that the HFO based mixtures are more impacting than the standard one. On the base of the known results, LHC experiments conservatively opted either to hold on the standard gas mixture (CMS) or replace part of the R134a with an equivalent amount of CO2 (ATLAS). Several variants of this type of mixture have been tested, observing an improved longevity, with respect to the standard gas mixture, for lower fractions both of R134a and SF_6 [289, 290]. After this test,ATLAS decided to modify the standard gas mixture in two steps: first using $CO_2/C_2H_2F_4$/i-C_4H_{10}/SF_6=30%/64%/5%/1% in 2024 run. Then experimental confirmation of the expectations about ageing, lead to halve in 2025 run the fraction of SF_6,

observing a further improvement (ATLAS internal). This allowed to safely lower the ATLAS CO_2 equivalent emissions by 25%. Given the very high GWP of SF_6 a dedicated investigation pointed out various alternatives [287, 291], in particular $C_3H_2ClF_3$ has been tested both for performance and longevity with very encouraging preliminary results [291].

35.6.6.5 *A new detector: the **R**esistive **C**ylindrical **C**ounter*

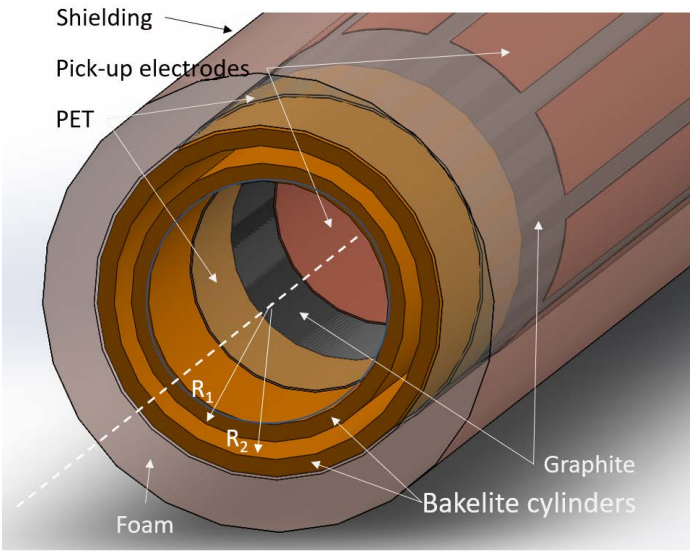

Figure 35.21: Schematic drawing of an RCC.

The RCC, illustrated in fig. 35.20, has been recently proposed as an evolution of the RPC [292] and is essentially an RPC warped to a cylindrical shape. The idea is to combine the advantages of parallel plate geometry and high pressure drift tubes in a single detector. The electric field $E(r)$, which is uniform in RPCs, here depends instead on the distance from the axis r, according to $E(r) = -\frac{V}{r\ln(R_1/R_2)}$. By choosing appropriate values for R_1, R_2, V and its polarization (the innermost cylinder is the cathode), it is possible to virtually segment the cylindrical gap in a innermost sensitive layer, where the field is sufficiently high to start the avalanche multiplication, and an outermost layer where the drift happens, increasing the induced signal with lower or no multiplication at all. This effect is called geometrical quenching and limits the avalanche growth without the necessity of electronegative gases. Moreover a geometrically quenched avalanche would have a much better prompt to total charge ratio, lowering the total operative current, hence increasing the rate capability. The cylindrical structure has a further major advantage with respect to the planar one, it can be easily pressurized overcoming the RPC limitation of working at atmospheric pressure only. Pressurization on one side increases the gaseous target density, thus increasing the efficiency of narrow gaps, on the other, it could largely improve RPC time resolution since the Townsend coefficient $\alpha = A\,p\cdot\exp(-Bp/E)$ (where p is the pressure, E the electric field and A,B are constants), as we learn from the RPC precursor, the Pestov spark chamber [231]. The preliminary performance of the first RCC prototypes in terms of efficiency, time resolution and counting rates are reported in [293] using the standard gas mixture. Further test will be needed to show the full potential of this device, such as its ability to work without fluorinated gases, and at high internal and external pressure, potentially extending its applicability range to space and under water applications.

35.7 LAr Time Projection Chamber

Written in October 2021 by F. Pietropaolo (CERN; INFN, Padova) and S. Pordes (FNAL). Revised in August 2025 by A. Fava (FNAL) and F. Pietropaolo (CERN; INFN, Padova).

35.7.1 *Introduction*

Liquid argon (LAr) is an attractive medium for particle detection. The most relevant physical properties of LAr are listed in Table 35.8; additional details can be found in [294]. In LAr, the energy deposited by charged particles is converted into ionization electrons and scintillation light; several tens of thousands scintillation photons and a similar number of ionization electrons are generated per MeV of deposited energy.

Table 35.8: Some physical properties of liquid argon from [295].

Property	Unit	Value
Boiling Point *(BP)* at 1013 hPa	K	87.3
Density (ρ) at 1013 hPa	kg m^{-3}	1395
d*(BP)*/dP	K hPa^{-1}	9×10^{-3}
dρ/dT	kg m^{-3} K^{-1}	-6.2
Latent Heat of Evaporation	kJ kg^{-1}	161
Freezing Point (1013 hPa)	K	83.8

The LAr's high density (relative density ∼1.4), the electron drift over long distances with minimal diffusion, and the commercial availability as a by-product of air distillation make LAr especially suitable for large time projection chambers (TPCs) aimed at rare event detection, as first proposed in [296, 297]. Since then, LAr TPC technology has matured into a high-resolution (∼mm^3), fully active detector offering excellent particle identification, calorimetric capabilities, and nearly 100% live-time. Operating a liquid argon TPC requires the following core components:

1. A cryostat and cryogenics system to maintain ultra-pure liquid argon,
2. An electric field to drift ionization electrons toward the readout,
3. Charge readout sensors and electronics to amplify and digitize the signals,
4. Photodetectors and associated electronics to capture scintillation light,
5. A data acquisition (DAQ) system for readout and storage,
6. Reconstruction and analysis software.

This article discusses the challenges and practical solutions related to items 1–4. Topics 5 and 6 —DAQ and data processing— are also briefly introduced due to their critical role in realizing the full potential of LAr TPCs [298–300]. A number of auxiliary systems have been developed to enhance LAr TPC performance, including: in-argon cameras [301], purity monitors for fast assessment of argon quality [302, 303], and UV lasers for mapping drift field distortions due to space charge or electric field irregularities [304].

Detectors of up to 800 tons of LAr have been constructed and operated, and designs for tens-of-kiloton-scale detectors are underway. Extensive reviews of existing and planned LAr TPC detectors can be found in [305, 306], as well as in detailed experiment reports [301, 307–316]. A summary of current and proposed LAr TPC experiments and their respective detector masses is provided in Table 35.9.

35.7.2 *Ultra-pure Liquid Argon*

A core requirement of the LAr TPC is the ability to maintain a large volume of ultra-pure liquid argon at stable temperature and pressure. This is achieved through a combination of cryostat design

Table 35.9: Summary of current and proposed accelerator-based LAr TPC experiments. For experiments on neutrino beams, the average energy is indicated.

Name	Total (fiducial) mass [t]	Beam type	$\langle E_\nu \rangle$ [GeV]	Location	Dates
ArCS	0.98(0.24)	p, μ, e, p, k	-	FNAL	2026
Argoneut	0.025	ν	3	FNAL	2009-10
DUNE 2x2	8.4(2.2)	ν	6	FNAL	2024-
DUNE ND-LAr	147(67)	ν	3	FNAL	2030-
DUNE FD	70k(40k)	ν	3	SURF	2027-
ICARUS	760(476)	ν	17	LNGS	2006-12
ICARUS	760(476)	ν	0.8	FNAL	2020-
LArIAT	0.76(0.24)	p, μ, e, p, k	-	FNAL	2015-17
MicroBooNE	170(85)	ν	0.8	FNAL	2014-21
ProtoDUNE	770(417)	p, μ, e, p, k	-	CERN	2018-
SBND	220(112)	ν	0.8	FNAL	2024-

and cryogenic purification systems. For detectors with masses on the order of 100 tons, double-walled, vacuum-insulated, evacuable cryostats are practical. However, for larger detectors, this approach becomes impractical. The development of techniques to achieve ultra-high purity without prior evacuation [303] has enabled the use of non-evacuable, foam-insulated cryostats—adapted from liquefied natural gas (LNG) transport technology [301]. These cryostats are modular and designed for underground assembly. Furthermore, their passive insulation offers improved safety over vacuum insulation, as the insulation performance cannot abruptly change, as it would happen in case of vacuum loss.

Maintaining an extremely low level of electronegative impurities —primarily oxygen and water— is critical to preserving ionization electrons as they drift to the charge sensors. These contaminants capture free electrons, forming negative ions that drift too slowly to be detected. The argon purity is quantified by the electron lifetime τ, which describes the average time an electron can drift before being captured. For example, at an oxygen concentration of 0.1 ppb (by volume), the electron lifetime is approximately 3 ms [317, 318]. Since electron drift times in large detectors are often in the millisecond range, achieving oxygen concentrations well below 0.1 ppb is essential.

To reach these purity levels, the cryostat is first purged with argon gas to displace air, typically reducing oxygen and nitrogen concentrations to ppm levels [319]. During filling, commercial liquid argon —often containing oxygen and water at ppm levels— is passed through purification filters. Molecular sieves and activated copper on alumina [320] are widely used to remove water and oxygen, respectively. The realization that these purification materials remain effective at cryogenic temperatures [321] allowed for high-throughput liquid-phase purification, a major advancement over earlier gas-phase methods. Once the detector is operational, continuous recirculation of both liquid and boil-off gas through the purification system ensures the removal of contaminants introduced through outgassing or micro-leaks. Cryogenic system schematics are available in [301, 309, 311]. While the ultimate measure of argon purity comes from track reconstruction, dedicated "purity monitors" —double-gridded ionization chambers— are commonly employed for rapid, real-time feedback [301].

Nitrogen is another possible contaminant. While it does not significantly impact electron lifetime at concentrations up to several ppm, it degrades scintillation light yield and transmission with the few ppm N2 concentration [322, 323]. Oxygen at ppm concentrations also affects scintillation

light [324], but in TPCs, this effect is typically negligible due to the stricter requirements imposed by charge readout.

35.7.3 *Charge and Light Signals*

Charged particles traversing liquid argon (LAr) deposit energy, producing both ionization electrons and scintillation light. Figure 35.22 (left) illustrates how these yields vary with applied electric field for a minimum ionizing particle (m.i.p.). The number of free electrons produced per unit energy is determined by the average energy required to form an electron-ion pair, $W_{el} = 23.6$ eV [325], the particle's energy loss rate (dE/dx), and the recombination factor R, which quantifies the fraction of electrons that escape recombination. Although several models have been proposed to describe recombination dynamics [326, 327], the "box model" [328], which assumes mobile electrons and stationary ions, is widely used for its realistic assumptions [329], and has very recently been further improved to include an angular dependent effect [330]. Measurements of electron yield across various fields and ionization densities show good agreement [330–335]. One commonly used parameterization, based on ICARUS data [334], is $R = \frac{0.8}{(1+0.049(dE/dx)/\mathcal{E})}$ with dE/dx in MeV/cm and $\mathcal{E}$ in kV/cm. At a field of 500 V/cm, this yields $R \approx 0.70$ for m.i.p.s. corresponding to about 30,000 electrons/MeV escaping recombination. A detailed review of charge yield and recombination models is given in [336]. Under a uniform electric field, free electrons drift toward the charge readout system. This process is characterized by:

1. **Drift velocity**, which depends on electric field and slightly on temperature (see Table 35.10). A widely used parametrization [337, 338] gives a drift velocity of 1.55 mm/μs at 500 V/cm and 89 K, shown in Figure 35.22 (right).
2. **Charge attenuation**, caused by capture on residual impurities. The surviving fraction after a drift time t is $\exp(-t/\tau)$, where τ is the electron lifetime. Lifetimes exceeding tens of milliseconds have been demonstrated [339–341].
3. **Diffusion**, which broadens the charge cloud. The spatial spread after time t is $\sigma_D^2 = 2Dt$, where D is the diffusion coefficient. Longitudinal diffusion measurements typically yield $D_L \approx 0.4$ mm^2/ms [333, 342–344], corresponding to a spread of ∼1.5 mm over a 3 ms drift.

Table 35.10: Some Detector Relevant Properties of liquid argon.

Property	Unit	Value
Stopping Power (m.i.p.)	MeV g^{-1} cm^2	1.51
Radiation Length	g cm^{-2}	19.6
Nuclear Interaction / Collision Length	g cm^{-2}	120 / 76
W_{el}, Energy to form one electron-ion pair	eV	23.6 (±0.3) [325, 345]
Ion mobility	cm^2 V^{-1} s^{-1}	1.6 ×10^{-3} [346]
Temperature dependence of drift velocity	% K^{-1}	-1.7 [338]
Longitudinal diffusion coefficient, D_L	mm^2 ms^{-1}	0.4 (see text)
W_{ph}, Energy to produce one scint. photon	eV	25 [347, 348]
Scintillation photon wavelength (vacuum)	nm	128 ±8 (FWHM) [349]
Scintillation light inverse velocity	ns m^{-1}	7.46 (±0.08) [350]
Rayleigh scattering length (predicted)	m	0.9 (±0.2) [350–352]
Scintillation Decay times fast/slow	ns	6 (±1)/1500 (±100) [322, 353, 354]
Dielectric strength	kV cm^{-1}	>40 [314, 355]

Scintillation light in LAr arises from the decay of excited argon dimers (excimers), Ar_2^*, produced via both direct excitation and electron-ion recombination [356]. The recombination contribution decreases with increasing electric field, as shown in Figure 35.22 (left). At a field of 500 V/cm, about 30,000 photons/MeV are emitted after recombination.

Excimers form in either singlet or triplet states, with lifetimes of approximately 6 ns and 1.5 μs, respectively. These nearly degenerate states decay radiatively, emitting vacuum ultraviolet (VUV) photons centered at 128 nm with a ∼16 nm FWHM [349]. The singlet-to-triplet ratio depends on ionization density: 1:3 for m.i.p.s and up to 3:1 for highly ionizing tracks [353]. The long-lived triplet component is particularly sensitive to quenching by impurities such as nitrogen and oxygen, which can non-radiatively absorb the excimer energy [322, 324].

Scintillation light propagation is influenced by **absorption** and **Rayleigh scattering**. Pure LAr is transparent to its own light due to a large Stokes shift [357], but trace levels of methane (ppb) [358] and nitrogen (ppm) [323] can significantly attenuate light. Rayleigh scattering, with a short mean free path in LAr, increases the photon path length and degrades spatial resolution in large detectors. To mitigate these effects, **wavelength-shifting dopants** have been proposed and tested. Xenon is a leading candidate: at tens of ppm concentrations, it efficiently absorbs excitation energy from argon dimers and re-emits photons at longer wavelengths, improving transparency and reducing scattering losses [359, 360].

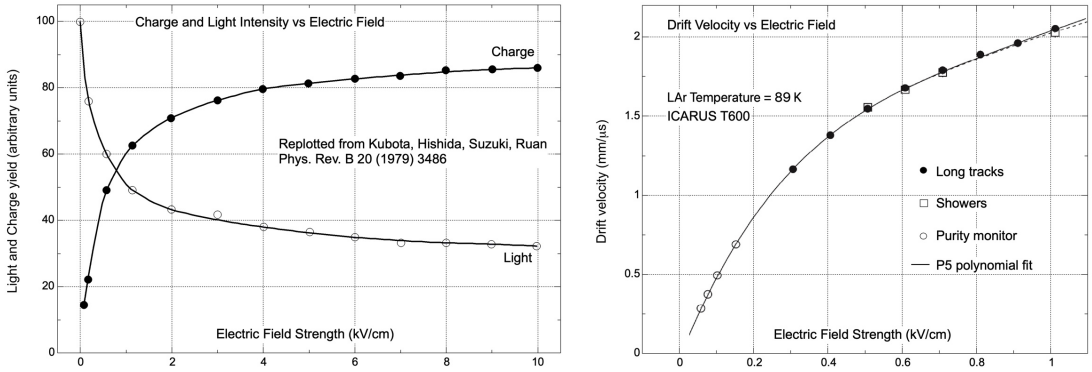

Figure 35.22: (*left*) the form of the light yield and the charge yield vs electric field redrawn from [356]; (*right*) electron drift velocity vs electric field redrawn from [337].

35.7.4 *LAr TPC topologies*

Single-phase detectors, ranging from small-scale prototypes to large multi-kiloton systems, share a common layout: a cathode and surrounding field cage establish a uniform electric field across the active volume, directing electrons toward anode planes at ground potential. To maximize mass for a given readout complexity, long drift distances are favored. As a result, TPCs are often built with single drift regions, dual-drift volumes sharing a central cathode, or multiple drift modules. A notable exception is the DUNE Near Detector, where high event rates necessitate segmentation into many small TPCs [313].

The electric field is typically established by a planar cathode held at high negative voltage (up to -300 kV), a field cage that linearly degrades the potential, and sense planes at a voltage around 0 V. Uniformity of the field is essential, though it can be distorted in surface detectors by the accumulation of slow-moving positive ions produced by cosmic ray interactions [336, 341, 361–363]. Key challenges in high-voltage delivery include designing robust feedthroughs that transport the HV into the cryostat without breakdown [309, 364], preventing damage from possible discharges [301],

and ensuring the integrity of the field cage resistor chains [365]. Maintaining HV stability in a medium designed for long-distance electron transport is one of the most demanding aspects of TPC design.

Figure 35.23 illustrates the typical single-phase geometry using wire planes with a horizontal drift field. Charge readout is performed by wire planes arranged perpendicularly to the drift direction, typically with two or three planes at different wire angles to enable 3D reconstruction. Although only two planes are strictly necessary to reconstruct the three-dimensional event topology, a third plane improves pattern recognition and mitigates inefficiencies due to noisy or dead channels. Wire pitch and inter-plane spacing are typically a few millimeters. The biasing scheme ensures that the drifting electrons pass through the intermediate planes and are collected on the final (collection) plane. Bipolar signals are induced on the induction planes, and a unipolar signal is recorded on the collection plane [366]. The condition for transparency is discussed in [367].

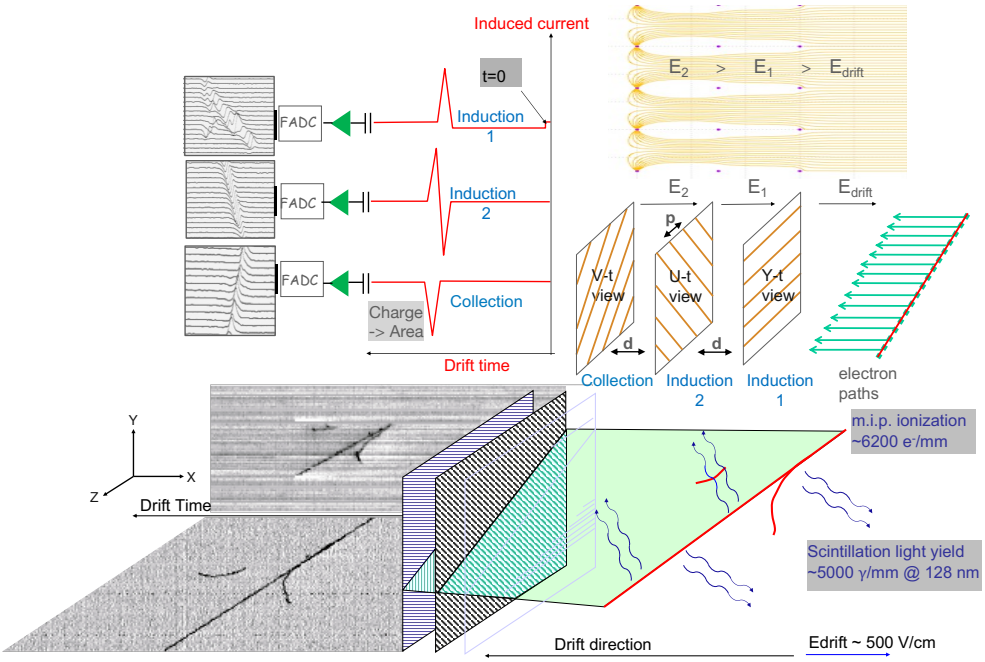

Figure 35.23: Schematic of an event in the ICARUS 3 t LAr TPC; *Top (from right to left)*: field lines from drift region to collection wires, electron flow & arrangement of wire-planes, signal shapes on the wires, and wave-forms from the continuous readout and digitization; *Bottom*: the passage of a muon. The gray scale on the track indicates the ionization density.

Signals are digitized at 2–2.5 MHz sampling rates over the full drift window. The 3D position of the charge deposit is reconstructed from the wire intersections and the drift time, converted to spatial coordinate via the known drift velocity.

Large-scale TPCs face intrinsic electrical design constraints: long cables between the sensing elements and amplifiers introduce capacitance and thus noise, while attempts to shorten cables can restrict sensor layout [366]. This challenge has been addressed by the development of cryogenic CMOS-based ASIC amplifiers that can operate directly in liquid argon [368, 369]. These cold electronics minimize noise and enable close proximity to the sensing elements, whether wires, strips, or pixels. The issue of routing hundreds of thousands of signals through the cryostat is further mitigated by implementing digitization and multiplexing within the cryostat itself [370], reducing

the number and complexity of feedthroughs.

These developments have enabled equivalent noise levels of a few hundred electrons [341, 371], compared to expected charge yields of ∼30,000 electrons/MeV, or 60,000 electrons/cm for minimum ionizing particles. This signal-to-noise ratio allows reliable detection of sub-MeV depositions and enables sub-centimeter spatial resolution with wire or pixel pitches below 5 mm.

Most large LAr TPCs also incorporate systems to detect primary scintillation light, which provides crucial timing information for 3D reconstruction [372], triggers [373, 374], complementary calorimetric information [341], and additional localization capability [298]. Given the VUV nature of LAr scintillation (128 nm), wavelength shifters are commonly employed to convert light into the visible range [375]. Photomultiplier tubes capable of cryogenic operation were originally developed for ICARUS [376], and recent systems increasingly use silicon photomultipliers (SiPMs). This allows for decoupling of the light collection and light detection components, and various strategies are being explored for each [301, 377, 378].

35.7.5 *Data Acquisition*

Operating large-mass LAr TPCs requires managing and processing immense volumes of data from digitized charge waveforms and scintillation light channels. For example, in the DUNE experiment, the data throughput is expected to reach up to 1.7 TB/s per detector module (with a 10 kt fiducial mass). To cope with this, several data reduction strategies are typically employed [379,380]:

1. **Zero suppression**: Applied channel-by-channel to digitized waveforms to discard time samples below a given threshold (generally related to the electronic noise level).
2. **Triggered readout**: Fast signals from photon detectors or external sources (e.g., a neutrino beam) trigger the readout of the TPC over a predefined time window. The trigger rate is tuned to match the DAQ throughput capabilities.

Historically, DAQ systems could not afford to buffer or process the full complement of TPC data. However, recent advances in computing and high-speed networking have reshaped this paradigm. It is now possible to read out and buffer the complete digitized TPC data in commercial off-the-shelf (COTS) computers, enabling online processing [381, 382] to identify regions with significant charge or light activity. These "trigger primitives" can be used by higher-level software triggers to selectively store data from all or parts of the TPC, similarly to how external triggers are used. Additionally, trigger primitives can be saved as a separate, low-volume data stream, enabling continuous activity monitoring with minimal bias.

This approach permits significant data reduction—up to a factor of 300 for DUNE's four 10 kt modules—while maintaining sensitivity to low-energy signals. It also allows for complementary integration of charge and photon detector information in real-time. This combined readout enhances detection capabilities, particularly for low-energy depositions at the MeV scale, such as supernova neutrino bursts or rare decay signatures.

35.7.6 *Event reconstruction*

The goal of LAr TPC event reconstruction is to extract the physics content of interactions: event topology, particle identification, and energy measurement. Reconstruction generally proceeds in the following stages:

1. **Signal Processing**: Raw waveforms, which reflect the charge collected over time on each readout channel, are processed to correct for pedestal shifts, suppress noise, and deconvolve the detector and electronics response. The result is a set of "hit" objects representing localized energy depositions in space and time [383–385].
2. **Pattern Recognition (PR)**: In wire-readout TPCs, the signal from each wire plane forms a 2D image (drift time vs. position). Typically, three planes at different orientations allow

stereo reconstruction of 3D structures. PR can be performed either by matching objects across 2D planes (as in Pandora [386]) or directly in 3D using tomographic reconstruction (as in WireCell [387]). The goal is to identify tracks, showers, common vertices, and the global event topology.

3. **Calorimetry and Particle Identification (PID)**: Reconstructed tracks and showers are calibrated and used to compute energy deposition per unit length (dQ/dx), which is further converted into dE/dx. This enables estimation of total energy and particle type [388].

Recent developments have made **machine learning (ML)** integral to LArTPC reconstruction. Early ML efforts included simple multivariate classifiers and boosted decision trees. More advanced techniques now dominate many tasks, particularly **convolutional neural networks (CNNs)**, which are applied for signal processing assistance [389, 390], semantic segmentation [391–393], and vertex reconstruction [394]. CNNs are also used for high-level reconstruction tasks such as PID [300, 395] and energy estimation [396].

Beyond CNNs, newer architectures include **Recurrent Neural Networks (RNNs)** for time-series energy reconstruction [397], **Graph Neural Networks (GNNs)** for hit clustering and labeling [398], and hybrid CNN-GNN models for full event reconstruction pipelines [399]. These developments are accelerated by the availability of public datasets [400] and integration of ML tools within GPU-accelerated software frameworks [299, 401].

35.7.7 *Developments*

The successful operation of the ICARUS T600 detector [402] provided a milestone in demonstrating the feasibility of large-scale liquid argon TPCs. Since then, the technology has rapidly evolved, with the community expanding significantly. Notable advancements include:

- **Cold electronics**: CMOS-based amplifiers now operate reliably within liquid argon.
- **Modern photon detectors**: Silicon Photomultipliers (SiPMs) and novel light collection designs and readout are increasingly replacing traditional photomultiplier tubes.
- **Improved light performance**: Dopants (e.g., xenon, TMG) and advanced wavelength shifters improve light yield and timing.
- **Scalable cryostat technology**: Membrane cryostats, as adopted in DUNE, enable safe and cost-effective scaling to tens of kilotons.
- **Pixelated readout**: Replaces traditional wire planes in high-rate or high-occupancy environments, allowing unambiguous 3D charge localization [403].
- **LAr Purification**: novel techniques to capture not only electronegative impurities but also Nitrogen dissolved in LAr through specific molecular sieves [404].

Several new directions are under exploration. These include the **vertical drift** single-phase TPC, proposed for the second DUNE far detector module, which uses perforated PCB strips for charge readout [405]; **optical-only dual-phase readout**, where the electroluminescence light is imaged by fast cameras [406]; and **photon sensors powered and readout by optical systems** (Power over Fiber, Signal over Fiber) [407] which enable light detection at arbitrary electric potentials and positions. In parallel, efforts are underway to **build high voltages in-situ** using Greinacher-style multipliers, eliminating the need for ultra-high-voltage feedthroughs [408]. Operation of a small **LAr-TPC in a magnetic field** of up to 0.7T is also being pursued [307] to investigate benefits of distinguishing particle's charge sign (enabling electron/positron discrimination and increasing electron/photon separation) and measuring momentum of particles via curvature (especially important for muons and pions exiting the detector).

Simultaneously, extensive datasets from current experiments are enabling deeper insights into

the argon medium [336,409] and revealing novel phenomena. These range from the detailed understanding of light propagation, scattering, and absorption, to the behavior of impurities and their impact on charge and light transport. Emerging topics—including the measurement of Rayleigh scattering, precise determination of water capture time, and the role of dopants—highlight the continuing richness of this research area.

The field is active, rapidly advancing, and full of opportunity.

35.8 Semiconductor detectors

Revised November 2025 by G. Kramberger (Jozef Stefan Inst.) and N. Wermes (Bonn U.).

Semiconductor detectors offer outstanding detection opportunities in terms of position, energy and also time resolution, often in combination. In accelerator experiments, they are most widely used as position-sensing devices, *e.g.* in tracking detectors, or as photodetectors (Sec. 35.2), for example in calorimeters (Sec. 35.10) or in imaging Cherenkov detectors (Sec. 35.5). In recent years, also precise time measurement ($\mathcal{O}$(10–30 ps)) with silicon detectors has come into the focus of developments. When comparing semiconductor detectors, particularly with gaseous detectors, the main features are high density and low ionisation threshold, providing in depleted substrates comparatively large signals even without intrinsic amplification. Silicon detectors with active layers only 50–300 µm thick provide adequately large and fast signals on a typical time scale[4] of 10–50 ns. Challenges are the purity of the semiconductor material, characterised by its mobility-lifetime ($\mu\tau$) product, and its radiation resistance. The development of modern semiconductor detectors is closely tied to integrated circuit (IC) technology. Micro-processing and micro-electronics technologies enable fabrication of high-density micron-scale electrodes on large wafers (6–8 in $\approx$ 15–20 cm diameter of sensor wafers) and allow for high-density amplification and readout circuits connected to them (chip-wafer sizes are up to 12 in $\approx$ 30 cm with typical reticles of 26$\times$33 mm^2). For larger than reticle-size area stitching over the reticle boundary is mandatory. In recent years stitching has been demonstrated even for wafer-scale area-sizes.

Some important material properties of common semiconductors used as detectors are summarised in Tab. 35.11. While for particle tracking the excellent position resolution is the main (but not the only) interest, high stopping power and high energy resolution are key parameters in X-ray, γ-ray, and β spectroscopy, for example, in neutrino-less double-beta decay searches. Due to its small bandgap, germanium excels in energy resolution but needs to be operated at very low temperatures (liq. N_2) to reduce thermally generated reverse bias current. Besides Ge, also GaAs, CdTe and CdZnTe (CZT) feature high atomic numbers and hence much higher stopping power and shorter absorption length than Si, which is important, especially for X-ray detection. Diamond, fabricated by chemical vapour deposition (CVD) and strictly speaking classified as an insulator with a large bandgap (Tab. 35.11), features low Z and large radiation length X_0. Thanks to its radiation hardness (Sec. 35.8.5), it is used for particle detection in dedicated applications, especially in zones with high particle flux (see *e.g.* [410] and references therein).

Materials R&D for radiation sensors extends to other bulk semiconductors as well, for example, ZnS, SiC, GaN or InP. SiC, in particular, shares most of the beneficial properties of diamond for particle detection and is available in high-quality, large-diameter wafers (see Tab. 35.11). Also, new material structures and metamaterials have come into focus. Examples are semiconductor Quantum Dots, realised by nanometer-sized semiconductor "particles" embedded in a semiconductor bulk, or graphene, which—as a zero-bandgap 2D material—features extraordinarily high conductivity (electrical and thermal) and outstanding photonic properties. A bandgap can be introduced by employing doped bi- or multi-layer graphene structures, thus rendering transistor and sensor

[4] Characterised here by the peaking time of the signal pulse.

realisations possible. The interested reader is referred to references [411] or [412], for example.

Operating usually without intrinsic amplification, semiconductor detectors crucially depend on low-noise electronics (see Sec. 35.9), so the detection sensitivity is determined largely by signal charge and input capacitance. Reviews of semiconductor detectors and electronics can be found, for example, in refs. [1, 8, 413–415].

Table 35.11: Properties of some detector-relevant semiconductors; temperature-dependent quantities given at 300 K (from [1, 416] and references therein).

Property	Si	Ge	GaAs	CdTe (CZT*)	Diamond	4H-SiC†
atomic number (Z)	14	32	31/33	48/(30)/52	6	14/6
density ρ (g/cm^3)	2.328	5.327	5.32	5.85	3.51	3.21
dielectric constant ϵ	11.9	16.0	13.1	10.2	5.7	9.72
semiconductor type	indirect	indirect	direct	direct	indirect	indirect
bandgap E_G (eV)	1.12	0.66	1.424	1.44(1.44–2.2)	5.5	3.26
intr. carrier density (cm^{-3})	1.09×10^{10}	2.4×10^{13}	2.1×10^{6}	10^7	≈ 0	≈ 0
radiation length X_0 (cm)	9.36	2.30	2.29	1.52	12.15	10.58
average energy w_i for (e/h) creation (eV)	3.65	2.96	4.35	4.43	13.1	7.8
mobility (cm^2/Vs)						
electrons μ_n	1450	3900	8500	1050	≈1800‡	950
holes μ_h	500	1800	400	90	≈2300‡	125
lifetime						
electrons τ_e	>100 µs	∼ms	1–10 ns	0.1–2 µs	≈100 ns	0.1–2 µs
holes τ_h	>100 µs	∼ms	20 ns	0.1–1 µs	≈ 50 ns	0.7 µs

*CZT = CdZnTe with the bandgap depending on the Cd to Zn ratio.
†4H-SiC = hexagonal silicon carbide with a 4-layer repeat structure.
‡Approximate averages. Mobility values for diamond quoted in the literature vary strongly.

35.8.1 *Signal generation in semiconductors*

35.8.1.1 *Creation of charges*

Semiconductor detectors are solid-state ionisation chambers. Absorbed energy forms electron-hole (e-h) pairs, *i.e.* negative and positive charge carriers which—when moving e.g. in an applied electric field—generate a signal current on the electrodes by electrostatic induction (see Sec. 35.8.1.2). For the signal charge carriers to (freely) drift in the electric field and become detectable, a semiconductor must feature a small intrinsic charge-carrier density (as exists, for example, in diamond and SiC, and to some extent also in GaAs and CZT) or they must be depleted by reverse-bias junction configurations (as for Si, Ge or CdTe). In addition, they should feature a low intrinsic density of defects which can act as trapping or generation/recombination centers (see Sec. 35.8.5).

The minimum energy required to form an e-h pair is the bandgap energy (1.12 eV in Si, 0.66 eV in Ge, 5.5 eV in diamond). However, impinging radiation or particles also release energy to lattice vibrations (phonons) such that the average energy for e-h pair creation is higher. In an "indirect"

semiconductor like Si, the valence-band maximum is not at the same position in k-space (crystal-momentum space) as the conduction-band minimum and additional momentum transfer is required for a band transition to occur. Since the "direct" bandgap energy without k-transfer in Si is 3.4 eV, photons with energies less than 3.4 eV must receive momentum from lattice phonons. Because phonons are Bose-Einstein distributed, the needed momentum kick causes a steep rise in photon absorption probability between 1.12 eV and about 3.4 eV (see e.g. [1]). For larger energy deposits, the average energy w_i needed to produce an e-h pair assumes a constant value of 3.65 eV at room temperature. For other semiconductors consult Tab. 35.11.

For minimum-ionising particles, the most probable charge deposition in a 300 µm thick silicon detector is about 3.7 fC (∼23 000 electrons). In tracking detectors, a particle's energy loss and scattering in the detector material should be minimal (large X_0), whereas, for energy spectroscopy, *e.g.* of X-ray photons, the stopping power should be maximised by choosing high-Z semiconductors[5]. A smaller bandgap (in fact a smaller w_i) leads to a larger signal per deposited energy and improves the energy resolution, but also (exponentially) increases thermally excited carrier generation. To cope with excessive leakage currents at room temperature, Ge diodes are typically operated at liquid nitrogen temperature (77 K). In pure Si at 300 K, the intrinsic carrier concentration is $n_i \simeq 10^{10}\,\mathrm{cm}^{-3}$ (Tab. 35.11), corresponding to a resistivity in the order of $\rho \simeq (e\mu n)^{-1} \approx 400\,\mathrm{k\Omega\,cm}$. In reality, crystal imperfections and minute impurity concentrations limit Si carrier concentrations to about $10^{11}\,\mathrm{cm}^{-3}$ at 300 K ($\rho \approx 40\,\mathrm{k\Omega\,cm}$). In practice, wafer resistivities up to 20 $\mathrm{k\Omega\,cm}$ are available, with mass production ranging from 1 to 10 $\mathrm{k\Omega\,cm}$.

The energy released in a semiconductor is absorbed by electronic excitations (e/h) and lattice excitations (phonons) in an anti-correlated way. Therefore, for a fixed released energy E (for example, of an X-ray photon), the variance in the number of charge carriers $N = E/w_i$ follows binomial statistics. Due to the energy constraint, this variance is reduced by the Fano factor F relative to Poisson statistics (F ≈ 0.1 in Si and Ge). Thus, $\sigma_N = \sqrt{FN}$ and the energy resolution is $\sigma_E/E = \sqrt{Fw_i/E}$. However, for semiconductors, the measured fluctuations of a detected energy signal are usually dominated by electronic noise rather than by signal fluctuations. The electronic noise contribution depends much on the detector leakage current and the electrode capacitance as well as on pulse shaping (*i.e.* the shaping time) in the signal processing electronics (see Sec. 35.9).

For X-ray detection, a major effort is made to find high-Z materials with a bandgap that is sufficiently large to allow for room-temperature operation while still providing good energy resolution. Compound semiconductors, *e.g.* CZT, can allow this, but typically suffer from charge collection problems, which are characterised by the product $\mu\tau$ of mobility and carrier lifetime; this is the depth per field strength that generated carriers can drift before being trapped.

In Si and Ge, $\mu\tau$ is orders of magnitude larger than in compound semiconductors for both electrons and holes (see Tab. 35.11). Since for holes $\mu\tau$ is typically much smaller than for electrons, detector configurations where the electron contribution to the charge signal near the readout electrode dominates (as *e.g.* in strip or pixel structures with electron collection) usually provide better performance (see also next section).

35.8.1.2 *Signal formation*

The signal and its pulse shape depend on the instantaneous carrier velocity $\vec{v}(\vec{x}) = \mu\vec{E}(\vec{x})$, μ = mobility, and on the electrode configuration and its geometry, which determine the form of the induced current according to the Shockley-Ramo theorem

$$i_S(t) = N_{e/h}\, e\, \vec{E}_w(\vec{x})\, \vec{v}(\vec{x}(t))\,, \tag{35.20}$$

[5] The cross section for photo effect scales as Z^5 (see Sec. 34)

where $N_{e/h}\,e$ represents a drifting charge cloud of $N_{e/h}$ elementary charges, $\vec{E}_w(\vec{x})$ is the "weighting field", which accounts for the coupling of the charge to a specific electrode and depends on the electrode configuration, and $\vec{v}$ is the drift velocity. Note the difference between the electric field $\vec{E}$ and the weighting field $\vec{E}_w$ and take account of the fact that the mobility is, in general, field-dependent, $\mu = \mu(E)$, with $v \approx const$ at high fields (velocity saturation, for electrons in Si approaching 10^7cm/s at $E > 10^4$ V/cm). Both electron and hole movements contribute to an electrode's signal. Hence, if the carrier mobility is very different for electrons and holes, like *e.g.* in CdTe where $\mu_h \ll \mu_e$ (Tab. 35.11), a photon signal, for example, can become absorption-point dependent.

Integration of the induced current signal on an electrode yields the "collected charge". The average time to collect the created charge decreases with increasing bias voltage (*i.e.* field strength) until velocity saturation occurs.

For a simple parallel-plate geometry with two electrodes, the weighting field is constant, whereas for structured electrode geometries, like for example strips or pixels, $\vec{E}_w$ is position dependent, which for small electrodes (compared to the sensor thickness) strongly enhances the contribution of the movement close to the electrode ("small-pixel effect"). More details and practical accounts of the Shockley-Ramo theorem and its usage can be found in [1, 8] and references therein.

Position resolution is ultimately limited by transverse diffusion of the moving charge cloud (typically 3–5 µm for 200–300 µm thickness) and by the emission of δ electrons. The performance then depends on optimal usage of charge sharing between neighbouring electrodes and on the noise. In magnetic fields, Lorentz drift deflects the electron and hole trajectories by an angle $\tan\alpha_L = \mu\, r_H B$, thus increasing the spatial spreading. The factor r_H accounts for the mobility difference with and without a magnetic field. For silicon at room temperature and small B-fields, $r_H \approx 1.15$ for electrons and $r_H \approx 0.8$ for holes; for large magnetic fields $r_H \approx 1$. The total spreading and hence charge sharing between electrodes can be tuned (increased or decreased) by tilting the detector relative to the incoming (average) particle direction. Overall spatial resolutions of 2–4 µm (rms) have been obtained.

35.8.2 *Junction detectors*

Si and Ge detector substrates must be—others like CdTe, GaAs should be, and CZT can be—depleted of free charge carriers by operating them as reverse-bias junctions (p-n or Schottky) to be sensitive to the charge created by impinging particles. SiC, although intrinsically almost free of charge carriers, usually comes as wafers with doped epitaxial layers of thickness $\lesssim 100$ µm and SiC detectors are hence built as junction detectors.

A typical cross-section of a junction detector is shown in Fig. 35.24, here with structured electrodes at the top. A p-n junction—even without external voltage—forms a sensitive space-charge region across itself, depleted of mobile charges, hence also called "depletion region". The space charge establishes an electric field corresponding to a "built-in" voltage V_{bi}. An additional reverse-bias voltage V, applied externally, increases the space-charge region, allowing radiation-generated charge to be swept to the electrodes by the existing field. Detectors typically use an asymmetric structure, for example, a thin and highly doped p^+ electrode[6] region and a lightly doped n^- substrate region – or vice versa, so that the depletion region extends predominantly into the more lightly doped bulk volume.

[6] $n^{+/++}$, $p^{+/++}$ as well as n^-, p^- qualitatively denote relative doping-concentration levels.

In such planar Si (or Ge) devices, the thickness of the depleted region is

$$d = \sqrt{2\epsilon\,(V + V_{bi})/Ne} = \sqrt{2\rho\mu\epsilon\,(V + V_{bi})} \tag{35.21}$$
$$\approx \frac{0.5}{\mu\mathrm{m}} \times \sqrt{\frac{\rho\,V}{\Omega\,\mathrm{cm}\cdot\mathrm{V}}} \qquad \text{for } n\text{-type Si bulk}$$
$$\approx \frac{0.3}{\mu\mathrm{m}} \times \sqrt{\frac{\rho\,V}{\Omega\,\mathrm{cm}\cdot\mathrm{V}}} \qquad \text{for } p\text{-type Si bulk}$$

with (values for Si)

V = external bias voltage
V_{bi} = "built-in" voltage ($\approx 0.5\,\mathrm{V}$ for typ. used resistivities)
N = doping concentration
e = elementary charge
ϵ = dielectric constant = $11.9\,\epsilon_0 \approx 1\,\mathrm{pF/cm}$
ρ = resistivity (typically 1–10 $\mathrm{k}\Omega\,\mathrm{cm}$)
μ = charge carrier mobility
($\sim 1450\,\mathrm{cm^2/Vs}$ (electrons), $\sim 500\,\mathrm{cm^2/Vs}$ (holes) [417])

The conductive p and n regions together with the depleted volume form a capacitor with capacitance per unit area

$$C' = \frac{\epsilon}{d} \approx \frac{1\,\mathrm{pF/cm}}{d} \qquad \text{in Si.} \tag{35.22}$$

The depletion depth d becomes as large as the sensor's thickness at the "full depletion voltage" $V = V_{fd}$ for which the sensor capacitance reaches a minimum (about $35\,\mathrm{pF/cm^2}$ for $d = 300\,\mu\mathrm{m}$). In strip and pixel detectors (see next section), the capacitance is dominated by the fringing capacitance to neighbouring electrodes as the electrode pitch is typically much smaller than the sensor thickness. For example, the strip-to-strip Si fringing capacitance is about 1–1.5 pF per cm of strip length at a strip pitch of 25–50 µm, depending also on the electrode width.

The electric field strength and shape inside the semiconductor bulk are important for efficient signal-charge collection. Governed not only by the applied external voltage, but also by the space charge inside the semiconductor bulk, the field strength decreases linearly (for constant space charge) from its maximum at the junction's boundary into the depleted semiconductor bulk. Apart from the doping atoms, space charge can also occur from ionised lattice defects which either naturally exist for example in GaAs or can be created by irradiation in any semiconductor material (see Sec. 35.8.5). This can lead to low-field regions as well as to changes in the field's shape (deviating from linear), both of which usually deteriorate the charge collection properties of a detector.

In partial depletion (*i.e.* $V < V_{fd}$), the field decreases to zero at the end of the depletion zone. Overbias ($V > V_{fd}$) adds a constant electric field component, which avoids a vanishing field region and also provides faster charge collection as long as the carrier drift velocity has not yet saturated. At an average field of $E = 10^4\,\mathrm{V/cm}$, the onset of velocity saturation, where $\mu_e \approx 7{\times}10^2\,\mathrm{cm^2/Vs}$, $\mu_h \approx 3.5{\times}10^2\,\mathrm{cm^2/Vs}$, the collection times for Si are about 15 ps/µm for electrons and 30 ps/µm for holes. In typical fully-depleted detectors, 100–300 µm thick, electrons are collected within less than about 5 ns, and holes within less than about 10 ns.

Large volume ($\sim 10^2 - 10^3\,\mathrm{cm^3}$) germanium detectors, especially for gamma-ray detection, are commonly configured in cylindrical or hexagonal rod shapes, for example, a 10 cm long cylindrical n-type crystal with 5–10 cm diameter with an inner 5–10 mm diameter n^+ electrode and an outer

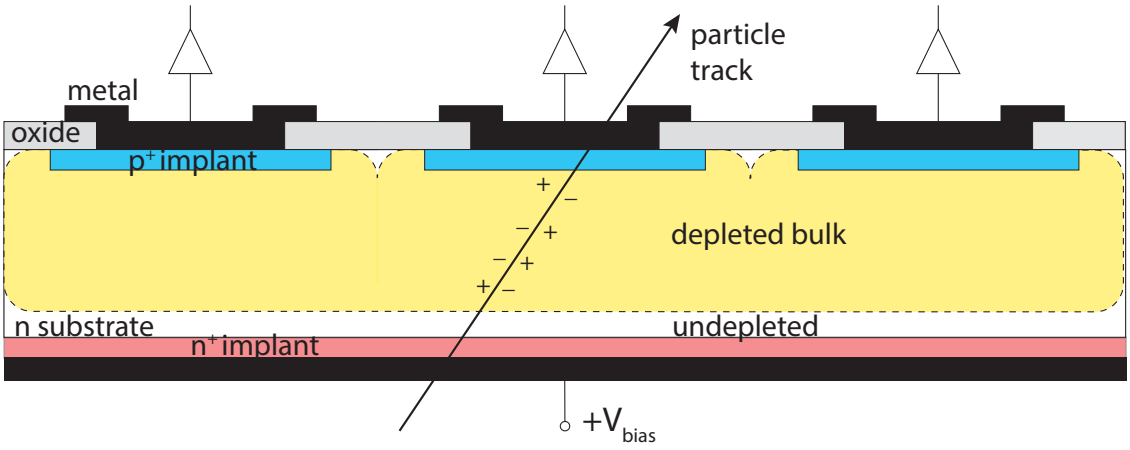

Figure 35.24: Reverse-bias junction detector with planar readout electrodes at the top in a standard sensor configuration (p^+-in-n): lightly doped n-type substrate with p^+ implants forming the diode junction at the top side. Electrons move to the bottom electrode and holes to the top. Both movements contribute to the (induced) signal at the top electrodes with amounts as specified by the weighting field (see Sec. 35.8.1.2). The n^+ implant at the bottom side forms an ohmic contact between bulk and metal.

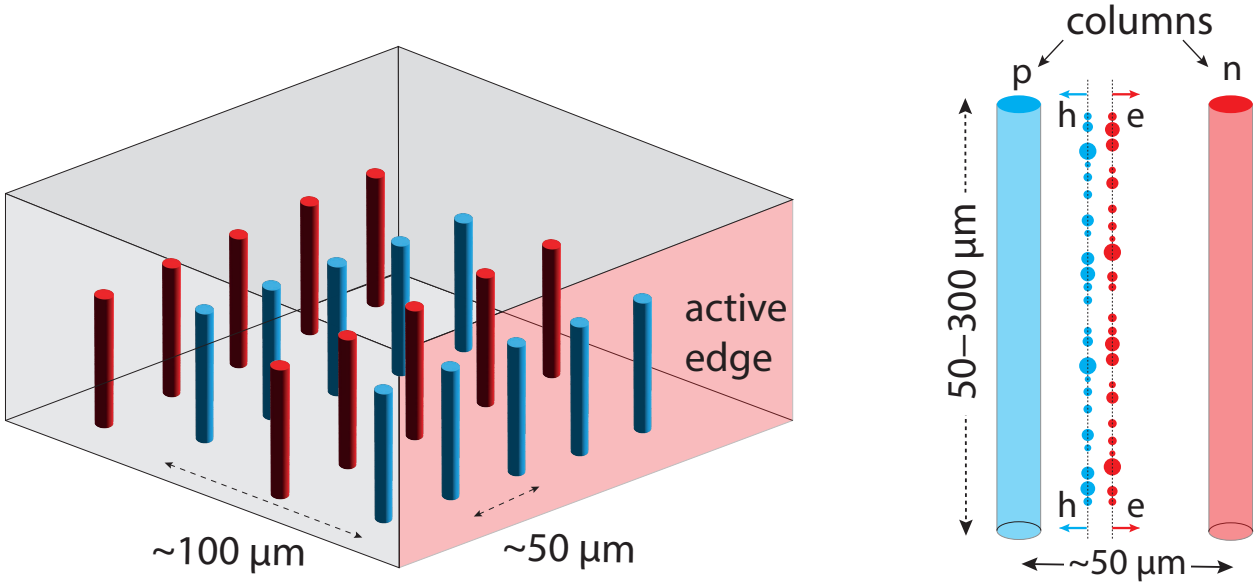

Figure 35.25: Junction detector with vertical electrodes, n (red) and p (blue), and "active" edges called 3D-Si. Dimensions given are typical. This electrode configuration provides short drift paths for moving charges while keeping a large sensing thickness. An active edge minimises dead areas at the sensor boundaries. This geometry has also been employed in CVD diamond substrates.

p^+ layer forming the diode junction. Germanium can be grown with fairly low impurity levels, 10^9–$10^{10}\,\mathrm{cm}^{-3}$ (HPGe, high-purity germanium), so these large volumes can be depleted with several kilovolts.

Diamond, featuring free charge carrier densities close to zero, needs no further depletion and is operated as a parallel plate capacitor with an insulator dielectric inside. Still, a substantial bias

voltage is required to overcome charge trapping.

35.8.3 *Detectors with structured electrodes*

35.8.3.1 *Microstrip-, Si-drift- and hybrid-pixel detectors*

In HEP experiments semiconductor detectors usually aim at good position resolution achieved with electrodes patterned in "strips" or "pixels" with typical dimension scales (electrode pitch) of 50–100 µm, or in "pads" (mm^2–cm^2) if coarser granularity is affordable for the benefit of fewer channels.

Electrodes are usually placed "planar", *i.e.* at the surface of the sensing Si bulk (Fig. 35.24). In an alternative, but more elaborate way, electrodes can be shaped as columns or trenches running orthogonally to the surface and hence parallel to the average direction of impinging particles (Fig. 35.25) [418]. This geometry which is termed "3D-Si", but is also exercised with diamond, enhances the radiation tolerance due to shorter drift distances of charges at the same thickness, hence decreasing the probability for carrier trapping (see also Sec. 35.8.5).

The 3D technology offers a large variety of cell geometries usually optimized for a given task, realized with column electrodes, trench electrodes (plane parallel-trench cells) or a combination of both. In recent years, manufacturing the vertical electrodes has advanced to simpler single-sided processing, reaching aspect ratios (diameter to depth) of up to 70, thus enabling smaller cells and thicker detectors. The processing techniques employed for 3D devices also enable the creation of continuous trenches with conductive sensor side-walls ("active edge" in Fig. 35.25), which are useful for laterally extending the depleted volume up to the physical edges.

In strip detectors, the strip ends are connected to dedicated readout ICs where the signals are amplified and processed. Two-dimensional readout is realised either by angled double-layers of strip detectors or by "double-sided" strip sensors, structured by readout strips on either side (see *e.g.* [1,414] and references therein). For the latter, one electrode surface features n^+n or p^+p strip junctions (rather than pn), respectively, which require dedicated measures, *e.g.* intermediate strips or special doping profiles to break the electron accumulation layer that occurs at an n^+n interface. For p^+p, intermediate n strips or similar are not necessary, owing to positive oxide charges residing at the Si/SiO_2 interface, thus preventing the formation of a hole accumulation layer.

Following the concept of gaseous drift chambers, silicon drift chambers provide the position of a hit orthogonal to a strip's coordinate from a measurement of the charge cloud's drift time, drifting over centimeter-long paths inside the silicon bulk (Fig. 35.26a). For this to work, the bulk is "sidewards depleted" by using junction strip-implants of the same polarity on both sides of the sensor (p in n or n in p, respectively), *i.e.* different to standard double-sided strip detectors (see *e.g.* [1]). This way, a quadratic potential minimum for electrons is created, confining them amidst the sensor bulk; holes, instead, drift to the sides. A constant potential (linear field) is superimposed in drift direction (Fig. 35.26c); near the anodes, electrons are pushed towards n-strip collection electrodes by appropriate biasing (Fig. 35.26d). Unlike strip detectors, far fewer electrodes are necessary for the same active area coverage. A drawback is the low rate capability of Si-drift detectors caused by the long drift path of the created charges. Arranged with only one small electrode with low capacitance in the center of a cylindrical disk, so-called silicon drift-diodes (SDD, Fig. 35.26b) are low-noise single-channel devices with large area coverage (typically cm^2), used for example in X-ray fluorescence analysis, electron microscopy and space applications.

Very small pixel structures for particle detection were first realised with CCDs (Charge Coupled Device) [419]. Most current applications, particularly those for high-rate applications such as at the LHC, employ the "hybrid-pixel" concept in which both the sensing diode structure as well as the readout IC have equal electrode structures and patterns (pixels). The connection is made by two-dimensional arrays of solder or indium bumps that mate the two parts by employing the

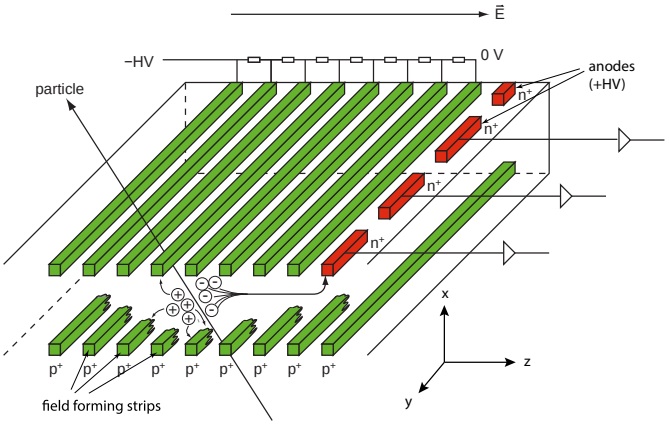

(a) Silicon drift chamber.

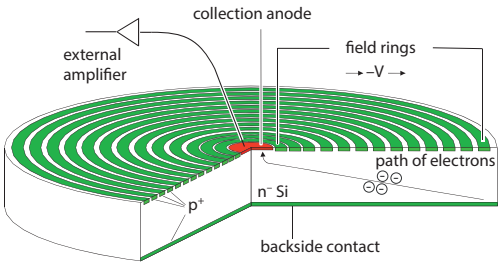

(b) Silicon drift-diode (SDD).

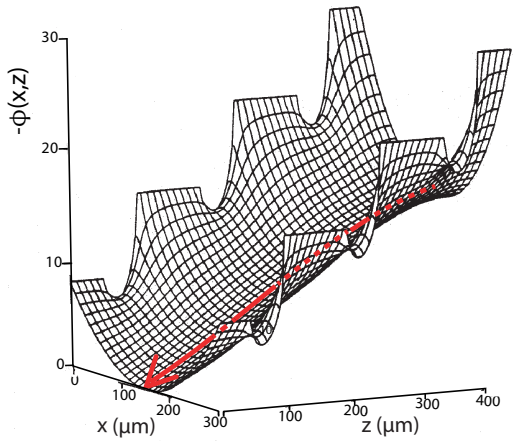

(c) Potential in the region of electron drift.

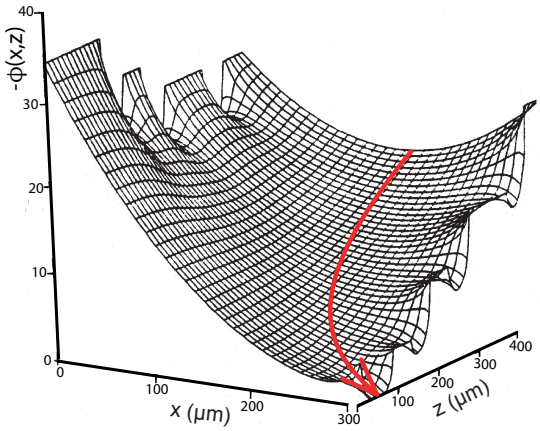

(d) Potential near the anode region.

Figure 35.26: Silicon drift detector: (a) Principle layout of an n-bulk Si drift chamber featuring field-forming p-strips on both sides and charge-collecting n-strip anodes. A linear field gradient, applied by a resistor chain, provides drift of electrons towards the anodes. (c) Shape of the electric potential in the drift region of the detector shown in (a). (d) Electric potential near the anode region. (b) Si drift diode featuring circular field rings and only one small collection anode in the center of the diode, constituting very low capacitance for the readout electronics.

flip-chip technology (Fig. 35.27, usually chip-to-(sensor)chip or several-chips-to-sensor; more details in [414,420,421]). Further advancements in bonding-technique development especially address chip-to-wafer or even wafer-to-wafer placements [420]. Attractive in this context of particle detectors are Cu–Cu, Cu–Sn, or oxide–oxide (SiO_2) diffusion bonding without solder. Also, SLID (Solid Liquid Interface Diffusion), which employs a very thin liquid metal layer (Sn) in between metals with higher melting points (*e.g.* Cu) is an option.

The hybrid approach excels in optimally utilising chip and sensor materials and technologies for radiation hardness and rate capability (see *e.g.* [420]). It is, therefore, the technology of choice for pixel trackers in high-rate, high-radiation environments optimised for that purpose by employing very thin modules ($\mathcal{O}(300\,\mu m)$ total). A disadvantage is the complex and cost-intensive module assembly.

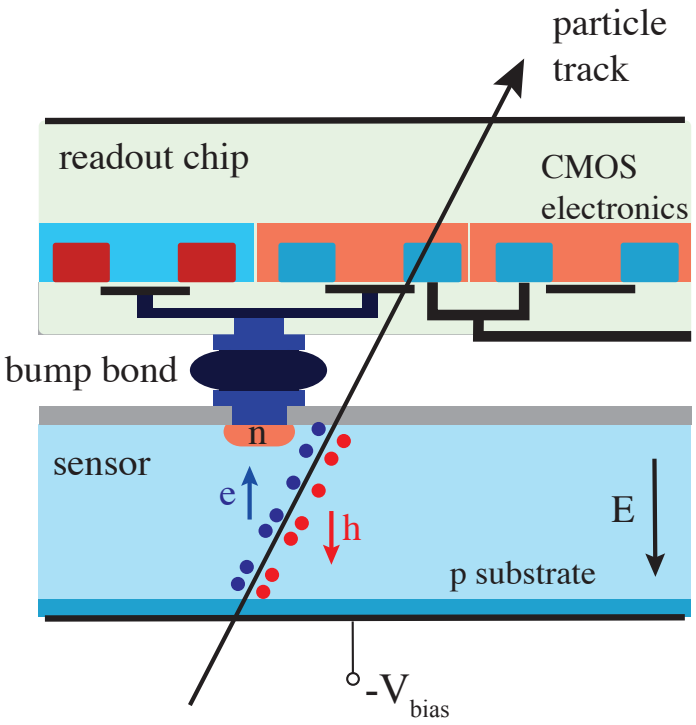

Figure 35.27: Cross-sectional view of a hybrid-pixel detector cell (one pixel) consisting of sensor (bottom) and readout chip (top) with CMOS circuitry illustrated by three transistors (red and blue implant areas plus metal lines). The sensor is a depleted diode structure (here p substrate with a highly doped n electrode). Both parts are mated by a microbond (bump bond), typically solder or indium.

35.8.3.2 *Monolithic pixels*

Partially or fully monolithic pixel detectors directly connect the generated signal charge with an embedded active electronics device (*i.e.* one or several transistors). An example of a partially monolithic device is the DEPFET (depleted p-channel FET) pixel sensor (see *e.g.* [422]), employed in the Belle-II pixel-vertex detector and—with circular cells—also developed for satellite experiments as shown in Fig. 35.28a. A single transistor (pMOSFET) is implemented in every pixel. The sensor substrate is "sidewards depleted"—as done similarly in Si driftchambers (Sec. 35.8.3.1)—employing the backside p-contact and several p regions near the transistor. Depletion is provided by the n^+ *clear* contact (see below) plus a bulk n-implant outside the matrix. In addition, the structure features a deep n-implant located a few micrometers underneath the transistor channel on floating potential. This implant becomes the most positive point of the structure, hence being an electron accumulation point which acts as an "internal gate" of the transistor. The gate voltage changes by an amount $\alpha q_S/C$, with signal charge q_S, gate-oxide capacitance $C = C_{ox}\,WL$ where $W \times L =$ gate area, and with $\alpha \lesssim 1$ accounting for stray capacitance. The gate voltage changes due to an accumulated signal charge q_S in the internal gate, leading to a detectable change in drain current (in saturation):

$$I_D = \frac{W}{2L}\,\mu C_{ox}\left(V_G + \frac{\alpha\, q_S}{C} - V_{th}\right)^2 . \tag{35.23}$$

Other elements in Fig. 35.28a like the external FET gate and the *clear* implant provide control and reset of the structure. The device gain $g_q = dI_D/dq_S \approx \alpha g_m/C$, with transconductance

$g_m = \mu C_{ox} \frac{W}{L}(V_G - V_{th})$, is of order 500 pA/e$^-$. The small capacitance of the internal gate (few fF) enables very low-noise operation ($\lesssim 2e^-$) when operating with long shaping times (cf. Sec. 35.9).

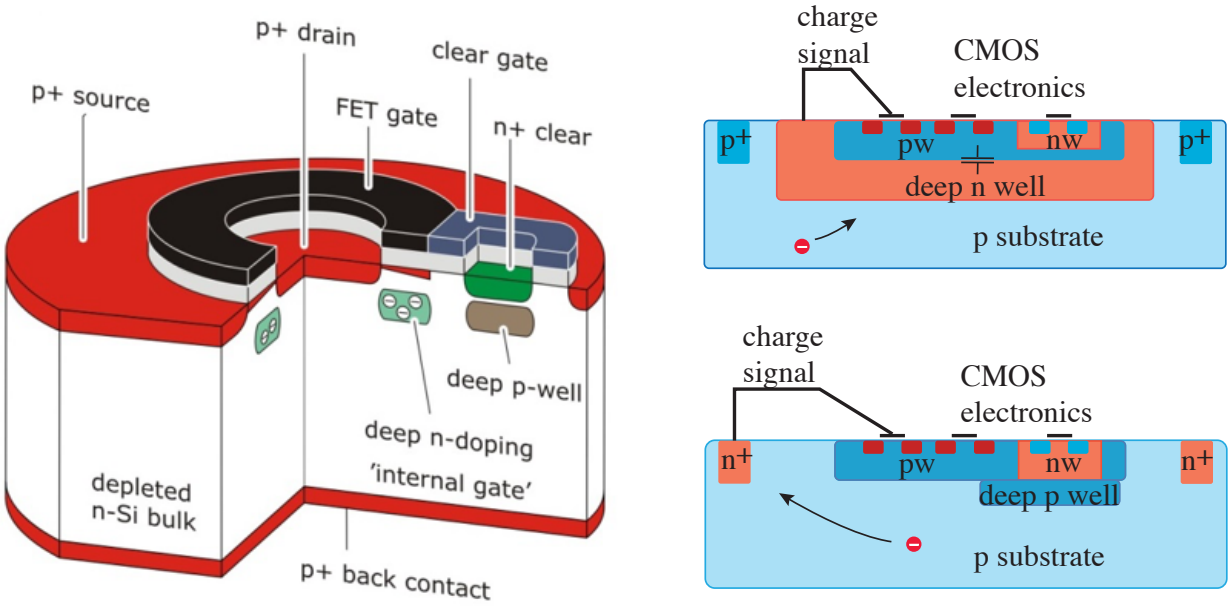

(a) DEPFET pixel structure.

(b) DMAPS pixel structures.

Figure 35.28: Partially (a) and fully (b) monolithic pixels: (a) A circular DEPFET pixel structure with an embedded pMOSFET transistor; source and drain are p implants (red), gate metal (black), oxide (grey), deep-n internal gate (light green), other metal (blue), clear contact (green), and deep p-well (brown). (b) Depleted MAPS with joint sensing and electronics volumes: (top) charge collection by a *large-electrode* which houses the electronics in a deep-n well; (bottom) charge collection by a *small electrode* set aside from the electronics area.

Fully monolithic pixels combine the sensing task and the complete readout circuitry, *i.e.* the two separated parts of hybrid pixels, in one chip. Both functions must be properly shielded from each other, which is achieved by exploiting multi-well IC technology. Realised as MAPS (monolithic active pixel sensors, see Fig. 35.28b), standard CMOS wafers can be used for pixel detector fabrication. CMOS wafers often feature a Si epitaxial layer where the transistors are implanted. It is possible to use this epi-layer as a sensitive detection volume for particle detection. However, in such detectors, usually only the immediate regions near the collection nodes are depleted. Outside these confined regions, there is no or little electric field and charge collection is dominantly governed by slow and non-directional charge diffusion, a problem for high-rate applications. Depleted MAPS (DMAPS) exploit non-standard high resistivity wafers or high-ohmic epi-layers, typically with resistivities $>1\,\mathrm{k\Omega\,cm}$, as well as high bias voltage (up to $\gtrsim 300\,\mathrm{V}$), resulting in charge collection by directed drift motion. Charge collecting electrodes are deep wells (n-wells in Fig. 35.28b), either formed as large (typ. $50\times100\,\mu\mathrm{m}^2$) structures to fully contain the CMOS circuitry (Fig. 35.28b, top) or as small nodes, set aside the electronics (Fig. 35.28b, bottom), with obvious pros and cons resulting from shorter average drift distance (large electrode) versus much smaller capacitance (small electrode). The former features a more uniform shape of the electric and the weighting field as well as short drift paths, benefiting radiation tolerance and timing performance in charge collection, whereas the latter allows for smaller pixels and benefits in noise and rise time from the small sensor

capacitance. Yet, in both approaches radiation tolerance levels of $\gtrsim 10^{15}\,\mathrm{n_{eq}/cm^2}$ (fluence) and 1 MGy (ion. dose) have been demonstrated.

A variant of the monolithic approach are SOI (silicon-on-insulator) pixel devices, providing high spatial resolution, but less radiation tolerance: A high-resistivity supporting wafer, employed for particle sensing, connects through an embedded insulator (a buried oxide layer, BOX) to the CMOS readout circuitry. The BOX separates the sensing volume from the electronics layer and provides shielding. Because the area between the BOX and the transistor layer acts as a "back-gate", transistor operation can be affected, requiring careful considerations of radiation tolerance (see *e.g.* [423]).

35.8.4 *Precise timing with silicon detectors*

Typical time scales for silicon detector output signals are several tens of nanoseconds (*e.g.* rise times, shaping times, etc.) accompanied by a typical time mark precision in the order of nanoseconds. Essential for achieving precision time resolution ($\sigma_t < 100\,\mathrm{ps}$) are a large and steep signal as well as low noise, because time jitter (σ_{jitter}) relates to signal-amplitude fluctuations as:

$$\sigma_{\mathrm{jitter}} = \frac{\sigma_n}{(dS/dt)_{\mathrm{trig}}} \approx \frac{t_r}{SNR}, \tag{35.24}$$

where σ_n is the rms noise, t_r the rise time, SNR the signal-to-noise ratio, and dS/dt the "slew rate" evaluated at trigger threshold (see also Sec. 35.9), in which S is the "signal", *e.g.* an induced current or a voltage. This, in turn, requires fast charge collection, *e.g.* in thin planar or 3D-Si detectors with high E-fields, as well as fast and high amplification, both together yielding large slew rates. Important parameters that influence timing precision are the detector capacitance (including stray contributions), leakage current and—if present—the size of the amplification gain.

Among the detectors that have achieved precise time measurement are so-called LGADs (low gain avalanche detectors, Fig. 35.29). Their planar electrode geometry includes an implanted low-gain ($g = 10$–50) amplification structure on either the top or bottom electrode side to maximise the slew rate. Electrons created from impinging ionising particles drift towards a very high field created by an amplification layer near the (here) top electrode, where impact ionisation creates a multitude of e-h pairs. They induce a fast and large signal rise, mainly governed by the holes' movement away from the amplification layer. Sufficiently low amplification gain minimises excess noise contributions and avoids the creation of hole-induced avalanches moving in the opposite direction to electron avalanches.

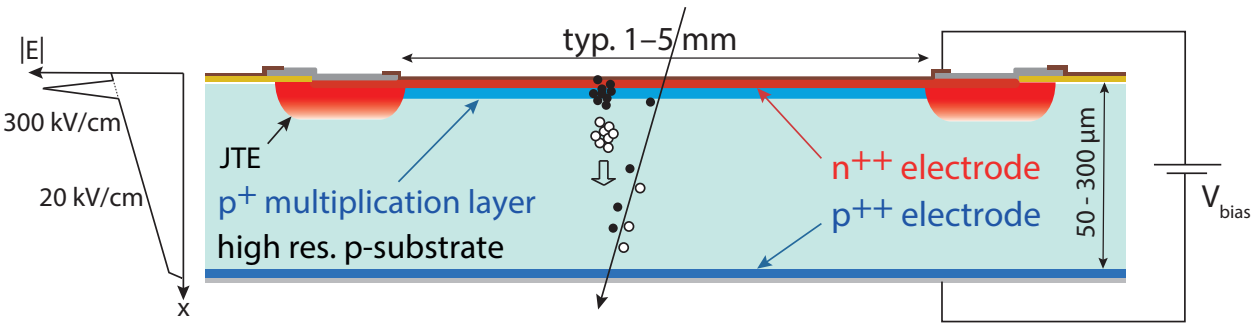

Figure 35.29: LGAD amplification structure for precision timing. Amplification (typ. $\times$ 10–50) occurs at the structure boundary in a highly doped p-n junction near the (here: top) surface (JTE = Junction Termination Extension, deep n-well).

The achievable time resolution has several contributions:

$$\sigma_t^2 \approx \left(\frac{\sigma_S^{thr}}{dS/dt}\right)^2 + \left(\frac{\sigma_n}{dS/dt}\right)^2 + \sigma^2_{\text{arrival}}(V_{thr}) + \sigma^2_{\text{dist}} + \sigma^2_{\text{TDC}}\,. \tag{35.25}$$

The first term represents "time walk" coming from Landau fluctuations, defined as originating from number and energy-transfer fluctuations in the energy-loss process with σ_S^{thr} being the signal-height variations at discriminator threshold (V_{thr}). This term can be kept minimal, *e.g.* by employing constant-fraction discrimination or by applying corrections using amplitude information. The second term is the contribution of noise to the time jitter. Both first terms are kept small by large signal slew rates. An irreducible contribution comes from fluctuations in non-uniform depositions of charge along the particle path (including fluctuations in the amplification process), which causes an intrinsic jitter in the arrival time (third term)[7]. The smaller the threshold and the thinner the detector, the less disturbing the effect is. If the amplification gain is mandatory for crossing V_{thr}, this term can become dominant as it explicitly depends on the gain. The fourth contribution is signal distortion due to non-uniform weighting-field regions and variations in (non-saturated) drift velocities. "Junction Termination Extensions" (JTE, see Fig. 35.29) serve to lower this term; it is usually marginal for LGADs with pitch/thickness $\gg 1$. The final term denotes time fluctuations due to uncertainties in digitisation, which can, however, be made negligible with GHz digital time conversion. Timing precision down to 15-20 ps for minimum-ionising particles has been reached for thin LGADs with relatively high gain (>40). Improving the time resolution for tracks beyond this value is possible by employing LGADs in multiple-layer structures.

Structural and operational variants to improve charge collection (uniform and efficient over the entire surface), position and also time resolution, are "resistive AC-coupled LGADs" (capacitively coupled electrodes on top of the gain layer), "inverse LGADs" (backside is segmented), "trench-isolated LGADs" (an oxide trench separates the electrodes) and other less mature ones like "deep junction LGADs". The LGAD technology is not limited to silicon detectors, but is also applicable, for example, in SiC: due to the doping profiles used in SiC, which are swapped compared to those in Fig. 35.29, dominantly holes are multiplied instead of electrons, albeit at higher electric fields. More details on LGADs can be found in [424] and [425].

Columnar electrode geometries such as shown in Fig. 35.25 with small diameter and small pitch are by design a very suitable choice for precision timing due to short collection paths and strong fields. Employing a trench-like shape of the columns, field- and weighting-field distortions are minimised and time resolutions in the order of 10 ps have been measured in prototypes [426].

High precision timing can also be approached by exploiting the benefits of SiGe BiCMOS technology: The strain mismatch of Si-Ge alloy layers results in a smaller bandgap as well as higher mobility, and hence larger transconductance. This benefits the speed in hetero-junction bipolar transistors (HBTs), which also feature less 1/f noise than MOS transistors. Resolutions of order 20 ps have been reached in a monolithic pixel matrix using this technology [427]. More elaborate discussions on timing with silicon detectors can be found *e.g.* in [428].

35.8.5 *Radiation damage in silicon detectors*

High channel density and response times in the nanosecond range render micro-patterned semiconductor detectors particularly suited for high particle rates. This is usually accompanied by high radiation, which causes damage to sensors and front-end electronics. We restrict ourselves here to the description of damage mechanisms typical in Si detectors and their electronics. Radiation damage occurs in semiconductor detectors through two basic mechanisms:

1. *Bulk damage* due to the displacement of atoms from their lattice sites, resulting in defect energy levels inside the bandgap. This leads to increased leakage current, carrier trapping, and

[7] In LGAD literature, these fluctuations are sometimes also referred to as "Landau fluctuations".

build-up of space charge that changes the required operating voltage. Displacement damage results from non-ionising energy loss (NIEL). The energy imparted to the recoil atoms can initiate a chain of subsequent displacements, including "damage clusters". For NIEL scaling (see below), it is critical to consider both particle type and energy: conventionally, for silicon, the received NIEL is normalised to the damage level caused by 1 MeV neutrons and specified in units of neutron-equivalent fluence Φ_{eq} with units n_{eq}/cm^2.

2. *Surface damage* due to charge build-up in surface layers and formation of interface traps at *e.g.* Si–SiO_2 boundaries. These influence transistor currents and thresholds or cause thin charge carrier layers at a silicon surface. This leads to increased surface leakage currents in sensors as well as circuits, affects the insulation of electrode implants and changes the characteristics of transistors. The effects of charge build-up are strongly dependent on the device structure and on fabrication details. The damage is mainly due to the ionising energy loss (IEL) and is hence proportional to the absorbed total ionisation dose (TID) measured in Gy (or rad), independent of the irradiating particle type.

We note that the increase in reverse bias generation current (leakage current) due to bulk damage is $\Delta I_L = \alpha_I \Phi_{eq} V$, where V is the depleted volume under an electrode and $\alpha_I \simeq 4 \times 10^{-17}$ A/cm, a universal constant when normalised to temperature (conventionally 20°C), and measured after annealing for 80 min at 60 °C. Note that for devices with intrinsic amplification, the generation current is amplified accordingly. Reverse bias leakage current depends strongly on temperature

$$I_L(T) \propto T^2 \exp\left(-\frac{E_a}{2kT}\right) , \tag{35.26}$$

where $E_a \approx 1.2$ eV (activation energy), so rather modest cooling can reduce the current substantially (∼7-fold reduction in cooling from room temperature to 0 °C).

For bulk damage in silicon, the *NIEL hypothesis* is a good first-order description of the observed damage (especially regarding I_L). It states that all lattice radiation damage in silicon linearly scales with NIEL and can be traced back to the abundance of primary defects (point defects and clusters), irrespective of their initial distribution over energy and space, that is, regardless of the damage's topology and origin. Under the NIEL hypothesis, the observed differences in damage caused by neutrons, protons, pions and electrons are therefore usually scaled to each other. For other damage manifestations besides I_L, the NIEL hypothesis is moderately violated.

Three main bulk displacement damage effects are sketched in Fig. 35.30: (a) defects acting as charged donors/acceptors, (b) deep defects (near the middle of the bandgap) causing increased leakage current, and (c) carrier trapping centers. Another consequence of deep defects is that any non-depleted bulk becomes more resistive, hence impacting the electric and the weighting field distributions. At very high fluences ($\Phi_{\mathrm{eq}} > 10^{16}$ cm^{-2}) also carrier mobilities decrease, leading to resistivities even lower than intrinsic.

Damage effects are not constant with time; for example, in n-type bulk, radiation-induced negative space charge anneals at first reaching a stable space charge minimum (beneficial annealing), but later electrically active defects (negative space charge from acceptor-type damage) build up over the time scale of months (reverse annealing) at room temperature and much longer at lower temperatures.

Acceptor- (usually dominant) or donor-like (deep) defects, when ionised, build up space charge (dominantly negative), which in turn normally requires an increase in the applied voltage to deplete the active volume of the detector and sweep the signal charge through the detector thickness. For n-type bulk starting material, however, shallow donor (*e.g.* phosphorus) removal is initiated by incipient radiation (production of lattice vacancies V) through formation of electrically inactive

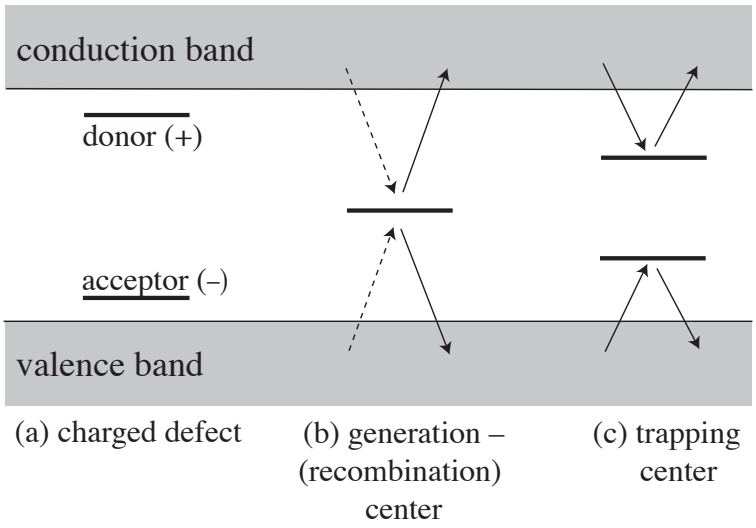

Figure 35.30: Characteristic locations of energy levels caused by bulk radiation damage and their main action effects.

vacancy-phosphorus (V-P) complexes. This leads to a faster decrease in depletion voltage (faster than only by the compensation of donors through generated deep acceptors) until positive and negative space charges effectively balance; only small bias voltage is then required for efficient operation (point of effective space charge inversion, also called "type inversion" (Fig. 35.31)). At larger fluences, the negative space charge dominates, and the required operating voltage increases proportionally to the increasing effective space charge density N_{eff}, also called effective doping concentration.

The drift of thermally generated electrons and holes (generation current) in opposite directions and their (partial) trapping leads to a surplus of these carriers at the electrodes on either side. This affects the charge state of the deep energy levels (more carriers are trapped) and hence the space charge distribution, which can no longer be regarded as constant and homogeneous over the detector volume. Hence, the linear slope of the electric field from the junction to the backside, as was introduced in Sec. 35.8.2, is distorted; instead "double-junction"-like field distributions typically occur. The magnitude of the effect depends on the material and the type of radiation.

Today, p-type bulk silicon with n^+ electrode-implants is the preferred choice for sensors operating in high-radiation environments for reasons of cost-effectiveness in production as well as high radiation hardness due to fast (high mobility) electron collection in high electric- and high weighting-field regions at small segmented n^+ electrodes. Space charge inversion is usually not observed since the initial space charge is negative already (Fig. 35.31).

Removal of initial shallow dopants (donor or acceptor) through irradiation plays a major role in the property changes of various detector technologies. The decrease of initial doping concentration ($N_{id,0}$) is exponential $N_{id} = N_{id,0} \exp(-c\Phi_{\text{eq}})$, with the removal constant c depending on $N_{id,0}$, particle type and on impurities in the semiconductor (see Fig. 35.32). Removal of acceptors (*i.e.* substitution of electrically active boron at its lattice site) in p material is found to be dominantly caused by interstitial silicon replacing boron on its lattice position. The highly active interstitial boron then can cause the formation of other defects such as interstitial oxygen-boron complexes (B_iO_i, subscript i for "interstitial") which absorb boron atoms into electrically active defects, dominantly as donors, that means that space charge can be changed twice.

Different techniques have been explored to neutralise radiation damage effects by defect en-

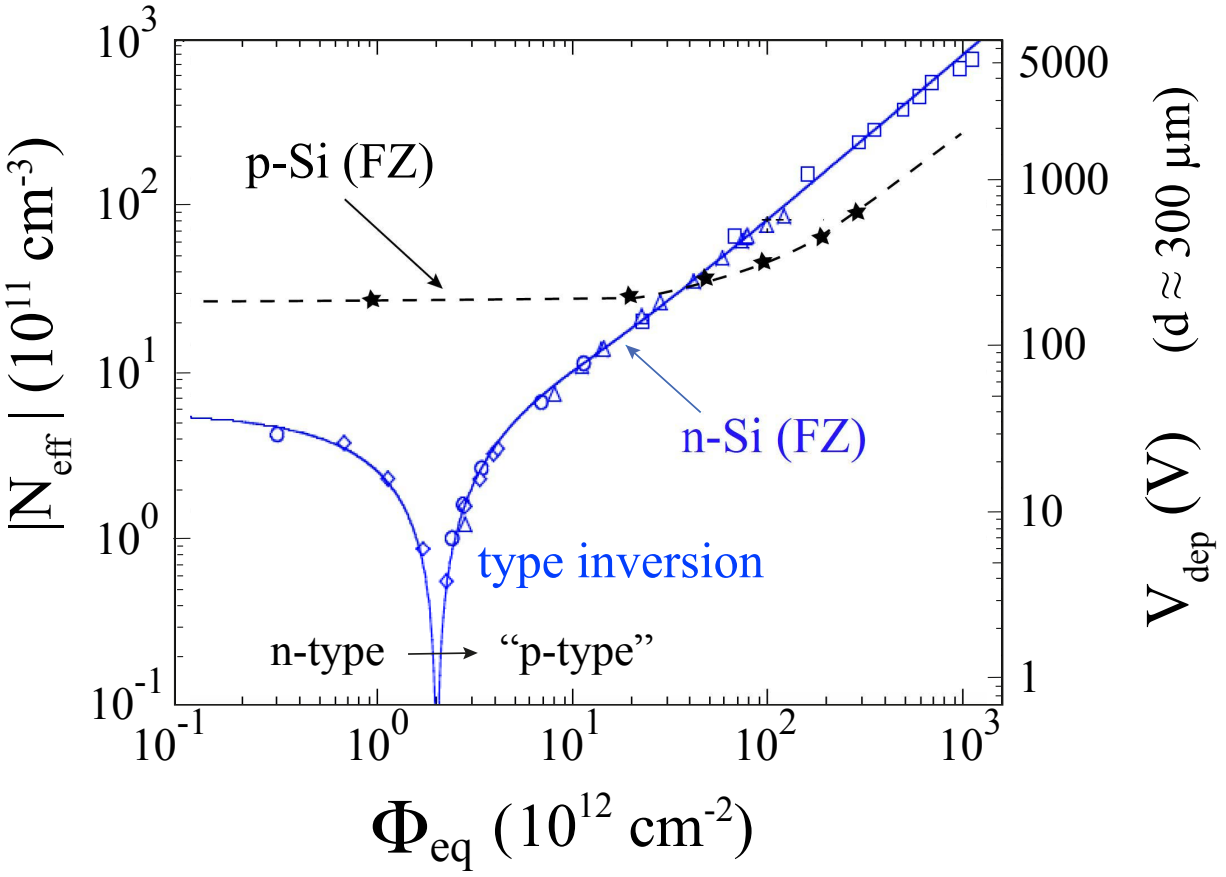

Figure 35.31: Effective space charge concentration N_{eff} (left axis) and required voltage for full depletion V_{dep} (right axis) of approximately 300 µm thick Si sensors as a function of neutron-equivalent radiation fluence for typical n-type (blue) and p-type (black) silicon float zone (FZ) material before annealing. While initial n-type Si inverts to effectively p-type Si, this is not observed for initial p-type silicon. Bias voltage supply for large systems is usually limited to less than 600–1000 V. Figure adapted using [429, 430] and [431].

gineering. For n-type material, oxygen enrichment, introduced during the Si growth, to a larger abundance than phosphorus, successfully reduces the formation of multi-vacancy, acceptor-like complexes, which are dominantly produced by charged-hadron irradiation. Instead, the oxygen enhances the formation of electrically neutral V-O complexes. For p-type Si, carbon enrichment reduces acceptor-dopant removal by building stable C_i-S_i complexes, thus trapping the Si interstitials, which could otherwise remove boron as described above.

Dopant removal plays a particularly important role in more complex sensor structures, such as DMAPS or LGADs. In particular, the high p-doping concentration in the LGAD's gain layer is vulnerable to acceptor removal, causing a drastic gain decrease with increasing fluence.

Deep level defects (Fig. 35.30b) typically are the origin of leakage current increase, whereas trapping centers (Fig. 35.30c) affect carrier trapping times and cause signal loss. The cumulative effect of different trapping centers can be expressed by effective trapping times of electrons and holes $\tau_{\text{eff},e/h}$. The induced current equation Eq. (35.20) is multiplied by $\exp(-\frac{t}{\tau_{\text{eff},e/h}})$, describing the reduction of the number of charge carriers $N_{e/h}$ due to trapping. The effective trapping probability

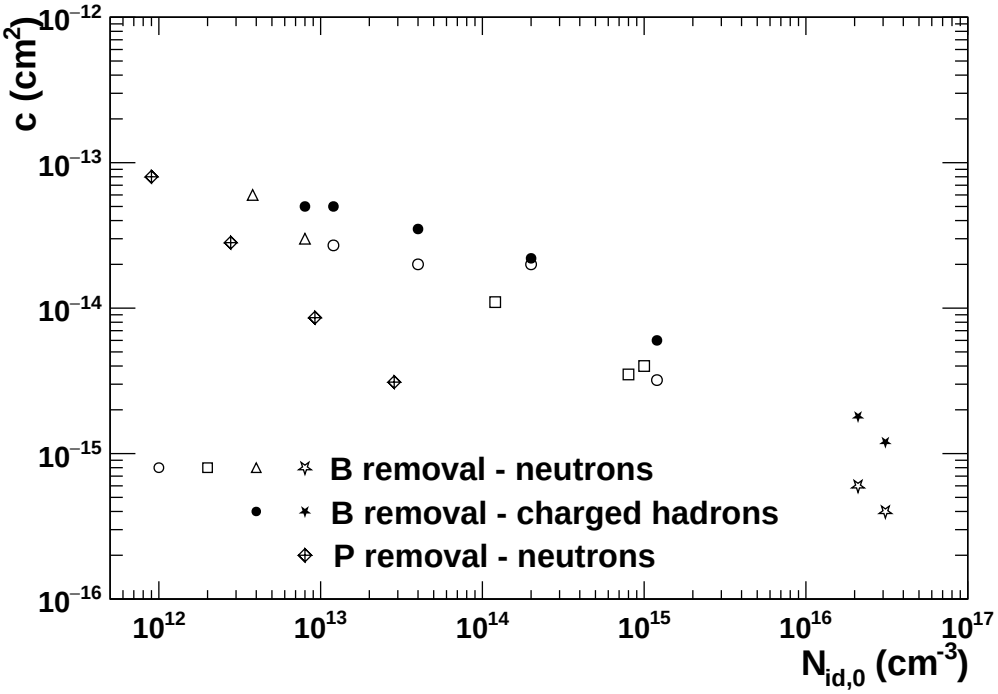

Figure 35.32: Initial dopant-removal (B boron, P phosphorous) constant c (immediately after irradiation) measured at different initial concentrations $N_{\mathrm{id},0}$ for silicon irradiated with charged hadrons and with neutrons. Different markers indicate different types of devices. Data from CERN RD48/RD50 studies.

of electrons and holes in silicon, proportional to $1/\tau_{\mathrm{eff},e/h}$, increases linearly with fluence up to around $10^{15}\,\mathrm{n_{eq}/cm^2}$, where $\tau_{\mathrm{eff},e/h}$ is of order 1 ns, and then exhibits saturation [432]. Performance implications of trapping mainly reduce the charge collection efficiency and affect charge sharing among electrodes. Due to their larger drift velocity and smaller trapping probability, electron collection is favoured in irradiated silicon devices.

The safe limit on the operating voltage ultimately limits the detector lifetime. Strip and pixel detectors, specifically designed for high voltages, have been extensively operated at bias voltages of 500–600 V. The limit of operation voltage in highly energetic particle environment is set by single event effects (SEE), which occur when highly ionising nuclear fragments originating from the impinging particle cause permanent detector breakdown, happening at average electric fields approaching $\sim$12 V/µm. Sensors with columnar electrodes normal to the surface (3D-Si, Fig. 35.25) need significantly lower voltages for full depletion and are prime contenders for radiation-hard sensors.

Synthetic CVD diamond has proven strong against radiation damage due to its large bandgap (see Tab. 35.11) and strong lattice binding with a roughly twice higher threshold ($\sim$ 40 eV) for the displacement of lattice atoms than silicon (see *e.g.* [410]). Even for polycrystalline material, charge collection distances (sum of the mean free paths $\mu\tau E$ of e and h over which charges reach the electrodes) of 300–400 µm have been achieved. The cost of diamond wafers, however, is very high in comparison. Smaller-scale diamond trackers acting *e.g.* as beam monitors have been built.

GaAs has received interest as a potentially radiation-hard material in the 1990s. For particle detection, it must still be depleted from charge carriers despite comparatively small intrinsic carrier densities (see Tab. 35.11). It suffers from a strong loss in charge collection efficiency when irradiated,

dominantly because of electron trapping. Other semiconductor materials such as SiC or GaN feature wider bandgaps (3.26 eV and 3.39 eV, respectively) than Si (but smaller than diamond) and possess other suitable properties relevant to high-fluence operation, such as density, e-h ionisation energy, and displacement energies. They have regained attention after the material quality has improved much due to an industrial push coming from power devices and LEDs. So far, charge collection degrades faster with radiation fluence than for Si and diamond, however.

Strip and pixel detectors have remained functional in large detectors even at particle fluences well beyond $10^{15}\,\mathrm{n_{eq}/cm^2}$ where charge loss due to recombination and trapping becomes significant. Thin planar ($\sim$100 µm) and 3D silicon detectors have been successfully operated at fluences of 2 and $3\times10^{16}\,\mathrm{n_{eq}/cm^2}$, respectively, and measurements indicate that operation above $10^{17}\,\mathrm{n_{eq}/cm^2}$ does not seem impossible. The large SNR obtainable with low capacitance pixel structures extends the detector lifetime. The higher mobility of electrons makes them less sensitive to carrier lifetime than holes, so detector configurations that emphasize the electron contribution to the charge signal are advantageous, *i.e.* n^+ strips or pixels on p- or n-substrates. The occupancy of the defect charge states is strongly temperature dependent; competing processes can increase or decrease space charge and the required operating voltage. It is critical to choose the operating temperature judiciously (−30 °C to 0 °C in typical collider detectors) and to limit warm-up periods during maintenance. Detailed discussions of radiation damage and its effects on semiconductor detectors can be found *e.g.* in [430, 433]; an introduction to the subject is given in [1].

Tolerance against surface damage, especially in SiO_2 layers as in gates and in oxide trenches of CMOS transistor structures, largely depends on the feature size of a technology and on appropriately designed circuitry. Deep submicron technology nodes of 130 nm and 65 nm sustain total ionisation doses of up to 5 MGy (500 Mrad), corresponding to fluences of up to $5\times10^{15}\,\mathrm{cm^{-2}}$ of minimum ionising pions or protons.

35.9 Low-noise detector readout

Revised November 2025 by J. Kaplon (CERN), revised November 2021 by N. Wermes (Bonn U.)

Many detectors rely critically on low-noise readout electronics for the best energy resolution or to allow low thresholds. A typical detector front-end is shown in Fig. 35.33.

In a model relevant to most readout applications, the detector, represented by a capacitance C_d, delivers a delta-function-shaped current signal, represented by a current source in parallel. Bias voltage is applied through resistor R_b, and the signal is (often) coupled to the amplifier through a blocking capacitor C_c. The series resistance R_s represents the sum of all resistances present in the input signal path, *e.g.* the electrode resistance, connection lines, any input protection network, and parasitic series resistances in the input transistor.

The amplification stage contains the preamplifier providing gain and a pulse shaper, which tailors the overall frequency response to optimise the signal-to-noise ratio (SNR), while limiting the duration of the signal pulse to accommodate the signal-pulse rate.

Detectors are often segmented with a granularity that matches the spatial resolution requirements of the experiment. In this case, the input stage must ensure efficient readout of the charge despite the presence of parasitic capacitances between adjacent detector electrodes. In order to minimise the cross-talk to adjacent channels, a low input impedance of the preamplifier is required. The basic solution for the input stage, which effectively addresses cross-talk and ensures efficient signal collection, is the charge-sensitive amplifier (CSA). This amplifier features high open-loop gain and employs shunt-shunt feedback through an integrating capacitor C_f, along with either an active or a passive discharging circuitry (for example, resistor R_f in Fig. 35.33) to prevent saturation of this stage within the signal processing chain. The CSA gain is primarily determined by the value

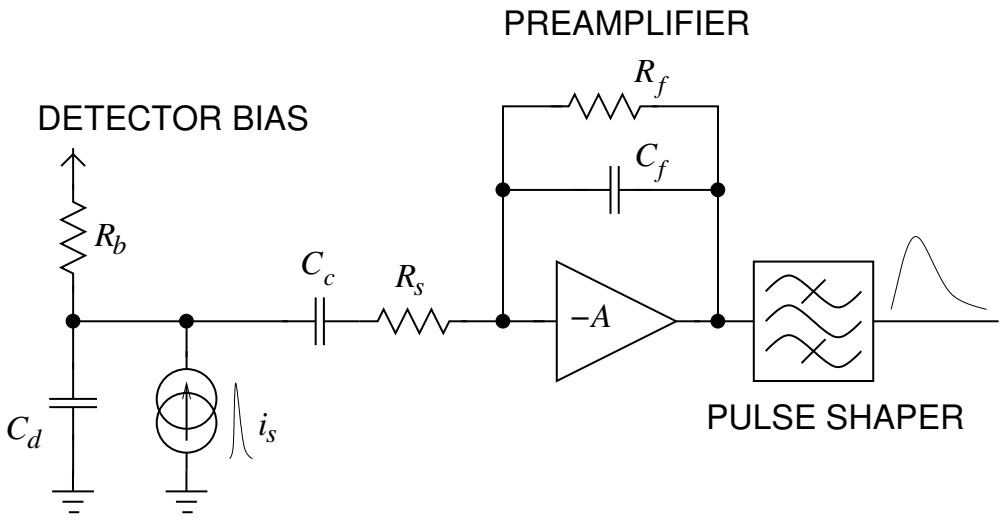

Figure 35.33: A typical front-end amplifier for a detector, with the shaper represented as an idealized band-pass filter. The operation of a charge-sensitive amplifier (CSA) relies on the feedback capacitor C_f, which determines the gain of the preamplifier.

of the feedback capacitor and does not depend on the detector capacitance.

In addition to the widely used charge-sensitive amplifiers in traditional tracking detectors, other low-noise architectures are employed for different applications. Transimpedance amplifiers (TIA) and wide-band voltage amplifiers are used when very high timing precision is required and the power budget is less constrained. Low-power voltage amplifiers are also employed in circuits with extremely low input capacitance—in the femtofarad range—where they can achieve adequate gain, avoiding significant power consumption. A typical example is monolithic active pixel sensors with small charge collection nodes. Although the following analysis focuses on the noise performance of CSA amplifiers, the applied methodology as well as conclusions *i.e.*, formulas for the equivalent input noise, are equally applicable to TIA and voltage preamplifiers working with capacitive sensors.

The classical theory of noise filtering, outlined in [434, 435] for nuclear spectroscopy systems, aims to maximise the signal-to-noise ratio, introducing the concept of the optimal noise filter. In modern high-energy physics experiments, front-end electronics must provide both amplitude measurement and precise timing requirements. Additionally, for multi-channel systems, minimizing power consumption and maintaining design simplicity are critical goals, which translates to enhanced robustness, particularly given the radiation-prone environments in which these chips typically operate. To balance performance with power consumption and design complexity, conventional band-pass filters, such as CR-$(\mathrm{RC})^{\mathrm{m}}$, are often preferred for multi-channel front-end chips. These filters consist of a differentiating stage to filter low-frequency noise, followed by m integrator stages that attenuate high-frequency components.

In high data-rate applications, avoiding CSA saturation requires a low feedback impedance, typically achieved by employing a low-value feedback resistor. In these configurations, the feedback resistor R_f and capacitor C_f usually constitute the first CR (differentiation) stage of the pulse shaper, placing the charge-sensitive amplifier in what is referred to as transimpedance mode. This mode is commonly employed in the front-end input stages of modern detector readout electronics, as it accommodates high signal rates and reduces input impedance, thereby minimising cross-talk and offering advantages over a basic CSA configuration. It is essential to note that placing the high-pass CR filter—either in the preamplifier feedback loop or within the shaper stage—has no

impact on the input noise analysis and is equivalent in terms of signal processing.

Assuming an ideal amplifier with infinite open-loop gain A and unlimited bandwidth to facilitate analysis, the Laplace-domain transfer function $H(s)$ of a charge-sensitive amplifier followed by an m-order CR-RC filter with equal differentiation and integration time constants τ is given by

$$H(s) = \frac{1}{s\,C_f}\frac{s\,\tau}{(1+s\,\tau)^{m+1}}\,, \tag{35.27}$$

where s denotes the complex frequency variable in the Laplace domain, and τ represents the time constant of the filter. The response in the time domain to the Dirac delta function of the preamplifier connected to a CR-$(\mathrm{RC})^{\mathrm{m}}$ filter is given by the formula

$$V_{out}(t) = \mathcal{L}^{-1}\Big\{H(s)\Big\} = \frac{\left(\frac{t}{\tau}\right)^m\ e^{-\frac{t}{\tau}}}{C_f\ \Gamma(1+m)}\,, \tag{35.28}$$

where $\mathcal{L}^{-1}$ is the inverse Laplace transform and Γ is the Euler Gamma-function. The signal reaches its peak at the time $t_p = m\,\tau$, commonly referred to as the shaping time. The response amplitude, G_{FE}, representing the overall gain of the processing chain, is given by

$$G_{FE} = \frac{m^m\ e^{-m}}{C_f\ \Gamma(1+m)} \tag{35.29}$$

35.9.1 *Principal noise origins*

It is useful to distinguish between noise inherent to a detector's signal amplification and processing circuitry (per channel) on the one hand, and — on the other hand — external noise sources propagated as a radiated or conducted electromagnetic interference (EMI) introduced *e.g.* by systems external to a specific readout circuit often resulting in "common-mode" noise, *i.e.* common to all channels. External noise can be introduced by power supplies, digital signal switching, RF pick-up, or effects due to "common grounding" allowing noise to couple to the current loop connecting the detector to the preamplifier. These noise sources differ from setup to setup and must be addressed individually, ideally to be eliminated. In the following, therefore, only the noise inherent to typical detector signal processing is discussed.

As principal noise origins in circuit elements, we distinguish *thermal noise*, *shot noise*, and *low-frequency* $1/f$ *noise*. Generally, noise is a fluctuation of current or voltage around a base level. Since the average value of noise is zero, noise is quantified by the variance of this fluctuation, $\langle v^2\rangle$ or $\langle i^2\rangle$. Noise sources are characterised by their power spectral densities, *i.e.*, $d\langle v^2\rangle/df$ and $d\langle i^2\rangle/df$, where f is the frequency.

Thermal noise results from the thermal random motion of charge carriers in a conductor (Brownian motion). In any conductor or resistor at a temperature $T > 0$, the random motion of electrons leads to current fluctuations giving rise to a voltage appearing across its terminals. For a resistor R, the (power) spectral density is proportional to the Boltzmann constant k and the temperature T. In electronic circuits, it can be represented either by a current or a voltage source with spectral densities given as:

$$d\langle i^2\rangle = 4\,k\,T\,\frac{1}{R}\,df \qquad\qquad d\langle v^2\rangle = 4\,k\,T\,R\,df \tag{35.30}$$

The spectral density distribution of thermal noise is 'white', *i.e.*, all frequencies contribute equally to the total noise intensity.

Shot noise arises from the discrete nature of charge carriers, creating discrete current fluctuations when crossing a potential barrier in electronic devices. Examples include fluctuations in the

current flowing through a semiconductor junction or a metal-semiconductor junction. In contrast, a simple conductor or resistor lacks such a barrier and therefore does not exhibit shot noise.

The current spectral density is described as

$$d\langle i^2\rangle = 2\,q\,I\;df\;, \tag{35.31}$$

where q is the elementary charge and I is the DC current. Shot noise also exhibits a ′white′ frequency spectrum.

Low frequency $1/f$ *noise*, also known as flicker noise, or pink noise, is a widespread phenomenon that appears not only in electronic devices but also in a variety of natural systems other than electronics. Common to all is a similar spectral density behaviour which is proportional to $1/f^{\alpha_f}$ with α_f between 0.5 and 2. In metal-oxide-semiconductor (MOS) devices, $1/f$ noise primarily arises from two mechanisms. The first involves the surface properties of the material, specifically, charge trapping and detrapping at the interface between the transistor channel and the gate insulating layer. The second mechanism, which becomes more significant in deep-submicron technologies, is due to mobility fluctuations caused by the scattering of charge carriers within the MOS channel. Enhanced surface treatment during manufacturing and the overall size of the transistor gate are key factors influencing the level of flicker noise.

35.9.2 *Noise in MOS devices*

In the following, we focus on the noise sources in MOSFETs, as the majority of front-end circuits used in today's HEP experiments are based on MOS transistor technology.

The primary noise source observed in MOSFETs is *thermal noise* in the transistor channel, which acts as a conductor. To calculate its spectral density, we employ the model proposed by Van der Ziel [436], adapted for devices implemented in integrated circuits that share a common substrate—thereby accounting for the noise contribution from the bulk transconductance g_{mb}—and operating in any inversion [8] region [437]. The current noise generator i_{nd} is placed between the drain and source of the input transistor, with its noise spectral density given by[9]

$$d\langle i_{nd}^2\rangle = 4\,k\,T\;n\;\gamma\;g_m\;df\;. \tag{35.32}$$

The noise contribution from the bulk transconductance, g_{mb}, is represented by a technology-dependent parameter n, known as the slope factor, which typically ranges from 1.25 to 1.45. It is defined as the ratio $n = (g_m + g_{mb})/g_m$, where g_m is the gate transconductance, hereafter referred to simply as transconductance.

The bias-dependent parameter γ ranges from 1/2 in weak inversion to 2/3 in strong inversion for an ideal long-channel transistor. While this assumption holds well for long-channel devices, it does not account for short-channel effects, which introduce excess noise. A practical approach to this issue is to use an excess noise factor α_w, which is usually characterised for a given technology and transistor length. In submicron technologies used today for HEP applications, transistors with channel lengths approximately twice the minimum feature size—thus avoiding short-channel

[8] Inversion in a MOS device occurs when the gate voltage attracts minority carriers to the semiconductor surface, forming a conductive channel under the gate that enables current flow between the source and drain—a fundamental principle of MOSFET operation. In strong inversion, where the gate voltage exceeds the threshold and a well-defined channel is formed, conduction is drift-dominated, and transconductance is given by $g_m = \sqrt{2\,K_p\,I_d\,W/(n\,L)}$, where K_p is the technology-dependent transconductance parameter, n is the slope factor, I_d is the drain current, and W and L are the transistor's width and length respectively. Here, g_m scales with the square root of current and depends on device dimensions. In weak inversion (sub-threshold operation), the device conducts a small diffusion-driven current even below the threshold voltage. The transconductance is given as $g_m = I_d/(n\,V_T)$, where V_T is the thermal voltage (∼26 mV at room temperature), so it scales linearly with current and is independent of transistor geometry. In the moderate inversion region (between weak and strong inversion), transconductance is typically modeled using semi-empirical interpolation functions, such as those found in the EKV model.

[9] Here and in the following, the subscript part n always denotes *noise*, whereas further subscript letters denote specifics of this noise density.

effects—typically exhibit an excess noise factor α_w below 1.1 when operating in the weak to moderate inversion region.

The next source of noise taken into account in this analysis is *1/f noise*. In the commonly used model of 1/f noise, the current noise generator is placed between the drain and source of the MOS transistor. The power spectral density is given by:

$$d\langle i_{nf}^2 \rangle = \frac{K_f}{f} \frac{g_m^2}{C_{ox}} \, df \ . \tag{35.33}$$

The technology-dependent parameter K_f is highly sensitive to the fabrication process, typically ranging from 1×10^{-24} to 1×10^{-25} Joule. Its value also depends on the device type and is typically lower for PMOS transistors. The values of K_f are also affected by transistor bias conditions and short-channel effects. C_{ox} represents the so-called gate-oxide capacitance of the transistor, defined as

$$C_{ox} = W \, L \, \frac{\varepsilon_{ox}}{t_{ox}} \ , \tag{35.34}$$

where W and L denote the gate's width and length; ε_{ox} is the permittivity of the silicon oxide, and t_{ox} represents the gate oxide thickness. Thus, the 1/f noise is inversely proportional to the transistor gate area.

Further noise nomenclature, such as *RTS (random telegraph signal) noise*, also known as burst noise or popcorn noise, is also related to its origin to trapping/detrapping processes in small MOS devices, where a single trap can cause a considerable variation in the channel current. For larger devices with many trapping centers, the popping-up nature of individual RTS bursts eventually leads to the $1/f$ noise spectral density when the noise from multiple traps with a wide range of trapping time constants is superimposed. Noise optimisation in front-end circuits typically involves using relatively large-area MOS transistors, where RTS noise is usually not observed. Consequently, the RTS noise is omitted in the following for simplicity reasons.

Another noise phenomenon observed in MOS devices at higher frequencies is known as *gate-induced current noise (GIC)*. Thermal fluctuations of current within the device channel couple to the transistor gate via the gate-oxide capacitance, resulting in an induced frequency-dependent current that acts as an additional noise source correlated with the channel thermal noise. Noise expressions for GIC have been derived in [436] for an ideal MOS transistor operating in strong inversion. Adapted to apply across all inversion regions and including also the noise contribution from the bulk transconductance, the GIC power spectral density is expressed as:

$$d\langle i_{ng}^2 \rangle = 8 \, \gamma \, k \, T \, g_g \, df \qquad \text{with} \qquad g_g = \frac{4}{45} \frac{\omega^2 \, C_{ox}^2}{n \, g_m} \ , \tag{35.35}$$

where γ and n parametrise transistor operation modes and technology features, respectively and $\omega = 2\pi f$. The correlation between channel thermal noise and gate-induced noise is given by:

$$d\langle i_{ng} \; i_{nd}^* \rangle = \frac{\gamma}{6} \, j \, \omega \, C_{ox} \, 4 \, k \, T \, df \ , \tag{35.36}$$

where j denotes the imaginary unit and i_{nd}^* is the complex conjugate of i_{nd}.

35.9.3 *Equivalent noise analysis*

The equivalent circuit used for noise analysis (Fig. 35.34) illustrates the contributions of all previously discussed noise sources at various points in the circuit.

Shot noise, arising from fluctuations in detector leakage current, is modelled as a current noise source placed at the amplifier input in parallel with the detector. Its spectral density depends

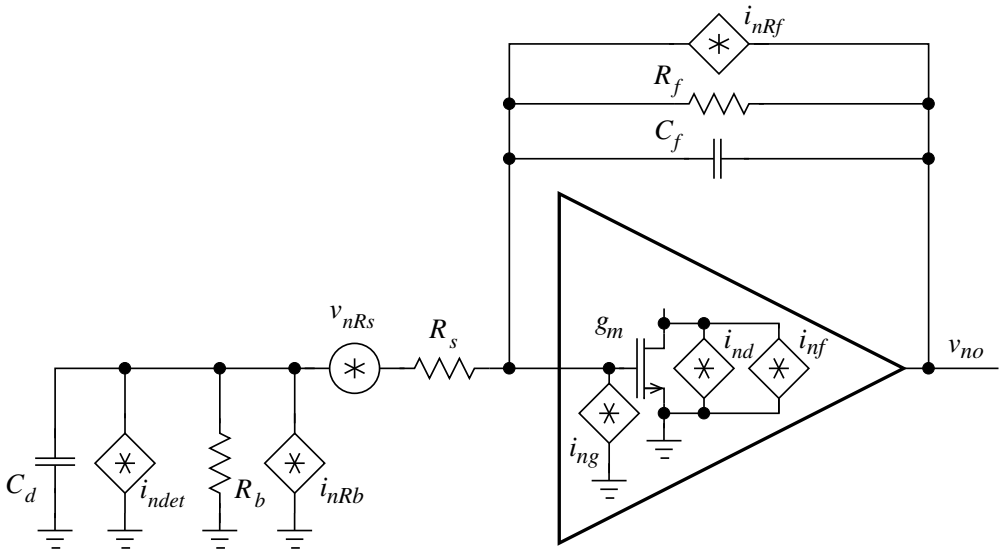

Figure 35.34: Equivalent front-end circuit diagram of the CSA showing the basic noise sources.

entirely on the magnitude of the leakage current I_{det} and can be expressed as

$$d\langle i_{ndet}^2 \rangle = 2\ q\ I_{det}\ df\ . \tag{35.37}$$

Although any voltage source in series with a resistor can be transformed into an equivalent current source in parallel with a resistor (according to Norton's theorem), it is a common practice to represent (parallel) input-shunting resistors as noise current sources and series resistors at the amplifier input as noise voltage sources. These are typically referred to as equivalent input *parallel* and *series* noise sources, respectively. The noise spectral densities for the detector bias resistor R_b (parallel noise) and the series resistor R_s (series noise) are respectively given by:

$$d\langle i_{nRb}^2 \rangle = \frac{4\,k\,T}{R_b}\,df \qquad \text{and} \qquad d\langle v_{nRs}^2 \rangle = 4\,k\,T R_s\,df\,. \tag{35.38}$$

The value of the detector bias resistor is typically chosen such that its noise contribution to the overall noise can be neglected. The feedback resistor R_f also acts as a parallel noise source. It is particularly relevant for preamplifiers operating in transimpedance mode, contributing with a noise spectral density as in Eq. (35.38) (left) with R_b being replaced by R_f.

An important noise source is the preamplifier input stage, specifically the active devices operating within the circuit. In a well-designed input stage—characterised by high gain and degenerated active loads—the dominant noise source is the input transistor. Both flicker and channel thermal current noise generators are internal to the preamplifier structure (see Fig. 35.34). To evaluate their contribution to the output noise—without requiring knowledge of the amplifier's internal details—they are represented as equivalent noise sources at the preamplifier input, exploiting the definition of the input transistor's transconductance, $g_m = \partial I_d\ /\partial V_{gs}$, where I_d and V_{gs} are drain current and gate-to-source voltage, respectively. This leads to:

$$d\langle v_{nd}^2 \rangle = d\langle i_{nd}^2 \rangle \frac{1}{g_m^2} = \frac{4\,k\,T\ n\ \gamma}{g_m}\,df \qquad \text{and} \qquad d\langle v_{nf}^2 \rangle = d\langle i_{nf}^2 \rangle \frac{1}{g_m^2} = \frac{K_f}{f\,C_{ox}}\,df\ . \tag{35.39}$$

Noise spectrum calculation is simplified by assuming that filtering takes place in the shaper stage treating the feedback resistor solely as a noise source. The CSA output noise spectral density

is obtained by accounting for all parallel and series noise sources. Series noise at the input is first converted to equivalent parallel noise via the input conductance $s\,C_{in}$, then all contributions are transferred to the output through the feedback impedance $1/s\,C_f$, yielding:

$$\frac{d\langle v_{no}^2\rangle}{df} = \frac{d\langle v_{ns}^2\rangle}{df}\,\frac{C_{in}^2}{C_f^2} \;+\; \frac{d\langle i_{np}^2\rangle}{df}\,\frac{1}{\omega^2\,C_f^2} \quad , \tag{35.40}$$

where C_{in} represents the total input capacitance (including detector capacitance C_d, input transistor gate capacitance C_g, and any additional parasitic capacitance at the preamplifier input), the term $d\langle v_{ns}^2\rangle/df$ represents the noise spectral density of any series-noise source as shown in Eq. (35.39) and Eq. (35.38) (right equation), whereas $d\langle i_{np}^2\rangle/df$ is the noise spectral density of any parallel-noise source as in Eq. (35.35), Eq. (35.37) and Eq. (35.38) (left equation). The transfer function of the CR-(RC)$^{\mathrm{m}}$ filter in the Laplace domain is given by Eq. (35.41).

$$T(s) = \frac{s\,\tau}{(1+s\,\tau)^{m+1}} \;. \tag{35.41}$$

Consequently, the RMS value of noise at the shaper output can be obtained by integrating the preamplifier output noise spectra density, coming from all partial contributions, over the entire frequency range, taking into account the frequency characteristic of the applied filter:

$$\sigma_n^2 = \int_0^\infty \frac{d\langle v_{no}^2\rangle}{df}\,\frac{\omega^2\,\tau^2}{(1+\omega^2\,\tau^2)^{m+1}}\;df \;. \tag{35.42}$$

Dividing the result by the signal gain given by Eq. (35.29) we obtain the equivalent input noise charge:

$$ENC = \frac{\sigma_n}{G_{FE}} = \sigma_n\,\frac{C_f\;\Gamma(1+m)}{m^m\;e^{-m}} \;. \tag{35.43}$$

It is convenient to perform the above integral and ENC calculation for the individual noise sources separately. Table 35.12 summarises the individual contributions to the total ENC, where the coefficients F_V, F_I, F_F, F_G, and F_C depend on the filter characteristic. The table also includes the GIC–thermal noise correlation term; however, its calculation is omitted here for brevity. In particle physics, ENC is often quoted in units of electrons (e^-) by dividing (35.43) by the elementary charge q.

For the example of a first-order CR-RC filter, the filter coefficients F_V, F_I, F_F, F_G, and F_C are evaluated to be 0.96, 0.96, 1.92, 0.41, and 0.56, respectively. Finally, the total ENC squared is obtained by the quadrature sum of the individual contributions:

$$ENC^2 = \sum_{k=1}^{7} ENC_k^2 \;. \tag{35.44}$$

The formulas in Table 35.12 show that the first three contributions from series noise sources are directly proportional to the input capacitance and, except for 1/f noise, inversely proportional to the square root of the signal shaping time. Often, the dominant contribution comes from channel thermal noise (first entry in Table 35.12). Large thermal noise contribution must be compensated by a large transconductance g_m, or longer shaping time. Since g_m is determined by both the bias current and the transistor's dimensions, the first step in optimisation of the preamplifier involves sizing the input transistor appropriately to the detector capacitance and the target bias current. Furthermore, flicker noise as well as GIC and the GIC-thermal correlation term are also affected by the transistor's dimensions through its gate capacitance. A compact model like

Table 35.12: Partial contributions to the total ENC.

k		ENC_k
1	channel thermal	$F_V \frac{C_{in}}{\sqrt{t_p}} \sqrt{\frac{4\,k\,T\,\gamma\,n}{g_m}}$
2	series resistor	$F_V \frac{C_{in}}{\sqrt{t_p}} \sqrt{4\,k\,T\,R_s}$
3	flicker	$F_F\,C_{in} \sqrt{\frac{K_f}{C_{ox}}}$
4	feedback resistor	$F_I \sqrt{t_p}\ \sqrt{\frac{4\,k\,T}{R_f}}$
5	detector leakage	$F_I \sqrt{t_p}\ \sqrt{2\,q\,I_{det}}$
6	GIC	$F_G \frac{C_{ox}}{\sqrt{t_p}} \sqrt{\frac{4\,k\,T\,\gamma}{n\,g_m}}$
7	GIC-thermal corr.	$F_C \frac{\sqrt{C_{ox}\,C_{in}}}{\sqrt{t_p}} \sqrt{\frac{4\,k\,T\,\gamma}{g_m}}$

EKV [437] is essential, providing accurate, temperature-aware expressions for transconductance and gate capacitances across all inversion regions. Finally, noise optimisation can be achieved by selecting a shaping time that balances series and parallel noise contributions (series noise decreases with longer shaping time, while parallel noise increases; see Table 35.12). This optimisation is limited by the time resolution requirements of the front-end electronics, which impose an upper bound on the shaping time. In systems with high parallel noise and low series noise, the theoretically optimal very short shaping time may be unattainable due to technological constraints, such as the transistor transit frequency that limits the maximum operational speed of the electronics. If balancing parallel and series noise sources fails to meet noise specifications, the front-end design requirements may need to be revised. Increasing the bias current of the input transistor can improve transconductance and help suppress thermal noise. If excessive parallel noise is caused by radiation-induced leakage current, it may be necessary to adjust the detector segmentation—which will also impact the contribution from series noise—or improve cooling efficiency to operate at lower temperatures.

Figure 35.35 shows an example of the noise analysis for a preamplifier designed in 130 nm CMOS technology and developed for the ATLAS ITK strip tracker (ABCStar chip). The design is intended for short silicon strips with lengths ranging from 1.8 cm to 5.5 cm, corresponding to input capacitances between 2 pF and 7 pF. The ENC is shown as a function of shaping time,

with individual contributions explicitly illustrated for two detector capacitance values representing different strip lengths. The optimal shaping time depends strongly on the detector capacitance. In

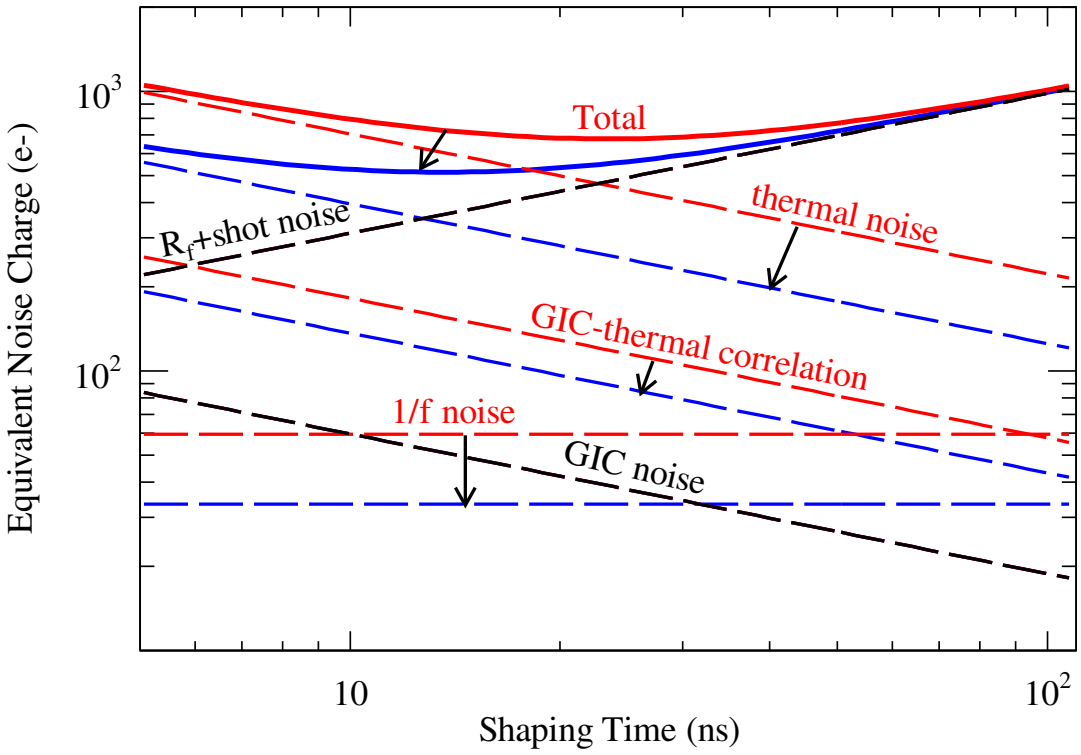

Figure 35.35: Equivalent noise charge as a function of the shaping time for the ABCstar front-end. Individual contributions include series channel thermal and 1/f noise, parallel shot and thermal R_f noise, as well as GIC noise and the GIC-thermal correlation. The contributions are shown for two detector capacitance values: 6 pF (RED traces), for which the input transistor was optimized, and 3 pF (BLUE traces), corresponding to the 2.4 cm strips. Noise contributions independent of the input capacitance, namely from the feedback resistor (105 kΩ), shot noise from detector leakage current (1 μA), and GIC noise, are shown in BLACK.

particular, the contributions from series noise, flicker noise, and the GIC–thermal noise correlation term scale with input capacitance, whereas parallel noise and GIC contributions are independent of it. In the presented example, a shaping time of 22 ns is chosen, as it meets timing requirements, optimizes noise for the longer strips, and satisfies the stricter ENC limits for shorter strips, imposed by higher expected radiation damage. Analysing the individual contributions to the ENC from various noise sources reveals that, in the example under consideration—front-end designed for high signal rates and operation in radiation environments with significant sensor leakage—the dominant noise contributors are the input transistor channel thermal noise and the parallel noise resulting from the shot noise of the sensor leakage current and the preamplifier feedback resistor. However, in low-rate, low-radiation applications where the contribution from the feedback resistor can be minimised and sensor leakage current is negligible, longer shaping times can be employed. Then, flicker noise becomes the primary factor limiting the minimum achievable noise level.

The impact of GIC noise on the front-end amplifier's overall noise performance can be as-

sessed by analysing the expressions for GIC noise and the correlation term, each normalized to the originating thermal noise. These normalised contributions are roughly $\approx 0.42\, C_{ox}/(n\, C_{in})$ and $\approx 0.58\, \sqrt{C_{ox}/(n\, C_{in})}$, respectively. It can be observed that when the front-end is connected to the sensor and $C_{in} \gg C_{ox}$, both contributions become negligible, since they combine with the thermal noise and finally with the total ENC in quadrature. In contrast, these contributions may become visible when evaluating the amplifier without a connected sensor, particularly in scenarios where the parallel noise from the feedback circuit is negligible.

35.9.4 *Timing measurements*

In timing measurements, the slope-to-noise ratio must be optimized, rather than the signal-to-noise ratio alone, so the rise time t_r of the pulse is important. The "jitter" σ_t of the timing distribution is

$$\sigma_t = \frac{\sigma_n}{(dS/dt)_{\text{trig}}} \approx \frac{t_r}{SNR}, \tag{35.45}$$

where σ_n is the rms noise, SNR the signal-to-noise ratio—defined for a CSA as the ratio of a MIP signal to the ENC—, and the slope dS/dt, *i.e.* the derivative of the signal, is evaluated at the discrimination level. The rise time of an amplifier, t_r, in the absence of a shaper, is limited by internal parasitic capacitances, which reduce its bandwidth and effectively act as a low-pass filter. Approximating the amplifier's behaviour with a CR-RC response, we find that linearly decreasing t_p leads to an ENC increase proportional to $\sqrt{t_p}$ from series noise sources, while the ENC contributions from parallel noise sources decrease (see Table 35.12). Therefore, from a jitter perspective, enhancing the amplifier's response time—even if it results in a noise increase—can be beneficial. However, preserving an adequate signal-to-noise ratio, which is critical for maintaining acceptable noise occupancy, imposes a fundamental constraint. Another undesired effect of increasing the front-end speed and input stage bandwidth will be higher susceptibility to the EMI interferences. From an EMI sensitivity standpoint, systems and detectors that employ higher-granularity sensors characterized by low parasitic capacitance offer an advantage.

For timing measurements with standard or 3D sensors, the preferred preamplifier is typically a CSA based on a buffered cascode [10] featuring high open-loop gain, operating in transimpedance mode. The rise time of the preamplifier response—more precisely, the integration time constant—is given by:

$$\tau_i = \frac{C_0}{g_m}\,\frac{C_{in}}{C_f}\,, \tag{35.46}$$

where the C_0 is the parasitic capacitance at the cascode output defining its bandwidth, g_m is the transconductance of the input transistor, C_{in} is the total capacitance at the preamplifier input and C_f is the feedback capacitance. As Eq. (35.46) shows, good timing performance can be achieved by minimizing the total input capacitance, which aligns well with the characteristics of pixel sensors. While increasing C_f can enhance timing performance, it is constrained by the requirement to maximise the stage gain, which is inversely proportional to C_f. Increasing g_m by raising the bias current improves the timing response. However, to maintain all transistors within their proper operating region, it eventually becomes necessary to increase the transistor dimensions, which in turn raises the parasitic capacitance C_0. The optimal g_m/C_0 ratio defines the maximum achievable Gain-Bandwidth-Product (GBP) of the cascode. For a given architecture, the GBP reaches a limit that can only be improved through technology scaling. The discharge time constant (τ_d), in turn, is defined by the product $R_f\, C_f$. The advantage of the CSA is that GBP optimisation can be achieved

[10] The cascode amplifier is a two-stage topology—comprising a common-source stage followed by a common-gate stage—widely used in analog design for its high gain-bandwidth product. Behaving like a single-stage amplifier, it exhibits one dominant pole, which simplifies frequency compensation in feedback systems such as charge-sensitive amplifiers. In CSA applications, the cascode topology enables the use of large input transistors—optimized for low noise—while preserving high-speed performance by suppression of the Miller effect thanks to a low input impedance of the common-gate stage.

without necessarily increasing power consumption; the transistor dimensions and bias current can be scaled down according to the power budget and noise performance requirements.

For timing measurements with low-gain sensors of a few picofarad capacitance (LGAD, [424]), a common approach is a transimpedance amplifier based on a non-buffered cascode, featuring a resistive or active load (R_l) and resistive feedback through R_f. The input impedance R_{in} is determined by the g_m of the input transistor and the resistances R_f and R_l, and is approximately given by $R_f/[g_m\,(R_l \parallel R_f)]$. In contrast to the CSA, the rise time of the TIA amplifier is independent of the input capacitance, which is a significant advantage for timing detectors using sensors with higher capacitance. The integration time constant expressed by:

$$\tau_i = C_0\ (R_l \parallel R_f)\ , \tag{35.47}$$

is instead determined by the parasitic capacitance at the cascode output C_0 and the resistance formed by the parallel combination of the feedback and load resistances. The discharge time constant is set by the input capacitance C_{in} and input impedance R_{in}. The response amplitude scales inversely with C_{in} and is amplified by the cascode gain $g_m\,(R_l \parallel R_f)$. Although the front-end amplifier is a typical TIA in topology, it behaves more like a voltage amplifier sensing current integrated on the input capacitance. This results from the resistive feedback defining a constant input impedance, while the sensor's capacitance dominates at high frequencies, presenting a lower impedance path for fast and prompt signals.

Optimal noise filtering is achieved when the integration (τ_i) and discharge (τ_d) time constants are matched, yielding a CR-RC-like shaping response. In this case, the timing jitter can be estimated by applying the ENC formulas from Table 35.12 in conjunction with Eq. (35.45). It is important to note that, to optimise the signal-to-noise ratio, the intrinsic response time of the amplifier should not be significantly faster than the rise time of the signal from the sensor. This consideration is particularly important for the TIA architecture presented here, which is capable of providing a very fast intrinsic rise time. To align the amplifier's response with the sensor signal, the practical implementations usually incorporate a switchable capacitive matrix at the cascode output, slowing down the integration time constants.

The time resolution of binary electronics with a leading-edge discriminator is limited by signal jitter and time walk, *i.e.*, timing variations due to amplitude-dependent threshold crossing. These amplitude fluctuations arise from the Landau signal distribution and charge sharing in segmented sensors. Time walk can be corrected using the time-over-threshold (ToT) value, which is correlated with pulse height. In systems with a high signal-to-noise ratio, constant-fraction discriminators can be used to provide timing information independent of signal amplitude.

35.9.5 *Digital signal processing*

The filtering principles apply to both analog and digital signal processing. In digital signal processing, the pulse shaper shown in Fig. 35.33 is replaced by an analog to digital converter (ADC) followed by a digital processor that determines the pulse shape. Digital signal processing allows great flexibility in implementing filtering functions. The software can be changed readily to adapt to a wide variety of operating conditions and it is possible to implement filters that are impractical or even impossible using analog circuitry. However, this comes at the expense of increased circuit complexity and increased demands on the ADC compared to analog shaping.

If the sampling rate of the ADC is too low, high-frequency components will be transferred to lower frequencies ("aliasing"). The sampling rate of the ADC must be high enough to capture the maximum frequency component of the input signal. Apart from missing information on the fast components of the pulse, undersampling introduces spurious artefacts. If the frequency range of the input signal is much larger than the sampling rate, the noise at the higher frequencies will be

transferred to lower frequencies and will increase the noise level in the frequency range of pulses formed in the subsequent digital shaper. The Nyquist criterion states that the sampling frequency must be at least twice the maximum relevant input frequency. This requires that the bandwidth of the circuitry preceding the ADC must be limited. The most reliable technique is to insert a low-pass filter.

The digitisation process also introduces inherent noise, since the voltage range ΔV corresponding to a minimum bit step introduces quasi-random fluctuations relative to the exact amplitude

$$\sigma_n = \frac{\Delta V}{\sqrt{12}}\,. \tag{35.48}$$

When the Nyquist condition is fulfilled, the noise bandwidth Δf_n is spread nearly uniformly and extends to 1/2 the sampling frequency f_S, so the spectral noise density is

$$\frac{\sigma_n}{\sqrt{\Delta f_n}} = \frac{\Delta V}{\sqrt{12}} \cdot \frac{1}{\sqrt{f_S/2}} = \frac{\Delta V}{\sqrt{6 f_S}}\,. \tag{35.49}$$

Sampling at a higher frequency spreads the total noise over a larger frequency range, so oversampling can be used to increase the effective resolution. In practice, this quantisation noise is increased by the ADC's differential non-linearity (DNL). Furthermore, the equivalent input noise of ADCs is often rather high, so the overall gain of the stages preceding the ADC must be sufficiently large for the preamplifier to override the ADC input noise.

35.9.6 *What to use when?*

When implemented properly, digital signal processing provides significant advantages in systems where the shape of detector signal pulses changes greatly, for example, in large semiconductor detectors for gamma rays or in gaseous detectors (*e.g.* TPCs) where the duration of the current pulse varies with drift time, which can range over orders of magnitude. Analog signal processing is best or most efficient in systems that require a fast time response, but the high power requirements of high-speed ADCs are prohibitive. Systems that are not sensitive to pulse shape can use fixed shaping time constants and rather simple filters (like CR–RC), which can be either continuous or sampled. In high-density systems that require small circuit area and low power (*e.g.*, in strip and pixel detectors), analog filtering often yields the required response and tends to be most efficient.

As stressed already in the introduction, it is important to consider that additional noise is often introduced externally. Recognising additional noise sources and minimising cross-coupling to the detector current loop is often essential to obtain the best overall noise performance. Understanding basic physics and its practical effects is important in forming a broad view of the detector system and recognising potential problems (*e.g.* modified data), rather than merely following standard recipes. More comprehensive treatments of low-noise detector readout and signal processing can be found, for example, in [1, 8, 421, 438–440].

35.10 Calorimeters

35.10.1 *Introduction*

Revised August 2023 by F. Sefkow (DESY, Hamburg) and F. Simon (KIT).

A calorimeter measures the energy and direction of particles by absorption in the detector material and registration of the energy deposited in an (ideally) contained electromagnetic (EM) or hadronic shower. Calorimeters are central components of modern high energy physics experiments, due to their ability to measure not only the energy of charged particles (with the exception of muons), but also of photons and neutral hadrons, thus enabling the reconstruction of π^0 and η

decays and of exclusive final states involving long-lived neutral kaons, or neutrons. They are indispensable for the measurement of particle jets and for the reconstruction of total event properties, which, via the measurement of missing energy (or missing transverse energy in hadron colliders). enable the detection of the presence of "invisible" particles such as neutrinos and hypothetical particles such as dark-matter candidates. Calorimeters are also important for the identification of particle species, using information on the longitudinal and transverse shape of the energy deposition to separate electrons, photons, hadrons and muons. While the performance of calorimeters is typically assessed by the quality of their energy measurements, position resolution, both for EM and hadronic showers, is also highly relevant, for example for the reconstruction of effective jet masses. The capability to measure high-level observables that serve to classify events, such as particle and jet energies, missing energy and isolated leptons, makes calorimeters central components of the trigger systems in high-energy physics experiments.

In collider experiments, the importance of calorimeters tends to increase with increasing collision energies since the relative energy resolution improves with increasing particle energy while the depth required for full containment of the showers shows only logarithmic growth with energy. This is in contrast to the precision of track-based measurements, which is decreasing with increasing momentum. With recent advances in timing capabilities calorimeters are also contributing to the rejection of pile-up from multiple interactions within the same bunch crossings at colliders.

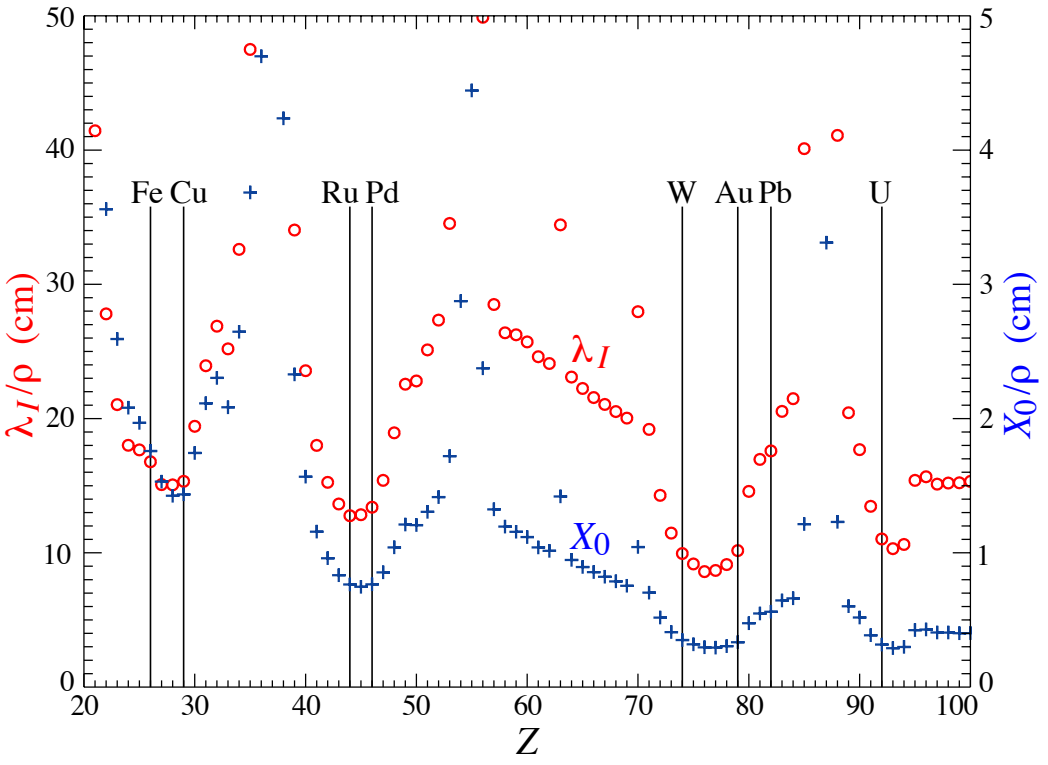

Figure 35.36: Nuclear interaction length λ_I/ρ (circles) and radiation length X_0/ρ (+'s) in cm for the chemical elements with $Z > 20$ and $\lambda_I < 50$ cm.

The characteristic length scale for EM showers is the radiation length X_0, which ranges from 1.8 cm (13.8 g cm^{-2}) in iron to 3.2 mm (6.0 g cm^{-2}) in uranium for materials used to generate showers in calorimeters.[11] Similarly, the characteristic nuclear interaction length λ_I varies from

[11] $X_0 = 120\ \mathrm{g\,cm^{-2}}\ Z^{-2/3}$ to better than 5% for $Z > 23$.

16.8 cm (132.1 g cm^{-2}) (Fe) to 11.0 cm (209 g cm^{-2}) (U).[12] There is a premium on small λ_I/ρ and X_0/ρ (both with units of length). These quantities are shown for elements with $Z > 20$ in Fig. 35.36. The minima for both X_0 and λ_I correspond to elements between W and Au. Some of these elements are very difficult to work with (e.g. W) or expensive (e.g. Au), so, depending on the application (size of the required calorimeter) other materials, such as Fe, Cu, Pb, and different alloys like brass and CuW are often chosen. For EM calorimeters high Z is preferred; here Pb is a popular choice, while W provides even higher density and is generally affordable due to the limited volume of EM systems.

Most existing calorimeters are subdivided into a front EM section (ECAL) and a hadronic part (HCAL) behind; electrons and photons are measured in the ECAL, while hadrons and jets are measured in the combined ECAL and HCAL system. The detailed design depends on energy range and performance requirements as well as on size and cost constraints for the entire system. EM calorimeters tend to be 15–30 X_0 deep, while hadronic calorimeters are usually optimised for cost and performance at 5–8 λ_I. The depth of the ECAL typically corresponds to approximately 1 λ_I, with the exact value depending on the material. This means that approximately 70% of all hadronic showers will already begin in the electromagnetic calorimeter, making its response to a hadronic cascade highly relevant for the overall performance of the system. The choice of the calorimeter technology for the ECAL is thus a result of simultaneous optimisation for EM and hadronic performance of the overall system.

Sampling calorimeters consist of a high-density, normally metallic absorber sandwiched (or threaded) with an active material which generates a signal in response to shower particles. The active medium may be a scintillator, a noble liquid, a gas, silicon, or a Cherenkov radiator. These active media all have a relatively low Z, a significantly lower density, and larger X_0 and λ_I values than typical absorber materials. The average radiation and interaction lengths in the full detector are thus larger than those of the absorber alone.

There are also *homogeneous calorimeters*, in which the entire volume contributes to the signal. Homogeneous calorimeters may be built with inorganic heavy scintillating crystals or non-scintillating Cherenkov radiators such as lead glass and lead fluoride. Nuclear interaction lengths in inorganic crystals range from 17.8 cm ($LuAlO_3$) to 42.2 cm (NaI). Materials with low X_0 used in large systems are for example BGO with $\lambda_I = 22.3\,\text{cm}$ and $X_0 = 1.12\,\text{cm}$, and $PbWO_4$ (20.3 cm and 0.89 cm). Properties of these and other commonly used inorganic crystal scintillators can be found in Table 35.5. Cryogenic noble liquids, where scintillation light and/or inonization can be detected, are also suitable materials for homogeneous detectors.

Homogeneous calorimeters at colliders are usually only used for the EM section. For the use of homogeneous calorimeters for hadron energy measurement, the large differences in the response to EM and hadronic parts of the shower are a significant challenge, as is the three-dimensional segmentation. This is still requiring substantial R&D, including the search for affordable materials. In non-accelerator physics experiments or at neutrino beams, homogeneous calorimeters, where the sensitive medium can be water or ice, scintillator, a noble liquid or the atmosphere itself, are used to detect both EM and hadronic showers.

Comprehensive tables of particle-physics calorimeters are given as Appendix C in Ref. [441].

35.10.1.1 *Energy Resolution and System Performance*

The energy resolution of calorimeters is a complex observable, due to the variety of contributing processes with different energy dependencies, and response functions often not perfectly Gaussian. Nevertheless, a simplified picture is useful in practice, and in particular for EM calorimeters also numerically accurate. For hadronic calorimeters additional complications must be taken into ac-

[12] $\lambda_I = 37.8\ \text{g cm}^{-2}\ A^{0.312}$ to within 0.8% for $Z > 15$.
See https://pdg.lbl.gov/current/AtomicNuclearProperties for actual values.

count. In such a simplified picture, due to the stochastic nature of shower evolution, the intrinsic calorimeter energy resolution, σ, is proportional to $\sqrt{E}$, as the number of charged particles, or the total ionising track length in a shower are on average proportional to the incident particle energy E. The relative resolution σ/E therefore improves with $A/\sqrt{E}$, where A denotes the so-called *stochastic term*. The readout system of the active medium will contribute noise to the resolution, $\sigma_N = B$, which in general is not energy-dependent. Effects that are proportional to the total deposited energy result in a *constant term*, $\sigma_C = C \cdot E$. Different sources contribute to this term, depending on the type of calorimeter. For both EM and hadronic calorimeters, imperfections of the detector, inhomogeneities such as density variations or those introduced by the detector mechanics, instabilities in time, imperfections of the readout or incorrect calibration of channels contribute. Shower leakage, which depends on particle energy, also contributes to the resolution with approximately linear dependence on energy. In non-compensating hadronic calorimeters, fluctuations of the EM fraction f_{em} from shower to shower, together with the energy dependence of the average f_{em} value, can lead to a significant constant term that often dominates over the instrumental effects. Adding up all contributions in quadrature yields the standard parameterisation of the relative energy resolution of a calorimeter:

$$\frac{\sigma}{E} = \frac{A}{\sqrt{E}} \oplus \frac{B}{E} \oplus C\,. \tag{35.50}$$

In particular the effects specific to hadronic showers give rise to non-Gaussian distributions of the energy response. Therefore care must be used in performance comparisons, as different parameterisations of the line shape and different definitions of the resolution are in use. In some cases, a linear rather than a quadratic addition of the stochastic and constant term may provide a better description of the energy resolution as a function of energy. It should be noted that the individual terms then lose the simplified interpretation discussed above, and care has to be taken when comparing performance based on fits to the energy dependence of the resolution.

Typically, primarily the stochastic term — which is determined by the calorimeter design in terms of material and geometry — is considered in order to describe the overall properties of a calorimeter. For the calorimeters of the multi-purpose experiments at the LHC, the stochastic terms are $3-10\%$ for electromagnetic and $50-80\%$ for hadronic calorimeters. In practice, the energy resolution of a calorimeter at high energies is limited by the constant term C, which in the EM case mainly reflects the precision and stability of the mechanical construction, electronic readout system and calibration. Typical constant terms are a few per-mil for EM and a few percent for hadronic calorimeters. For concrete examples and references see Tables 35.13 and 35.15.

For sampling calorimeters, the stochastic term depends on the *sampling fraction* $f_{\rm samp}$, i.e. the ratio of energies deposited in the active and passive material. Also the *sampling frequency* enters, which is determined by the number N of different sampling elements present in the region in which the shower develops. The stochastic term A scales approximately with $1/\sqrt{f_{\rm samp}}$, and for given $f_{\rm samp}$ and total depth, with $1/\sqrt{N}$.

While the energy resolution for single hadrons (most commonly pions) is often used as the key performance criterion for a hadronic calorimeter, it has to be noted that this value is only of limited relevance in high-energy physics experiments. In most experiments, the calorimetric measurement of hadrons is based on the combined system consisting of ECAL and HCAL. Moreover, for the physics capabilities of a detector at a high-energy particle collider, also the combined calorimetric resolution for single hadrons is not a sufficient criterion to fully characterise hadronic performance, but rather the jet energy resolution, the resolution for missing (transverse) energy, and the capability to cope with high background and pile-up levels. These quantities cannot be measured directly with prototypes in beam tests, and strongly depend on overall system aspects and reconstruction tools. However, the performance in these observables can be reliably inferred from system simulations

once the simulated response to single particles and the simulated topology of showers has been validated in detail by beam tests.

Besides energy resolution, response linearity is an important factor in the design of calorimeters. While a non-linear response for single particles can be corrected for if appropriate calibration measurements exist, such corrections deteriorate the energy resolution, in particular in the case of superposition of several showers, as it often occurs in jets. Sources for non-linearities can be intrinsic to the design, for example due to saturation effects in the active medium with increasing energy density, due to leakage, or connected to shower physics as discussed in section 35.10.3.

The energy resolution for hadrons is intrinsically limited by large event-to-event fluctuations of the shower evolution and of "invisible" components not contributing to the detector signal. It remains the limiting factor for single particles and for the high-level performance for jets and total event properties. This has motivated intense research in the past decades. One direction aims at improving the hadronic resolution by extracting additional signals to disentangle the shower composition, e.g.with so-called dual read-out methods, and is explained in the hadron calorimeter section 35.10.3. Another, so-called "particle flow" approach described below optimises the combination of measurements of individual particles in different detector components. Ideally, both methods can be combined.

35.10.1.2 *Role of Simulations*

Simulations have become indispensable for the design of detectors and the development of reconstruction algorithms. Since event-to-event fluctuations drive calorimeter performance, Monte Carlo techniques that accurately model the evolution of particle cascades in material are required. By far the most common computer code in use today is the *GEANT4* toolkit [442, 443], which provides a step-based simulation of the passage of particles through matter. Thanks to the relative simplicity of EM cascades, simulations of EM showers are typically highly accurate. The modelling of hadronic showers is more complex, and suffers from larger uncertainties. Significant improvement has been achieved in this area, moving from simpler parameterised models to physics-driven interaction models. From early on, detailed codes and data describing nuclear break-up and neutron transport like *CALOR* [444] or *FLUKA* [445,446] contributed crucially to the understanding of hadron calorimetry. The simulations reproduce the general features of the substructure of hadronic showers, characterised by dense shower activity and sparser ionising track segments, and their accuracy is adequate for most purposes of quantitative design optimisations. Details of the implementation of physics models in *GEANT4* are discussed in [447].

35.10.1.3 *Particle flow approach*

In a typical collider experiment, the EM and hadronic calorimeter system surrounds a charged-particle tracking volume devised for momentum measurement in a magnetic field. Matching tracks to calorimetric energy deposits provides corrections for the magnetic deflection of the charged particles, necessary for the reconstruction of invariant masses in multi-jet final states, or of the total momentum imbalance. Furthermore, for charged particles the track-based measurements are far more precise for particles in jets with energies of up to several hundred GeV, so using these instead of calorimeter energies may optimise the jet energy resolution. This so-called "particle flow" approach aims at reconstructing each particle individually, using a combination of the best measurements from the detector.

About 60% of the energy in a typical jet is carried by charged particles, predominantly hadrons, 30% by photons and only 10% by long-lived neutral hadrons (K_L^0 and n), for which hadronic calorimetry is unavoidable. Assuming, as motivated by detector designs proposed for a future Higgs factory, $15\%/\sqrt{E(\mathrm{GeV})}$ for photons and $55\%/\sqrt{E(\mathrm{GeV})}$ for hadrons, then, in the ideal case, where each particle is resolved, a jet energy resolution of $19\%/\sqrt{E(\mathrm{GeV})}$ could be obtained. Here

the dominant part ($18\%/\sqrt{E(\mathrm{GeV})}$) is still due to the calorimeter resolution for neutral hadrons.

The particle flow method places high demands on the imaging capabilities of the calorimeters, and on the pattern recognition performance of the reconstruction algorithms. Only energy deposits not associated with charged particles and not identified as photons, will be interpreted as neutral hadrons. In practice, this cannot always be done unambiguously, and mis-assignments give rise to an additional measurement uncertainty, which is called *confusion*. For simulated detectors at proposed future Higgs factories jet energy resolutions of 3-4% have been demonstrated, significantly larger than in the ideal case, but sufficient for the required efficient separation of W and Z hadronic final states.

Particle flow-like techniques were first applied in the ALEPH detector [448], which achieved a jet energy resolution of $60\%/\sqrt{E}$, or 6.2 GeV for hadronic Z decays. More recently, particle flow techniques are successfully used in the CMS experiment [449], for example improving the missing energy resolution by one third over a wide range.

The Pandora particle flow algorithm (PFA) [450] is the most developed and best performing today in the context of future lepton colliders. The algorithms make use of topological information, including the sub-structure of showers, as well as the compatibility of calorimetric and track-based measurements. In this way the purely calorimetric performance for the jet is either retained or improved. In the framework of studies for CLIC [451], it was shown that the required jet energy resolution of 3.5% can be achieved with the PF technique for jet energies up to 1500 GeV.

For the use of energy-momentum matching in the assignment of energy depositions, and for energy flow treatment of dense jets, particle flow calorimeters with their emphasis on imaging must still feature a good energy resolution. Furthermore, the neutral hadron energy uncertainty is the dominant contribution to the jet resolution for low energy jets, where particles are well separated, while at higher energies the confusion effects take over.

High granularity in all three space dimensions comparable to or smaller than the length scales of particle showers given by X_0 and ρ_M for both ECAL and HCAL brings additional advantages; for example it offers ideal conditions for the application of software compensation methods, which improves the intrinsic resolution and also reduces "confusion" [452]. A particular strength is the possibility to use topological information such as the reconstructed starting point of the shower for the estimation of leakage. Moreover, the combination of fine-grained topological reconstruction and cuts on cluster-wise timing with a precision of few tens of pico-seconds allows for powerful pile-up rejection. This extends the application range of particle flow methods towards collider environments with less benign background conditions, like multi-TeV e^+e^- collisions, and it is an asset on its own for high-intensity hadron colliders, even if particle flow methods are difficult to apply.

The performance of highly granular calorimeters depends, among others, on the particle separation and pattern recognition capabilities and on the single particle energy and timing resolution. They are thus not only optimised for energy measurement, but also for multi-dimensional shower reconstruction and particle separation in space and time. The potential of such calorimeters can be further enhanced by combining a fine spatial segmentation with maximised information on energy, time, and possibly the nature of the energy deposition, for example by using dual-readout methods. This may be achieved, for example, by combining multiple optical materials sensitive to different components in the shower in finely segmented sandwich calorimeters, or by using timing information to extract the position of the energy deposition along a fibre. For future collider experiments, different approaches based on silicon, scintillator, noble liquid, fibre and crystal readout are being pursued [453]. They all foresee, with different level of emphasis, high granularity to enable the application of particle flow methods, and in some cases to further enhance their performance by additional information not exploited in current algorithms. One such example is the proposal [454]

to benefit from the superior electromagnetic energy performance of crystals to pair photons from π^0 decays and thereby resolve jet finding ambiguities to improve the jet energy resolution.

35.10.2 *Electromagnetic calorimeters*

Revised August 2025 by C.L. Woody (BNL) and R.-Y. Zhu (HEP California Inst. of Technology).

The development of electromagnetic showers is discussed in the section on "Passage of Particles Through Matter" (Sec. 34 of this *Review*). Formulae are given which approximately describe average showers, but since the physics of electromagnetic showers is well understood, a detailed and reliable Monte Carlo simulation is possible. EGS4 [455] and GEANT [442] have emerged as the standards.

Table 35.13: Resolution of typical electromagnetic calorimeters. E is in GeV.

Technology (Experiment)	Depth	Energy resolution	Date
NaI(Tl) (Crystal Ball)	$20X_0$	$2.7\%/\mathrm{E}^{1/4}$	1983
$Bi_4Ge_3O_{12}$ (BGO) (L3)	$22X_0$	$2\%/\sqrt{E} \oplus 0.7\%$	1993
CsI (KTeV)	$27X_0$	$2\%/\sqrt{E} \oplus 0.45\%$	1996
CsI(Tl) (BaBar)	16–$18X_0$	$2.3\%/E^{1/4} \oplus 1.4\%$	1999
CsI(Tl) (BELLE)	$16X_0$	1.7% for $E_\gamma > 3.5$ GeV	1998
CsI(Tl) (BES III)	$15X_0$	2.5% for $E_\gamma = 1$ GeV	2010
$PbWO_4$ (PWO) (CMS)	$25X_0$	$3\%/\sqrt{E} \oplus 0.5\% \oplus 0.2/E$	1997
$PbWO_4$ (PWO) (ALICE)	$19X_0$	$3.6\%/\sqrt{E} \oplus 1.2\%$	2008
Lead glass (OPAL)	$20.5X_0$	$5\%/\sqrt{E}$	1990
PbF_2 (g-2)	$15X_0$	$3.6\%/\sqrt{E} \oplus 1.9\%$	2019
Liquid Kr (NA48)	$27X_0$	$3.2\%/\sqrt{E} \oplus 0.42\% \oplus 0.09/E$	1998
Scintillator/depleted U (ZEUS)	20–$30X_0$	$18\%/\sqrt{E}$	1988
Scintillator/Pb (CDF)	$18X_0$	$13.5\%/\sqrt{E}$	1988
SciFi/Pb spaghetti (KLOE)	$15X_0$	$5.7\%/\sqrt{E} \oplus 0.6\%$	1995
SciFi/W (sPHENIX)	$20X_0$	$13\%/\sqrt{E}$	2022
Liquid Ar/Pb (NA31)	$27X_0$	$7.5\%/\sqrt{E} \oplus 0.5\% \oplus 0.1/E$	1988
Liquid Ar/Pb (SLD)	$21X_0$	$8\%/\sqrt{E}$	1993
Liquid Ar/Pb (H1)	20–$30X_0$	$12\%/\sqrt{E} \oplus 1\%$	1998
Liquid Ar/depl. U (DØ)	$20.5X_0$	$16\%/\sqrt{E} \oplus 0.3\% \oplus 0.3/E$	1993
Liquid Ar/Pb accordion (ATLAS)	$25X_0$	$10\%/\sqrt{E} \oplus 0.4\% \oplus 0.3/E$	1996

Electromagnetic calorimeters are devices that are designed to measure the total energy of electrons and photons by total absorption. They come in two general categories: homogeneous and sampling. In a homogeneous calorimeter, all of the particle's energy is deposited in the active detector volume and is used to produce a measurable signal (either scintillation light, Cherenkov light or charge). Homogeneous electromagnetic calorimeters are typically constructed using high density, high Z inorganic scintillating crystals such as BaF_2, BGO, CsI, CsI(Tl), LYSO, NaI(Tl) and PWO, non-scintillating Cherenkov radiators such as lead glass and lead fluoride (PbF_2), or ionizing noble liquids such as liquid argon, liquid krypton or liquid xenon. The properties of some commonly used inorganic crystal scintillators can be found in Table 35.5. Total absorption homogeneous calorimeters, such as those built with heavy crystal scintillators, provide the best energy

resolution for measuring electromagnetic showers and are generally used when the best possible performance is required, particularly at lower energies. Attention, however, needs to be paid to radiation damage in inorganic scintillators when exposed to the typical environment of high luminosity proton colliders, as discussed below and in Section 35.4. In addition, it is often challenging to achieve high segmentation with homogeneous radiator materials, both longitudinal and transverse, which is necessary for techniques such as particle flow analysis.

A sampling calorimeter consists of an active medium which generates a signal and a passive medium which functions as an absorber. In this case, most of the particle's energy is deposited in the absorber and only a fraction of the energy is detected in the active medium. The ratio of energy in the sampling medium to the total enegy in calorimeter is called the sampling fraction. The active medium may be a scintillator, an ionizing noble liquid, a semiconductor, or a gas ionization detector. The absorber is typically a heavy metal with a high Z such as lead, tungsten, iron, copper, or depleted uranium. The active material is interspersed with the passive absorber in a variety of ways, e.g. by using alternating plates of active material and absorber, or embedding the active material, such as scintillating fibers, into the absorber.

The main difficulty in this approach is extracting the signal from the active material. One possibility is a simple stack of alternating absorber and active material. However, this usually leads to gaps for the readout and services and hence non-uniformities. This can be improved by using a so-called "spaghetti" design, where scintillating fibers are brought to the front or back of the detector and read out. This can also be done with either wavelength shifting plates or fibers, such as in a so-called "shashlik" design where wavelength shifting fibers run through the stack of alternating scintillator and absorber plates and are read out at one or both ends, or embedding wavelength shifting fibers in the scintillating plates which are then brought out to the edges or back of the detector and read out. Another similar design is the Tungsten SciFi (W/SciFi) configuration, which consists of a matrix of tungsten powder and epoxy with embedded scintillating fibers that are brought out to the back and form a bundle that is read out with silicon photomultipliers (SiPMs). This design was utilized for the sPHENIX EMCAL at RHIC and will be used for the Forward EMCAL for the ePIC Experiment at the EIC.

For sampling calorimeters that use ionizing liquids as the sampling medium, there is also an "accordion" design which avoids all gaps for services, where the absorber plates are folded into an accordion shape along with interspersed electrodes to collect the ionization charge [456]. While these readout schemes are generally more complicated than those for homogeneous calorimeters, the sampling calorimeter design allows more flexibility in terms of segmentation and the construction of very large calorimeters at much lower cost than homogeneous calorimeters.

The energy resolution σ_E/E of a calorimeter can be parameterized as $a/\sqrt{E} \oplus b \oplus c/E$, where $\oplus$ represents the square root of the sum in quadrature of the three terms, and E and σ_E are in GeV. The stochastic term a represents statistics-related fluctuations such as intrinsic shower fluctuations, photoelectron statistics, dead material at the front of the calorimeter, and sampling fluctuations for minimum ionizing particles. For a fixed number of radiation lengths, the stochastic term a for a sampling calorimeter is expected to be proportional to $\sqrt{t/f}$, where t is plate thickness and f is sampling fraction [457–459]. The stochastic term a is typically of the order of a few percent for a homogeneous calorimeter, and is generally in the range of 8 to 20% for sampling calorimeters, depending on the sampling fraction.

The main contributions to the systematic, or constant, term b are detector non-uniformity and calibration uncertainties. In the case of hadronic cascades discussed below, non-compensation also contributes deviations from $\sqrt{E}$ scaling. Another important contribution to the energy resolution of calorimeters that are used in high radiation environments such as high lumnosity colliders is radiation damage of the active medium. Radiation damage can induce optical absorption in scin-

tillating materials which reduces the measured light output and produces non-uniformities in light collection. This can be mitigated by developing radiation-hard active media [460], by reducing the signal path length [461] and by frequent *in situ* calibration and monitoring [103, 459]. With effort, the constant term b can be reduced to below one percent. The term c is due mainly to electronic noise summed over the readout channels required to measure the shower energy (typically a few Molière radii).

The position resolution depends on the effective Molière radius and the transverse granularity of the calorimeter. Like the energy resolution, it can be factored as $a/\sqrt{E} \oplus b$, where a is the stochastic term, typically of the order of a few mm to 20 mm, and b can be as small as a fraction of mm for a dense calorimeter with fine granularity. Fine granularity also helps particle flow analysis discussed in the hadron calorimeters section below.

Electromagnetic calorimeters may also provide angular and pointing measurements for electrons and photons. This is particularly important for photon-related physics to identify the correct primary vertex, since photons are not detected by the tracking system of the overall experiment. The typical photon angular resolution is about 45 mrad$/\sqrt{E}$, which can be achieved by implementing longitudinal segmentation [456] for a sampling calorimeter or by adding a preshower detector [462] for a homogeneous calorimeter without longitudinal segmentation.

There have been many electromagnetic calorimeters built and used in particle physics experiments for a variety of applications. Table 35.13 provides a short list of the major ones used in some of the larger experiments. Also listed are calorimeter depths in radiation lengths (X_0) and the achieved energy resolution. Whenever possible, the performance of the calorimeters *in situ* is quoted, which is usually in good agreement with prototype test beam results as well as EGS or GEANT simulations, provided that all systematic effects are properly included. Details about detector design and performance can be found in Appendix C of reference [459] and Proceedings of the International Conference series on Calorimetry in High Energy Physics.

35.10.3 *Hadronic calorimeters*

Revised August 2025 by F. Sefkow (DESY, Hamburg) and F. Simon (KIT).

Hadronic calorimetry [441, 463, 464] is considerably more complex than electromagnetic (EM) calorimetry due to the wider range and different nature of physical processes contributing to shower development and energy deposition, which in turn are characterised by different length and time scales. Hadronic showers are initiated by inelastic strong interactions of highly-energetic charged and neutral hadrons with atomic nuclei. These interactions result in the production of secondary particles, which drive the development of the shower. Among these are energetic hadrons, as well as lower-energy nucleons, photons and nuclear fragments. Energy transferred to nuclear break-up, excitation or recoil does not, in general, produce a signal, but remains *invisible*, and event-to-event fluctuations of this invisible energy deposit ultimately limit the resolution of hadronic calorimeters (HCALs).

The length scale of the interaction of relativistic hadrons is given by the nuclear interaction length λ_I. As discussed in Section 35.10.1, λ_I is a factor 10 to 30 larger than X_0 for common materials used in the construction of calorimeters. HCALs thus require a significantly larger geometrical depth for full containment than electromagnetic calorimeters (ECALs), albeit not by the factor suggested by the ratio of λ_I/X_0 due to the different nature of the showers. A key role is played by the production of π^0s and their subsequent decay into two photons. These result in the formation of electromagnetic sub-showers which evolve on the scale given by the radiation length X_0, and thus require sufficiently fine sampling of the shower activity to capture also this electromagnetic component. The two different length scales occurring in hadronic showers, and the large fluctuations of hadronic, electromagnetic and invisible activity, result in significant event-to-event

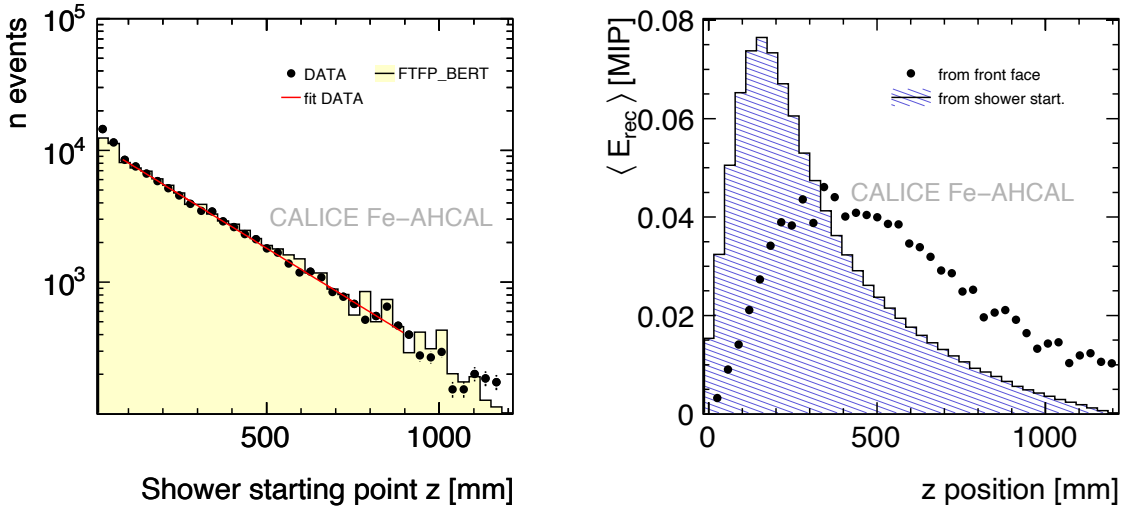

Figure 35.37: Longitudinal profile of hadronic showers induced by 45 GeV negative pions measured in he CALICE highly-granular steel-scintillator sampling calorimeter [465]. Left: Reconstructed position of the first inelastic interaction, compared to simulations (GEANT4 9.4p03, FTFP_BERT), and an exponential fit yielding a slope consistent with the expected pion interaction length. Right: Longitudinal shower profile measured from the front face of the calorimeter (dots, without corrections for dead cells) and relative to the position of the shower start given by the first inelastic interaction (filled histogram). The visible energy is given in units of the most probable energy loss of a minimum-ionizing particle (MIP). The integrals of the distributions are normalized to unity.

variations of the energy response and of the shower topology. This topology is characterized by a lumpy structure, with compact regions of high local energy density originating from electromagnetic sub-showers, and sparser hadronic activity with minimum-ionizing hadrons.

Figure 35.37 (left) shows the distribution of the longitudinal position of the first inelastic interaction measured for pion-induced hadronic showers with the highly-granular scintillator-steel HCAL of the CALICE collaboration [465]. The figure illustrates the exponential distribution, with a slope consistent with the pion interaction length expected from the geometry and material composition of the calorimeter. This distribution is well reproduced by simulations using GEANT4 [442, 447]. Figure 35.37 (right) shows the mean longitudinal shower profile, given by the mean energy deposition in each calorimeter layer, both relative to the front face of the calorimeter (dots, without corrections for dead cells) and relative to the measured shower starting point given by the first inelastic interaction (filled histogram). The latter is much more compact than the former, which is a convolution of the latter with the distribution of shower starting point shown in the left panel of the figure. This shows that the detector depth required for adequate shower containment is significantly influenced by the fluctuations of the position of the first hadronic interaction. Detection of this position allows for an estimate of leakage from a finite calorimeter volume, and it enables stringent tests of shower evolution models. In the past years, motivated by precision needs at the next generation of e^+e^- colliders, the CALICE collaboration has constructed a number of prototypes with high 3-dimensional spatial granularity and recorded large sets of data at test beams, allowing for studies of shower evolution processes in unprecedented detail. The refined simulations support the trend to proceed from research focused on understanding the global intrinsic properties of showers, e.g. for the purpose of compensation, towards the study of detailed information, in space, time, and energy deposition type, through many and multiple readout channels.

In an inelastic hadronic collision a significant fraction f_{em} of the energy is removed from further hadronic interaction by the production of secondary π^0/η's, whose decay photons generate high-energy electromagnetic showers. Charged secondaries ($\pi^{\pm}$, p, ...) deposit energy via ionization and excitation, but also interact with nuclei, producing evaporation neutrons, spallation protons and neutrons, and heavier spallation fragments. The charged collision products produce detectable ionization, as do the showering γ-rays from the prompt de-excitation of highly excited nuclei. The recoiling nuclei generate little or no detectable signal, as mentioned previously. The neutrons lose kinetic energy in elastic collisions which generate ionization signals via recoiling protons, thermalize on a time scale of several μs, and are finally captured, with the production of more γ-rays—usually outside the acceptance gate of the electronics. Between endothermic spallation losses, nuclear recoils, and late neutron capture, a significant fraction of the hadronic energy (20%–40%, depending on the absorber and energy of the incident particle) is used to overcome nuclear binding energies and is therefore lost or "invisible."

In a hadron-nucleus collision a large fraction of the incident energy is carried by a "leading particle" with the same quark content as the incident hadron. If the projectile is a charged pion, the leading particle is usually a pion, which can be neutral and hence contributes to the EM sector. This is not true for incident protons. The result is an increased mean hadronic fraction for incident protons.

The complexity of hadronic showers also has a significant impact on the energy measurement. In contrast to EM showers, hadronic cascade processes are characterised by the production of relatively few high-energy particles. The number multiplicity of these particles produced in hadronic interactions increases only logarithmically with energy. The lost energy and f_{em} are highly variable from event to event, and on average increase with increasing energy [466]. Electromagnetic sub-showers typically result in a higher response than the hadronic parts of the cascade, where undetectable energy loss due to nuclear dissociation, the long time scales and the material dependence of neutron signals, as well as other effects reduce the measured signal. This difference in response is often expressed by the $\langle h/e \rangle$ ratio, a calorimeter-dependent quantity which is smaller than unity for many, but not all, HCALs. The increase of the electromagnetic fraction with energy thus introduces a non-linear contribution to the response. Combined with the significant event-by-event fluctuations between electromagnetic and hadronic fractions of the showers and between different hadronic processes the non-equality of h and e deteriorates the energy resolution of HCALs. Different strategies to address this exist, as discussed further below.

Most large HCALs are parts of complex 4π detectors at colliding beam facilities. To date, all these HCALs are sampling calorimeters. This choice is imposed by the physics of hadronic showers, both by the required depth for containment which favours high-density materials with short λ_I, and by the differences in response to electromagnetic and hadronic parts of the cascade, which are particularly severe for homogeneous calorimeters. Common absorber materials are Fe, Cu, Pb, and U, with W also used occasionally. A large variety of different active materials are used, depending on application and optimisation, from plastic scintillators (plates, tiles, bars, fibers), crystals and Cherenkov media, silicon, liquid argon (LAr), to gaseous detectors. The energy loss of particles in the active medium is either detected directly by collecting charge, or via scintillation or Cherenkov light observed with conventional photomultipliers (PMTs), photodiodes or silicon photomultipliers (SiPMs). The choice of both active and passive materials is driven by different, sometimes conflicting, constraints, including performance requirements, space and other mechanical boundary conditions, radiation tolerance, and cost considerations.

A wide range of different geometries of absorbers and sensors is used, with design choices depending on the chosen priorities of addressing these constraints, also considering the need to bring

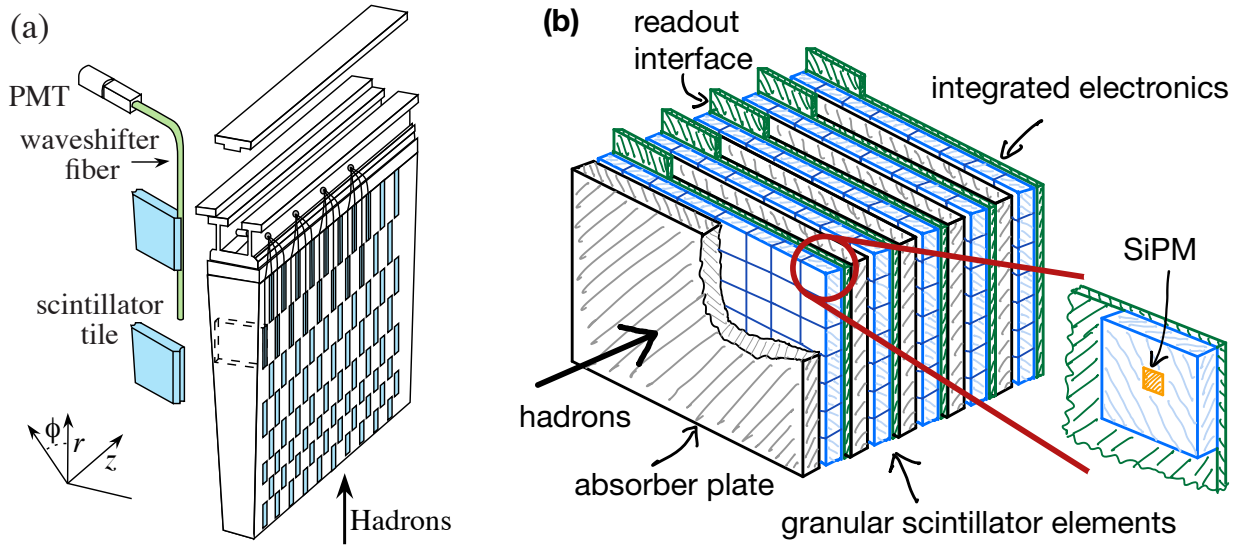

Figure 35.38: Two examples of geometrical structures of scintillator-based HCALs. (a) A wedge of the ATLAS central tile calorimeter consisting of scintillator tiles in iron, read out via wavelength-shifting fibers and PMTs [467]. The coordinate system is that of the ATLAS calorimeter within the experiment, with the z axis along the beam direction, r pointing radially outward, and ϕ being the azimuthal angle. (b) An illustration of the "SiPM-on-tile" structure used in the CALICE analogue HCAL prototype, and in the CMS High-Granularity Calorimeter (HGCAL), highly granular calorimeters with steel absorbers and small scintillator tiles directly read out via SiPMs with embedded electronics [464, 468–470].

the signals to the outside of the detector while achieving a hermetic coverage and other constraints. In this context it is important to note that a classic sandwich structure with absorber plates and active elements approximately perpendicular to the particle incidence is not required, and arbitrary orientations are viable for good calorimetric measurements, as long as channelling, meaning the extended passage of primary particles through low-density active regions, is excluded. Figure 35.38 shows two examples of plastic scintillator-based calorimeters to illustrate differences in design between coarsely-segmented and highly-granular calorimeters. The ATLAS tile calorimeter [467] uses scintillator tiles coupled to wavelength-shifting fibers which collect the light from the tiles and guide them to PMTs outside of the active region of the calorimeter. The calorimeter is segmented in ϕ (azimuthal angle) and η (pseudorapidity, defined as $\eta = -\ln\tan(\theta/2)$, where θ is the angle relative to the beam axis), with coarse longitudinal segmentation. The technological prototype of the CALICE analog HCAL, a highly granular SiPM-on-tile calorimeter is based on scintillator tiles directly coupled to SiPMs, which, together with the front-end electronics, are embedded inside of the the active volume of the calorimeter. The CMS HGCAL [470] uses the same concept in part of the detector, and in addition embeds elements for digital data concentration and power distribution in the active volume. Other detector solutions include scintillating fibres threading an absorber [471], liquid-argon-filled tubes [472] and the "accordion" LAr detector [473]. The latter has zig-zag absorber plates to minimize channeling effects; the calorimeter is hermetic (no cracks), and plates are oriented so that cascades cross the same plate repeatedly.

In particular, but not exclusively, the combination of heavy absorber materials (Pb, U) with plastic scintillators allows the construction of HCALs that have a near-equal response to electromagnetic and hadronic parts of the cascade, so-called compensating calorimeters [474]. In this first

study, it was recognized that nuclear fission can amplify the hadronic signal when using uranium absorbers. However, the key drivers of compensation are the reduction of the electromagnetic response with high-Z absorbers and an increased sensitivity to neutrons, which are strongly correlated to otherwise invisible energy loss due to nuclear dissociation, with a hydrogeneous active medium [475–479]. Since the electromagnetic cross section increases, and the critical energy decreases with Z, and since most of the energy of an electromagnetic shower is deposited by low-energy, short-range electrons, a disproportionate fraction of the total electromagnetic energy is deposited in the absorber in the high-Z case. Hydrogenous active media, such as organic scintillators, have a high sensitivity to spallation neutrons via elastic $n-p$ scattering. The number of produced neutrons is highly correlated with the invisible energy of the hadronic cascade. Increasing the sensitivity to these particles can thus boost the visible hadronic signal. Achieving compensation requires carefully-chosen sampling fractions and frequencies, with the response to the hadronic parts of the shower also sensitive to the integration time of the electronics due to the time structure of the neutron component of the signal.

Since Cherenkov light, for example in quartz plates or fibers, or in crystals, is produced only by relativistic particles in the cascade and thus predominantly by the electromagnetic component of the shower, such media are less common in hadronic than in ECALs. Notable exceptions are applications that require high radiation tolerance, and dual-readout calorimeters which specifically exploit this feature, as discussed below.

Silicon offers high compactness, high granularity, high radiation tolerance, long-term stability and fast charge collection, and is thus an interesting active material for sampling calorimeters. A thorough overview of the development and of the features of this technology can be found in a recent review paper [480]. The first silicon-based calorimeter in a collider experiment was a HCAL, the H1 PLUG calorimeter [481] covering the very forward region of the H1 experiment at HERA. The SICAPO collaboration has demonstrated the conceptual possibility of constructing compensating HCALs using silicon sensors [482]. Silicon is currently the technology of choice for several ECALs for future Higgs factories [483–485]. It is also being used extensively in the CMS HGCAL [470] in both electromagnetic and hadronic sections, complemented by scintillator tiles with on-tile SiPM readout where the radiation levels allow.

More generally, high-granularity calorimeters play an increasingly important role, in particular motivated by the use of particle-flow algorithms for global event reconstruction (see Section 35.10.1). The associated technologies for both electromagnetic and HCALs have been pioneered by the CALICE collaboration, which has built and tested an increasingly sophisticated series of "imaging" calorimeters with a highly granular readout [486]. In the area of HCALs, this includes the scintillator-based analog HCAL [487] with the latest SiPM-on-tile technological prototype with fully-integrated electronics having approximately 22,000 channels [468,469], as well as digital [488] and semidigital [489] calorimeters using gas detectors, such as RPCs (Sec. 35.6.6) and micropattern gas detectors (Sec. 35.6.3), with channel counts of up to 500,000. The large numbers of channels of high-granularity calorimeters presents a significant integration challenge for full detector systems, and requires the full integration of the front-end electronics inside of the active volume of the detector, as well as very compact data concentration and interface units. The first such detector in construction for a collider experiment is the CMS HGCAL [470]. Beam tests with a combined prototype using both silicon and scintillator-SiPM instrumented active layers have confirmed simulation-based expectations [490]. The timing resolution is found to be 60ps for single-channel measurements and better than 20ps for full showers at the highest energies [491], setting excellent perspectives for the HGCAL calorimeter performance at the HL-LHC. The total silicon area of the full HGCAL amounts to about 600 m^2, and about 240,000 SiPMs are foreseen. The calibration of such calorimeters requires the monitoring of a large number of cells, which is achieved in-situ using

reconstructed track segments within hadronic showers [470,492] or externally identified muons. For this method, the capability to detect the most probable energy loss of a minimum-ionizing particle in a single cell is essential. This is required over the full lifetime of the detector, also after the active elements have received significant radiation damage, resulting in increased noise and reduced charge or signal collection efficiency. Due to the large number of cells contributing to the measurement of one shower, the requirements on the precision of the calibration of individual cells is relaxed relative to the global energy calibration of the calorimeter.

The energy resolution of HCALs is severely affected by fluctuations between different components of the cascade, exacerbated by differences in response to purely hadronic and to electromagnetic sub-showers. In many detectors, fluctuations in the electromagnetic energy fraction, f_{em}, and the related, consequential variations in nuclear energy dissociation losses, represent the biggest single contribution to the hadron energy resolution. One strategy to address this problem is the construction of intrinsically-compensating calorimeters, which imposes stringent constraints on materials and geometries as discussed above. Compensating calorimeters are not used in current large collider experiments, and are at the moment not considered for future collider detectors. Two different strategies are presently followed to improve the energy resolution in non-compensating calorimeters: Offline weighting or software compensation in longitudinally-segmented or in highly-granular calorimeters; and dual-readout calorimetry.

Software compensation and *Machine Learning* techniques exploit the fact that electromagnetic sub-showers typically have a higher spatial density than the purely hadronic parts of the cascade. Amplitude (or energy-density) dependent weights are applied in the reconstruction to reduce the effects of shower-to-shower fluctuations. These techniques were pioneered by the CDHS collaboration for a longitudinally segmented steel-plastic scintillator calorimeter [493], where an improvement of the energy resolution of 10% (at 10 GeV) to 30% (at 140 GeV) for charged pion showers was achieved. Similar techniques were successfully applied in the H1 [494] liquid argon calorimeter system resulting in a stochastic term of $51\%/\sqrt{E}$, and in the ATLAS [495] endcap calorimeters, also based on liquid argon, with an energy resolution of $84\%/\sqrt{E}$. Inspired by these approaches, a software compensation technique using the detailed spatial information provided by highly-granular calorimeters of the CALICE collaboration has been developed, achieving up to 25% improvement of the energy resolution compared to the resolution without software compensation, resulting in a stochastic term of $45\%/\sqrt{E}$ [496] in a scintillator tile calorimeter with steel absorbers. This technique has also been successfully transferred to particle-flow reconstruction [497], resulting in an improvement of the jet-energy resolution in simulated events by 8% - 15%, depending on jet energy. Highly-granular calorimeters with software compensation and particle-flow reconstruction are currently studied as the baseline configuration for several Higgs-factory detectors.

The wealth of detailed information provided by highly granular calorimeters with timing capabilities suggests the application of machine learning (ML) methods to optimise their performance. Using test beam data collected with CALICE and CMS HGCAL prototypes, significant improvements have been demonstrated for the hadron shower energy resolution [498,499] as well as for the separation of showers [500] in multi-particle events for particle flow reconstruction.

The *dual-readout method*, originally proposed by Mockett in 1983 [501], measures f_{em} event by event in parallel to the total deposited energy. It uses the fact that most of the relativistic particles in the shower originate from the electromagnetic part, and that only those produce Cherenkov light, while the signal of the hadronic part is mostly due to non-relativistic protons. In practice either two different active media, e.g. scintillator and quartz, are used to register scintillation and Cherenkov light, respectively, or the optical signals from the two processes occurring in heavy crystals are disentangled, using their different spectral, directional or timing properties.

The Cherenkov and scintillation signals, normalised to the response for electrons, are given by

$$C = [f_{\rm em} + (h/e)_C(1 - f_{\rm em})]E\,, \tag{35.51}$$
$$S = [f_{\rm em} + (h/e)_S(1 - f_{\rm em})]E\,, \tag{35.52}$$

respectively, which can be solved for the fraction $f_{\rm em}$ and the energy

$$E = (\xi S - C)/(\xi - 1)\,, \tag{35.53}$$

where $\xi = [1 - (h/e)_C]/[1 - (h/e)_S]$ and $(h/e)_{C,S}$ denote the average ratios of hadronic to electromagnetic response in the Cherenkov and scintillator parts, respectively. This is illustrated in Figure 35.39, which shows their correlation for a set of simulated negative pion events [502] using FLUKA [446].

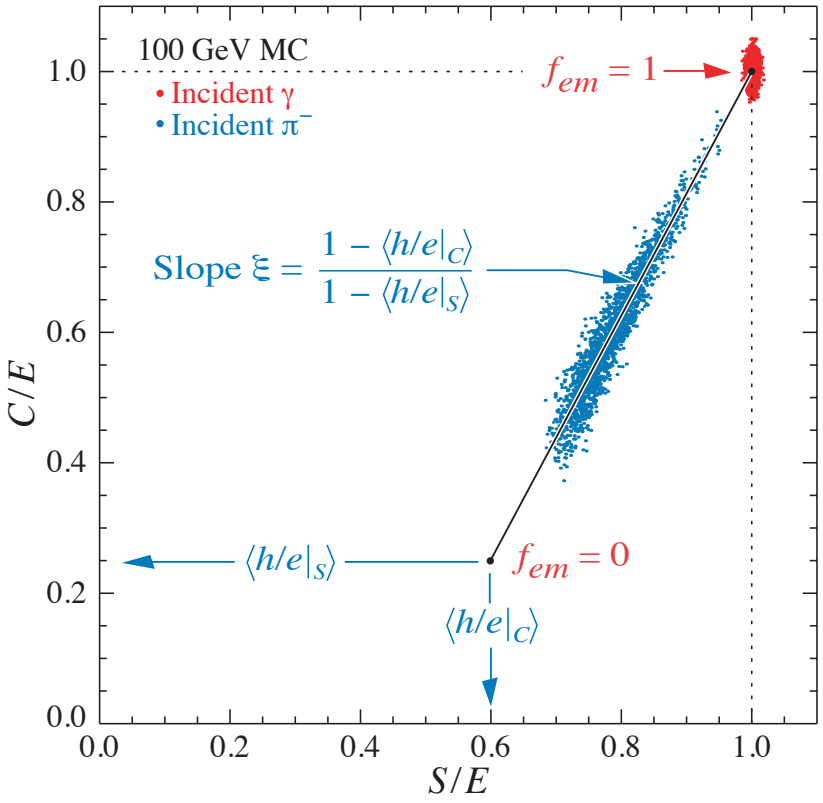

Figure 35.39: Scatter plot of Monte Carlo C/E (Cherenkov) vs S/E (scintillator) signals for individual events in a dual-readout calorimeter for 100 GeV negative pions and photons. Hadronic events are shown in blue, and scatter about the indicated event locus. Electromagnetic events cluster about $(C/E, S/E) = (1,1)$. In this case worse resolution (fewer p.e.'s) was assumed for the Cherenkov events, leading to the "elliptical" distribution.

It was noted that the method demands a steep slope ξ, which implies that the scintillator readout should be as compensating as possible, which however reduces the room for improvement by adding Cherenkov information.

The method was tested by the DREAM/RD52 collaboration [503, 504], using a 1 ton copper matrix with embedded quartz and scintillating fibers. The value of ξ was about 3 in this detector. With this detector, a resolution of $70\%/\sqrt{E(GeV)}$ was obtained for single hadrons [505]. Due to

the small size of the module, this includes contributions from transverse leakage which prevent the full exploitation of key features of dual readout, and thus underestimates the potential of the method.

The separate Cherenkov read-out evidently provides excellent pion-electron separation for particle identification. In another RD52 prototype, each fiber is read out individually by SiPMs, giving also a superior transverse granularity. A fiber-based calorimeter with full solid-angle coverage requires a pointing geometry due to the limited or missing longitudinal segmentation. The resulting challenges for a mechanical design are studied in the framework of the IDEA detector concept [506].

Table 35.14: Energy resolution of selected hadron calorimeters for single charged hadrons obtained in beam tests.

Calorimeter	Passive	Active	Resolution	Ref.
Bernardi *et al.*	Pb	Scintillator layers	$44.2\%/\sqrt{E}$ §	[507]
CALICE AHCAL	Fe	Scintillator tiles	$44.3\%/\sqrt{E} \oplus 1.8\%$ †	[496]
CALICE W-AHCAL	W	Scintillator tiles	$57.9\%/\sqrt{E} \oplus 4.6\% \oplus 0.065/E$ §	[508]
CDHS	Fe	Scintillator layers	$58\%/\sqrt{E}$ ♯	[493]
DREAM/RD52	Pb	Scint.+ Quartz fibers	$70\%/\sqrt{E}$ *	[505]
HELIOS	U	Scintillator layers	$34\%/\sqrt{E}$ §	[509]
SPACAL	Pb	Scintillating fibers	$33.3\%/\sqrt{E} \oplus 2.2\%$ §	[510]

§ Bernardi *et al.*, CALICE W-AHCAL, HELIOS, SPACAL: (near-)compensating calorimeters.

† CALICE AHCAL: Local software compensation exploiting the high granularity of the calorimeter.

♯ CDHS: Offline weighting using longitudinal information.

* DREAM/RD52: Due to the relatively small transverse size of the detector lateral leakage was significant, deteriorating the energy resolution with respect to the full potential of the dual readout method.

Table 35.14 shows selected examples of the energy resolution of HCALs for single charged pions achieved in beam tests. The examples are selected to illustrate the performance achieved with different designs ranging from intrinsic compensation to software compensation and dual readout, with a focus on results by R&D projects. It should be noted that the exact values of the different resolution terms depend on the functional form used in the fit, here the addition in quadrature is used for the cases where more than just the stochastic term is quoted. The results shown in the table illustrate that (close to) compensating calorimeters with optimized sampling fraction and frequency, such as HELIOS (U-plastic scintillator) and SPACAL (Pb-plastic scintillator), achieve a very good energy resolution. The comparison with Bernardi *et al.*, which has the same Pb/scintillator ratio by volume as SPACAL, but coarser sampling in a sandwich structure, illustrates the importance of the geometrical details. Beyond the examples shown in the table, liquid argon has also been explored as an active medium, for example in the context of the SLD detector with different absorber options [511]. Due to the reduced sensitivity to neutrons in the shower, not the same resolution as for plastic-scintillator-based systems is achieved. This technology has also been used in the D0 experiment, as discussed below. The dual-readout method has the potential to reach or surpass this performance, but would require a prototype sufficiently large for full longitudinal and transverse shower containment for an experimental demonstration. The two CALICE calorimeters shown, which use the same active elements (5 mm thick scintillator tiles) but different absorbers (21.4 mm Fe vs 10 mm W + 4 mm Fe) per layer, illustrate the impact of the absorber choice on energy resolution and reconstruction possibilities. While the tungsten-based W-AHCAL setup

is very close to compensating, the steel-based AHCAL achieves a better energy resolution when software compensation is applied, profiting from the finer sampling of the electromagnetic parts of the cascade and the correction for shower-to-shower fluctuations of the electromagnetic fraction in the reconstruction. In the case of tungsten, software compensation does not significantly improve the energy resolution, as expected. The comparison of the CALICE AHCAL performance with the one of CDHS illustrates the benefits of higher granularity for software compensation techniques, but it should be noted that the absorber thickness of the latter is 25 mm, with the same scintillator thickness as in the case of CALICE.

As explained in the introduction, in most high-energy physics experiments, the HCAL follows after an ECAL, making the response of the latter to hadronic cascades highly relevant for the overall performance of the combined ECAL HCAL system. For scenarios where the electromagnetic and the HCAL have very different $\langle h/e \rangle$, as is typically the case for crystal-based ECALs, the fluctuations of the fraction of the hadronic shower contained within the ECAL result in a significant deterioration of the energy resolution for hadrons. A deterioration of the hadronic performance also results from larger amounts of not-instrumented material, e.g. supports and services, between electromagnetic and hadronic sections. In particle-flow calorimeters, a large value of the λ_I/X_0 ratio of the absorber material, like in tungsten, maximises the longitudinal separation of electromagnetic and hadronic showers. This is reflected in the design of particle-flow-based detector concepts for future Higgs Factories.

Table 35.15: Energy resolution of selected combined electromagnetic and hadronic calorimeter systems in past and present high-energy collider experiments for single hadrons. The results are taken from beam tests of prototypes with the electromagnetic calorimeter upstream of the hadronic calorimeter.

Experiment	technology (ECAL, HCAL)	Combined hadronic resolution	Reference
H1	Pb/LAr, Steel / LAr	$46\%/\sqrt{E} \oplus 2.6\% \oplus 0.73/E$	[512]
ZEUS	depleted U / plastic scintillator	$35\%/\sqrt{E}$	[513]
CDF	Pb/plastic scint., Steel/plastic scint.	$68\%/\sqrt{E} \oplus 4.1\%$	[514]
D0	depleted U / LAr	$44.6\%/\sqrt{E} \oplus 3.9\%$	[515]
ATLAS	Pb/LAr, Steel/plastic scintillator	$52\%/\sqrt{E} \oplus 3.0\% \oplus 1.6/E$	[516]
CMS	$PbWO_4$, brass/plastic scintillator	$84.7\%/\sqrt{E} \oplus 7.4\%$	[517]

Table 35.15 summarizes the single hadron energy resolution obtained from test beams of the combined ECAL and HCAL systems of the large multi-purpose experiments at HERA, the Tevatron and at the LHC. These systems are examples of different optimization strategies. D0 and ZEUS are near-compensating systems with the same technology in ECAL and HCAL emphasizing hadronic performance. ATLAS and H1 use sampling ECALs with good electromagnetic resolution and weighting techniques exploiting longitudinal and transverse shower information for hadronic energy reconstruction. CMS, with a crystal ECAL and a scintillator-brass HCAL, prioritizes electromagnetic performance, with very different $\langle h/e \rangle$ in the electromagnetic and hadronic system. Of the detectors shown in the table, CMS has the best electromagnetic resolution by a comfortable margin, but consequently the weakest hadronic resolution. The best hadronic performance is achieved with the compensating calorimeter of ZEUS, which however has a weaker electromagnetic performance than the other calorimeter systems shown here. It should be noted that an excellent single-hadron resolution in general does not fully propagate into the jet-energy performance. Inac-

tive material in front of the calorimeter can significantly worsen the energy resolution for jets, with an impact in particular on lower-energy particles. For example, the core of the invariant mass distribution of hadronically-decaying Z^0 bosons measured in ZEUS, which had a superconducting coil in front of the calorimeter, is well described by a Gaussian with a σ of 6 GeV [518], approximately 40% wider than would be expected for a jet-energy resolution that is identical to the single-hadron performance.

35.10.4 *Free electron drift velocities in liquid ionization chambers*

Revised August 2009 by W. Walkowiak (Siegen U.).

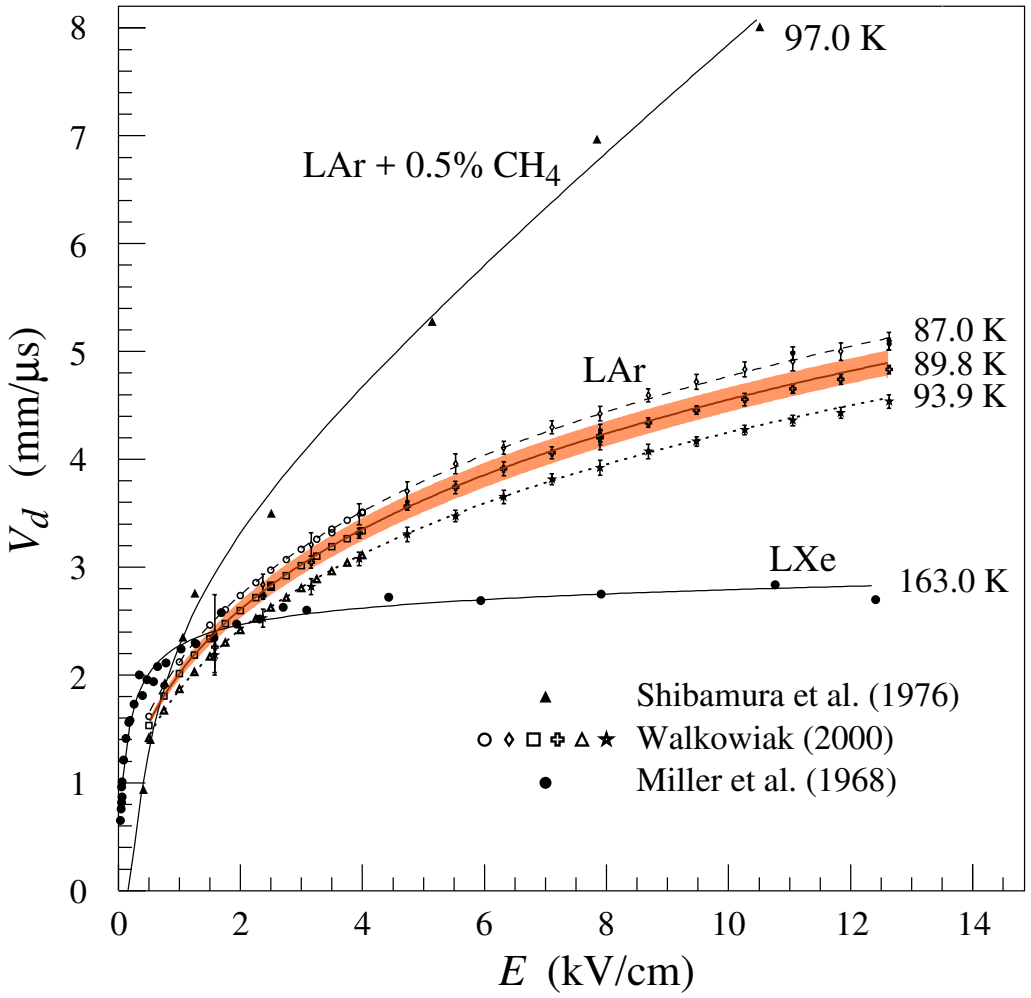

Figure 35.40: Drift velocity of free electrons as a function of electric field strength for LAr [338], LAr + 0.5% CH_4 [519] and LXe [520]. The average temperatures of the liquids are indicated. Results of a fit to an empirical function [521] are superimposed. In case of LAr at 91 K the error band for the global fit [338] including statistical and systematic errors as well as correlations of the data points is given. Only statistical errors are shown for the individual LAr data points.

Drift velocities of free electrons in LAr [338] are given as a function of electric field strength for different temperatures of the medium in Fig. 35.40. The drift velocites in LAr have been measured using a double-gridded drift chamber with electrons produced by a laser pulse on a gold-plated cathode. The average temperature gradient of the drift velocity of the free electrons in LAr is

described [338] by

$$\frac{\Delta v_d}{\Delta T\, v_d} = (-1.72 \pm 0.08)\ \%/\mathrm{K}. \tag{35.54}$$

Previous measurements [519,520,522,523] range from 13% higher [520] to 18% lower [522] than these measurements. They used different techniques and show drift velocities for free electrons which cannot be explained by the temperature dependence mentioned above.

Drift velocities of free electrons in LXe [519] as a function of electric field strength are also displayed in Fig. 35.40. The drift velocity saturates for $|E| > 3$ kV/cm, and decreases with increasing temperature for LXe as well as measured e.g. by [524].

The addition of small concentrations of other molecules like N_2, H_2 and CH_4 in solution to the liquid typically increases the drift velocities of free electrons above the saturation value [519,522], see example for CH_4 admixture to LAr in Fig. 35.40. Therefore, actual drift velocities are critically dependent on even small additions or contaminations.

35.11 Superconducting magnets for collider detectors

Revised August 2025 by Y. Makida (KEK).

35.11.1 *Solenoid Magnets*

In all cases SI unit are assumed, so that the magnetic field, B, is in Tesla, the stored energy, E, is in joules, the dimensions are in meters, and vacuum permeability of $\mu_0 = 4\pi \times 10^{-7}$.

The magnetic field (B) in an simple solenoid with a flux return iron yoke, in which the magnetic field is lower than magnetic saturation of < 2 T, is given by

$$B = \frac{\mu_0\, n\, I}{L} \tag{35.55}$$

where n is the number of turns, I is the current and L is the coil length.

In an air-core solenoid case, the central field is given by

$$B(0,0) = \mu_0\, n\, I \frac{1}{\sqrt{L^2 + 4R^2}}\ , \tag{35.56}$$

where R is the coil radius.

In most cases, momentum analysis is made by measuring the circular trajectory of the passing particles according to $p = mv = qrB$, where p is the momentum, m the mass, q the charge, r the bending radius. By using the sagitta, s, of the trajectory, p is given by

$$s = q\, B\, \ell^2/8p\ , \tag{35.57}$$

where ℓ is the path length in the magnetic field as shown in Fig. 35.41 .

In a practical momentum measurement in colliding beam detectors, it is more effective to increase the magnetic volume than the field strength, since

$$dp/p \propto p/B\, \ell^2\ , \tag{35.58}$$

where ℓ corresponds to the solenoid coil radius R. The energy stored in the magnetic field of any magnet is calculated by integrating B^2 over all space:

$$E = \frac{1}{2\mu_0} \int B^2 dV \tag{35.59}$$

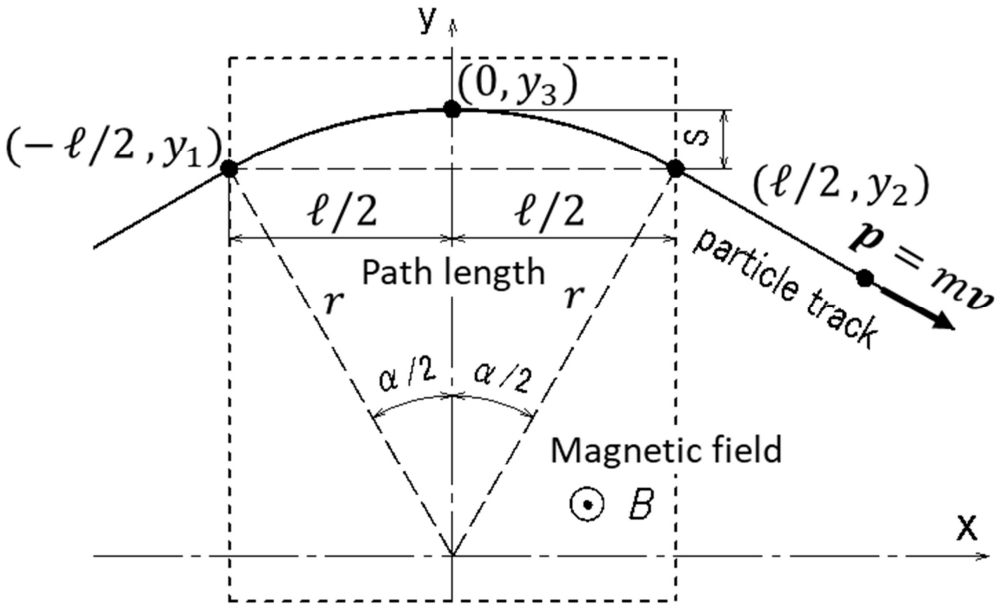

Figure 35.41: Geometric relation of sagitta between path length.

If the coil thin and inside an iron return yoke , (which is the case if it is to superconducting coil), then

$$E \approx (B^2/2\mu_0)\pi R^2 L \ . \tag{35.60}$$

For a detector in which the calorimetry is outside the aperture of the solenoid, the coil must be transparent in terms of radiation and absorption lengths. This usually means that the superconducting solenoid and its cryostat is of minimum real thickness and is made of a material with long radiation length. There are two major contributors to the thickness of a thin solenoid:

1. The conductor consisting of the current-carrying superconducting material (usually Nb-Ti/Cu) and the quench protecting stabilizer (usually aluminum) are wound on the inside of a structural support cylinder (usually aluminum alloy). The coil thickness scales as B^2R, so the thickness in radiation lengths (X_0) is

$$t_{\rm coil}/X_0 = (R/\sigma_h X_0)(B^2/2\mu_0) \ , \tag{35.61}$$

   where $t_{\rm coil}$ is the physical thickness of the coil, X_0 the average radiation length of the coil/stabilizer material, and σ_h is the hoop stress in the coil [525]. $B^2/2\mu_0$ is the magnetic pressure. In large detector solenoids, the aluminum stabilizer and support cylinders dominate the thickness; the superconductor (Nb-TI/Cu) contributes a smaller fraction. The main coil and support cylinder components typically contribute about 2/3 of the total thickness in radiation lengths.
2. Another contribution to the material comes from the outer cylindrical shell of the vacuum vessel. Since this shell is susceptible to buckling collapse, its thickness is determined by the diameter, length and the modulus of the material of which it is fabricated. The outer vacuum shell represents about 1/3 of the total thickness in radiation length.

Table 35.16: Progress of superconducting magnets for particle physics detectors.

Experiment	Laboratory	B [T]	Radius [m]	Length [m]	Energy [MJ]	X/X_0	E/M [kJ/kg]
TOPAZ*	KEK	1.2	1.45	5.4	20	0.70	4.3
CDF*	Tsukuba/Fermi	1.5	1.5	5.07	30	0.84	5.4
VENUS*	KEK	0.75	1.75	5.64	12	0.52	2.8
AMY*	KEK	3	1.29	3	40	†	
CLEO-II*	Cornell	1.5	1.55	3.8	25	2.5	3.7
ALEPH*	Saclay/CERN	1.5	2.75	7.0	130	2.0	5.5
DELPHI*	RAL/CERN	1.2	2.8	7.4	109	1.7	4.2
ZEUS*	INFN/DESY	1.8	1.5	2.85	11	0.9	5.5
H1*	RAL/DESY	1.2	2.8	5.75	120	1.8	4.8
BaBar*	INFN/SLAC	1.5	1.5	3.46	27	†	3.6
D0*	Fermi	2.0	0.6	2.73	5.6	0.9	3.7
BELLE*	KEK	1.5	1.8	4	42	†	5.3
BES-III	IHEP	1.0	1.475	3.5	9.5	†	2.6
ATLAS-CS	ATLAS/CERN	2.0	1.25	5.3	38	0.66	7.0
ATLAS-BT	ATLAS/CERN	1	4.7–9.75	26	1080	(Toroid)†	
ATLAS-ET	ATLAS/CERN	1	0.825–5.35	5	2×250	(Toroid)†	
CMS	CMS/CERN	4	6	12.5	2600	†	12
SiD**	ILC	5	2.9	5.6	1560	†	12
ILD**	ILC	4	3.8	7.5	2300	†	13
SiD**	CLIC	5	2.8	6.2	2300	†	14
ILD**	CLIC	4	3.8	7.9	2300	†	13
FCC**		6	6	23	54000	†	12

* No longer in service
** Conceptual design in future
† EM calorimeter is inside solenoid, so small X/X_0 is not a goal

35.11.2 *Properties of collider detector magnets*

The physical dimensions, central field stored energy and thickness in radiation lengths normal to the beam line of the superconducting solenoids associated with the major collider are given in Table 35.16 [526]. Fig. 35.42 shows thickness in radiation lengths as a function of B^2R in various collider detector solenoids.

The ratio of stored energy to cold mass (E/M) is a useful performance measure. It can also be expressed as the ratio of the stress, σ_h, to twice the equivalent density, ρ, in the coil [525]:

$$\frac{E}{M} = \frac{(B^2/2\mu_0)\pi R^2 L}{\rho\, 2\pi t_{\rm coil} RL} \approx \frac{\sigma_h}{2\rho} \tag{35.62}$$

The E/M ratio in the coil is approximately equivalent to H,[†††] the enthalpy of the coil, and it determines the average coil temperature rise after energy absorption in a quench:

$$E/M = H(T_2) - H(T_1) \approx H(T_2) \tag{35.63}$$

where T_2 is the average coil temperature after the full energy absorption in a quench, and T_1 is the initial temperature. E/M ratios of 5, 10, and 20 kJ/kg correspond to ∼65, ∼80, and ∼100 K,

[†††]The enthalpy, or heat content, is called H in the thermodynamics literature. It is not to be confused with the magnetic field intensity B/μ.

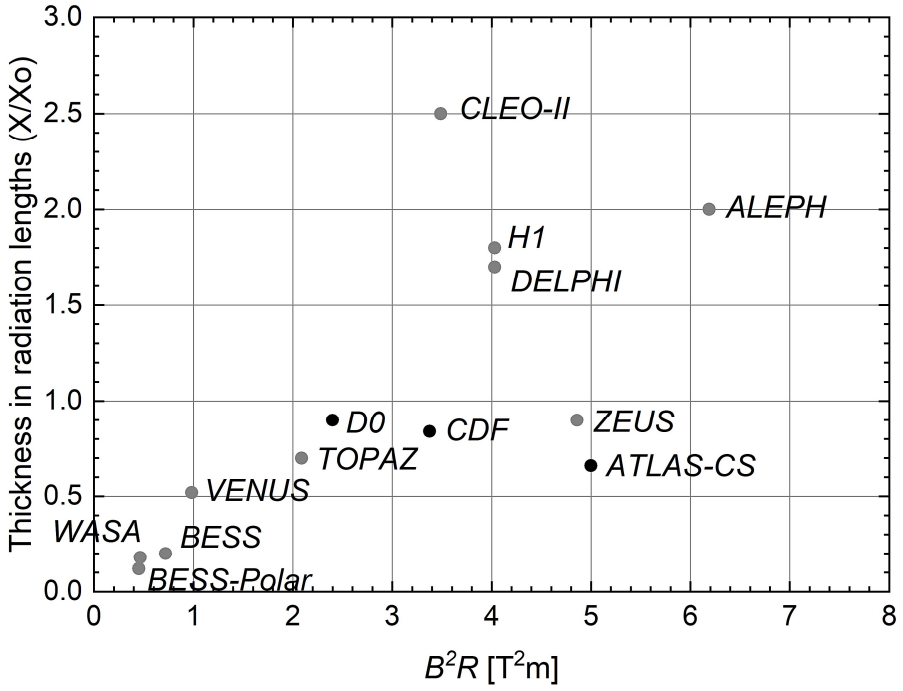

Figure 35.42: Magnet wall thickness in radiation length as a function of B^2R for various detector solenoids. Gray entries are for magnets no longer in use.

respectively. The E/M ratios of various detector magnets are shown in Fig. 35.43 as a function of total stored energy. One would like the cold mass to be as small as possible to minimize the thickness, but temperature rise during a quench must also be minimized. An E/M ratio as large as 12 kJ/kg is designed into the CMS solenoid, with the possibility that about half of the stored energy can go to an external dump resistor. Thus the coil temperature can be kept below 80 K if the energy extraction system works well. The limit is set by the maximum temperature that the coil design can tolerate during a quench. This maximum local temperature should be <130 K (50 K + 80 K), so that thermal expansion effects, which are remarkable beyond 80 K, in the coil are manageable less than 50 K.

35.11.3 *Toroidal magnets*

Toroidal coils uniquely provide a closed magnetic field without the necessity of an iron flux-return yoke. Because no field exists at the collision point and along the beam line, there is, in principle, no effect on the beam. On the other hand, the field profile generally has $1/R$ dependence. R is the distance from the center of the toroid. The particle momentum may be determined by measurements of the deflection angle combined with the sagitta. The deflection (bending) power BL is

$$BL \approx \int_{R_i}^{R_0} \frac{B_i R_i \, dR}{R \sin\theta} = \frac{B_i \, R_i}{\sin\theta} \ln(R_0/R_i) \ , \tag{35.64}$$

where R_i is the inner coil radius, R_0 is the outer coil radius, and θ is the angle between the particle trajectory and the beam line axis . The momentum resolution given by the deflection may be expressed as

$$\frac{\Delta p}{p} \propto \frac{p}{BL} \approx \frac{p \sin\theta}{B_i R_i \ln(R_0/R_i)} \ . \tag{35.65}$$

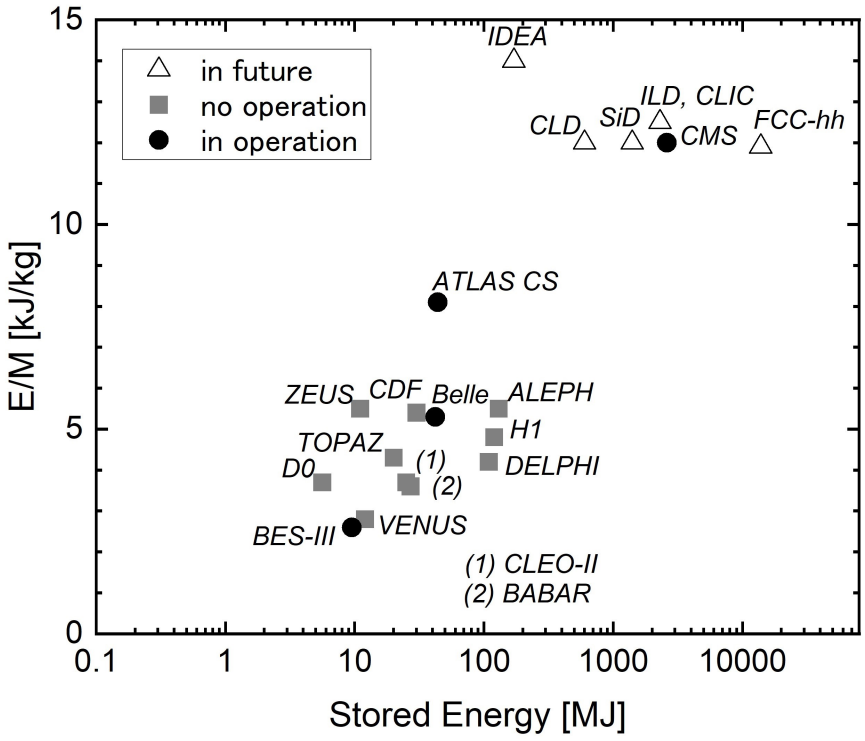

Figure 35.43: Ratio of stored energy to cold mass for major detector solenoids. Gray indicates magnets no longer in operation.

The momentum resolution is better in the forward/backward (smaller θ) direction. The geometry has been found to be optimal when $R_0/R_i \approx 3$–4. In practical designs, the coil is divided into 6–12 lumped coils in order to have reasonable acceptance and accessibility. This causes the coil design to be much more complex. The mechanical structure needs to sustain the decentering force between adjacent coils, and the peak field in the coil is 3–5 times higher than the useful magnetic field for the momentum analysis [527].

35.12 Measurement of particle momenta in a uniform magnetic field

The trajectory of a particle with momentum p (in GeV/c) and charge ze in a constant magnetic field $\vec{B}$ is a helix, with radius of curvature R and pitch angle λ. The radius of curvature and momentum component perpendicular to $\vec{B}$ are related by

$$p \cos\lambda = 0.3\, z\, B\, R\ , \tag{35.66}$$

where B is in tesla and R is in meters.

The distribution of measurements of the curvature $k \equiv 1/R$ is approximately Gaussian. The curvature error for a large number of uniformly spaced measurements on the trajectory of a charged particle in a uniform magnetic field can be approximated by

$$(\delta k)^2 = (\delta k_{\rm res})^2 + (\delta k_{\rm ms})^2, \tag{35.67}$$

where δk = curvature error
$\delta k_{\rm res}$ = curvature error due to finite measurement resolution
$\delta k_{\rm ms}$ = curvature error due to multiple scattering.

If many ($\geq$ 10) uniformly spaced position measurements are made along a trajectory in a uniform medium,

$$\delta k_{\rm res} = \frac{\epsilon}{L'^2}\sqrt{\frac{720}{N+4}}, \tag{35.68}$$

where N = number of points measured along track
L' = the projected length of the track onto the bending plane
ϵ = measurement error for each point, perpendicular to the trajectory.

If a vertex constraint is applied at the origin of the track, the coefficient under the radical becomes 320.

For arbitrary spacing of coordinates s_i measured along the projected trajectory and with variable measurement errors ϵ_i the curvature error $\delta k_{\rm res}$ is calculated from:

$$(\delta k_{\rm res})^2 = \frac{4}{w}\,\frac{V_{ss}}{V_{ss}V_{s^2s^2} - (V_{ss^2})^2}, \tag{35.69}$$

where V are covariances defined as $V_{s^m s^n} = \langle s^m s^n - \rangle s^m \langle s^n$ with $\rangle s^m = w^{-1}\sum({s_i}^m/{\epsilon_i}^2)$ and $w = \sum {\epsilon_i}^{-2}$.

The contribution due to multiple Coulomb scattering is approximately

$$\delta k_{\rm ms} \approx \frac{(0.016)({\rm GeV}/c)z}{Lp\beta\cos^2\lambda}\sqrt{\frac{L}{X_0}}, \tag{35.70}$$

where p = momentum (GeV/c)
z = charge of incident particle in units of e
L = the total track length
X_0 = radiation length of the scattering medium (in units of length; the X_0 defined elsewhere must be multiplied by density)
β = the kinematic variable v/c.

More accurate approximations for multiple scattering may be found in the section on Passage of Particles Through Matter (Sec. 34 of this *Review*). The contribution to the curvature error is given approximately by $\delta k_{\rm ms} \approx 8 s^{\rm rms}_{\rm plane}/L^2$, where $s^{\rm rms}_{\rm plane}$ is defined there.

References

[1] H. Kolanoski and N. Wermes, *Particle Detectors - Fundamentals and Applications*, Oxford University Press (2020), ISBN 978-0-19-885836-2.

[2] T. Ferbel, *Experimental techniques in high energy physics; 1st ed.*, Frontiers in physics, Addison-Wesley, Menlo Park, CA (1987), URL https://cds.cern.ch/record/110951.

[3] K. Kleinknecht, *Detectors for particle radiation* (1998), ISBN 978-0-521-64854-7.

[4] G. Knoll, *Radiation Detection and Measurement (4th ed.)*, John Wiley, Hoboken, NJ (2010), ISBN 978-0-470-13148-0.

[5] D. Green, *The physics of particle detectors*, Cambridge University Press, Cambridge, UK (2000), ISBN 9780521675680.

[6] C. Leroy and P.-G. Rancoita, *Principles of radiation interaction in matter and detection*, World Scientific, Singapore (2011), ISBN 978-981-238-909-1.

[7] C. Grupen and B. Schwartz, *Particle detectors*, Cambridge University Press, Cambridge, UK (2008), ISBN 9780521187954.

[8] H. Spieler, *Semiconductor Detector Systems*, Oxford University Press, Oxford (2005), ISBN 978-0-19-852784-8.

[9] K. Arisaka, Nucl. Instrum. Meth. **A442**, 80 (2000).

[10] N. Matsunaga (ed.), *Photomultiplier Tubes: Basics and Applications*, 4th edition, Hamamatsu Photonics K.K., Hamamatsu (2017), https://www.hamamatsu.com/resources/pdf/etd/PMT_handbook_v4E.pdf.

[11] M. Böhm *et al.*, JINST **15**, 11, C11015 (2020).

[12] M. J. Minot *et al.*, Nuovo Cim. C **43**, 1, 11 (2020).

[13] A. Braem *et al.*, Nucl. Instrum. Meth. **A518**, 574 (2004).

[14] S. Korpar *et al.*, Nucl. Instrum. Meth. A **766**, 145 (2014).

[15] R. Arnold *et al.*, Nucl. Instrum. Meth. **A314**, 465 (1992).

[16] P. Mangeot *et al.*, Nucl. Instrum. Methods **A216**, 79 (1983).

[17] R. Apsimon *et al.*, IEEE Trans. **NS33**, 112 (1986).

[18] R. Arnold *et al.*, Nucl. Instrum. Meth. **A270**, 255 (1988).

[19] D. Aston *et al.*, Nucl. Instrum. Meth. **A283**, 582 (1989).

[20] R. Haitz *et al.*, J. Appl. Phys. **36**, 3123 (1965).

[21] R. McIntyre, IEEE Trans. Electron Devices **13**, 164 (1966).

[22] H. Dautet *et al.*, Applied Optics, **32**, 3894 (1993).

[23] Perkin-Elmer Optoelectronics, *Avalanche Photodiodes: A User's Guide*, (2003).

[24] P. Buzhan *et al.*, Nucl. Instrum. Meth. **A504**, 48 (2003).

[25] Z. Sadygov *et al.*, Nucl. Instrum. Methods **A504**, 301 (2003).

[26] V. Golovin and V. Savelev, Nucl. Instrum. Meth. **A518**, 560 (2004).

[27] F. Simon, Nuclear Instruments and Methods in Physics Research Section A: Accelerators, Spectrometers, Detectors and Associated Equipment **926**, 85–100 (2019), ISSN 0168-9002, URL http://dx.doi.org/10.1016/j.nima.2018.11.042.

[28] S. Korpar *et al.*, Nucl. Instrum. Meth. **A766**, 107 (2014).

[29] R. H. Pots *et al.*, Nucl. Instrum. Meth. **A940**, 254 (2019).

[30] D. R. Schaart *et al.*, Nuclear Instruments and Methods in Physics Research Section A: Accelerators, Spectrometers, Detectors and Associated Equipment **809**, 31 (2016).

[31] M. Petrov, M. Stapelbroek, and W. Kleinhans, Appl. Phys. Lett. **51**, 406 (1987).

[32] M. Atac and M. Petrov, IEEE Trans. **NS36**, 163 (1989).

[33] M. Atac *et al.*, Nucl. Instrum. Meth. **A314**, 56 (1992).

[34] B. Korzh *et al.*, Nature Photonics **14**, 250 (2020).

[35] J. S. Carlson *et al.*, J. Am. Chem. Soc. **139**, 28, 9621 (2017).

[36] J.B. Birks, *The Theory and Practice of Scintillation Counting*, Pergamon, London (1964).

[37] D. Clark, Nucl. Instrum. Meth. **117**, 1, 295 (1974).

[38] Y. Kharzheev, J. Laser Opt. Photonics **4**, 1 (2017).

[39] S. Moser *et al.*, Rad. Phys. and Chem. **41**, 1, 31 (1993).

[40] M. Moszyński and B. Bengtson, Nucl. Instrum. Methods **158**, 1 (1979).

[41] J. B. Birks, Proc. Phys. Soc. **A64**, 874 (1951).

[42] T. Gangwer and J. K. Thomas, Radiation Research **54**, 192 (1973).

[43] D. Dexter, J. Chem. Phys. **21**, 836 (1953).

[44] C. Dujardin and M. Hamel, *Introduction—Overview on Plastic and Inorganic Scintillators*, 3–33, Springer International Publishing, Cham (2021), URL 10.1007/978-3-030-73488-6_1.

[45] M. Böhles *et al.* (NuDoubt++), Eur. Phys. J. C **85**, 2, 121 (2025), [arXiv:2407.05999].

[46] O. B. Rodrigues *et al.*, A prototype reactor-antineutrino detector based on ^{6}Li-doped pulse-shaping-discriminating plastic scintillator (2025), [arXiv:2505.05696], URL https://arxiv.org/abs/2505.05696.

[47] C. Cook, C. Blanco and J. Smirnov, Phys. Rev. D **112**, 083005 (2025).

[48] C. Chandler *et al.*, Addit. Manuf. **73**, 103688 (2023).

[49] B. Li *et al.*, J. Instrum. **20**, 04, P04008 (2025).

[50] S. Lee, M. Livan and R. Wigmans, Rev. Mod. Phys. **90**, 025002 (2018).

[51] R. C. Ruchti, Ann. Rev. Nucl. Part. **46**, 281 (1996).

[52] C. Joram, G. Haefeli and B. Leverington, JINST **10**, 08, C08005 (2015).

[53] T. Weber *et al.*, Commun. Eng. **4**, 41 (2025).

[54] D. Horstmann and U. Holm, Radiat. Phys. Chem. **41**, 1, 395 (1993).

[55] J. Cumalat *et al.*, Nucl. Instrum. Meth. **A293**, 3, 606 (1990).

[56] K. Abe *et al.* (T2K), JINST **17**, P10028 (2022).

[57] Y. Kharzheev, Phys. Part. Nucl. **50**, 1, 42 (2019).

[58] C. Zorn, in F. Sauli, editor, "Instrumentation in high-energy physics, Advanced Series on Directions in High Energy Physics," volume 9, 218, World Scientific (1992), URL 10.1142/9789814360333_0004.

[59] CMS Collaboration, J. Instrum. **15**, 06, P06009 (2020).

[60] K. Gillen and R. Clough, Polymer **33**, 4358 (1992).

[61] T. Seguchi *et al.*, Radiat. Phys. Chem. **17**, 195 (1981).

[62] B. Kronheim *et al.*, NIM **A1059**, 168922 (2024).

[63] P. Feng and et al., *Organic glass scintillators*, 243–283, Springer International Publishing, Cham (2021), URL 10.1007/978-3-030-73488-6_1.

[64] S.E. Derenzo, W.-S. Choong and W.W. Moses, Phys. Med. Biol. **59**, 3261 (2014).

[65] L. Shook, T.A. Laplace, M.S. Boswell, E.D. Bourret, S.E. Derenzo and B.L. Goldblum, Nucl. Instrum. Methods **A1075**, 170389S (2025) database of inorganic and organic scintillator properties",.

[66] C. Melcher and J. Schweitzer, Nucl. Instrum. Methods **A314**, 212 (1992).

[67] D.W. Cooke *et al.*, J. Appl. Phys. **88**, 7360 (2000).

[68] J.M. Chen *et al.*, IEEE Trans. **NS54**, 718 (2007).

[69] J.M. Chen *et al.*, IEEE Trans. **NS54**, 1319 (2007).

[70] M. Nicl and C. Pedrini, Sol.St.Comm. 90, 155 (1994) (2015).

[71] E. Auffray *et al.*, Nucl. Instrum. Methods **A380**, 524 (1996).

[72] E.V.D. van Loef *et al.*, Nucl. Instrum. Methods **A486**, 254 (2002).

[73] W. Drozdowski *et al.*, IEEE Trans. **NS55**, 1391 (2008).
[74] M.S. Alekhin *et al.*, Appl. Phys. Lett. **102**, 161915 (2013).
[75] C. Kuntner *et al.* (Crystal Clear), Nucl. Instrum. Meth. **A493**, 131 (2002).
[76] M. Nicl *et al.*, Adv. Optical Mater. 3 463 (2015).
[77] M.T. Lucchini *et al.*, Nucl. Instrum. Methods **A816**, 176 (2016).
[78] E. Auffray *et al.*, Rad. Phys. Chem. 164, 108365 (2019).
[79] C. Hu *et al.*, Nucl. Instrum. Methods **A954**, 161723 (2020).
[80] C. Hu *et al.*, IEEE Trans. **NS69**, 181 (2022).
[81] N. Akchurin *et al.*, Nucl. Instrum. Meth. **A595**, 359 (2008).
[82] H. Wenzel, Journal of Physics: Conference Series **404**, 012049 (2012).
[83] A. Benaglia *et al.*, IEEE Transactions on Nuclear Science **63**, 2, 574 (2016).
[84] R.H. Mao, L.Y. Zhang and R.-Y. Zhu, IEEE Trans. **NS59**, 2229 (2012).
[85] G. Tang *et al.*, Optical Materials 130 112585 (2022).
[86] L. Zhang and R.-Y. Zhu, EPJ Web of Conferences 320, 00062 (2025).
[87] E. Auffray *et al.*, J. Phys.:Conf.Ser.587. 012062 (2015).
[88] V. Dormenev *et al.*, IEEE Trans. **NS72**, 2007 (2025).
[89] R.-Y. Zhu, TIPP 2017, SPPHY 213, 70 (2018).
[90] C. Hu *et al.*, IEEE Transactions on Nuclear Science **66**, 7, 1854 (2019).
[91] S Gundacker *et al.*, Phys. Med. Biol. 66, 114002 (2021).
[92] R. Cala' *et al.* JINST 20 P04004 (2025).
[93] W.W. Moses, W.-S. Choong and S.E. Derenzo, Acta Physica Polonica **B7**, 725 (2014).
[94] R.H. Mao, L.Y. Zhang and R.-Y. Zhu, IEEE Trans. **NS55**, 2425 (2008).
[95] P. Dorenbos, J. T. M. de Haas, and C. W. E. van Eijk, IEEE Trans. **NS42**, 2190 (1995).
[96] B.D. Rooney and J.D. Valentine, IEEE Trans. **NS44**, 509 (1997).
[97] W.W. Moses *et al.*, IEEE Trans. **NS55**, 1049 (2008).
[98] A.N. Vasilev *et al.*, IEEE Trans. **NS55**, 1054 (2008).
[99] R.T. Williams *et al.* Phys. Status Solidi B, vol. 248, 426 (2011).
[100] Q. Li *et al.* J. Appl. Phys., vol. 109, 123716 (2011).
[101] S.A. Payne *et al.*, IEEE Trans. **NS58**, 3392 (2011).
[102] I. V. Khodyuk and P. Dorenbos, IEEE Trans. **NS42**, 3320 (2012).
[103] G. Gratta, H. Newman and R.-Y. Zhu, Ann. Rev. Nucl. Part. Sci. **44**, 453 (1994).
[104] R.-Y. Zhu, in "Handbook of Particle Detection and Imaging," 1–25, Springer International Publishing (2020).
[105] F. Yang *et al.*, IEEE Trans. **NS63**, 612 (2016).
[106] F. Yang *et al.*, IEEE Trans. **NS64**, 665 (2017).
[107] C. Hu *et al.*, IEEE Transactions on Nuclear Science **67**, 6, 1086 (2020).
[108] G. Dissertori *et al.*, Nucl. Instrum. Methods **745**, 1 (2014), and references therein.
[109] S. Ecklund, C. Field and G. Mazaheri, Nucl. Instr. and Meth. Res. Sect. **A463**, 68 (2001).
[110] M. G. Albrow *et al.*, JINST **7**, P10027 (2012), [arXiv:1207.7248].

[111] B. Aubert *et al.* (BaBar), Nucl. Instr. and Meth. Res. Sect. **A479**, 1 (2002), [hep-ex/0105044].

[112] E. Torassa (Belle-II PID Group), Nucl. Instr. and Meth. Res. Sect. **A824**, 152 (2016).

[113] G. Bayatian *et al.* (CMS), Eur. Phys. J. **C53**, 139 (2008).

[114] Y. Fukuda *et al.* (Super-Kamiokande), Nucl. Instr. and Meth. Res. Sect. **A501**, 418 (2003).

[115] Proceedings of the International Workshops on Ring Imaging Cherenkov Detectors, Nucl. Instr. and Meth. Res. Sect. **A343**, 1 (1993); Nucl. Instr. and Meth. Res. Sect. **A371**, 1 (1996); Nucl. Instr. and Meth. Res. Sect. **A433**, 1 (1999); Nucl. Instr. and Meth. Res. Sect. **A502**, 1 (2003); Nucl. Instr. and Meth. Res. Sect. **A553**, 1 (2005); Nucl. Instr. and Meth. Res. Sect. **A595**, 1 (2008); Nucl. Instr. and Meth. Res. Sect. **A639**, 1 (2011); Nucl. Instr. and Meth. Res. Sect. **A766**, 1 (2014); Nucl. Instr. and Meth. Res. Sect. **A876**, 1 (2017); Nucl. Instr. and Meth. Res. Sect. **A 952**, 1 (2019).

[116] https://www.sciencedirect.com/special-issue/10TGK7NM7NB.

[117] https://www.sciencedirect.com/special-issue/10S11JC46SX.

[118] J. Litt and R. Meunier, Ann. Rev. Nucl. Part. Sci. **23**, 1 (1973).

[119] D. Bartlett *et al.*, Nucl. Instr. and Meth. Res. Sect. **A260**, 55 (1987).

[120] A. Abashian *et al.*, Nucl. Instr. and Meth. Res. Sect. **A479**, 117 (2002).

[121] B. N. Ratcliff, Nucl. Instr. and Meth. Res. Sect. **A502**, 211 (2003).

[122] T. Iijima *et al.*, Nucl. Instr. and Meth. Res. Sect. **A548**, 383 (2005), [arXiv:physics/0504220].

[123] B. Ratcliff and J. Va'vra, Nucl. Instrum. Meth. **A**, 163442 (2020).

[124] W. Blum, W. Riegler, and L. Rolandi, *Particle Detection with Drift Chambers*, Springer-Verlag, Berlin (2008).

[125] R. M. Sternheimer and R. F. Peierls, Phys. Rev. B **3**, 3681 (1971); L. Landau, J. Phys. (USSR) **8**, 201 (1944); W. W. M. Allison and J. H. Cobb, Ann. Rev. Nucl. Part. Sci. **30**, 253 (1980).

[126] I. Smirnov, Nucl. Instrum. Meth. **A554**, 474 (2005); I. Smirnov, HEED - High Energy Electro Dynamics, http://ismirnov.web.cern.ch/ismirnov/heed.

[127] L.G. Christophorou, *Atomic and Molecular Radiation Physics*, John Wiley & Sons, Hoboken (1971); J. Berkowitz, *Atomic and Molecular Photoabsorption*, Academic Press, Cambridge (2015).

[128] F. Sauli, *Gaseous Radiation Detectors: Fundamentals and Applications*, Cambridge University Press (2014).

[129] H. Bichsel, Nucl. Instrum. Meth. **A562**, 154 (2006).

[130] R. Veenhof, Garfield - Simulation of Gaseous Detectors, http://garfield.web.cern.ch/garfield/.

[131] Degrad - cluster size distribution and primary cluster distribution in gas mixtures for minimum ionising particles and X-rays, http://magboltz.web.cern.ch/magboltz/.

[132] S. F. Biagi, Nucl. Instrum. Meth. **A421**, 1-2, 234 (1999).

[133] S. Biagi, R. Veenhof, Magboltz - Boltzmann transport equations for electrons in gas mixtures under the influence of electric and magnetic fields, http://magboltz.web.cern.ch/magboltz/.

[134] S. Mukhopadhyay and N. Majumdar, in "17th DAE-BRNS High Energy Physics Symposium," (2007), [arXiv:physics/0703009].

[135] H. Fischle, J. Heintze and B. Schmidt, Nucl. Instrum. Meth. **A301**, 202 (1991).

[136] M. M. F. R. Fraga *et al.*, Nucl. Instrum. Meth. A **504**, 88 (2003).

[137] A. Peisert and F. Sauli, Drift and Diffusion of Electrons in Gases: A Compilation (With an Introduction to the Use of Computing Program)CERN-84-08, CERN-YELLOW-84-08 (1984).

[138] https://us.lxcat.net/.

[139] O. Şahin, T. Z. Kowalski and R. Veenhof, Nucl. Instrum. Meth. A **768**, 104 (2014).

[140] O. Şahin *et al.*, JINST **5**, 05, P05002 (2010); O. Şahin, JINST **16**, 03, P03026 (2021).

[141] E. McDaniel and E. Mason, *The Mobility and Diffusion of Ions in Gases*, John Wiley & Sons, Hoboken (1973); G. Schultz, G. Charpak and F. Sauli, Rev. Phys. Appl. **12**, 1, 67 (1977).

[142] Y. Kalkan *et al.*, JINST **10**, 07, P07004 (2015).

[143] T. Ikeda *et al.*, JINST **15**, 07, P07015 (2020), [arXiv:2004.09706].

[144] G.F. Knoll, *Radiation Detection and Measurement*, 3nd edition, John Wiley & Sons, New York (1999).

[145] G. Charpak *et al.*, Nucl. Instrum. Methods **A62**, 262 (1968).

[146] G. Charpak and F. Sauli, Ann. Rev. Nucl. Sci. **34**, 285 (1984).

[147] G. Charpak *et al.*, Nucl. Instrum. Methods **A97**, 377 (1971).

[148] W. Blum, W. Riegler, and L. Rolandi, *Particle Detection with Drift Chambers*, Springer-Verlag, Berlin (2008).

[149] G. Charpak *et al.*, Nucl. Instrum. Methods **A167**, 455 (1979).

[150] A.H. Walenta *et al.*, Nucl. Instrum. Methods **A92**, 373 (1971).

[151] A. Breskin *et al.*, Nucl. Instrum. Methods **A124**, 189 (1975).

[152] A. Breskin *et al.*, Nucl. Instrum. Methods **A156**, 147 (1978).

[153] R. Bouclier *et al.*, Nucl. Instrum. Meth. **A265**, 78 (1988), [,556(1987)].

[154] H. Drumm *et al.*, Nucl. Instrum. Methods **A176**, 333 (1980).

[155] D.R. Nygren and J.N. Marx, Phys. Today **31N10**, 46 (1978).

[156] C. Grupen, *Particle Detectors*, Cambridge Monographs on Particle Physics, Nuclear Physics and Cosmology, Cambridge University Press (2008).

[157] M. P. Titov, ICFA Instrum. Bull. **26**, 002 (2004), [,199(2004)], [arXiv:physics/0403055]; M. P. Titov *et al.*, ICFA Instrum. Bull. **24**, 22 (2002), [hep-ex/0204005].

[158] G. F. Tassielli *et al.*, JINST **15**, 09, C09051 (2020), [arXiv:2006.02378].

[159] P. S. Baringer *et al.*, Nucl. Instrum. Meth. **A254**, 542 (1987).

[160] J. Virdee, Phys. Reports **403**, 401 (2004).

[161] A. Sergi, Phys. Procedia **37**, 530 (2012).

[162] A. H. Walenta, Phys. Scripta **23**, 354 (1981).

[163] J. A. Kadyk, Nucl. Instrum. Meth. A **300**, 436 (1991); J. Va'vra, ICFA Instrum. Bull. **24**, 1 (2002).

[164] M. Aleksa *et al.*, Nucl. Instrum. Meth. **A446**, 435 (2000).

[165] A. Oed, Nucl. Instrum. Meth. **A263**, 351 (1988).

[166] F. Sauli, Nucl. Instrum. Meth. **A386**, 531 (1997).

[167] Y. Giomataris *et al.*, Nucl. Instrum. Meth. **A376**, 29 (1996).

[168] Input to the European Particle Physics Strategy no. 87 (2019), S. Dalla Torre, E. Oliveri, L. Ropelewski, M. Titov, Development of the Micro-Pattern Gaseous Detector Technologies: an overview of the CERN-RD51 Collaboration, https://indico.cern.ch/event/765096/contributions/3295721.

[169] F. Sauli, *Micro-pattern gaseous detectors principles of operation and applications*, World Scientific, Singapore (2020).

[170] R. Bouclier *et al.*, Nucl. Instrum. Meth. A **381**, 289 (1996); Y. Bagaturia *et al.*, Nucl. Instrum. Meth. A **490**, 223 (2002).

[171] A. Bressan *et al.*, Nucl. Instrum. Meth. **A425**, 262 (1999).

[172] S. Bachmann *et al.*, Nucl. Instrum. Meth. **A479**, 294 (2002); A. Bressan *et al.*, Nucl. Instrum. Meth. **A424**, 321 (1999).

[173] M. Alfonsi *et al.*, Nucl. Instrum. Meth. A **671**, 6 (2012).

[174] J. Derre *et al.*, Nucl. Instrum. Meth. A **459**, 523 (2001).

[175] A. Breskin *et al.*, Nucl. Instrum. Meth. **124**, 189 (1975).

[176] J. Benlloch *et al.*, IEEE Trans. Nucl. Sci. **45**, 234 (1998).

[177] Y. Giomataris, Nucl. Instrum. Meth. **A419**, 239 (1998).

[178] M. Chefdeville *et al.*, Nucl. Instrum. Meth. A **556**, 490 (2006).

[179] J. Leidner, F. Murtas and M. Silari, Applied Sciences **11**, 1 (2021).

[180] A. Curioni *et al.*, Nucl. Instrum. Meth. A **849**, 60 (2017).

[181] R. Chechik *et al.*, Nucl. Instrum. Meth. A **535**, 303 (2004); M. Alexeev *et al.*, JINST **8**, C12005 (2013).

[182] L. Moleri *et al.*, JINST **12**, 10, P10017 (2017), [arXiv:1707.00125].

[183] T. Alexopoulos *et al.*, Nucl. Instrum. Meth. A **640**, 110 (2011).

[184] Y. Bilevych *et al.*, Nucl. Instr. and Meth. A **629**, 66 (2011), ISSN 0168-9002, URL https://www.sciencedirect.com/science/article/pii/S016890021002663X.

[185] A. Ochi, PoS **TIPP2014**, 351 (2015).

[186] Y. Lv *et al.*, Nucl. Instr. and Meth. A **958**, 162759 (2020), ISSN 0168-9002, URL https://www.sciencedirect.com/science/article/pii/S0168900219312148.

[187] F. Yamane *et al.*, Nucl. Instrum. Meth. A **951**, 162938 (2020), [arXiv:1901.03836].

[188] G. Bencivenni *et al.*, JINST **10**, 02, P02008 (2015), [arXiv:1411.2466].

[189] G. Bencivenni *et al.*, Nuclear Instruments and Methods in Physics Research Section A: Accelerators, Spectrometers, Detectors and Associated Equipment **1069**, 169725 (2024), ISSN 0168-9002, URL https://www.sciencedirect.com/science/article/pii/S016890022400651X.

[190] D. Abbaneo *et al.*, Nucl. Instrum. Meth. A **718**, 383 (2013).

[191] T. Alexopoulos *et al.*, Nucl. Instrum. Meth. A **617**, 161 (2010); L. Lavezzi *et al.*, in "2017 IEEE Nuclear Science Symposium and Medical Imaging Conference," (2017), [arXiv:1803.07266].

[192] J. Bortfeldt *et al.*, Nucl. Instrum. Meth. A **903**, 317 (2018), [arXiv:1712.05256].

[193] A. Balla *et al.*, Nucl. Instrum. Meth. A **732**, 221 (2013).

[194] DRD1 Collaboration: https://drd1.web.cern.ch ; A. Colaleo, L. Ropelewski *et al.* (2024), URL https://cds.cern.ch/record/2885937.

[195] D.R. Nygren and J.N. Marx, Phys. Today **31N10**, 46 (1978).

[196] J. Alme *et al.*, Nucl. Instrum. Meth. **A622**, 316 (2010), [arXiv:1001.1950].

[197] J. Adolfsson *et al.*, Journal of Instrumentation **16**, 03, P03022 (2021), URL https://doi.org/10.1088/1748-0221/16/03/p03022.

[198] N. Abgrall *et al.* (T2K ND280 TPC), Nucl. Instrum. Meth. A **637**, 25 (2011), [arXiv:1012.0865].

[199] A. H. Walenta *et al.*, Nucl. Instrum. Meth. **161**, 45 (1979).
[200] H. Aihara *et al.*, IEEE Trans. **NS30**, 63 (1983).
[201] K. Dehmelt (sPHENIX), PoS **MPGD2017**, 044 (2019).
[202] P. Colas, I. Giomataris and V. Lepeltier, Nucl. Instrum. Meth. **A535**, 226 (2004).
[203] X. Artru, G. B. Yodh and G. Mennessier, Phys. Rev. **D12**, 1289 (1975).
[204] J. Alozy *et al.*, Nucl. Instrum. Meth. **A961**, 163681 (2020).
[205] M. L. Cherry *et al.*, Phys. Rev. **D10**, 3594 (1974).
[206] B. Dolgoshein, Nucl. Instrum. Meth. **A326**, 434 (1993).
[207] A. Andronic and J. P. Wessels, Nucl. Instrum. Meth. **A666**, 130 (2012).
[208] S. Acharya *et al.* (ALICE), Nucl. Instrum. Meth. **A881**, 88 (2018), [arXiv:1709.02743].
[209] M. Petris *et al.*, Nucl. Instrum. Meth. **A714**, 17 (2013).
[210] T. Akesson *et al.* (ATLAS TRT), Nucl. Instrum. Meth. **A522**, 131 (2004).
[211] M. Ambriola *et al.*, Nucl. Instrum. Meth. **A522**, 77 (2004).
[212] J. Adelman (ATLAS), Nucl. Instrum. Meth. **A706**, 33 (2013).
[213] T. Kirn (AMS 02 TRD), Nucl. Instrum. Meth. **A706**, 43 (2013).
[214] G. M. Garibian, L. A. Gevorgian and C. Yang, Nucl. Instrum. Meth. **125**, 133 (1975).
[215] P. Nevski, Nucl. Instrum. Meth. **A522**, 116 (2004).
[216] J. Alozy *et al.*, Nucl. Instrum. Meth. **A927**, 1 (2019), [arXiv:1901.11265].
[217] V. M. Grishin and S. S. Sadilov, Nucl. Instrum. Meth. **A522**, 122 (2004).
[218] B. Beischer *et al.*, Nucl. Instrum. Meth. **A583**, 485 (2007).
[219] A. A. Savchenko *et al.*, JINST **15**, 06, C06024 (2020).
[220] T. Akesson *et al.* (ATLAS TRT), Nucl. Instrum. Meth. **A412**, 200 (1998).
[221] D. Errede *et al.*, Nucl. Instrum. Meth. A **309**, 386 (1991).
[222] M. Albrow *et al.*, Nucl. Instrum. Meth. A **1055**, 168535 (2023).
[223] M. Ave *et al.*, Nucl. Instrum. Meth. **A654**, 140 (2011).
[224] M. L. Cherry, Nucl. Instrum. Meth. **A706**, 39 (2013).
[225] F. Hartjes *et al.*, Nucl. Instrum. Meth. **A706**, 59 (2013).
[226] J. Alozy *et al.*, J. Phys. Conf. Ser. **1690**, 1, 012041 (2020).
[227] M. Brigida *et al.*, Nucl. Instrum. Meth. **A706**, 69 (2013).
[228] V. V. Berdnikov *et al.*, Nucl. Instrum. Meth. **A706**, 65 (2013).
[229] R. Santonico and R. Cardarelli, Nucl. Instrum. Meth. **187**, 377 (1981).
[230] V. Parkhomchuck, Y. Pestov and N. Petrovykh, Nucl. Instrum. Meth. **93**, 2, 269 (1971).
[231] G. V. Fedotovich, Y. N. Pestov and K. N. Putilin, in "International Conference on Instrumentation for Colliding Beam Physics," 127–131 (1982).
[232] E. Cerron Zeballos *et al.*, Nucl. Instrum. Meth. **A374**, 132 (1996).
[233] J. Juita *et al.*, Fire Science Reviews **1** (2012).
[234] P. Fonte, JINST **8**, 04, P04017 (2013).
[235] G. Aielli *et al.*, Nucl. Instrum. Meth. **A508**, 6 (2003).
[236] J. M. Meek, Phys. Rev. **57**, 722 (1940).

[237] R. Cardarelli, R. Santonico and V. Makeev, Nucl. Instrum. Meth. **A382**, 470 (1996).

[238] R. Cardarelli, A. Di Ciaccio and R. Santonico, Nucl. Instrum. Meth. **A333**, 399 (1993).

[239] R. Cardarelli, Sci Acta **8**, 159 (1993).

[240] P. Camarri *et al.*, Nucl. Instrum. Meth. **A414**, 317 (1998).

[241] L. Pontecorvo, ATLAS Muon Internal note **20** (1993).

[242] W. Riegler, JINST **11**, 11, P11002 (2016).

[243] R. Santonico, Nucl. Instrum. Meth. **A456**, 1 (2000).

[244] R. Cardarelli *et al.*, JINST **8**, P01003 (2013).

[245] G. Aielli *et al.*, JINST **9**, 09, C09030 (2014).

[246] S. Simsek (ATLAS Muon), Nucl. Instrum. Meth. A **1063**, 169298 (2024).

[247] G. Aad *et al.* (ATLAS), JINST **3**, S08003 (2008).

[248] S. Chatrchyan *et al.* (CMS), JINST **3**, S08004 (2008).

[249] G. Aielli *et al.*, Nucl. Instrum. Meth. A **562**, 92 (2006).

[250] A. Bertolin *et al.*, Nucl. Instrum. Meth. A **602**, 631 (2009).

[251] Aielli, Giulio *et al.*, Eur. Phys. J. C **80**, 12, 1177 (2020).

[252] M. Bauer *et al.*, ANUBIS: Proposal to search for long-lived neutral particles in CERN service shafts (2019), [arXiv:1909.13022].

[253] M. Bedjidian *et al.*, JINST **6**, P02001 (2011), [arXiv:1011.5969].

[254] P. Fonte, A. Smirnitsky and M. C. S. Williams (ALICE), Nucl. Instrum. Meth. **A443**, 201 (2000).

[255] M. Abbrescia, V. Peskov and P. Fonte, *Resistive Gaseous Detectors: Designs, Performance, and Perspectives*, Wiley (2018), ISBN 9783527340767.

[256] W. Riegler and C. Lippmann, Nucl. Instrum. Meth **A508**, 14 (2003).

[257] P. Fonte (2018), URL https://cds.cern.ch/record/2319919.

[258] A. Akindinov *et al.*, Eur. Phys. J. Plus **128**, 44 (2013).

[259] D. Belver *et al.*, Nucl. Instrum. Meth. A **602**, 687 (2009).

[260] A. Schuttauf (FOPI), Nucl. Instrum. Meth. A **533**, 65 (2004).

[261] M. Ablikim *et al.*, Nucl. Instrum. Meth. A **614**, 3, 345 (2010).

[262] e. a. P. Fonte, Nucl.Instrum.Meth.A **1051** (2023).

[263] I. Deppner and N. Herrmann, JINST **15**, 10, C10030 (2020).

[264] J. P. Chen *et al.*, A White Paper on SoLID (Solenoidal Large Intensity Device) (2014), [arXiv:1409.7741].

[265] M. Benoit *et al.*, JINST **11** (2015).

[266] G. Proto, Nucl. Instrum. Meth. **1070**, 170014 (2025).

[267] A. Blanco *et al.*, JINST **7**, P11012 (2012).

[268] C. Iacobaeus *et al.*, Nucl. Instrum. Meth. **A513**, 244 (2003), [arXiv:physics/0210006].

[269] G. Aielli *et al.*, Nucl. Instrum. Meth. **A456**, 82 (2000).

[270] G. Aielli *et al.*, Nucl. Instrum. Meth. **533**, 1, 86 (2004).

[271] H. Sakai *et al.*, Nucl. Instrum. Meth. **A484**, 153 (2002).

[272] G. A. et al., Nucl. Instrum. Meth. **515**, 1, 335 (2003), ISSN 0168-9002, proceedings of the International Workshop on Aging Phenomena in Gaseous Detectors.

[273] G. A. et al., Nuclear Science, IEEE Transactions on **53**, 567 (2006).

[274] M. A. et al., Nucl. Instrum. Meth. **533**, 1, 102 (2004), ISSN 0168-9002.

[275] M. C. et al., Nucl. Instrum. Meth. **661**, S214 (2012), ISSN 0168-9002, x. Workshop on Resistive Plate Chambers and Related Detectors (RPC 2010).

[276] R. Santonico, JINST **8**, P04023 (2013).

[277] L. Lopes *et al.*, Nucl. Instrum. Meth. **A533**, 69 (2004).

[278] European Commission website (2024), URL https://eur-lex.europa.eu/legal-content/EN/TXT/PDF/?uri=OJ:L_202400573.

[279] B. Liberti *et al.*, JINST **11**, 09, C09012 (2016).

[280] S. Pisano *et al.* (EEE), JINST **14**, 08, C08008 (2019), [arXiv:1806.03918].

[281] X. Fan *et al.*, Nucl. Instrum. Meth. **1024**, 166124 (2022), ISSN 0168-9002.

[282] L. Q. et al., Nucl. Instrum. Meth. **1080**, 170770 (2025).

[283] G. Proto, Il Nuovo Cimento C **2-3** (2021).

[284] L. Quaglia and e. a. Ramos, D, The European Physical Journal Plus **140** (2025).

[285] R. G. et al., Nucl. Instrum. Meth. **1054**, 168393 (2023), ISSN 0168-9002.

[286] G. Rigoletti, B. Mandelli and R. Guida, JINST **15**, 11, C11003 (2020).

[287] R. Guida, B. Mandelli and G. Rigoletti, Nucl. Instrum. Meth. **1039**, 167045 (2022).

[288] G. Proto *et al.*, JINST **17**, 05, P05005 (2022).

[289] S. Simsek, Nucl. Instrum. Meth. **1079**, 170618 (2025).

[290] G. Rigoletti *et al.*, Nucl. Instrum. Meth. **1075**, 170331 (2025).

[291] G. Proto, O. Kortner and H. Kroha, JINST **20**, 06, P06031 (2025).

[292] R. Cardarelli, JINST **16**, 05, C05004 (2021).

[293] R. Cardarelli *et al.*, Nucl. Instrum. Meth. **1058**, 168822 (2024).

[294] Summary of Liquid Argon PropertiesAccessed August 2021, URL https://lar.bnl.gov/properties/.

[295] E. W. Lemmon *et al.*, NIST Standard Reference Database 23: Reference Fluid Thermodynamic and Transport Properties-REFPROP, Version 10.0, National Institute of Standards and Technology (2018), URL https://www.nist.gov/srd/refprop.

[296] C. Rubbia, "The liquid-argon time projection chamber: a new concept for neutrino detectors: CERN-EP-INT-77-8," (1977), URL https://cds.cern.ch/record/117852.

[297] H. H. Chen and J. F. Lathrop, Nucl. Instrum. Meth. **150**, 585 (1978).

[298] P. Abratenko *et al.* (MicroBooNE), JINST **16**, 06, P06043 (2021), [arXiv:2011.01375].

[299] M. Wang *et al.*, Front. Big Data **3**, 604083 (2021), [arXiv:2009.04509].

[300] B. Abi *et al.* (DUNE), Phys. Rev. D **102**, 9, 092003 (2020), [arXiv:2006.15052].

[301] A. A. Abud *et al.* (DUNE (protoDUNE-SP)) (2021), [arXiv:2108.01902].

[302] G. Carugno *et al.* (ICARUS), Nucl. Instrum. Meth. A **292**, 580 (1990).

[303] M. Adamowski *et al.*, JINST **9**, P07005 (2014), [arXiv:1403.7236].

[304] C. Adams *et al.* (MicroBooNE), JINST **15**, 07, P07010 (2020), [arXiv:1910.01430].

[305] A. Marchionni, Ann. Rev. Nucl. Part. Sci. **63**, 269 (2013), [arXiv:1307.6918].

[306] K. Majumdar and K. Mavrokoridis, Appl. Sciences **11**, 6, 2455 (2021), [arXiv:2103.06395].

[307] M. Del Tutto, ArCS: A Magnetized Liquid Argon Time Projection Chamber for Neutrino Physics and Beyond (2025), URL https://indico.cern.ch/event/1488822/contributions/6480006/.

[308] F. Arneodo *et al.* (The ICARUS-Milano Collaboration), Phys. Rev. D **74**, 112001 (2006).

[309] S. Amerio *et al.* (ICARUS), Nucl. Instrum. Meth. A **527**, 329 (2004).

[310] C. Anderson *et al.* (ArgoNeuT), JINST **7**, P10019 (2012), [arXiv:1205.6747].

[311] R. Acciarri *et al.* (MicroBooNE), JINST **12**, 02, P02017 (2017), [arXiv:1612.05824].

[312] R. Acciarri *et al.* (LArIAT), JINST **15**, 04, P04026 (2020), [arXiv:1911.10379].

[313] A. Abed Abud *et al.* (DUNE) (2021), [arXiv:2103.13910].

[314] B. Abi *et al.* (DUNE), JINST **15**, 08, T08010 (2020), [arXiv:2002.03010].

[315] B. Russell (DUNE), PoS **TAUP2023**, 221 (2024).

[316] S. Collaboration *et al.*, The Short-Baseline Near Detector at Fermilab (2025), [arXiv:2504.00245], URL https://arxiv.org/abs/2504.00245.

[317] G. Bakale, U. Sowada and W. F. Schmidt, The Journal of Physical Chemistry **80**, 23, 2556 (1976).

[318] A. Bettini *et al.* (ICARUS), Nucl. Instrum. Meth. A **305**, 177 (1991).

[319] W. Jaskierny *et al.* (Fermilab-TM-2384-E), Technical report (2006), URL https://lss.fnal.gov/archive/test-tm/2000/fermilab-tm-2384-e.pdf.

[320] Sigma-Aldrich 4A, BASF Copper Getter CU-0226S.

[321] P. Cennini *et al.*, Nucl. Instrum. Meth. A **333**, 567 (1993).

[322] R. Acciarri *et al.* (WArP), JINST **5**, P06003 (2010), [arXiv:0804.1217].

[323] B. J. P. Jones *et al.*, JINST **8**, P07011 (2013), [Erratum: JINST 8, E09001 (2013)], [arXiv:1306.4605].

[324] R. Acciarri *et al.* (WArP), JINST **5**, P05003 (2010), [arXiv:0804.1222].

[325] M. Miyajima *et al.*, Phys. Rev. A **9**, 1438 (1974).

[326] G. Jaffe, Annalen der Physik **42**, 12, 303 (1913).

[327] L. Onsager, Phys. Rev. **54**, 554 (1938).

[328] J. Thomas and D. A. Imel, Phys. Rev. A **36**, 614 (1987).

[329] C. Adams *et al.* (MicroBooNE), JINST **15**, 03, P03022 (2020), [arXiv:1907.11736].

[330] P. Abratenko *et al.*, Journal of Instrumentation **20**, 01, P01033 (2025), URL https://dx.doi.org/10.1088/1748-0221/20/01/P01033.

[331] R. T. Scalettar *et al.*, Phys. Rev. A **25**, 2419 (1982).

[332] E. Aprile *et al.*, Nucl. Instrum. Meth. A **261**, 519 (1987).

[333] P. Cennini *et al.* (ICARUS), Nucl. Instrum. Meth. A **345**, 230 (1994).

[334] S. Amoruso *et al.* (ICARUS), Nucl. Instrum. Meth. A **523**, 275 (2004).

[335] R. Acciarri *et al.* (ArgoNeuT), JINST **8**, P08005 (2013), [arXiv:1306.1712].

[336] T. Yang, Instruments **5**, 1, 2 (2020), [arXiv:2012.01319].

[337] S. Amoruso *et al.* (ICARUS), Nucl. Instrum. Meth. A **516**, 68 (2004).

[338] W. Walkowiak, Nucl. Instrum. Meth. A **449**, 288 (2000).

[339] M. Antonello *et al.* (ICARUS), JINST **9**, 12, P12006 (2014), [arXiv:1409.5592].

[340] V. Meddage (MicroBooNE), in "Meeting of the APS Division of Particles and Fields," (2017), [arXiv:1710.00396].

[341] B. Abi *et al.* (DUNE), JINST **15**, 12, P12004 (2020), [arXiv:2007.06722].

[342] Y. Li *et al.*, Nucl. Instrum. Meth. A **816**, 160 (2016), [arXiv:1508.07059].

[343] P. Agnes *et al.* (DarkSide), Nucl. Instrum. Meth. A **904**, 23 (2018), [arXiv:1802.01427].

[344] P. Abratenko *et al.* (MicroBooNE), JINST **16**, 09, P09025 (2021), [arXiv:2104.06551].

[345] M. Miyajima *et al.*, Phys. Rev. A **10**, 1452 (1974).

[346] N. Gee *et al.*, Journal of Applied Physics **57**, 4, 1097 (1985).

[347] T. Doke *et al.*, Nucl. Instrum. Meth. A **269**, 291 (1988).

[348] T. Doke, K. Masuda and E. Shibamura, Nucl. Instrum. Meth. A **291**, 617 (1990).

[349] T. Heindl *et al.*, EPL **91**, 6, 62002 (2010), [arXiv:1511.07718].

[350] M. Babicz *et al.*, JINST **15**, 09, P09009 (2020), [arXiv:2002.09346].

[351] G. M. Seidel, R. E. Lanou and W. Yao, Nucl. Instrum. Meth. A **489**, 189 (2002), [hep-ex/0111054].

[352] E. Grace and J. A. Nikkel, Nucl. Instrum. Meth. A **867**, 204 (2017), [arXiv:1502.04213].

[353] A. Hitachi *et al.*, Phys. Rev. B **27**, 5279 (1983).

[354] P. Adhikari *et al.* (DEAP), Eur. Phys. J. C **80**, 4, 303 (2020), [arXiv:2001.09855].

[355] M. Auger *et al.*, JINST **11**, 03, P03017 (2016), [arXiv:1512.05968].

[356] S. Kubota *et al.*, Phys. Rev. B **20**, 8, 3486 (1979).

[357] F. Spiegelmann and J.-P. Malrieu, Chemical Physics Letters **57**, 2, 214 (1978), ISSN 0009-2614.

[358] B. Jones *et al.*, JINST **8**, P12015 (2013), [arXiv:1308.3658].

[359] A. Buzulutskov, EPL **117**, 3, 39002 (2017), [arXiv:1702.03612].

[360] J. Soto-Oton (DUNE), in "International Conference on Technology and Instrumentation in Particle Physics," (2021), [arXiv:2109.05858].

[361] P. Abratenko *et al.* (MicroBooNE), JINST **15**, 12, P12037 (2020), [arXiv:2008.09765].

[362] M. Antonello *et al.* (ICARUS), JINST **15**, 07, P07001 (2020), [arXiv:2001.08934].

[363] S. Palestini, Instruments **5**, 1, 9 (2021), [arXiv:2102.06082].

[364] C. Cantini *et al.*, JINST **12**, 03, P03021 (2017), [arXiv:1611.02085].

[365] J. Asaadi *et al.*, JINST **9**, P09002 (2014), [arXiv:1406.5216].

[366] V. Radeka *et al.*, J. Phys. Conf. Ser. **308**, 012021 (2011).

[367] O. Bunemann, T. E. Cranshaw and J. A. Harvey, Canadian Journal of Research **27a**, 5, 191 (1949).

[368] H. Chen *et al.*, Phys. Procedia **37**, 1287 (2012).

[369] S. Li *et al.*, IEEE Transactions on Nuclear Science **60**, 6, 4737 (2013).

[370] H. Chen *et al.*, Nucl. Instrum. Meth. A **936**, 271 (2019).

[371] R. Acciarri *et al.* (MicroBooNE), JINST **12**, 08, P08003 (2017), [arXiv:1705.07341].

[372] P. Cennini *et al.* (ICARUS), Nucl. Instrum. Meth. A **432**, 240 (1999).

[373] D. Caratelli (MicroBooNE), JINST **15**, 03, C03023 (2020).
[374] B. Ali-Mohammadzadeh *et al.* (ICARUS), JINST **15**, 10, T10007 (2020), [arXiv:2006.05261].
[375] M. Kuźniak and A. M. Szelc, Instruments **5**, 1, 4 (2020), [arXiv:2012.15626].
[376] A. Ankowski *et al.* (ICARUS), Nucl. Instrum. Meth. A **556**, 146 (2006).
[377] N. Anfimov *et al.*, JINST **15**, 07, C07022 (2020).
[378] E. Segreto *et al.*, JINST **15**, 05, C05045 (2020).
[379] M. Antonello *et al.*, JINST **9** (2014), URL https://iopscience.iop.org/article/10.1088/1748-0221/9/08/P08003/pdf.
[380] H. Chen *et al.*, 16th IEEE-NPSS Real Time Conference 159–162 (2009), URL https://ieeexplore.ieee.org/document/5322032.
[381] B. Abi *et al.* (DUNE) (2018), [arXiv:1807.10327].
[382] B. Abi *et al.* (DUNE) (2018), [arXiv:1807.10340].
[383] R. Acciarri *et al.*, JINST **12**, 08, P08003 (2017), [arXiv:1705.07341].
[384] C. Adams *et al.*, JINST **13**, 07, P07006 (2018), [arXiv:1802.08709].
[385] B. Abi *et al.*, JINST **15**, 12, P12004 (2020), [arXiv:2007.06722].
[386] R. Acciarri *et al.* (MicroBooNE), Eur. Phys. J. C **78**, 1, 82 (2018), [arXiv:1708.03135].
[387] X. Qian *et al.*, JINST **13**, 05, P05032 (2018), [arXiv:1803.04850].
[388] P. Abratenko *et al.* (MicroBooNE), JHEP **2021**, 153 (2021), [arXiv:2109.02460].
[389] L. Uboldi *et al.*, Nucl. Instrum. Meth. A **1028**, 166371 (2022), [arXiv:2106.09911].
[390] R. Acciarri *et al.* (ArgoNeuT), JINST **17**, 01, P01018 (2022), [arXiv:2103.06391].
[391] A. Abed Abud *et al.* (DUNE), Eur. Phys. J. C **82**, 10, 903 (2022), [arXiv:2203.17053].
[392] C. Adams *et al.* (MicroBooNE), Phys. Rev. D **99**, 9, 092001 (2019), [arXiv:1808.07269].
[393] P. Abratenko *et al.* (MicroBooNE), Phys. Rev. D **103**, 5, 052012 (2021), [arXiv:2012.08513].
[394] A. A. Abud *et al.* (DUNE), Eur. Phys. J. C **85**, 697, 697 (2025), [arXiv:2502.06637].
[395] P. Abratenko *et al.* (MicroBooNE), Phys. Rev. D **103**, 9, 092003 (2021), [arXiv:2010.08653].
[396] J. Liu *et al.* (DUNE) (2020), [arXiv:2012.06181].
[397] P. Abratenko *et al.* (MicroBooNE), Phys. Rev. D **110**, 9, 092010 (2024), [arXiv:2406.10123].
[398] A. Aurisano *et al.*, Phys. Rev. D **110**, 3, 032008 (2024), [arXiv:2403.11872].
[399] F. Drielsma *et al.*, in "34th Conference on Neural Information Processing Systems," (2021), [arXiv:2102.01033].
[400] G. Cerati (MicroBooNE), EPJ Web Conf. **295**, 08012 (2024), [arXiv:2309.15362].
[401] T. Cai *et al.*, Comput. Softw. Big Sci. **7**, 1, 11 (2023), [arXiv:2301.04633].
[402] C. Rubbia *et al.* (ICARUS), JINST **6**, P07011 (2011), [arXiv:1106.0975].
[403] D. A. Dwyer *et al.*, JINST **13**, 10, P10007 (2018), [arXiv:1808.02969].
[404] D. Cardoso *et al.*, JINST **19**, 08, C08001 (2024).
[405] B. Baibussinov *et al.* (ICARUS), JINST **13**, 03, T03001 (2018), [arXiv:1711.06781].
[406] A. Lowe *et al.*, Instruments **4**, 4, 35 (2020), [arXiv:2011.02292].
[407] M. Arroyave *et al.*, JINST **19**, 10, P10019 (2024), [arXiv:2405.16816].
[408] A. Ereditato *et al.*, JINST **8**, 07, P07002 (2013), [arXiv:1304.6961].
[409] E. Segreto, Phys. Rev. D **103**, 4, 043001 (2021), [arXiv:2012.06527].

[410] L. Bäni *et al.* (RD42), J. Phys. Conf. Ser. **2374**, 1, 012172 (2022).

[411] A. Rogalski, Adv. Opt. Photon. **11**, 2, 314 (2019).

[412] V. Saraswat, R. Jacobberger and M. Arnold, ACS Nano 15:3, 3674–3708 (2021).

[413] G. Lutz, *Semiconductor Radiation Detectors*, Springer (1999), ISBN 978-3-540-64859-8.

[414] F. Hartmann, *Evolution of Silicon Sensor Technology in Particle Physics: Basics and Applications*, volume 293, Springer (2024), ISBN 978-3-031-59719-0, 978-3-031-59720-6.

[415] G. Lutz and R. Klanner, *Particle Physics Reference Library (Vol. 2, Ch. 5., Solid State Detectors), Eds. Fabjan, C. W. and Schopper, H.*, Springer Nature (2020), ISBN 978-3-030-35317-9, 978-3-030-35318-6.

[416] T. Kimoto and J. A. Cooper, *Fundamentals of Silicon Carbide Technology: Growth, Characterization, Devices, and Applications*, John Wiley & Sons (2014), ISBN 9781118313527.

[417] Landolt-Börnstein, Springer (Berlin), 2002, https://doi.org/10.1007/10832182_456 and https://doi.org/10.1007/10832182_458.

[418] C. Da Via *et al.*, Nucl. Instrum. Meth. **587**, 243 (2008).

[419] C. Damerell, Nucl. Instrum. Meth. A **342**, 78 (1994).

[420] M. Garcia-Sciveres and N. Wermes, Rept. Prog. Phys. **81**, 6, 066101 (2018).

[421] L. Rossi *et al.*, *Pixel Detectors – From Fundamentals to Applications*, Springer, Berlin (2006), ISBN 978-3-540-28332-4, 978-3-540-28333-1, URL https://doi.org/10.1007/3-540-28333-1.

[422] H.-G. Moser *et al.*, PoS **VERTEX2007**, 022 (2007).

[423] Y. Arai *et al.*, Nucl. Instrum. Meth. A **623**, 186 (2010).

[424] H. Sadrozinski, A. Seiden and N. Cartiglia, Rept. Prog. Phys. **81**, 2, 026101 (2018).

[425] M. Ferrero *et al.*, *Ultra-Fast Silicon Detectors*, CRC Press, Open Access, Creative Commons (2021), ISBN 978-1-003-13194-6.

[426] A. Lampis *et al.*, JINST **18**, 01, C01051 (2023).

[427] S. Zambito *et al.*, JINST **18**, 03, P03047 (2023).

[428] W. Riegler and G. Aglieri Rinella, JINST **12**, 11, P11017 (2017).

[429] R. Wunstorf, *Systematische Untersuchungen zur Strahlenresistenz von Silizium-Detektoren für die Verwendung in Hohenergiephysikexperimenten*, Ph.D. thesis, Universität Hamburg (1992), URL https://www-library.desy.de/preparch/desy/int_rep/fh1k-92-01.pdf.

[430] M. Moll, IEEE Trans. Nucl. Sci. **65**, 8, 1561 (2018).

[431] G. Kramberger, Initial acceptor removal in p-type siliconTalk at 26th CERN-RD50 Workshop, Santander (2015), https://indico.cern.ch/event/381195/contributions/905665/.

[432] W. Adam *et al.*, JINST **11**, P04023 (2016).

[433] G. Kramberger, *Particle Physics Reference Library (Vol. 2, Ch. 21., Solid State Detectors for High Radiation Environments), Eds. Fabjan, C. W. and Schopper, H.*, Springer Nature (2020), ISBN 978-3-030-35317-9, 978-3-030-35318-6.

[434] V. Radeka and N. Karlovac, Nuclear Instruments and Methods **52**, 1, 86 (1967), ISSN 0029-554X, URL https://www.sciencedirect.com/science/article/pii/0029554X67905617.

[435] V. Radeka, IEEE Transactions on Nuclear Science **15**, 3, 455 (1968), URL https://doi.org/10.1109/TNS.1968.4324970.

[436] A. van der Ziel, *Noise in Solid State Devices and Circuits*, John Wiley & Sons, Inc. (1986), ISBN 978-0471832348.

[437] C. C. Enz, F. Krummenacher and E. A. Vittoz, Analog Integr Circ Sig Process **8**, 83 (1995), URL https://doi.org/10.1007/BF01239381.

[438] W. Blum, L. Rolandi and W. Riegler, *Particle detection with drift chambers*, Particle Acceleration and Detection, Springer (2008), ISBN 978-3-540-76683-4, 978-3-540-76684-1, URL https://doi.org/10.1007/978-3-540-76684-1.

[439] V. Radeka, Ann. Rev. Nucl. Part. Sci. **38**, 217 (1988), URL https://doi.org/10.1146/annurev.ns.38.120188.001245.

[440] A. Rivetti, *CMOS: Front-End Electronics for Radiation Sensors*, CRC Press (2015), URL https://doi.org/10.1201/b18599.

[441] R. Wigmans, *Calorimetry*, International Series of Monographs on Physics, Oxford University Press (2017).

[442] S. Agostinelli *et al.* (GEANT4), Nucl. Instrum. Meth. A **506**, 250 (2003).

[443] J. Allison *et al.*, IEEE Trans. Nucl. Sci. **53**, 270 (2006).

[444] T. Gabriel and L. Charlton (1997).

[445] T. T. Böhlen *et al.*, Nucl. Data Sheets **120**, 211 (2014).

[446] A. Ferrari *et al.* (2005).

[447] J. Allison *et al.*, Nucl. Instrum. Meth. A **835**, 186 (2016).

[448] D. Buskulic *et al.* (ALEPH), Nucl. Instrum. Meth. A **360**, 481 (1995).

[449] A. M. Sirunyan *et al.* (CMS), JINST **12**, 10, P10003 (2017), [arXiv:1706.04965].

[450] M. A. Thomson, Nucl. Instrum. Meth. A **611**, 25 (2009), [arXiv:0907.3577].

[451] L. Linssen *et al.* (2012), [arXiv:1202.5940].

[452] H. L. Tran *et al.*, Eur. Phys. J. C **77**, 10, 698 (2017), [arXiv:1705.10363].

[453] M. Aleksa *et al.*, Eur. Phys. J. Plus **136**, 10, 1066 (2021), [arXiv:2109.00391].

[454] M. T. Lucchini *et al.*, JINST **15**, 11, P11005 (2020), [arXiv:2008.00338].

[455] W.R. Nelson, H. Hirayama, and D.W.O. Rogers, SLAC-265 (1985) .

[456] ATLAS Collab., CERN/LHCC 96-41 (1996).

[457] D. Hitlin *et al.*, Nucl. Instrum. Meth. **137**, 225 (1976).

[458] W. J. Willis and V. Radeka, Nucl. Instrum. Meth. **120**, 221 (1974).

[459] R. Wigmans, *Calorimetry: Energy Measurement in Particle Physics*, Inter. Series of Monographs on Phys. **107**, Second Edition, Oxford Schlarship Online (2017).

[460] R.-Y. Zhu, Nucl. Instrum. Meth. **A413**, 297 (1998).

[461] R.-Y. Zhu, Journal of Physics: Conference Series **587**, 012055 (2015).

[462] CMS Collab., CERN/LHCC 97-33 (1997).

[463] C. Leroy and P. Rancoita, Rept. Prog. Phys. **63**, 505 (2000).

[464] F. Sefkow and F. Simon, *Calorimeters*, in Fleck I., Titov M., Grupen C., Buvat I. (eds) Handbook of Particle Detection and Imaging, Springer (2021), ISBN 978-3-319-47999-6.

[465] C. Adloff *et al.* (CALICE), JINST **8**, 07005 (2013).

[466] T. A. Gabriel *et al.*, Nucl. Instrum. Meth. **A338**, 336 (1994).

[467] F. Ariztizabal *et al.* (RD-34), Nucl. Instrum. Meth. **A349**, 384 (1994).

[468] F. Sefkow and F. Simon (CALICE), J. Phys. Conf. Ser. **1162**, 1, 012012 (2019), [arXiv:1808.09281].

[469] A. White *et al.* (CALICE), JINST **18**, 11, P11018 (2023), [arXiv:2209.15327].
[470] CMS, CERN-LHCC-2017-023, CMS-TDR-019 (2017).
[471] N. Akchurin *et al.*, Nucl. Instrum. Meth. **A399**, 202 (1997).
[472] A. Artamonov *et al.*, JINST **3**, P02010 (2008).
[473] B. Aubert *et al.*, Nucl. Instrum. Meth. **A321**, 467 (1992).
[474] C. W. Fabjan *et al.*, Nucl. Instrum. Meth. **141**, 61 (1977).
[475] J. Brau *et al.*, Nucl. Instrum. Meth. **A238**, 489 (1985).
[476] H. Brückmann and H. Kowalski, ZEUS Int. Note 86/026 DESY, Hamburg (1986).
[477] R. Wigmans, Nucl. Instrum. Meth. **A259**, 389 (1987).
[478] R. Wigmans, Nucl. Instrum. Meth. **A265**, 273 (1988).
[479] J. E. Brau and T. A. Gabriel, Nucl. Instrum. Meth. A **275**, 190 (1989).
[480] J. C. Brient, R. Rusack and F. Sefkow, Ann. Rev. Nucl. Part. Sci. **68**, 271 (2018).
[481] E. Fretwurst *et al.* (1989), URL http://cds.cern.ch/record/368113.
[482] E. Borchi *et al.* (SICAPO), Nucl. Instrum. Meth. **A279**, 57 (1989).
[483] H. Abramowicz *et al.* (2013), [arXiv:1306.6329].
[484] N. Alipour Tehrani *et al.* (CLICdp) (2017), CLICdp-Note-2017-001.
[485] N. Bacchetta *et al.* (2019), [arXiv:1911.12230].
[486] https://twiki.cern.ch/twiki/bin/view/CALICE/CaliceDetectors.
[487] C. Adloff *et al.* (CALICE), JINST **5**, P05004 (2010), [arXiv:1003.2662].
[488] M. Chefdeville *et al.* (CALICE), Nucl. Instrum. Meth. A **939**, 89 (2019), [arXiv:1901.08818].
[489] G. Baulieu *et al.*, JINST **10**, 10, P10039 (2015), [arXiv:1506.05316].
[490] B. Acar *et al.* (CMS, CALICE), JINST **18**, 08, P08014 (2023), [arXiv:2211.04740].
[491] B. Acar *et al.* (CMS HGCAL), JINST **19**, 04, P04015 (2024), [arXiv:2312.14622].
[492] C. Adloff *et al.* (CALICE), JINST **8**, P09001 (2013), [arXiv:1305.7027].
[493] H. Abramowicz *et al.*, Nucl. Instrum. Meth. **180**, 429 (1981).
[494] B. Andrieu *et al.* (H1 Calorimeter Group), Nucl. Instrum. Meth. A **336**, 499 (1993).
[495] C. Cojocaru *et al.* (ATLAS Liquid Argon EMEC/HEC), Nucl. Instrum. Meth. A **531**, 481 (2004), [arXiv:physics/0407009].
[496] C. Adloff *et al.* (CALICE), J. Instr. **7**, 09, P09017 (2012).
[497] H. L. Tran *et al.*, The European Physical Journal C **77**, 10, 698 (2017).
[498] S. Lai *et al.* (CALICE), JINST **19**, P04037 (2024), [arXiv:2403.04632].
[499] M. Aamir *et al.* (CMS HGCAL, CALICE AHCAL), JINST **19**, 11, P11025 (2024), [arXiv:2406.11937].
[500] S. Lai *et al.* (CALICE), JINST **19**, 10, P10027 (2024), [arXiv:2407.00178].
[501] P. Mockett, SLAC-267, 335 (1983).
[502] D. E. Groom, Nucl. Instrum. Meth. **A572**, 633 (2007), erratum: Nucl. Instrum. Meth. **A593**, 628 (2008).
[503] R. Wigmans, *Proc. 7th Inter. Conf. on Calorimetry in High Energy Physics*, 182 World Scientific, River Edge, NJ, (1998);.
[504] S. Lee, M. Livan and R. Wigmans, Rev. Mod. Phys. **90**, 2, 025002 (2018).

[505] S. Lee *et al.*, Nucl. Instrum. Meth. A **866**, 76 (2017), [arXiv:1703.09120].

[506] M. Antonello *et al.*, JINST **15**, 06, C06015 (2020).

[507] E. Bernardi *et al.*, Nucl. Instrum. Meth. **A262**, 229 (1987).

[508] M. Chefdeville *et al.* (CALICE), JINST **10**, 12, P12006 (2015), [arXiv:1509.00617].

[509] T. Akesson *et al.*, Nucl. Instrum. Meth. **A262**, 243 (1987).

[510] D. Acosta *et al.*, Nucl. Instrum. Meth. **A308**, 481 (1991).

[511] R. Dubois *et al.*, IEEE Trans. Nucl. Sci. **33**, 194 (1986).

[512] B. Andrieu *et al.* (H1 Calorimeter Group), Nucl. Instrum. Meth. A **336**, 460 (1993).

[513] A. Bernstein *et al.* (ZEUS Barrel Calorimeter Group), Nucl. Instrum. Meth. A **336**, 23 (1993).

[514] J.-b. Liu (CDF), in "7th International Conference on Calorimetry in High-Energy Physics (ICCHEP 97)," 237–240 (1997).

[515] S. Abachi *et al.* (D0), Nucl. Instrum. Meth. A **324**, 53 (1993).

[516] G. Aad *et al.* (ATLAS), JINST **3**, S08003 (2008).

[517] S. Abdullin *et al.* (USCMS, ECAL/HCAL), Eur. Phys. J. C **60**, 359 (2009), [Erratum: Eur.Phys.J.C 61, 353–356 (2009)].

[518] H. Abramowicz *et al.* (ZEUS), Phys. Lett. B **718**, 915 (2013), [arXiv:1210.5511].

[519] E. Shibamura *et al.*, Nucl. Instrum. Methods **A316**, 184 (1975).

[520] L. S. Miller, S. Howe and W. E. Spear, Phys. Rev. **166**, 871 (1968).

[521] A.M. Kalinin *et al.*, ATLAS-LARG-NO-058 (1996).

[522] K. Yoshino, U. Sowada and W. F. Schmidt, Phys. Rev. **A14**, 438 (1976).

[523] A.O. Allen *et al.*, NSRDS-NBS-58 (1976).

[524] P. Benetti *et al.*, Nucl. Instrum. Methods **A32**, 361 (1993).

[525] A. Yamamoto, Nucl. Instrum. Meth. **A453**, 445 (2000).

[526] A. Yamamoto and Y. Makida, Nucl. Instrum. Meth. **A494**, 255 (2002).

[527] T. M. Taylor, Phys. Scripta **23**, 459 (1981).

[528] R. L. Gluckstern, Nucl. Instrum. Meth. **24**, 381 (1963).

[529] V. Karimaki, Nucl. Instrum. Meth. **A410**, 284 (1998).